

# **Composite Crashworthy Structures: Manufacture and Modelling**

by

Michael Silcock,  
BEng. Aerospace (Hons)

Submitted in fulfilment of the requirements for the degree of  
Doctor of Philosophy

Deakin University

December, 2006

**DEAKIN UNIVERSITY**  
**CANDIDATE DECLARATION**



I certify that the thesis entitled

Composite Crashworthy Structures: Manufacture and Modelling

submitted for the degree of

Doctor of Philosophy

is the result of my own work and that where reference is made to the work of others, due acknowledgment is given.

I also certify that any material in the thesis which has been accepted for a degree or diploma by any university or institution is identified in the text.

Full Name.....

Signed .....

Date.....

## **Publications and Patents from this Thesis**

Silcock, M. Hall, W. and Fox, B. L., *Finite Element Modelling of Composite Tubular Crash Structures with an Explicit Code*, Proceedings of the 6th Annual Automotive Composites Conference (Society of Plastics Engineers), Detroit, Michigan. September, (2006).

Silcock, M. Hall, W. Fox, B. L. and Warrior, N. *Finite Element Modelling of Metallic Tubular Crash Structures with an Explicit Code*, International Journal of Vehicle Safety, accepted 15/05/06 - in press.

Silcock, M. Garschke, C. Hall, W. and Fox, B. L. *Rapid Composite Tube Manufacture Utilising the Quickstep Process*, Journal of Composite Materials, accepted 22/03/06 - in press.

Silcock, M. Garschke, C. Hall, W. and Fox, B. L. *A Novel Method of Tube Manufacture for Vehicle Crashworthiness Utilising the Quickstep Process*. Proceedings of the 26<sup>th</sup> International SAMPE Europe conference, Paris, France, April 5-7, pp. 239-244. (2005).

Silcock, M. *Part and Parcel*, In Crash Test Technology International, September edition, pp. 66-67. (2006).

Silcock, M. and Graham, N. *Composite Tube Production*, Quickstep Technologies Pty Ltd, International Patent Application. Patent no. PCT/AU2006/000382. (2006).

## **Acknowledgments**

I would like to thank my supervisors, Bronwyn Fox and Wayne Hall, whose guidance and patience was unwavering.

Thanks to the Deakin University staff; Peter Hodgson, Marilyn Fisher, John Vella, John Whale, Rob Pow and Gabby.

Special thanks to my colleagues who would regularly listen to my concerns over a coffee and a game of table tennis; in no particular order Mike Pereira, Ash Denmead, Tim DeSouza and Mandy Herring.

Thanks to Aaron Brighton, Brett Smith and Ben Adamson for their assistance.

I would to thank my family; Peter, Jackie, Caroline, Richard and Jackson for all their love, support and encouragement. Last but by no means least, special thanks to my partner Farrell, for her love, perseverance and understanding throughout this process.

*Dedicated to the loving memory of Granny Mee and Gumbar*

# Table of Contents

<b>1</b>	<b>Introduction</b>	<b>1</b>
1.1	Thesis Objectives	7
<b>2</b>	<b>Literature Review</b>	<b>8</b>
2.1	Accidents are a Part of Life...	8
2.1.1	Crashworthiness	8
2.1.2	Frontal Impacts	9
2.1.3	Limits of Human Tolerance	11
2.1.4	The Weight of Safety	12
2.1.5	Composites and Crashworthiness	13
2.2	Crush Performance and Characteristics of Tubes	13
2.2.1	Specific Energy Absorption - SEA	14
2.3	Metallic Tubes	15
2.4	Composite Tubes	18
2.4.1	Failure Modes & Resulting Energy Absorption	21
2.4.2	Friction Effects	26
2.4.3	Parameters Affecting Energy Absorption	29
2.5	Current Methods of Composite Tube Manufacture	40
2.5.1	The Autoclave	40
2.5.2	Pultrusion	42
2.5.3	The Quickstep™ Process	43
2.6	Finite Element Modelling	45
2.6.1	Modelling of Composite Materials	46
2.6.2	Modelling of Composite Tubes	47
2.6.3	Modelling of Composite Delamination	58
2.7	Summary	61
<b>3</b>	<b>Materials and Characterisation</b>	<b>64</b>
3.1	Material Types	64
3.2	Material Characterisation	65
3.2.1	Specimen Preparation	66
3.2.2	Digital Speckle Photography (DSP)	67
3.2.3	In-plane Tensile Tests	70
3.2.4	In-plane Compressive Tests	72
3.2.5	Shear Tests	75
3.2.6	Through-Thickness Compression Tests	77
3.2.7	3-Point Bend Tests	78
3.2.8	Double Cantilever Beam Tests	79
3.2.9	End Notch Flexure Tests	81
3.3	Discussion	82
<b>4</b>	<b>Rapid Composite Tube Manufacture</b>	<b>84</b>
4.1	The Process	84
4.2	Test Specifications	90
4.3	Results	93

4.3.1	Cure Cycle Optimisation	94
4.3.2	Lay-up Optimisation	97
4.3.3	Specific Energy Absorption Optimisation	100
4.4	Discussion	109
4.4.1	Rapid Tube Manufacture	109
4.4.2	Toray G83C Crush Performance	112
<b>5</b>	<b>Finite Element Modelling</b>	<b>115</b>
5.1	Composite Tube Models	116
5.1.1	Model Geometry and Mesh Specification	117
5.1.2	Initiator Modelling	120
5.1.3	Material Modelling	123
5.1.4	Delamination Modelling	131
5.1.5	Contact and Friction	132
5.2	Modelling Detail	133
5.3	Summary	134
<b>6</b>	<b>Delamination Modelling</b>	<b>135</b>
6.1	Delamination Modelling Methodology	135
6.2	Delamination Modelling Results	141
6.2.1	Double Cantilever Beam Simulations	141
6.2.2	End Notch Flexure Simulations	146
6.3	Summary	150
<b>7</b>	<b>Force-Based Delamination - Tube Modelling</b>	<b>152</b>
7.1	Results	153
7.1.1	Flat-Platen Simulations	153
7.1.2	Plug Initiator Simulations	161
7.2	Discussion	179
<b>8</b>	<b>Strain-Controlled Delamination - Tube Modelling</b>	<b>186</b>
8.1	Strain-Controlled Spotweld Behaviour	187
8.2	Results	189
8.2.1	Flat-platen	189
8.2.2	Plug Initiator Simulations	192
8.3	Discussion	202
<b>9</b>	<b>Conclusions and Further Work</b>	<b>209</b>
9.1	Thesis Summary	210
9.2	Conclusions	214
9.2.1	Manufacture	214
9.2.2	Modelling	214
9.3	Further Work	217
<b>A1</b>	<b>Finite Element Modelling of Metallic Tubular Crash Structures with an Explicit Code</b>	<b>220</b>
<b>A2</b>	<b>CFRM Properties and Behaviour</b>	<b>239</b>

<b>A3</b>	<b>MATLAB Input Deck Generator</b>	<b>244</b>
<b>A4</b>	<b>Effective Beam Stiffness Calculation</b>	<b>259</b>
<b>A5</b>	<b>Force-Based Delamination - Tube Modelling Results</b>	<b>261</b>
<b>A6</b>	<b>Strain-Controlled Delamination - Tube Modelling Results</b>	<b>269</b>
	<b>References</b>	<b>274</b>

## **Abstract**

Composites can provide notable reductions in structural weight together with significant improvements in crashworthiness. However, the automotive industry is yet to fully exploit this class of material due to the high associated cost of component manufacture and design. The aim of this research was to develop enabling technologies which will allow manufacturers to design, test and implement composite material crash structures economically. Two aspects of composite production are investigated; manufacture and modelling.

A novel method for producing composite tubular structures utilising the Quickstep™ process was developed with which carbon/epoxy Toray G83C tubes can be cured in 7 minutes – 95% quicker than autoclave curing. Optimisation of the process was performed through DMTA, DSC, porosity and axial crush testing of the tubular members (allowing the crashworthiness of the Toray material to be evaluated). The reduction in cure cycle time means that the rate-limiting step is shifted to the lay-up process; reducing production costs and forcing further progression.

Likewise, the development of accurate modelling techniques for simulating the crushing response of composite materials will reduce the need to prototype components, delivering more efficient designs from the first iteration. Initially, a simple force-based delamination approach was adopted and its ability to accurately represent the interlaminar material was validated through the simulation of various coupon tests in LS-DYNA. Development of a holistic modelling methodology for the simulation of the axial crush of composite tubes was then undertaken. This model employed a multi-shell approach,

inclusive of the features pertinent to the crushing process, which was used to simulate the axial crushing of Toray G83C carbon/epoxy and Continuous Filament Random Mat (CFRM) glass/polyester tubes on a flat-platen and various radius plug-initiators.

Despite correctly reproducing the behaviour in coupon simulations and accurately predicting the failure mode in all but one instance, poor steady-state load predictions were observed. Specifically, the force-based delamination approach adopted incorrectly considered the Mode II interlaminar deformation. This problem was rectified by controlling the interlaminar material using a yield stress and plastic strain limit; ensuring the correct energy is absorbed through interlaminar material deformation. Significant improvements in the interlaminar material behaviour and load-displacement response were observed while in several instances, a change in the failure mode necessitated recalibration of the material model. It was found that a simple force-based delamination model can accurately reproduce the behaviour in regions where a Mode I delamination is expected but significantly underestimates the energy absorbed through Mode II deformation.

# 1 Introduction

It has been estimated that 1.2 million people die as a result of vehicular accidents every year [1]. In the year 2004, 42,636 people died on US roads [2] accounting for 95% of all transportation fatalities [3] and the leading cause of death for every age-group between 3 and 33 [2]. In the same year 1,596 people died on Australian roads [4]. For Australians alone, the annual cost of vehicular accidents has been estimated at AUS\$10 billion [5]. Furthermore, despite significant improvements in active safety systems, which aid in accident avoidance, the number of fatal accidents is steadily increasing [2]. Not surprisingly, the public are more aware of vehicle safety now than ever before and consumers currently evaluate vehicles based equally on fuel economy, performance, quality and safety [6].

In the event of an accident, passive safety systems are designed to dissipate the impact energy and protect the vehicle occupants. For many years, steel has been the material of choice for reasons of low cost and ease of production. In a frontal impact (58% of the fatal accidents in the US [2]), energy is absorbed through the progressive plastic folding of the chassis rails [7]. In this type of impact, the chassis rails can absorb as much as 60% of the impact energy making their behaviour critical to the survival of the occupants [8]. Extensive research has focussed on improving the crash performance of steel, which in recent times has provided only incremental improvements. However, despite their widespread use, metallic crash structures exhibit characteristics that are undesirable to crashworthiness engineers.

Chassis rails are often realistically idealised as tubes under axial compression for research purposes. Under this loading, metallic structures typically generate a highly oscillatory load-displacement response, a result of the plastic folding. Peak loads can often be a multiple of the average crush load from which the absorbed energy is calculated, as shown in Figure 1.1. Furthermore, as these loads translate to instantaneous decelerations, ensuring that the peak loads remain within the limits of human tolerance means that the average load is well below the optimum value. Consequently, the efficiency of metallic crash structures is less than ideal.

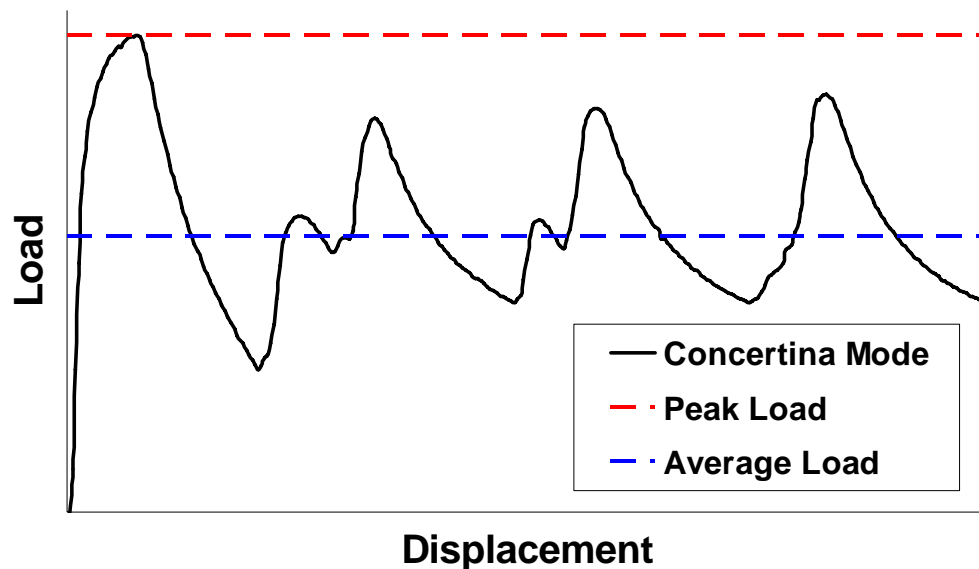


Figure 1.1. Load-displacement graph of a concertina mode collapse showing the difference between the peak and average loads - translating to occupant decelerations.

In addition to safety improvements, the automotive sector is now under pressure from increasingly stringent emission laws to reduce vehicular structural weight. This has forced manufacturers to investigate new materials such as high strength steels, aluminiums and other lightweight metals, which have shown the potential for a degree of weight reduction. Composite materials, on the other hand, have the ability to simultaneously provide significant improvements in both structural weight and crashworthiness.

In contrast to the relatively poor crashworthiness characteristics of metallic members, composites typically produce significantly higher levels of Specific Energy Absorption (SEA [kJ/kg]) and do so with a comparatively constant load profile. This leads to lighter, more efficient crash structures in which the average crush load is close to the peak crush load. Subsequently, crash structures can be designed to more closely approach human limits in deceleration - making composite material crash energy management structures highly desirable. The most compelling demonstration of the potential for composites to improve vehicle safety is in the extraordinary levels of safety in Formula 1 racing. Despite this, composites only appear in the crash structures of a handful of ultra-high-performance production vehicles. Without question, the fundamental reason for the lack of widespread use of composites in the automotive industry is cost [9].

First and foremost, the high associated cost of composite component manufacture prohibits manufacturers from extensive prototyping programmes resulting in final products that are not optimised, failing to justify the financial outlay. Secondly, the difficulty in predicting the crushing behaviour of composite materials through computational methods means manufacturers have little choice but to continue using the well known metallic materials. In its most fundamental form, the aim of this thesis is to reduce the associated cost of composite component processing and manufacture. However, in order to achieve this, a multi-faceted approach has been adopted – namely addressing both manufacture and modelling independently.

## *Manufacture*

The recent development of a new process for curing composite materials has shown the potential to significantly reduce cure cycle times, increasing production rates and thus reducing end part cost. The Quickstep™ process ([www.quickstep.com.au](http://www.quickstep.com.au)) is an alternative to autoclave curing which makes use of a liquid heat transfer medium, rather than nitrogen, to heat the part. The higher coefficient of heat transfer of liquid means that the part can reach the desired temperature significantly quicker than in autoclave processing. At the beginning of this study, the tool designed for the Quickstep plant was only capable of curing relatively flat and shallow panels. Subsequently, attention was given to adapting this technology to the curing of tubular profiles which could be used in crashworthy structures. An optimisation study revealed that for the chosen carbon/epoxy material, a cure cycle of 7 minutes was possible with only a minor increase in porosity.

To this effect, Chapter Three will introduce both the carbon/epoxy (specifically Toray G83C) and glass/polyester materials that are studied throughout this thesis. Furthermore, it presents work on the characterisation of the mechanical (mostly in-plane) properties of the carbon/epoxy which satisfies the requirements of the modelling efforts presented in later chapters. Chapter Four will cover the specifics of the manufacturing process along with the results of the optimisation study. In this study, one form of quantifying the production improvements is through comparison of the energy absorption of Toray G83C in axial crush. Subsequently, the crashworthiness of this material is presented. The results from these studies are used in the development of a holistic modelling methodology for the accurate reproduction of the behaviour of composite materials under axial crush.

## *Modelling*

Over the past two decades, many modelling approaches have been tested [10-12] and yet there is still no universal approach which can reproduce the stiffness, strength or post-failure response of composites in a general shape. This stems from both the anisotropy and quasi-brittle material response of composites, together with the numerous failure mechanisms that are interactively controlled by the various intrinsic and extrinsic parameters that exist in a given test. Subsequently, representation of the many fracture, friction, delamination and folding processes that can take place in a composite tube crush is highly complex [13-15].

The selection of the modelling approach can dictate the number of these failure mechanisms that can be included. For instance, representation of the entire tube wall thickness with a single shell element, though very computationally efficient, cannot predict delamination. The approach best suited to capturing the real behaviour of composite tubes is a multiple-shell model in which a shell is used to represent each lamina in the tube wall [16]. Therefore, the choice of the delamination modelling approach becomes critical. For its simplicity and usefulness, a force-based approach is adopted in which normal and shear interface forces determine the onset of delamination. However, the typical application of this approach involves numerically tying adjacent nodes until failure, resulting in the incorrect laminate stiffness.

A method is presented in which the correct interlaminar elasticity is reproduced and confirmed by simulations of interlaminar fracture toughness tests. This approach is then substituted into full simulations of the experimental crush tests presented in Chapter Four and the results compared. The elastic force-

based approach presented correctly reproduces the behaviour under a Mode I loading in the tube simulations, but falls extremely short of capturing the correct Mode II loading. As a result, an elastic strain-controlled delamination is adopted and the improved results are presented.

The global modelling methodology is introduced in Chapter Five and specific difficulties encountered in achieving a robust simulation. The selected methodology was developed to ensure the inclusion of the features pertinent to a tube crush experiment. Additionally, this chapter introduces the delamination modelling methodology and the method by which it is applied.

Chapter Six presents the interlaminar fracture toughness simulations, confirming both the correct flexural stiffness and failure behaviour are achieved by this relatively simple delamination approach.

The delamination approach is then employed in tubular crush simulations and the results are presented in Chapter Seven. Specific attention is given to the complete and accurate representation of the observed crushing response and steady-state crush loads. Subsequently, the inability for the force-based delamination model to reproduce the correct Mode II interlaminar deformation is highlighted. The appropriateness of the Mode II End Notch Flexure test is therefore questioned with respect to its reproduction of the deformation observed in a tube crush test.

Chapter Eight presents the changes made to the delamination modelling methodology in order to account for micro-cracking and hackles which appear under shear loading. Impressive improvements are made in some cases while in others, a change in the predicted failure mode highlights the need for repeated recalibration of the material behaviour.

## 1.1 Thesis Objectives

---

The aim of this thesis is to develop enabling technologies which can reduce the associated cost of composite component manufacture, thus allowing the exploitation of their benefits in the automotive industry by;

- Reducing the cost of manufacture through shorter cure cycles,
- Providing industry with further information on the performance of composite materials in crash structures,
- Providing advanced techniques for the simulated reproduction of the behaviour of composite materials in crash structures.

These goals will be accomplished by completing the following tasks;

- Develop a manufacturing method for accelerated curing of composite tubular structures,*
- Characterise the experimental crush performance of Toray G83C,*
- Develop a force-based delamination modelling methodology that accurately reproduces the interlaminar stiffness,*
- Develop a holistic modelling methodology of axial tube crush which includes the features pertinent to the crushing process,*
- Validate the performance of the combined delamination and tubular modelling approaches through simulation of experimental axial tube crush tests.*

## **2 Literature Review**

### **2.1 Accidents are a Part of Life...**

---

The number of vehicles on the road and the distance travelled by each vehicle is increasing. The National Centre for Statistics and Analysis (NCSA) reports that during the ten year period 1990 to 2000, the number of vehicles registered in the USA increased by 18%. For the same period, the distance travelled by each vehicle increased by 25% [3]. Despite significant advances in vehicle safety, the number of fatal accidents is steadily increasing [2].

In 2004, there were 42,636 fatalities as a result of vehicle related accidents on USA roads [2]. This number accounts for 95% of all transportation fatalities including air (2%) and rail (2%) accidents [3] and places it fourth in causes of death behind heart disease, cancer and stroke [6]. Not surprisingly, the public are more aware of vehicle safety now than ever before and consumers currently evaluate vehicles based equally on fuel economy, performance, quality and crashworthiness [6].

#### **2.1.1 Crashworthiness**

The ability of a structure to absorb impact energy is termed crashworthiness [17]. In terms of the automotive industry, this definition is refined slightly to “the ability for a structure to plastically deform and maintain sufficient survival space for its occupants in an impact” [6]. The energy is dissipated or absorbed through the progressive plastic deformation of the structure [7]. Consequently, over the past years, manufacturers have contributed significant amounts of time

and effort towards ensuring that vehicles conform to the applicable safety regulations.

The most significant development in the history of crashworthiness was the inclusion of seatbelts as an option in 1956. In the year 2004, an estimated 15,434 lives were saved on US roads by seatbelts, and almost 40% of the occupants in fatal accidents that year were unrestrained. Had all passengers worn seatbelts, an estimated 21,273 lives would have been saved. Of particular interest is the frontal collision, the scenario in 58% of fatal passenger vehicle accidents in the USA in 2004 [2].

### **2.1.2 Frontal Impacts**

In a low-speed frontal impact (below ~30km/h), the urethane bumper bars and their metallic structural reinforcements are designed to absorb the energy without affecting the greater structure (chassis rails, passenger compartment etc.). In a severe impact (eg. the EuroNCAP requirements of a 64km/h frontal crash into an offset, solid object [18] – see Figure 2.1) the behaviour of the entire frontal structure is critical to the occupant's survivability. This is primarily the function of the chassis rails which dissipate as much as 60% of the energy in a frontal impact [8].



Figure 2.1. Image taken during EuroNCAP crash test. (Image taken from <http://crash.citroen1.info/C8/>)

### 2.1.2.1 Chassis Rails

At high impact speeds, the behaviour of the entire frontal section and to a lesser degree, the entire car, contribute to ensuring the safety of its occupants. The frontal structure (everything forward of the firewall/A-pillars – excluding engine – see Figure 2.2) must collapse in such a way that the maximum energy is absorbed without the occupant experiencing intolerable decelerations, as described in the following section. In an ideal crashworthy structure, the chassis rails would collapse in a manner that, regardless of speed or angle of impact, the deceleration remains constant and within the limits of human tolerance.



Figure 2.2. Two images of the frontal structures in different modern vehicles showing the bumper support, chassis rails and firewall. (left image taken from [www.sweden.se](http://www.sweden.se) – right photo taken by M.Silcock at JEC Expo, Paris, 2005)

The chassis rails can be idealised as tubular structures under axial load [19]. However, it must be acknowledged that this is a significant simplification of what takes place in a real vehicular impact. Significant work has been done concerning the design and material selection of these tubular structures, which has indirectly improved the performance of the passenger cell. The design objective for the passenger cell (everything between the firewall and rear seat) dictates that no foreign objects should breach its periphery [20]. However, this objective can be compromised by trade-offs in vehicle weight, manufacturing methods and costs, and component packaging [6]. Therefore, it is vital that the chassis rails dissipate the crash energy in a manner which ensures a constant deceleration within the limits of human tolerance, but equally importantly, they must ensure the impact is stopped within a certain distance, avoiding penetration of the passenger cell.

### **2.1.3 Limits of Human Tolerance**

In a frontal impact between a vehicle and a rigid object, the kinetic energy of the vehicle is dissipated primarily through the plastic deformation of the frontal crash structure. The profile of this energy transfer and the time over which it occurs are critical to the safety of the occupants.

The Federal Motor Vehicle Safety Standards (FMVSS) dictate that an occupant shall not experience more than a 60g resultant chest deceleration [21] or a 1020kg femur load [8]. Likewise, the human brain can only tolerate a certain deceleration before irrecoverable damage is likely to result. Various methods of quantifying the damage have been investigated, but the Head Injury Criterion (HIC) is the most widely accepted of these methods [3]. However, it is still in need of further work as it does not consider the rotational deceleration

produced as the head rolls forward chin-down. This criterion can be seen below in Equation 2.1.

$$HIC = \max(t_2 - t_1) \left( \frac{1}{t_2 - t_1} \int_{t_1}^{t_2} a(t).dt \right)^{2.5} < 1000 \quad (2.1)$$

In any case, minimisation of the HIC comes from minimising the impulse transferred to the vehicle occupant. This is ensured by maximising the duration over which the impact takes place, consequently minimising the force transferred to the occupant, according to Newton's second law. Similarly, reduction of the relative velocity of impact and the vehicular weight reduces the kinetic energy, effectively producing the same outcome.

#### **2.1.4 The Weight of Safety**

In an effort to increase the survivability of a crash, various passive and active safety technologies have been developed (including but not limited to seat belts, collapsible steering columns, blind-spot detection devices, airbags, engine ejection devices, Anti-Lock Braking systems (ABS) and collision prevention systems). While these systems contribute to a vehicle's safety and crashworthiness, they also contribute to a vehicle's weight which generally increases with each model year [22]. The effect of adding weight to a vehicle has numerous ramifications. Larger brakes, engines, hardware mounts, heat dissipation systems, fuel tanks, wheels and power assisting systems are required which further contribute to a vehicle's weight in a cascade effect. Similarly, reducing a vehicle's weight by a small percentage in one component produces a cascade effect where the effective reduction is a multiple of the initial reduction [22, 23]. Furthermore, stringent emissions laws are forcing manufacturers to improve vehicle efficiency; one effective method is to reduce

vehicular weight. Therefore, automotive manufacturers are seeking materials which can provide improved crashworthiness while simultaneously reducing structural mass.

### **2.1.5 Composites and Crashworthiness**

One class of materials capable of significant improvements in crashworthiness combined with equally impressive reductions in mass is composites. Composite tubes have demonstrated an ability to absorb energy in a highly efficient manner while producing an almost ideal crush response [24, 25]. Consequently, composites are well-suited to vehicle crashworthiness applications potentially providing increased occupant survivability together with a significant reduction in mass. When correctly designed, carbon-fibre can save 75-80% weight over steel, up to 50% over fibreglass and between 30-40% over aluminium [23]. Benefits such as manufacturing quality, styling enhancements, improved corrosion and dent resistance [21], infinite fatigue life [26, 27] and improved safety [22, 28] exemplify the advantages of composites. When coupled with the emissions requirements, it is clear that these materials hold many of the answers for not only the auto-manufacturers but potentially all sectors of transportation. The primary aim of this literature review is to identify the key historical improvements in vehicle crashworthiness and isolate the parameters critical to the performance of such structures.

## **2.2 Crush Performance and Characteristics of Tubes**

In order to improve the crashworthiness of consumer vehicles through new materials technology, it is first necessary to completely understand the behaviour of the existing materials and draw conclusions on their limitations. This benchmarking process provides a standard to which comparisons can be

made. Further to this, gaining an understanding of the experimental behaviour of such structures is beneficial as it provides a foundation on which finite element modelling work can be built. A review of the research completed to date, on the crashworthiness behaviour of both metallic and composite tubular structures, is undertaken and compared in the following sections.

### 2.2.1 Specific Energy Absorption - SEA

The most useful method of comparing the performance of structures in a crashworthiness context, particularly where weight is a consideration, is through Specific Energy Absorption values or SEA (some literature refers to this value as  $E_s$ ). This is a measure of the energy absorbed, per unit mass of material, the units for which are kJ/kg, as shown in Equation 2.2.

$$SEA = \frac{\text{Energy}_{\text{absorbed}}}{\text{Mass}_{\text{of}_{\text{crushed}_{\text{material}}}}} \left[ \frac{\text{kJ}}{\text{kg}} \right] \quad (2.2)$$

Consider a frontal impact between a 2000kg vehicle and a solid immovable object where the vehicle is travelling at 60km/h. In its most basic form, 278kJ (using  $\frac{1}{2}mv^2$ ) of energy must be removed from the system in order to stop the vehicle. With a SEA value of 20kJ/kg, 13.8kg of the absorbent material would be required to dissipate the kinetic energy. However, if the SEA was significantly increased to 80kJ/kg, then the total mass required reduces to just 3.47kg, demonstrating the usefulness and importance of this value, and the need to develop materials with high SEA values.

In recent years, automobiles have been required to satisfy strict legislation in relation to occupant safety. As a result, tubular metallic crash structures are now commonly employed to absorb kinetic energy in frontal impact events

[29]. Axial crushing of metallic tubes has been shown to be representative of the behaviour of crash structures in frontal impacts [19].

## 2.3 Metallic Tubes

---

When crushed under an axial load, metallic tubes absorb energy by progressive plastic folding during the post-buckling phase of the collapse [30] and extensive research has been carried out on their behaviour [7, 29, 31]. Additionally, several theoretical models of the collapse have been developed [32, 33].

Metallic tubes fail in one of three modes when axially compressed. These modes are: axisymmetric progressive collapse (concertina), asymmetric progressive collapse (diamond) and catastrophic buckling (Euler). The failure mode is determined primarily by the  $t/D$  ratio (thickness to diameter –  $D/t$  or  $D/h$  in some literature) but the  $D/L$  ratio (diameter to length) also influences the collapse mode [3]. Figure 2.3 shows a mode classification chart for circular aluminium tubes which allows accurate prediction of the failure mode based on geometrical properties. A region of ‘mixed mode’ has also been identified in which both progressive failure modes can be observed [34]. Axisymmetric folding typically produces the highest levels of energy absorption [34].

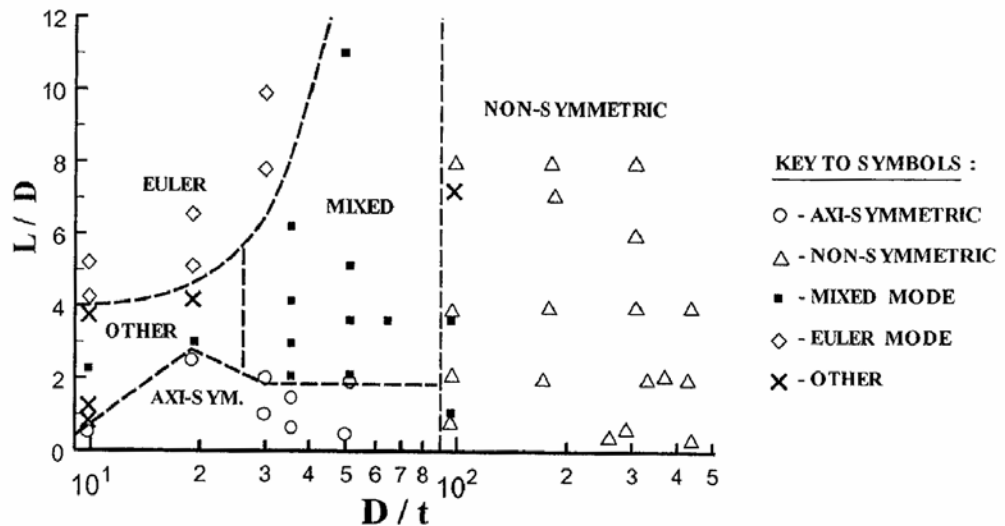


Figure 2.3. Mode classification chart for Aluminium circular tubes [35].

In crashworthiness applications, a stable crush force is highly desirable as it translates to a constant deceleration which suggests that the response of metallic tubes is less than ideal. Both progressive crush modes tend to produce significant initial peak loads with the subsequent behaviour varying significantly. Following the initial peak, the subsequent folds are produced at a considerably lower load – a result of the presence of fold initiators in the form of the previous folds. Typical load-displacement curves for both diamond and concertina modes produced in circular steel tubes can be seen in Figure 2.4. The tubes shown possess different geometric properties and therefore are not directly comparable. The large oscillations created by each distinct fold in concertina mode can be observed together with the smaller and less frequent oscillations produced by diamond mode collapse. The behaviour and performance of tubes which fail by concertina or diamond modes, are extremely repeatable [31]. Steel and aluminium metallic tubes are reported to have typical SEA values of between 15 and 30kJ/kg respectively [31, 36].

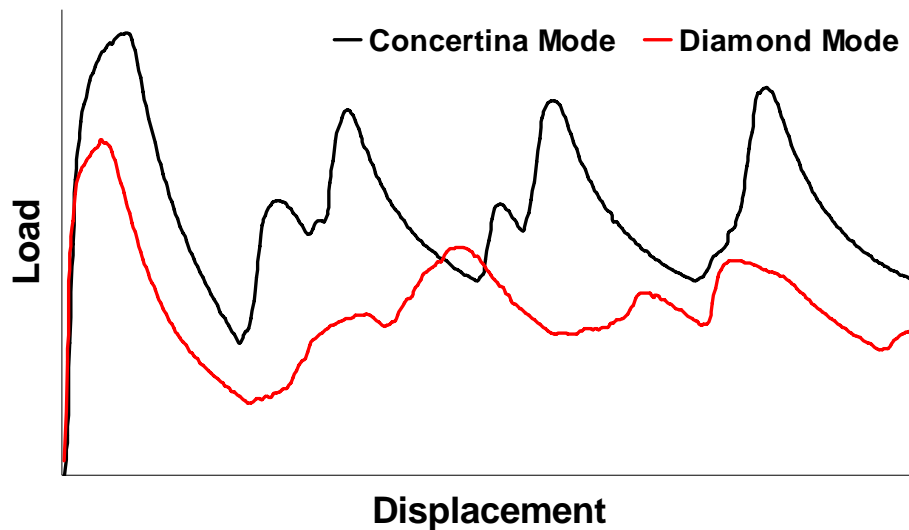


Figure 2.4. Typical load-displacement response of metallic tubes which fail by concertina and diamond modes.



Axisymmetric

Asymmetric

Figure 2.5. Images of axisymmetric (concertina) and asymmetric (diamond) collapse modes [31].

The behaviour of metallic tubular structures under axial crush loads has been well-documented and characterised. From a crashworthiness perspective, the oscillatory nature of the crush process and comparatively poor SEA values produced by metallic structures in general, are not ideal. Recent work on the crush behaviour of aluminium tubes with initiators has shown that this material can provide reduced weight and a flatter load-displacement profile compared to mild steels [37, 38]. Current research is focussing on heat treated aluminium

and high strength steels which are likely to produce improved performance. However, these structures are unlikely to match the SEA values, weight savings or desirable collapse characteristics of composite materials.

## 2.4 Composite Tubes

Recently, composite materials have been utilised in impact absorbing roles in several commercial production vehicles. Specifically, Lotus Engineering utilise a composite crush box in the ‘Elise’ which dissipates the crash energy in low-to-moderate speed frontal accidents, avoiding damaging the intricate aluminium chassis. Weighing only 7.5kg, this box provides hinge points and numerous component mounting points, while completely absorbing the energy from a 30mph (48.2km/h) frontal crash test [22]. An image of this box can be seen in Figure 2.6.



Figure 2.6. Lotus Elise composite crush box. (photo taken by M.Silcock at JEC Expo, Paris, 2005)

Additionally, the Mercedes McLaren SLR uses two carbon-reinforced composite cones, which are 620mm in length and weigh just 3.4kg each. These cones have been incorporated into the bumper structure to absorb the impact energy. The Aston Martin Vanquish employs a complete carbon-reinforced

composite front structure which contains several mounting points including the radiator supports and bonnet latch (Figure 2.7). Furthermore, other vehicles such as the BMW M3, GM Z06 Corvette, Porsche Carrera GT, Dodge Viper and Ferrari Enzo use composite components which contribute to the crash performance.



Figure 2.7. Aston Martin Vanquish composite crash structure. (photo taken by M.Silcock at JEC Expo, Paris, 2005)

There are several reasons for the outstanding ability of composite tubular specimens to form crash structures. These include the almost ideal shape of the load-displacement curve, high SEA values, and crushing efficiency. Typically, when a progressive failure mode is initiated, the load-displacement curve has an almost flat load response, which is ideal for crashworthiness [28]. During a compression test, the load increases until the point at which the failure mode is initiated. This load is maintained throughout the remainder of the crush with only very small oscillations. These oscillations are a result of the numerous microscopic fracture, delamination and friction processes occurring within the crush zone [39]. Figure 2.8 shows a typical load-displacement response of a

composite tube crushed on a flat-platen with an initiator. A curve of this shape allows a structural design to conform much closer to the limits of human tolerance since the force is directly related to the deceleration produced. Metallic structures, on the other hand, require an allowance for the large oscillatory loads seen in Figure 2.4, leading to inefficient designs.

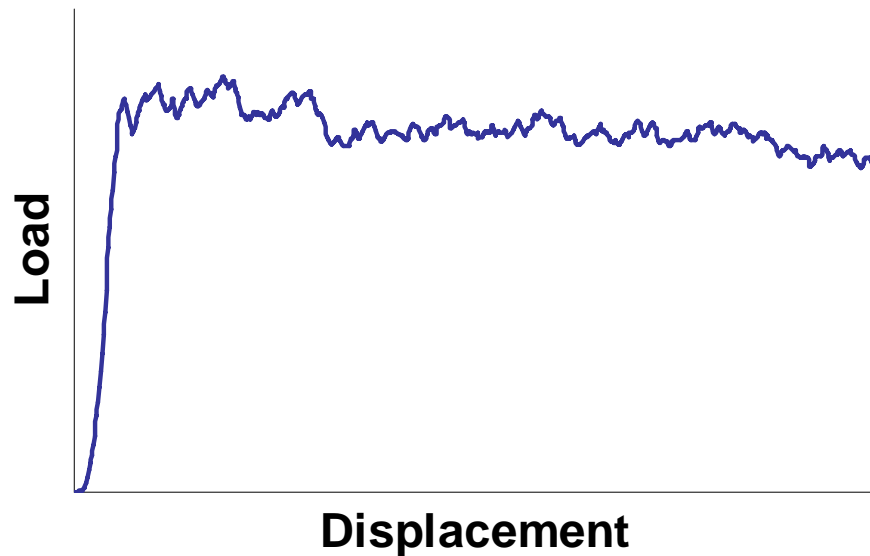


Figure 2.8. Typical experimental load-displacement response of a composite tube failing in a progressive mode.

Additionally, the exceptional energy absorption of composite structures has been well documented and Figure 2.9 shows several typical composite and metallic materials and the significant increase in SEA that composites can achieve [3]. Studies of the energy-absorption behaviour of composite materials and structures have been published by Thornton [40], Gupta [41] and Hull [42], to name a few.

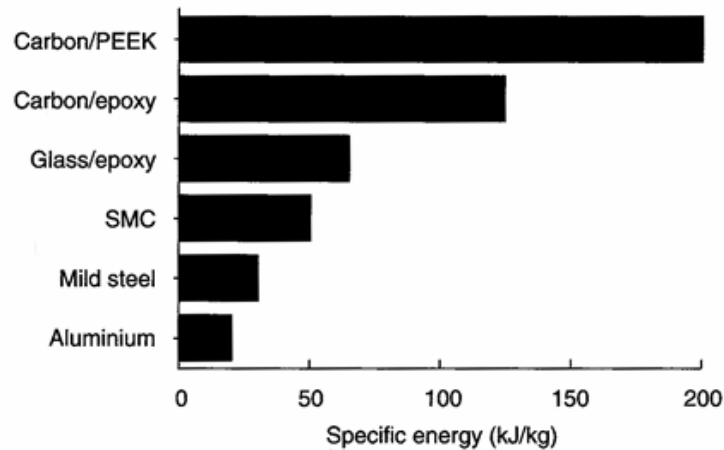


Figure 2.9. Typical values of Specific Energy Absorption (SEA) for various materials [36].

### 2.4.1 Failure Modes & Resulting Energy Absorption

Hamada [43] identified numerous intrinsic and extrinsic variables which interact to alter the failure mode and energy absorption of composite tubes. The intrinsic variables are broadly classified as; fibre and matrix materials, fibre orientation, fibre form (random mat, unidirectional, woven, knitted), stacking sequence, ratio of hoop to axial fibres, fibre content and, fibre/matrix interfacial bonding strength. The extrinsic variables include: tube shape and geometry, initiator geometry, loading direction, testing speed, temperature and environment factors.

When a composite tube is placed under an axial load, the use of an initiator is required to prevent catastrophic collapse [42]. Like metallic tube crushing, catastrophic collapse is highly undesirable from a crashworthiness perspective, producing erratic load-displacement results and low SEA values [39]. Typically, a 45° chamfer is turned into one end of a composite tube to initiate progressive collapse [44]. However, a controlled collapse can also be produced through the use of plug initiators, which then also form a practical attachment point for use in automotive bumpers [21].

When progressive collapse is initiated, a composite tube can fail by:

- Progressive folding,
- Euler buckling, or
- Progressive crushing.

Similar load-displacement trends can be observed for both composite and metallic tubes which fail by progressive folding or Euler buckling modes. In the case of progressive folding, cyclic oscillations are evident throughout the crush. This mode is apparent in tubes which utilise ductile fibre-reinforcement such as aramid [39]. Euler buckling is a mode encountered typically in slender tubes [26]. In composite materials, these failure modes tend to produce low values of SEA which, together with the undesirable crush behaviour, make them of little interest to the design of crashworthy structures and these will not be discussed further.

Progressive crushing, or brittle fracture, is a failure mode unique to composite tubes. This mode produces higher energy absorption than the aforementioned modes and as such, is of greatest interest<sup>1</sup> [28]. Hull [42] covered the progressive crushing of composite tubes most comprehensively and recognised two major crushing mechanisms. These are identified as ‘splaying’ and ‘fragmentation’, though most specimens exhibit elements of both. The following describes each mechanism observed in progressive crushing.

---

<sup>1</sup> It should be noted here that catastrophic collapse can, in fact, absorb significant amounts of energy but the load-displacement profile of progressive crushing modes makes them far more suitable for decelerating objects such as humans in a crash.

### 2.4.1.1 Transverse Shearing (Fragmentation)

This mode is characterized by a wedge-shaped laminate cross-section, a result of the lamina bundles fracturing and shearing from the crush zone. The resulting surface is scalloped such that the axial load is not transferred uniformly and the process continues as further fibres break. Development of this process can be seen in Figure 2.10 and an example of such a failure can be seen in Figure 2.11.

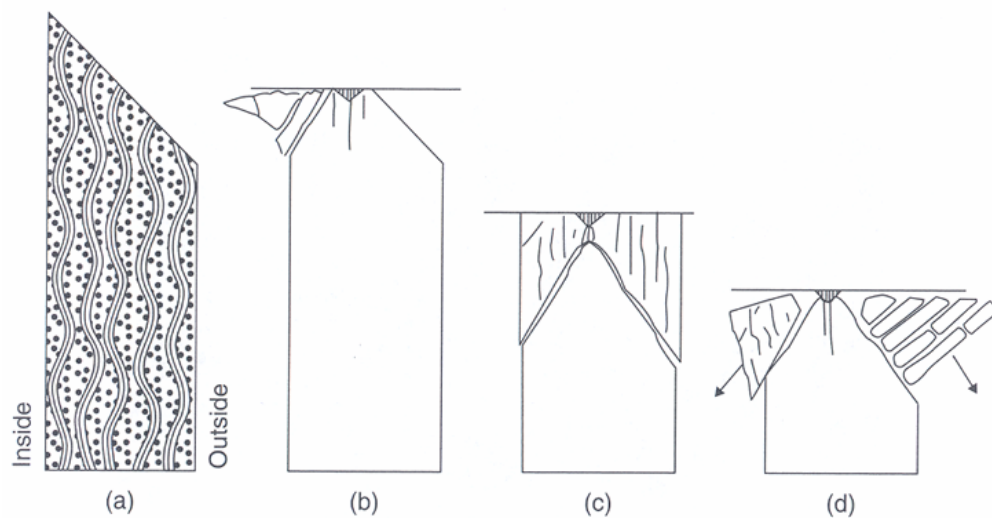


Figure 2.10. From a) to d), the progressive development of the transverse shearing/fragmentation mode of collapse [42].

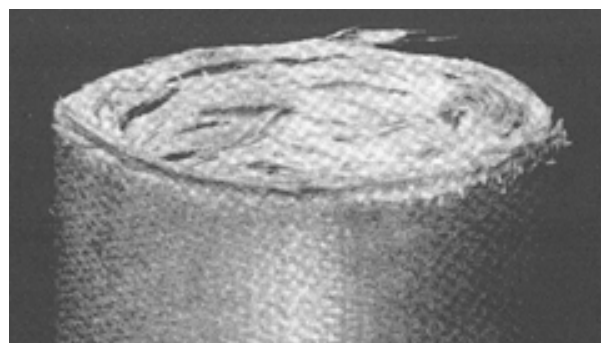


Figure 2.11. An example of transverse shearing [42].

### 2.4.1.2 Splaying Mode (Lamina Bending)

This mode is characterised by the production of long interlaminar cracks ahead of the crush zone parallel to the axis of crushing, the presence of a debris wedge and a flower or mushroom like post-failure appearance. Interlaminar

cracks penetrate between layers and the energy absorbed by a material is primarily a function of the matrix strength [42]. Figure 2.12 below shows how this mechanism develops.

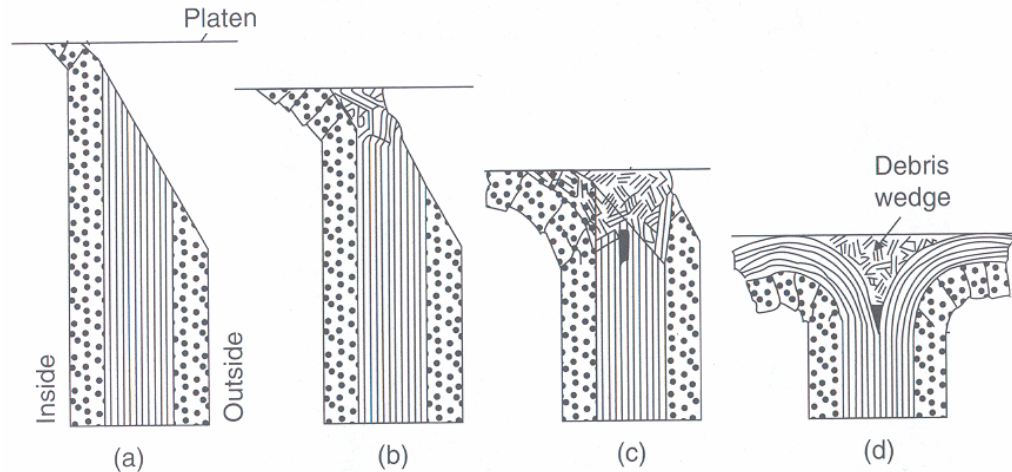


Figure 2.12. From a) to d). The progressive development of the splaying/lamina bending mode of collapse [42].

Shear fracture is observed in the early loading stages of the chamfer, resulting in pulverised material forming what is aptly termed, a ‘debris wedge’. Once formed, the debris wedge maintains a constant size and shape [45] and helps maintain the propagation of the central wall crack. The debris wedge can be observed in experimental tests as a ring on the face of the crushed surface of the tube in Figure 2.13.

The central wall crack extends some distance ahead of the crush zone and separates the tube wall. As the material enters the crush zone, it begins turning through a tight radius of curvature. The radius of curvature is dictated by the hoop constraints [42]. A high hoop constraint causes a small radius of curvature. As the material passes through the crush zone, interlaminar delamination is observed together with intralaminar and transverse shear cracking. Figure 2.14 shows a schematic of the crush zone which identifies the

contributing failure mechanisms for both  $0^\circ$  (along the tube's axis) and  $90^\circ$  (around the tube's circumference) fibres.



Figure 2.13. A crushed carbon/epoxy tube clearly showing the fronds, separated by axial tears and the ring of debris on the upper surface. (photo taken by M.Silcock)

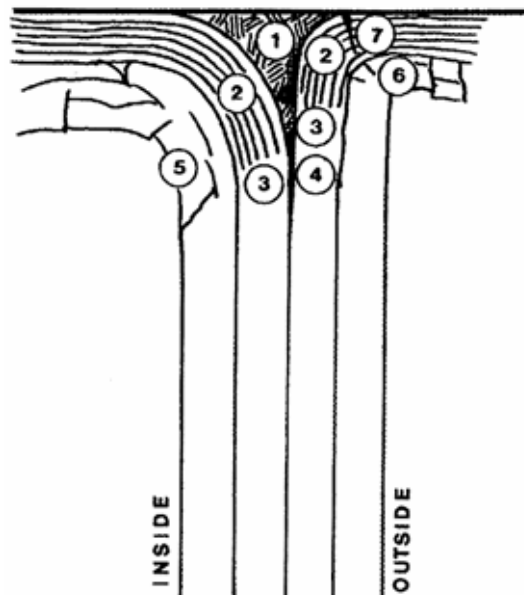


Figure 2.14. Features identified in a  $[90/0/0/90]$  glass/polyester tube [42]: 1) Debris wedge, 2) Intralaminar shear in axial layers parallel to fibres, 3) Limit of intralaminar shear, 4) Central wall crack, 5) Transverse shear, compressive buckling of inner hoop layers, 6) Transverse shear, tensile fracture of outer hoop layers, 7) Tensile or shear fracture of the axial layers at the sharp bend.

The material that folds outwards develops axial tears due to tensile hoop stresses, which separate into ‘fronds’ in a flower-like fashion, as can be seen in Figure 2.13. Similarly, material which folds to the inside experiences compressive hoop stresses and buckles. In addition, significant friction processes take place throughout the crush zone [28], as will be discussed shortly.

There are numerous factors that determine which of the aforementioned mechanisms will be dominant. A key factor is the relative strength in the axial and hoop directions. Lu [3] reports on work by Berry which demonstrates that in glass-cloth polyester tubes, when the ratio of hoop to axial fibres is high (4-8.5:1), transverse shearing is observed and the sustained loads are relatively low. In contrast, when the ratio is low (1:7-8.5) splaying is produced and a corresponding increase in the sustained crush load is observed. However, these trends are not true for carbon-fibre reinforced composites. Lu [3] also reports on work by Farley which shows an instance in which higher energy absorption figures are produced through transverse shearing than the splaying mode, as shown in Table 2.1.

Table 2.1. Effect of matrix failure strain on SEA figures for carbon/epoxy tubes.

Matrix Failure Strain	Lay-up	SEA [kJ/kg]	Failure Mode
0.020	[0/± 15] <sub>4</sub>	125	Transverse Shear
0.010	[0/± 15] <sub>4</sub>	94	Lamina Bending
0.020	[0/± 45] <sub>4</sub>	85	Transverse Shear
0.010	[0/± 45] <sub>4</sub>	69	Lamina Bending
0.020	[0/± 75] <sub>4</sub>	74	Transverse Shear
0.010	[0/± 75] <sub>4</sub>	54	Lamina Bending

#### 2.4.2 Friction Effects

Friction plays a significant role in the energy absorption of composite materials. Though it is apparent in tubes which fail by transverse shearing, it

contributes most significantly to the energy-absorbed through the splaying mode [46]. Fairfull and Hull [47] concluded that over half of the energy absorbed by a composite tube is through friction, not just between the specimen and the crushing surface, but within the tube's crush zone.

In progressive crushing, Fairfull and Hull [47] identified eight factors which contribute to the energy absorption, as shown in Figure 2.15. Of these, five are fracture based and three are frictional effects. This investigation utilised four platens of varying surface roughness to determine the influence on the energy-absorption. It was reported that on extremely rough surfaces, tube debris effectively filled the surface pits, reducing the coefficient of friction. The results showed that the combined frictional effects account for >50% of the total energy in glass/epoxy tubes, regardless of platen roughness. Mamalis' work on developing an analytical model demonstrated that these figures are accurate and confirmed that an approximately 48-50% of the total energy is dissipated through friction [48].

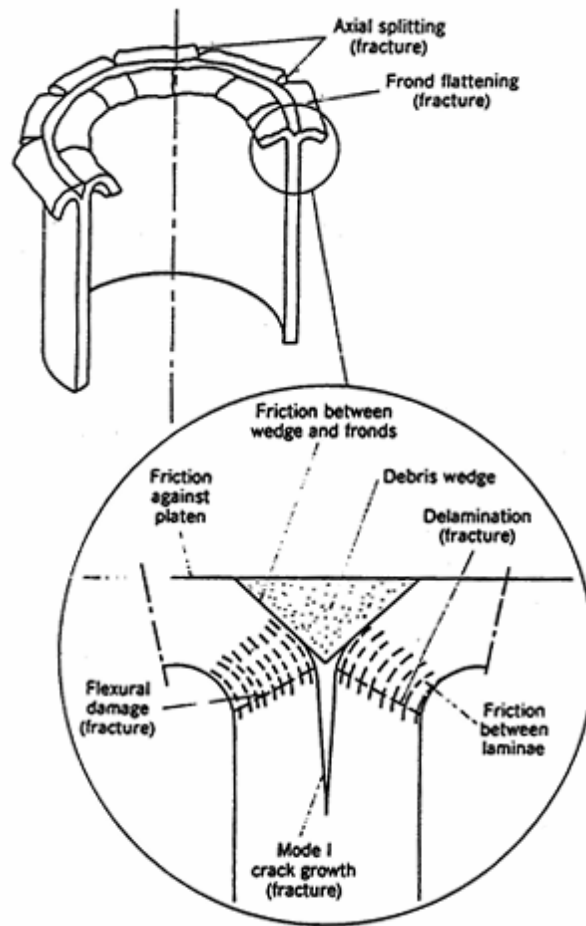


Figure 2.15. Factors which contribute to the energy absorption in crushed composite tubes [47].

In addition, Farley [46] investigated the effect of surface roughness on the energy-absorption of crash-structures with various combinations of geometrical and mechanical properties. It was reported that the performance of tubes with similar matrix and fibre failure strains was uninfluenced by the coefficient of friction of the crushing surface. Additionally, tubes with a matrix failure strain higher than that of the fibres would increase in energy-absorption as the platen friction decreased and vice versa. These frictional effects are only significant in tubes that fail in a splaying mode. None of transverse shearing, Euler or local buckling failure modes slide against the platen and as a result, are not influenced by surface roughness [46].

### 2.4.3 Parameters Affecting Energy Absorption

As identified by Hamada [43] and shown in Figure 2.16, numerous intrinsic and extrinsic variables control the behaviour and determine the energy-absorption of composite tubes. Importantly, Hamada not only identifies these variables but makes it clear that there is a significant interaction between them, and that isolating the importance of one is near impossible. As a result, key findings have been presented and the specific instance in which these findings are valid, have been identified. Unlike metallic structures, the interaction between variables means that commenting on general trends is exceedingly difficult.

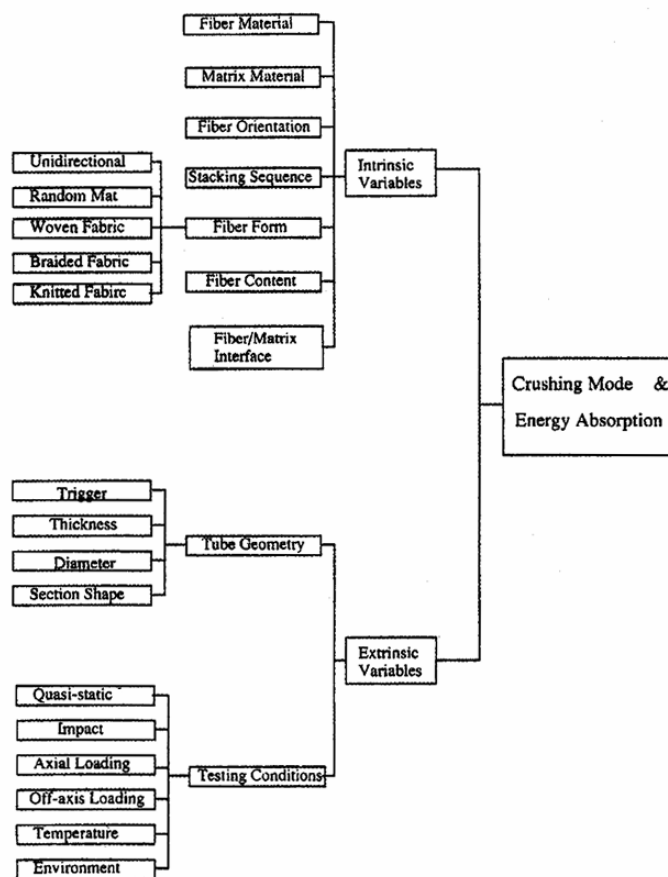


Figure 2.16. A schematic of the intrinsic and extrinsic variables which influence the failure mode and energy-absorption of composites [43].

Several of the parameters identified by Hamada can affect the energy absorption by up to a factor of 2. These are material selection, ply orientation,

geometry, strain-rate and temperature [26]. These effects, excluding temperature, will be covered here. Furthermore, other parameters that have demonstrated an ability to increase the energy absorption; such as tube filling and initiator type, are covered.

#### **2.4.3.1 Material**

Numerous combinations of composite materials have been investigated for their energy absorption ability but none more than glass/epoxy, aramid/epoxy and carbon/epoxy [39]. Farley [44, 49, 50], Thornton [40], and Farley and Jones [51] all report that in similar geometry tubes, carbon/epoxy specimens generally absorb more energy than glass or aramid composite tubes though aramid specimens possess a better post-crush integrity. Investigations on hybrid materials, such as carbon/aramid reinforcement [39] have demonstrated a performance not significantly better than tubes of a single fibre type [44].

A study into various braided materials was undertaken by Inai *et al.* [52]. The investigation included various braid angles and Hoop/Axial fibre ratios in carbon/epoxy tubes SEA and results of between 90 and 95kJ/kg were reported. These values were improved upon by Hamada [53] by altering the matrix material to Polyetheretherketone, or PEEK, which resulted in SEA values of almost double those typically produced for carbon/epoxy. Nevertheless, its prohibitive costs make this material less attractive for further work. Furthermore, dynamic testing on PEEK specimens has shown a severe strain-rate dependency with a reduction in SEA of around half at higher strain-rates [53].

One material of particular interest, which has shown excellent crashworthiness performance at a fraction of the cost of carbon/epoxy, is glass/polyester Continuous Filament Random Mat (CFRM). Cooper [54] reports a highest

SEA value of 96kJ/kg for this material, together with high repeatability and favourable load-displacement characteristics. Work on this material has largely been performed by the University of Nottingham and several documents exist on experimental investigations [31, 55, 56].

#### **2.4.3.2 Ply Orientation**

A high-performance composite is typically constructed from a number of lamina of prescribed orientations, stacked in a prescribed sequence forming the resultant laminate. The orientation of the fibres and the stacking sequence can have a significant effect on the behaviour of composite structures. This unique characteristic of composite materials is appealing to structural and crashworthiness engineers alike as they can tailor a structure for the particular load paths expected. Similarly, orientation of the fibres in tubular structures can yield vastly different results and these effects have been investigated in several bodies of research.

The effect of ply orientation on carbon, glass and aramid/epoxy tubes can clearly be seen in Figure 2.17 [44]. The longitudinal direction of the tube is taken as 0°.

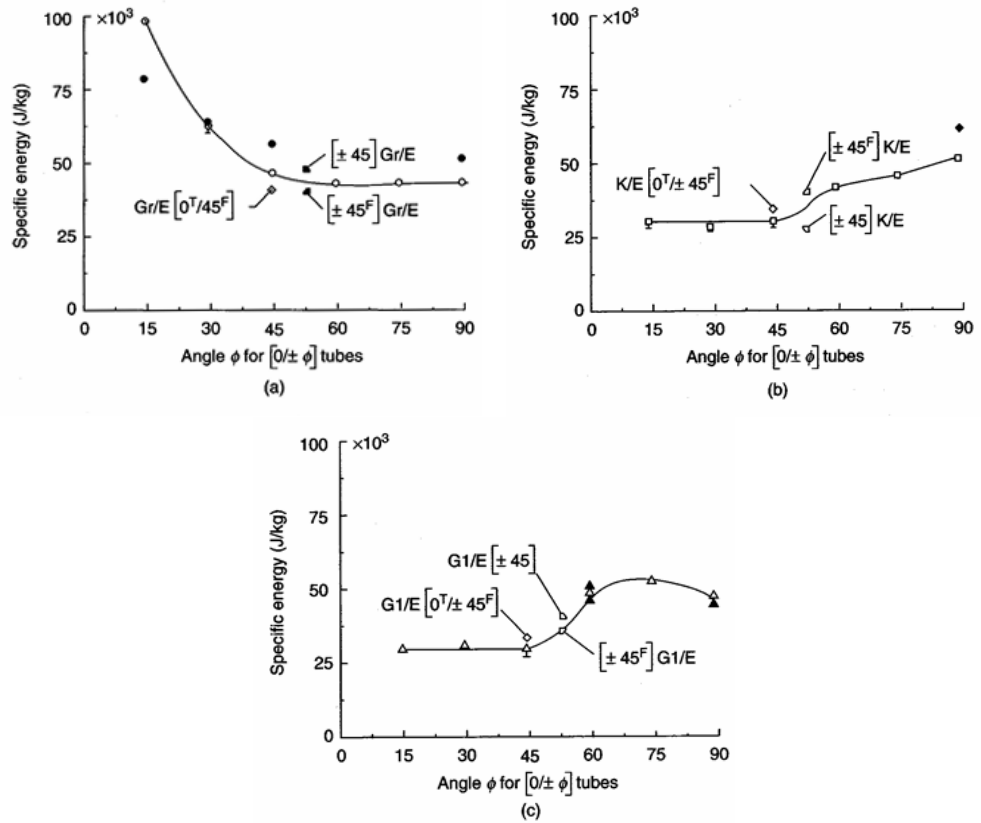


Figure 2.17. Effect of ply orientation on SEA values for: a) carbon/epoxy, b) Kevlar/epoxy, and, c) glass/epoxy tubes. [44].

Farley [44] investigated and characterised the effect of the ply orientation on carbon/epoxy tubes. As  $\theta$  (given as  $\Phi$  in Figure 2.17) increases from  $15^\circ$  to  $45^\circ$  ( $[0^\circ/\pm\theta]$ ), the sustained load decreases (corresponding to the energy absorption) with little change observed at greater angles. These results suggest that the fibres absorb the most energy when oriented in the direction of loading. However, a tube made entirely of  $0^\circ$  fibres would undoubtedly produce very low SEA figures due to extensive axial splitting and a resulting separation. Problematically, in the paper above, Farley gives little information about the construction of the tubes, making comparison difficult. Contrary to Farley's findings, Inai *et al.* [52] investigated three different braided ply orientations and produced the best results for a  $[0^\circ/\pm 60^\circ]$  lay-up, although this was possibly due to the vastly different hoop:axial fibre ratios.

The effects of ply orientation on glass and aramid/epoxy tubes differ from those reported for carbon/epoxy. Farley [44] observed that for these materials, the SEA values are unaffected by ply orientations between  $[0^\circ/\pm 15^\circ-45^\circ]$ . Additionally, for glass/epoxy tubes, a maximum SEA can be observed for a lay-up of  $[0^\circ/\pm 75^\circ]$  and for aramid/epoxy tubes, the SEA continues rising to a maximum at  $[0^\circ/\pm 90^\circ]$  suggesting that this material relies more heavily on hoop fibres. Not surprisingly then, Farley [44] identified that the effect of ply orientation on the SEA of a structure depends largely on its constituent materials.

#### **2.4.3.3 Geometry**

The influence of composite tube geometry has been investigated by several researchers. As reported by Farley, in numerous publications [28, 39], for a circular  $[\pm 45^\circ]$  carbon/epoxy tube, SEA decreases non-linearly as the  $t/D$  decreases (or  $D/h$  increases, as in Figure 2.18 below). Farley [51] also reports that tubes of  $t/D = 1$  ( $D/h$  in Figure 2.18) seldom failed by progressive crushing but more often, by catastrophic collapse. These results are all based on circular profiles as this geometry produces the highest levels of energy absorption [42].

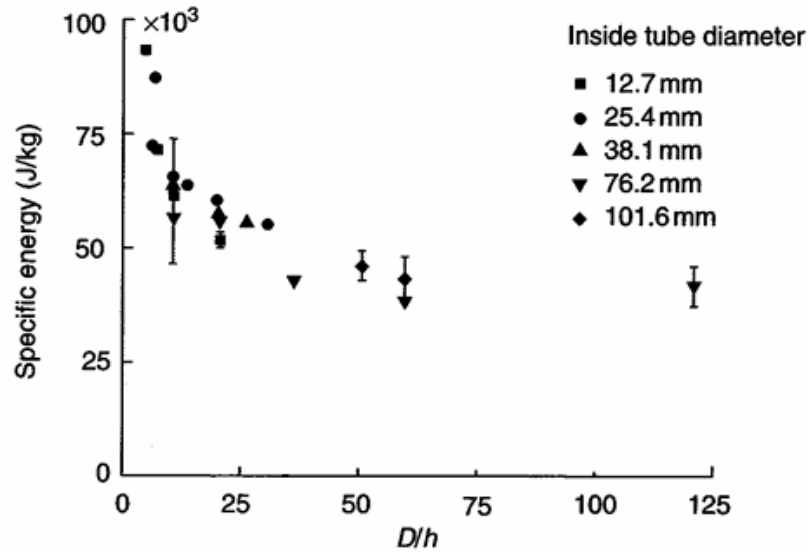


Figure 2.18. SEA of carbon/epoxy tubes for a range of D/h (t/D) ratios [28].

Mamalis has also contributed a significant amount of knowledge from investigations into various geometries such as circular and square tubes, conical shells, square frusta, and hourglass section shells [48, 57, 58]. Notably, his research into hourglass section shells (representative of chassis rails) for use in vehicles has produced higher SEA values than equivalent square tubes [58]. A cross-section of the tube can be seen in Figure 2.19.

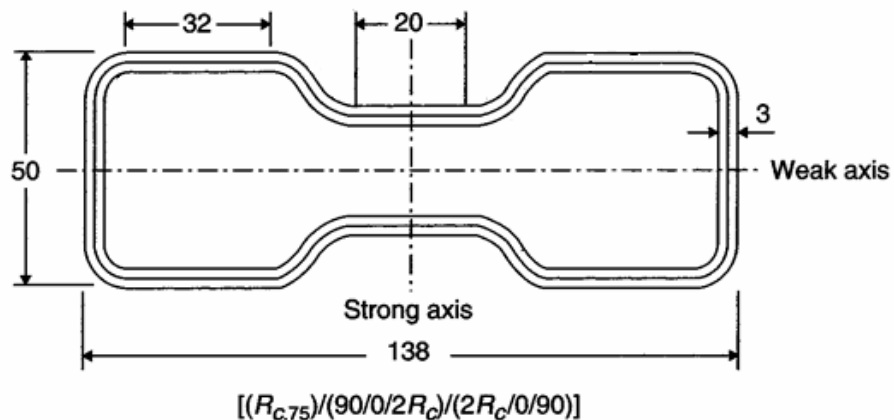


Figure 2.19. Cross-section of the hourglass frame rail investigated by Mamalis [58].

This work is significant as rectangular tubes typically absorb less energy than square tubes. Mamalis [39] reports on findings by Kindervater, who quantified the difference as being 0.5 and 0.8 of the specific energy of a similar circular

tube respectively. In separate studies, Mamalis *et al.* [57, 59] confirmed these observations attributing the difference to the corners of the profiles acting as stress-concentrators.

Observations of the effect of frustum (or semi-apical) angles on the energy absorption are similar for both metallic and composite frustra. The energy decreases with an increasing semi-angle to a critical value of between 15° and 20° beyond which unstable collapse is likely [3]. Two advantages of this geometry are that an initiator is not needed as these structures self-initiate, and that off-axis loads can be sustained without global failure. Work by Fleming and Vizzini [60] demonstrated that small side-loads can produce an increase in SEA which was confirmed by Karbhari and Chaoling [61], but this was only true for hybrid glass/carbon reinforced frustra. In the case of single fibre reinforced frustra, a constant reduction in SEA was observed as the loading angle deviated from axial.

#### **2.4.3.4 Strain-rate**

The loading rates experienced by crash structures can vary significantly. Consequently, it is critical that designers have a detailed understanding of a material's strain-rate dependency. The influence of strain-rate on the energy absorption of composite materials has not yet been completely characterised. Its influence varies depending on numerous intrinsic variables [28] and not surprisingly, conflicting reports on the effect of strain-rate are common. While some authors claim an increase in energy absorption due to increased strain-rate, others report a corresponding reduction. This inconsistency makes drawing overall conclusions difficult.

Key studies investigating the effect of strain-rate on  $[\pm\theta]$  and  $[0^\circ/\pm\theta]$  orientations in carbon/epoxy tubes have produced contradictory findings.

Farley [62] observed a 35% increase in SEA for  $[\pm\theta^\circ]$  carbon/epoxy tubes while no change was observed in tubes of  $[0^\circ/\pm\theta^\circ]$  as the strain-rate increased. This confirmed his earlier work on  $[0^\circ/\pm 45^\circ]$  which showed no influence under higher strain-rates [44]. Karbhari and Haller [63] tend to agree that improvements can be observed in carbon/epoxy tubes under impact. They reported a general increase in SEA with increasing strain-rate in a study of various materials and braids, which included carbon/epoxy. Additionally, Thornton [40] reported that dynamic testing of  $[0^\circ/90^\circ]$  carbon/epoxy tubes increased the SEA by only 2%. In direct contrast, reductions of up to 25% were reported by Kohlgruber and Kamoulakos [64] in carbon/epoxy  $[0^\circ/90^\circ]$  and  $[\pm 45^\circ]$  tube portions. Fernie also reported a significant SEA reduction in braided carbon/vinylester tubes [31].

Glass/polyester has shown a significant performance variation across a range of strain-rates and geometries. Fernie [31] reported on glass/polyester circular tubes in which a 35% reduction in SEA was observed at a crush speed of 7m/s. Likewise, Mamalis *et al.* [59] reported that thin-walled circular conical specimens of glass/polyester showed a reduction of 35% in SEA at a crush speed of 21m/s. The strain-rate dependence was attributed to the change in crushing mechanisms, resulting from the resin becoming increasingly brittle at higher strain-rates. However, Mamalis also found that square [57] and circular tubes of the same material were largely unaffected by strain-rate, contradicting Fernie's findings. Ribeaux and Warrior [65] bridge these findings, reporting a reduction of 12% in SEA values in dynamic testing of glass/polyester circular tubes. Interestingly, coupon tests on this material has shown strength increases of between 55% [66] and 100% [31] with the former noting that there was “no

significant change in tensile ductility”, conflicting the idea of the matrix becoming brittle at higher strain-rates.

Other materials affected by strain-rate are aramid/epoxy and carbon/PEEK. SEA values of aramid/epoxy tubes of  $[0^\circ/\pm\theta]$  and  $[\pm\theta]$  orientations, were shown to increase by 20-45% [62] but Thornton and Jeryan [21] report on work by Schmueser and Wickliffe in which a 30% SEA reduction was shown for orientations of  $[0^\circ/\pm45^\circ]$  as the strain-rate increased. The strain-rate dependence of carbon/PEEK tubes in various lay-ups has been studied by Ramakrishna and Hamada [36] who report that the dynamic conditions generally halve the SEA values observed in quasi-static testing.

#### **2.4.3.5 Tube Filling**

Polymer foam filling (such as polyurethane and PVC) is reported to have a greater influence on the specific energy absorption of composite tubes than is observed with metallic tubes. Carruthers [28] presents data for glass/polyester (GRP) and steel tubes respectively, crushed both with and without foam filling. Figure 2.20 shows a comparison of the SEA values of both materials, with and without filling. The use of foam filling in composite tubes reportedly stabilised the collapse mode of tubes that would otherwise fail catastrophically, thereby raising their SEA.

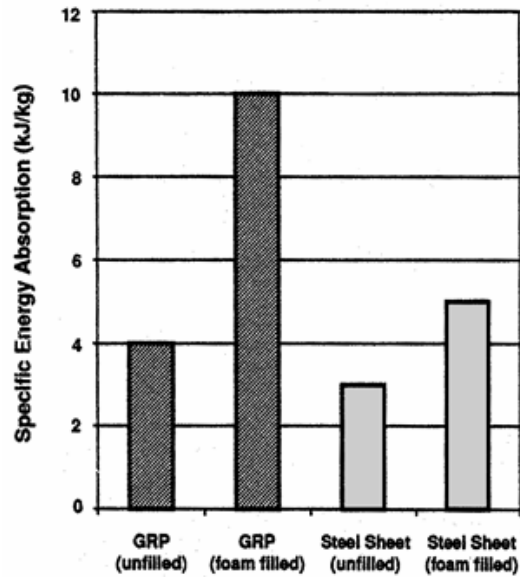


Figure 2.20. Effect of foam-filling on GRP and steel tubes [28].

#### 2.4.3.6 Initiator type

When crushing a tube onto a flat-platen it is recognised that an initiator is required to instigate a stable and progressive crush mode<sup>2</sup> [26]. While there are several types of initiator, most often a chamfer is used. Sigalas *et al.* [67] showed that the chamfer has the same effect whether on the inner or outer edge and that its angle has little effect on the behaviour or performance of the tube. However, for these structures to be considered for practical use, a useful method of attachment must be devised. Plug initiators combine both a method of attachment and an effective failure initiator [21]. Furthermore, plugs have shown to improve the energy absorption and behaviour in metallic tubes [38] and may improve the off-axis response of composite tubes [56].

The energy absorbed in this form of test is highly dependent on the plug radius. Cooper found that the peak energy absorption occurs when the plug radius is close to the thickness of the tube. This conclusion was based on tests of CFRM

<sup>2</sup> It is possible to achieve a progressive crush without an initiator although a significant peak load is produced before stabilising, conflicting with the requirements of a crashworthy structure [56].

tubes (glass/polyester random mat) with a range of plugs. However, Cooper also reports on similar work by Hull and Coppola on glass/vinylester and glass/epoxy composites who found that peak energy absorption occurs at a plug radius of 0.5 times the tube wall thickness. Where a plug initiator is adopted, the failure mode is typically a splaying mode as the tube's material is forced to stretch out along the plug radius. An image of several initiator types on square tubes can be seen in Figure 2.21. These can all be used on rectangular tubes but only the plug and chamfer initiators can be used when testing circular tubes.

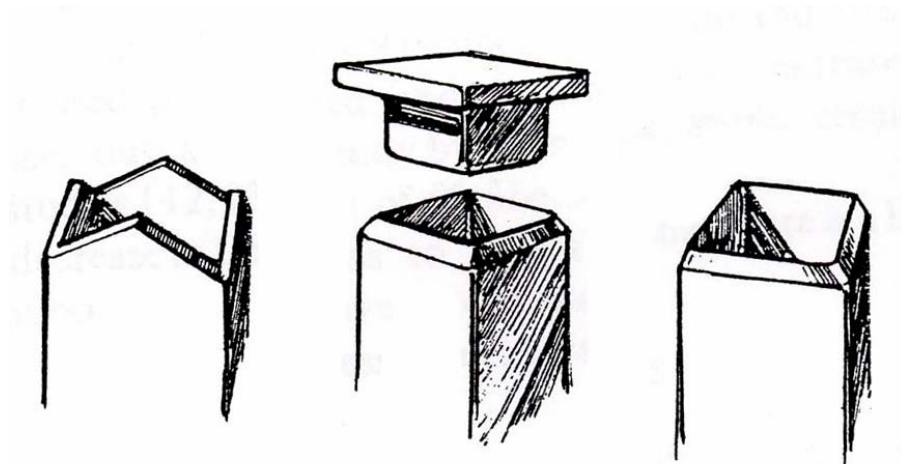


Figure 2.21. Composite tube initiator types from L-R - tulip, plug and chamfer [21].

It is clear that complete characterisation of the behaviour of composite materials is difficult given the interdependence of each of the controlling variables. Subsequently, for any given application, a reasonable degree of prototyping is required to ensure the necessary behaviour is produced. This makes cost effective composite component production a necessity.

## **2.5 Current Methods of Composite Tube Manufacture**

Despite the advantages of composite materials, one of the difficulty's that continues to restrict the use of composite materials is cost, particularly manufacture cost. An overview of the current methods of composite tube manufacture is presented. It should be noted that these subsequently mentioned processes can be used with both thermoset and thermoplastic composites. However, further options exist for the curing of thermoplastic composites such as Resin Transfer Moulding (RTM) and resin infusion. These will not be covered here as the manufacturing issues discussed in this thesis are focused primarily on the curing of thermoset resins.

### **2.5.1 The Autoclave**

The most common method of curing high-performance thermoset composite components is with an autoclave. This large pressurised chamber uses an inert gas and applies external pressure and heat to the part. Due to the large volume of gas and substantial structural reinforcement required to contain the approximately 600kpa pressure, low temperature gradients are produced, typically in the vicinity of 2.8°C/min [68]. Consequently, extremely long cure cycles are experienced which typically last many hours but can extend up to several days [69]. This means that the curing process is the rate-limiting step in the manufacture of high-performance composite components. Additionally, the costs associated with autoclave purchase, set-up, operation, labour, together with known reliability issues and the slow cure cycles all limit the attractiveness of this method for the curing of composites.

The manufacture of tubular components specifically is accomplished by applying the composite material onto the exterior of tubular mandrels which are placed in the autoclave for curing [70]. Several processes are available for

the application of the material prior to curing, such as filament winding, braiding and hand lay-up. The concept of a hand lay-up is rudimentary and will not be covered here, although brief descriptions of the other methods will be given.

#### **2.5.1.1 Filament Winding**

Filament winding has received a great deal of attention from researchers and numerous studies have been performed on this process [69]. The process involves the placement of a resin pre-impregnated tape or yarn on a rotating mandrel while under tension, allowing precise fibre placement [71]. Several disadvantages of this system include the capital involved in acquiring equipment, slow processing times [68], fibres cannot be wound onto convex surfaces or be made to change path easily and, typically, a poor external finish is produced [71]. While this process can be cost effective once established, the components typically require further curing/consolidation in autoclaves to achieve good mechanical properties, though curing by ovens, microwaves or atmospheric cures are possible.

#### **2.5.1.2 Braiding**

Likewise, braiding is used to produce un-cured composite components which must then be cured in a separate process. As the name suggests, this process involves the braiding of reinforcing fibres over a mandrel. In comparison, filament winding can achieve a higher fibre volume fraction though more complex shapes can be produced by braiding, while the inter-laced construction provides higher levels of structural integrity [71]. While filament winding has the mandrel rotated perpendicular to the material feeder, braided tubes are drawn away parallel to the material feeder. Bi-axial braids ( $[\pm\theta^\circ]$ ) are the most common however tri-axial braids ( $[0/\pm\theta^\circ]$ ) are currently in use.

Examples of the crush performance of braided tubes can be found in references [52, 72].

### 2.5.2 Pultrusion

The pultrusion process combines the lay-up and cure steps by pulling reinforcing fibres through a resin bath before being compacted through a heated die of the required profile. A schematic of the pultrusion process can be seen below in Figure 2.22. Consequently, this process does not require an autoclave. The heated die cures the resin and the cured section is pulled from the die in a continuous process before being cut-off at the required length.

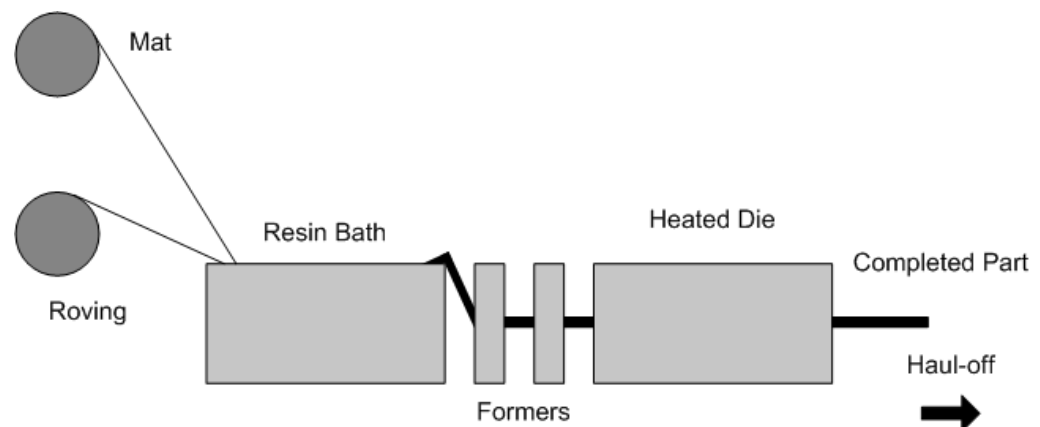


Figure 2.22. Schematic of a pultrusion line (image taken from <http://www.tangram.co.uk/TI-Polymer-Pultrusion.html>).

Due to its continuous and automatic nature, pultrusion can produce composite profiles quickly and cheaply. Production rates of 3m/min have been reported but significantly lower rates are more common as this rate can only be achieved with very thin wall thicknesses (<http://www.tangram.co.uk/>). This process is, however, limited to profiles of constant cross-section (no tapered sections), relatively large production runs and poor product performance due to fibre orientation. Additionally, this process is limited by resin type as polyester resins are preferred since they shrink during the cure, unlike the epoxies which tend to clog the die. Since fibres are pulled through the die, the predominant

fibre direction is longitudinal, which is reflected in the properties of the products which are usually strong and stiff in tension and bending but with poor transverse properties.

### **2.5.3 The Quickstep™ Process**

A recently developed alternative to the autoclave is called the Quickstep™ process. This process utilises the high thermal conductivity of liquid to achieve significantly higher heating rates, resulting in shorter cure cycles. Additionally, this process minimises the chances of exothermic reactions by removing excess heat from the curing part.

The unit consists of three fluid tanks, held at ambient, and two higher cure temperatures, set by the user and controlled from a connected PC. A screenshot of the control software is shown in Figure 2.23. As the fluid is pumped to the cure chamber, a booster heater can be used to offset the heat loss due to the latent heat of the piping. Fluid flow rates are controlled by a variable speed pump. The typical arrangement uses a clamshell style mould with flexible bladders to separate the fluid from the part. Several images of a QS5 plant are shown in Figure 2.24 below.

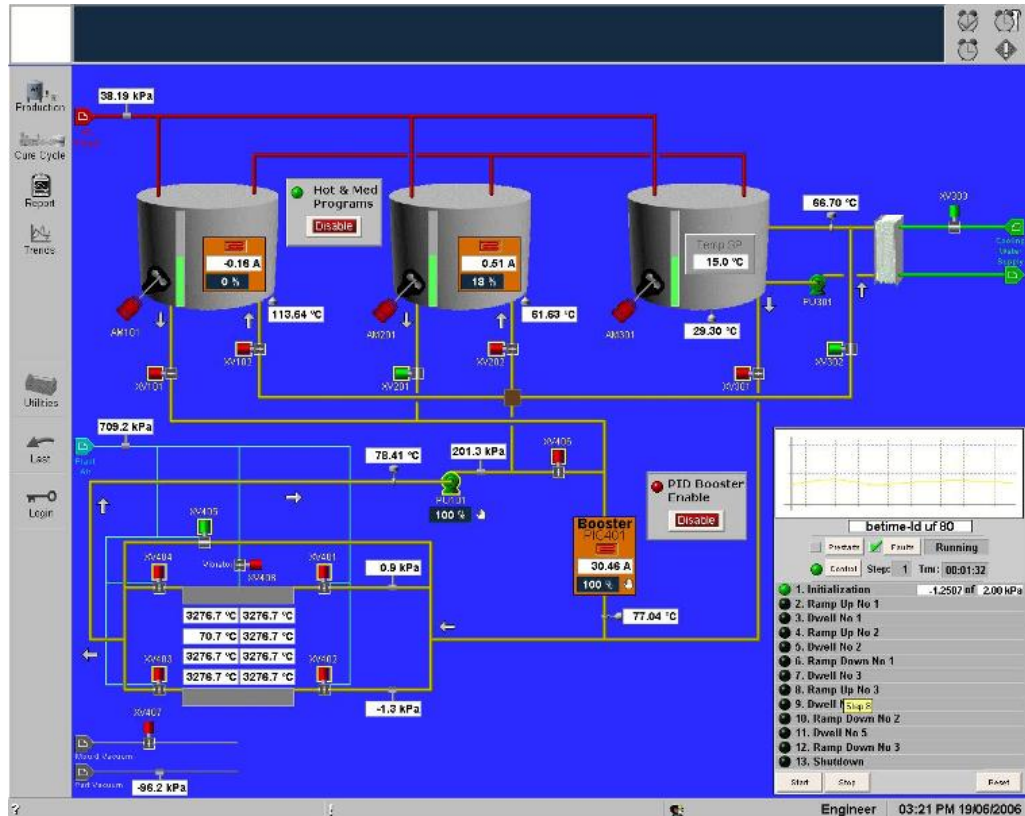


Figure 2.23. Screenshot of the control interface used by the Quickstep QS5 production plant.



Figure 2.24. Left: Image of backside of QS plant showing the three fluid storage tanks with the cure chamber in the background. Right: Front side of QS plant showing the clamshell cure chamber in the foreground. (photos taken by M.Herring, 2006)

This process has shown an ability to reduce cure cycle times significantly and as a consequence, improve a variety of mechanical properties [73]. The high heating rates also result in a rapid decrease in the initial resin viscosity, the effect of which is still being studied [74].

## 2.6 Finite Element Modelling

---

Finite Element (FE) modelling has allowed the automotive industry to obtain accurate designs without iteration and reduces the need for expensive prototyping and physical testing [75]. This has brought about its widespread use in this industry.

While it is possible to predict the behaviour of structures under certain load conditions using analytical and empirical methods, FE analysis allows designers to visually analyse and correlate the impact behaviour. Most importantly, in the case of vehicular crashworthiness, the use of FE permits visualisation of the interactions between components, allowing the designer to make appropriate changes. Additionally, the structural interactions and dynamic nature of an impact implies the load is time dependent and strain-rate effects are increasingly important, two aspects that can more easily be considered by FE than by experimental methods [29].

Two fundamental types of modelling software are available; implicit and explicit. Effectively, the use of an implicit solver permits large time increments, reducing the computer processing time and computational expense. The solution is iterated until it converges below a pre-determined value. On the other hand, explicit solvers are used to solve the equilibrium equations with an iterative solving method and very small time steps lending themselves to problems with high degrees of nonlinearity [76]. The duration of an explicit time step is dictated by element size and material density and stiffness [77]. The nature of the problem under consideration determines which solver would be best suited. Implicit solvers are better suited to linear problems where there is no contact or dynamic effects [54]. While it is possible for implicit solvers to consider material non-linearity, the stiffness matrix requires constant

recalculation which lengthens the analysis, using significant memory and disk space. Explicit solvers do not have this problem and can consider material non-linearity and large material deformation, lending themselves to crash analyses [77]. Typically, explicit analyses require thousands of time steps but an implicit solution may require only one [78].

The explicit code LS-DYNA was employed in preliminary work by the author, in an investigation on the modelling of metallic tubular crash structures. This work revealed the importance of predicting the correct mode of failure and its impact on obtaining good load-displacement and SEA predictions. Furthermore, several limitations of the modelling methodologies typically adopted for such simulations were identified. This was a prelude to modelling composite materials and the lessons learnt proved to be extremely valuable. Further details of this work can be found in Appendix One.

### **2.6.1 Modelling of Composite Materials**

Fibre-reinforced composite materials have received significant attention from the automotive industry since the early 1980's [63]. However, despite significant advances in the last decade, a suitable model for the simulation of the crash response of composite structures has not yet been developed [54]. Furthermore, no model could predict the stiffness, strength or post failure response of these materials in a general shape [19]. This difficulty stems from an inability to capture the numerous interactive failure mechanisms and the non-linear damage progression [79]. Fundamentally, the performance variation of the constituent materials, microscopic failure that may be dominated by either constituent, and the difficulty associated with characterising the behaviour of these materials makes development of a general modelling

approach extremely difficult. Consequently, many of the reported methodologies are sensitive to parametric changes.

With respect to modelling the laminate material behaviour, it has been accepted that an elastic damaging material is appropriate in most cases as this approach is well-suited to brittle materials whose strength degrades by micro-cracking [79]. Furthermore, while several researchers have presented work on microscopic modelling of the composite [13, 80-83], a macroscopic approach is the most practical method of quantifying the composite behaviour and reproducing the damage within it [84]. Experimental input data can be taken from laminate coupon tests in which both constituents and the interaction between them are considered. Further work in this field is aimed at the inclusion of strain-rate effects [85, 86] for which, LS-DYNA has recently released a material model (Material 158 [87]). However, until the experimental strain-rate behaviour can be characterised, attention should be given to reproducing the quasi-static behaviour accurately.

Numerous geometric shapes and test configurations have been investigated in the past. However, due to the various interactive failure mechanisms observed during a composite tube crush, the successful reproduction of the splaying mode of failure has been of significant interest. Such a methodology would maybe be applicable and accurate in many applications.

### **2.6.2 Modelling of Composite Tubes**

The simple model geometries and loading conditions in axial tubular crushing give an indication of the complexity of the failure mechanisms and how capturing the correct behaviour is extremely difficult [88]. In the past, FE modelling of tube crush events has been typically undertaken using one of four

approaches, as identified by Lourenco [89]. These are single shell, axisymmetric, multiple stacked shells and solid element approaches. The advantages and disadvantages of each approach will be discussed here together with past research.

### 2.6.2.1 Single Shell

In single shell modelling, as the name implies, a single shell element is used to represent the tube wall, as shown in Figure 2.25. A single shell through-thickness is an effective approach for structures which fail by local buckling or tearing, that is, structures whose energy absorbency is less than optimum [88]. This approach has been widely used in metallic tube crush modelling. However, even in this application, to which it is well-suited, care must be taken to ensure the correct behaviour is predicted [90], see Appendix Two. As a single shell element cannot consider the delamination processes common to composites, this approach is suitable only for ductile reinforced composite materials where typical failure modes include local folding and buckling [91]. When used to represent a laminate, the number of integration points selected through the thickness of the element typically reflects the number of material layers under consideration and each can be rotated to mimic the orthogonal orientations of the experimental lay-up.

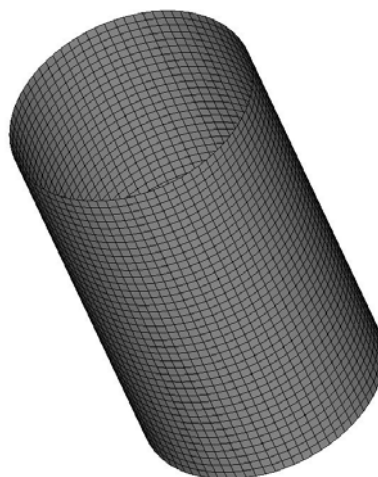


Figure 2.25. Single layer FE tube model.

Cooper [54] employed a single layer approach to develop an elastic-plastic composite material model. Models of circular CFRM tubes crushed on flat platens and various radius plug initiators were presented, an example of which can be seen in Figure 2.26. A single shell element which represents the entire tube wall is unable to account for the numerous fracture and friction processes inherent in composite crush [51], hence all forms of material damage were incorporated in a ‘plasticity’ term. An iterative approach to calibrating the plastic behaviour was required, but the final model was reported to be highly computationally efficient. A sensitivity study revealed the tensile post-failure behaviour was the critical parameter in this model.

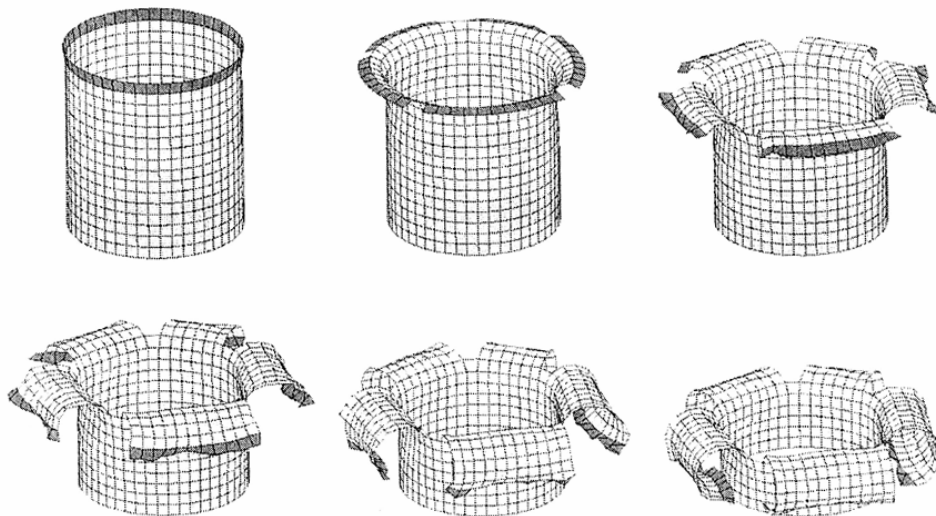


Figure 2.26. Single shell element approach to modelling composite tubes [54].

Kohlgruber and Kamoulakos [64] presented single layer models of cruciform helicopter floor structures made from carbon/aramid hybrids. Both folding and delamination failures were observed in the experimental test but only folding was considered in the simulation. The authors attribute the 30-40% under-prediction of the load to the material model (bi-phase model in PAM-CRASH,

an explicit software code) and the inability to capture delamination or ply separation with the shells.

Likewise, Botkin *et al.* [92] used a single layer of shells to represent square composite tubes in LS-DYNA, the failure mode for which was difficult to determine from the deformed failure plot. The predicted crush load is fractionally above the experimental value, although neither friction nor interlaminar delamination mechanisms are considered, suggesting a disproportionate contribution by other failure mechanisms.

### 2.6.2.2 Axisymmetric Modelling

Axisymmetric modelling, or phenomenological modelling, was most notably used by Hamada and Ramakrishna [43] to model the crushing processes in a 2-D cross-section of a tube wall, Figure 2.27. This model was based on a developed splaying mode which included a pre-defined debris wedge. Interlaminar fracture toughness controlled the central wall crack propagation and, when crushed over a small displacement ( $\sim 0.1\text{mm}$ ), the results were 8% and 16% too low for cloth and filament wound glass/epoxy tubes respectively.

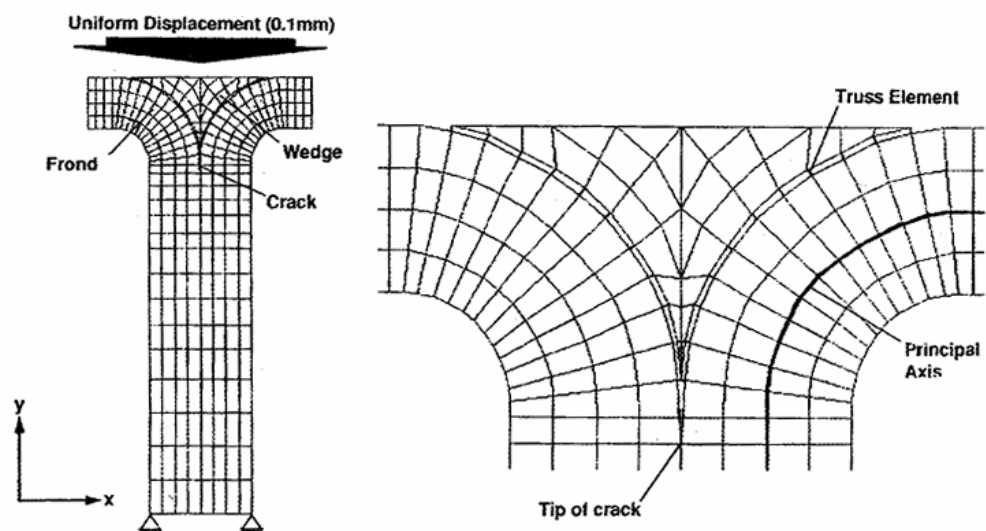


Figure 2.27. 2-D FE model of splaying mode [43].

The model did not include material failure or strength degradation due to the propagation of micro-cracks. Furthermore, the 2D model excludes numerous other contributing mechanisms such as hoop stresses, interlaminar delamination within the crush zone or any form of friction. It has been reported that for the same material, over 50% of the absorbed energy could be attributed to friction processes in the crush zone [47]. While Hamada and Ramakrishna suggest the inclusion of friction could lead to improved predictions, given its reported contribution, it would likely lead to a significant over-prediction of the crush loads. In addition, consideration of only a portion of a tube has been shown to reduce SEA values (as a result of the absence of hoop stresses) by up to 23% in a separate study by the authors on various glass/epoxy tubular sections (full, slotted,  $\frac{3}{4}$ ,  $\frac{1}{2}$  and  $\frac{1}{4}$  portions) [93]. A similar reduction was observed in glass/polyester CFRM tube portions reported by Duckett [55]. Consequently, this suggests that an additional degree of over-prediction may have resulted from consideration of the entire tube in the FE model.

Tay *et al.* [14] more recently studied axisymmetric models of the splaying mode of a 20-ply carbon/PEEK tube whose experimental behaviour was reported by Hamada and Ramakrishna [94]. Unlike the work described above, hoop stresses were at least partially accounted for. The use of solid elements limits the number of delamination interfaces that can be modelled (due to the high computational expense) and consequently, substantially less than the 20 experimental interfaces were included. A constraint-type delamination approach was employed (using stress in the normal and shear directions to determine failure) and reasonable agreement with experimental testing is reported. Interestingly, frictional effects were again ignored in this work. Despite this, the authors comment that "...many of the models used to date

have been rather simple...” which generally do not “...model pertinent features such as sliding friction and delaminations”. These features can be included in a multiple shell approach.

### **2.6.2.3 Multiple Stacked Shells**

Multi-shell models employ a single shell to represent each fibrous layer of the laminate material through-the-thickness. Each layer of shells must then be connected with an interlaminar modelling technique. A clear advantage of this approach is that delamination on any plane can be considered. Furthermore, once delamination takes place, lamina thicknesses can be maintained, providing an opportunity for the inclusion of the interlaminar friction processes. Feillard [16] reports that “multilayer modelling seems more adapted to represent the real crush behaviour” of the composite front-end rail he studied.

The first such model was presented by Farley and Jones [50] in which a four layer tube model was developed for prediction of the average crush force. Individual shell layers were connected with zero-length springs representative of the interlaminar material. Minimisation of the computational expense was accomplished by modelling one quarter of the tube’s circumference with appropriate boundary conditions. Furthermore, the model was just 12.7mm in length which was the original length of material observed to produce one buckling fold, the typical failure mode in metallic and ductile reinforced composite materials. A schematic of the model can be seen in Figure 2.28. Despite using an implicit solver, material non-linearity was included. However, frictional effects were again neglected in this model.

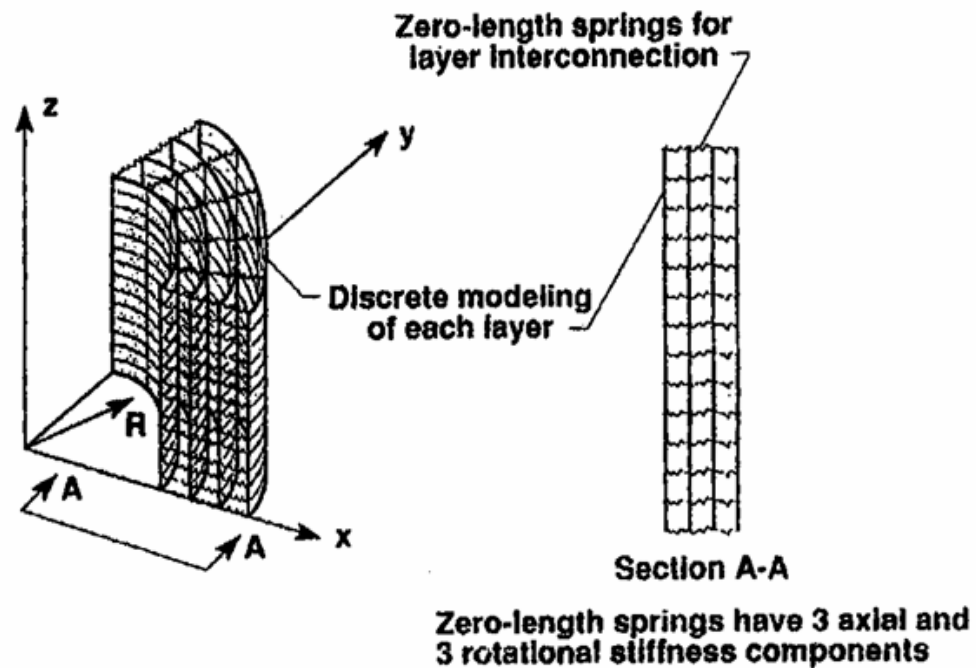


Figure 2.28. The section of tube modelled by Farley using a multi-shell approach [50].

The results showed a reasonable correlation for aramid/epoxy tubes, but poor results for carbon/epoxy tubes. This is due, in all likelihood, to the derivation of the model from a local buckling failure mode which is typically produced by aramid/epoxy tubes.

Morthorst and Horst [91] furthered the work by Farley and Jones by employing solid elements to represent the interlaminar resin, sandwiched between multiple shell elements. To maintain lamina thickness following delamination, offsets were applied to the shell elements which resulted in large overlaps between element types, leading to a degree of error. The model successfully reproduced the failure behaviour of glass/epoxy conical specimens of wall angles between  $5^\circ$  and  $25^\circ$  at loading angles of  $0^\circ$ ,  $10^\circ$  and  $20^\circ$  and in general, a good correlation across all samples, was reported. In this work, curve fitting was used to find model parameters which, after extensive testing, could not be determined experimentally. The authors claim reasonable simulation times yet

this combination of elements would probably be one of the more computationally expensive approaches.

Lourenco briefly investigated the use of a multi-shell approach to modelling CFRM and carbon tubes in PAM-CRASH. Six shells were used to represent the six layers of material, connected with a constraint-type delamination contact interface. Problems with numerical instability and a tendency for the layers to buckle, causing premature element elimination, were encountered. The author suggests that this is a result of the inability for shell elements to represent a chamfer (shown in Figure 2.29), as used in experimental tests. The ‘stepped’ cross-section resulted in large axial loads leading to a buckling failure mode. Consequently, Lourenco employed solid elements citing that the primary advantage was the satisfactory reproduction of the chamfer geometry, though a significant computational expense penalty was conceded, as will be discussed shortly.

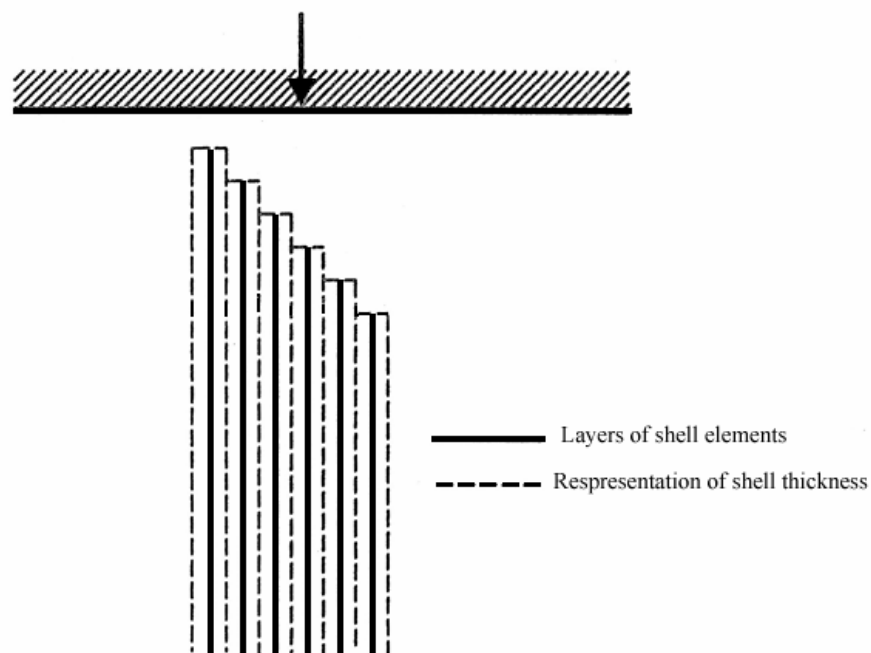


Figure 2.29. FE representation of the cross-section of a multi-shell chamfer [89]

Conversely, Curtis satisfactorily reproduced the chamfer behaviour in a separate study using a multi-shell approach in PAM-CRASH. This model used a similar constraint-type delamination interface modelling approach, despite initial testing showing significant errors with this method. The delamination modelling approach adopted was shown to incorrectly transfer the shear stiffness of the laminates resulting in an overly stiff material response. Various methods of delamination modelling will be introduced in the subsequent section. In general, predicted loads were substantially lower than expected which the author identified, was a result of poor representation of the material under crush conditions, difficulty in representing a continuous process with finite elements, and poor representation of the interlaminar bond.

In any case, the phenomenological ideology used to derive this modelling approach makes it an attractive approach when compared to axisymmetric and single shell methodologies. Solid element approaches have shown a generally good ability to represent the crushing process but are still hampered by long simulation times.

#### **2.6.2.4 Solid Elements**

Pinho *et al.* [95] furthered the axisymmetric work of Hamada and Ramakrishna and included hoop stress effects and friction to create a 3D model of a splaying mode of failure. Delamination was considered, though like Hamada and Ramakrishna, only along the central wall crack. The same delamination model was used to predict growth of axial tears, despite having discussed the development of in-plane failure criteria. Solid elements represented the tube material. A pre-defined debris wedge was included but no information was given on its dimensions or influence. 12 fronds were observed experimentally and as a result, only 1/12<sup>th</sup> of the tube is modelled (with a portion of tube either

side of an axial tear) to minimise computational expense. However, no mention is made of the computational expense and good results were reported. A sequence of the crush is shown below in Figure 2.30.

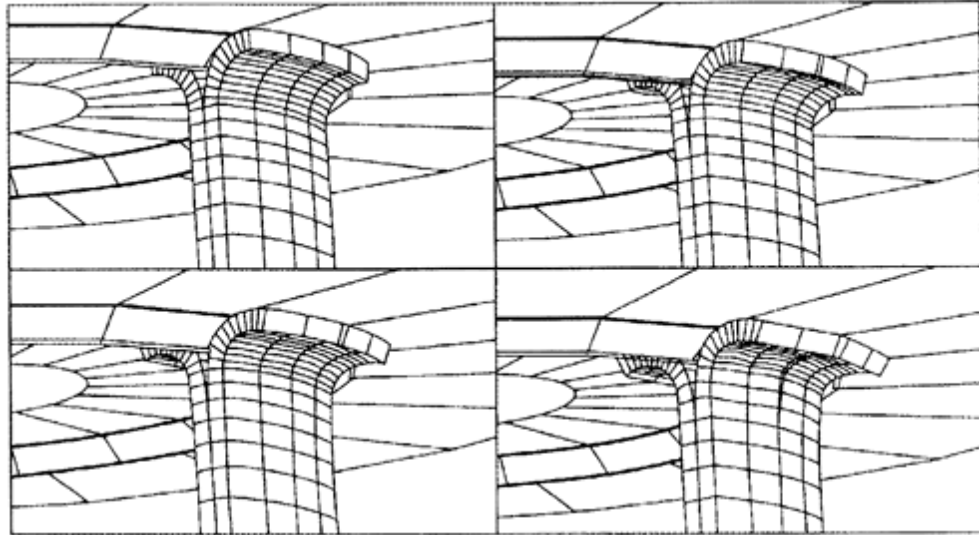


Figure 2.30. Solid element approach used by Pinho et al. with pre-defined delamination planes both for the central wall crack and axial tears [95].

Laananen and Bolukbasi [96, 97] presented a multilayered solid element approach to the crushing of composite plates which fail in a splaying mode. The symmetry of this failure mode was exploited and only half of the plate was modelled. Delamination was included as the boundary condition. While good results were reported, the model showed a high degree of sensitivity to the friction coefficients adopted.

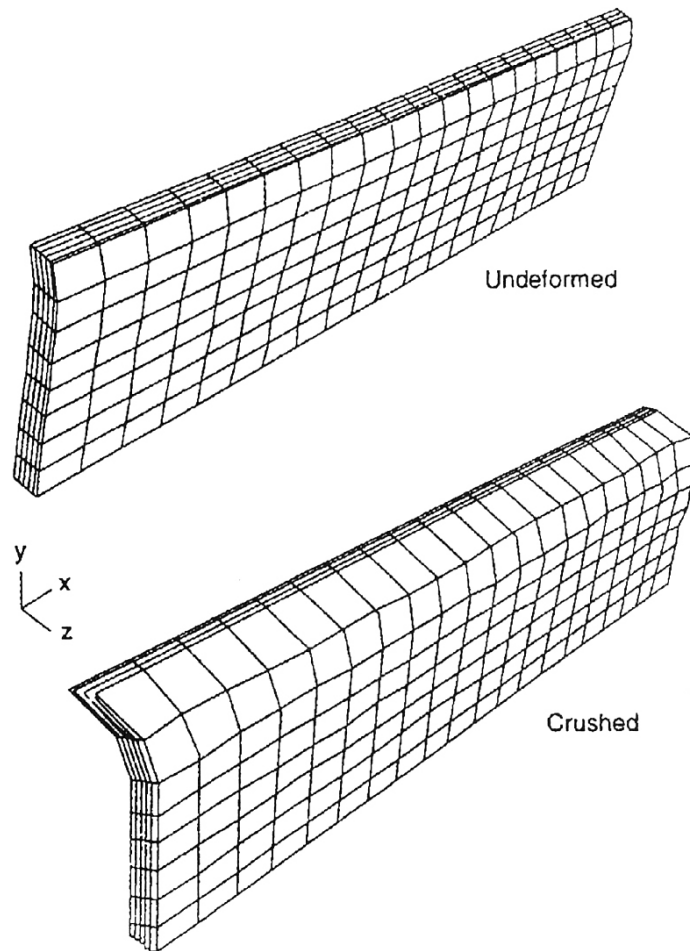


Figure 2.31. Schematic of the undeformed and deformed stages of a solid element model presented by Laananen [96] and Bolukbasi [97].

As previously mentioned, after encountering difficulty with shell elements, Lourenco [89] modelled CFRM and carbon/epoxy tubes with solid elements.  $1/16^{\text{th}}$  of the tube was modelled to minimise computational expense. The behaviour of the experimental chamfer was reportedly well captured, though the propagation of the central wall crack was not. In general, good results are reported for both material types.

Of the numerous approaches presented, it has been found that solid elements are too computationally expensive for use in larger simulations [64] while a single element through-thickness oversimplifies the crushing process [98]. Not surprisingly then, a multi-shell approach is best suited to accurately capturing the real crush behaviour in composite materials [16]. However, it is clear that

the success of an axisymmetric, multi-shell or solid element model depends largely on the correct representation of the delamination processes.

### **2.6.3 Modelling of Composite Delamination**

Precise modelling of the delamination processes in composites is extremely important to the accuracy of any particular tube crush model (provided delamination can be considered) as it has been observed to have an important influence on the failure mode and the resulting energy absorption [42, 51]. While several methods of delamination modelling exist, three primary approaches are discussed here; a force-based approach, a cohesive approach and the Virtual Crack Closure Technique (VCCT).

#### **2.6.3.1 Force-based Delamination**

The simplest approach is force-based (often referred to as the ‘spotweld method’) where nodal constraints are released once the axial/shear forces reach a user-defined force or stress limit. Nodes can be tied with springs, rigid beams or a constraint contact which prohibits movement. The modelled crack advances as each constraint is removed. Typically the failure values are determined empirically and upon reaching failure, connections are removed instantaneously. Force-based delamination has been employed successfully by Hormann and Wacker [99] to represent a single plane of delamination in a composite crush box. Reporting good results, the authors conclude that one of the reasons for the predicted discrepancies was the “limitations in the modelling technique of delamination”. Additionally, work by Xiao *et al.* [100] reported that “modelling shell layers with tiebreak contact interface appeared to be a valid approach” after achieving good correlation for a range of test types on square tubes with various numbers of layers and braid angles. Likewise, Smith *et al.* [101] and Kohlgruber [64] adopted this delamination

approach and reported a reasonable correlation in their respective simulations with Kohlgruber suggesting that further work should aim to calibrate the interlaminar behaviour with short beam bending tests.

In all of the reported work, material layers were tied through a ‘constraint type’ approach which fundamentally rigidly attaches adjacent nodes until the prescribed failure force/stress is met. However, this easy to apply method can affect the simulated material’s behaviour. Morthorst and Horst [91] report that in the explicit code LS-DYNA, a constraint type approach can result in the incorrect transfer of shear stiffness. This problem was also reported by Curtis [56] with the explicit code PAM-CRASH suggesting that this issue is not software related. While it has been suggested that the force at the crack tip is generally not a good indicator of the stress state around the crack front [88], the computational advantages of this approach make it highly attractive [102].

### **2.6.3.2 Cohesive Delamination**

A cohesive approach is applied in a similar manner to the force-based approach but uses values determined experimentally from critical energy release rates and harder-to-obtain cohesive zone length or critical force [102]. In this approach, developed by Reedy *et al.* [103], the response is controlled by classical cohesive failure behaviour where at some critical stress/nodal displacement value, failure occurs following a defined ‘unloading’ relationship. This unloading avoids spurious loads that would be introduced upon sudden element deletion and removes energy from the system as the crack advances. This approach can be used with specific cohesion elements or non-linear springs with a prescribed load-displacement relationship [104]. Fleming [102] used this approach in modelling DCB tests and reported difficulty in achieving the typical stick-slip behaviour at low-speed and

generally poor correlation at high test speeds. Additionally, Pinho [95] employs a similar approach in the solid element modelling discussed previously in 2.6.2.4.

### **2.6.3.3 Virtual Crack Closure Technique (VCCT)**

Commonly used for fracture mechanics, the third approach uses the principle that the work required to close a given delamination is equal to the energy absorbed in furthering the delamination a similar distance, thus termed the Virtual Crack Closure Technique, or VCCT. This approach, developed by Rybicki and Kanninen [105] is advantageous as the calculations are based on nodal displacements and forces surrounding the crack-tip, which are then compared to experimentally determined property data. However, such calculations can be extremely computationally expensive [102]. Furthermore, with this approach, initial imperfections are required along the anticipated delamination plane [102]. Sankar and Hu [106] showed an earlier application of this method. In a recent publication, Jiang *et al.* [107] report that VCCT can only consider self-similar delamination and resolve this by developing an interface element based on a cohesive approach.

In a review of delamination modelling, Fleming [88] reports that regardless of the approach chosen, each is sensitive to mesh refinement so care must be taken when developing models. Furthermore, he concluded that until material characterisation issues are resolved for determination of the necessary parameters within cohesive and VCCT methodologies, a force-based modelling approach presents the best choice for crash models, subsequently employing this approach in modelling the delamination within a aerospace fuselage subfloor structure [108]. However, it is clear from the works of Morthorst and Horst [91] and Curtis [56] specifically, that an approach is required, that can

suitably transfer the shear stiffness between laminae, accurately representing the interlaminar material.

## **2.7 Summary**

---

The benefits of composites as crashworthy structures have become apparent through the numerous studies undertaken and an overview of the factors influencing their behaviour has been presented. Several critical variables which control the failure modes and resulting energy absorption, of composite tubular structures have been identified; material selection, ply orientation, geometry, strain-rate, tube filling and initiator type. As a result, it has become apparent that the effect of each variable is intertwined with several other parameters. Consequently, complete characterisation of the composite materials in crush is near impossible as many of the observed results are specific to the parameters of the given test. For instance, the hoop:axial strength of a tube dictates the failure mode observed, but this is heavily influenced by the stacking sequence. This link between controlling factors is further complicated by test variables such as temperature and strain-rate.

Restricting the application of composite materials is their high production cost. In manufacturing terms, this stems from high material cost, long cure cycle times, subsequent labour costs, plus maintenance and operational costs of equipment such as autoclaves. Given the significant improvements in performance possible with these materials, it is clear that attention must be given to reducing the production cost. The Quickstep™ process has demonstrated the ability to significantly reduce cycle times, at a much reduced operational cost [109]. However, the current Quickstep™ tooling systems are only capable of curing relatively shallow panels. In addition, the author is

unaware of any prior work which relates the crush performance to changes in the manufacturing process. Accordingly, attention will be given to reducing the production cost of composite tubular structures, primarily through reduced cure cycle times, and performance will be measured according to crash performance, amongst other criterion.

In addition, a consequence of the high production cost is the reduced ability to prototype components. This restriction could be alleviated with the provision of suitable computational methods for reproducing the crush behaviour of composite materials. However, many of the models proposed to date have ignored features which are pertinent to the crushing process [14]. In order to reproduce these features, it has been suggested that a multi-shell methodology is the best approach. However, in this model, the correct representation of the delamination is vital in the accuracy of the entire model.

Of the delamination approaches presented, the VCCT approach appears best suited to accurately represent the delamination processes in composite materials. However, the high computational expense of this approach, (which requires a fine mesh size in the area adjacent to a crack [102]) makes this approach undesirable. Furthermore, the most easily implemented force-based method showed no significant disadvantages over the cohesive or VCCT approaches in a review of composite delamination modelling [88]. However, a clear limitation of this approach is the incorrect representation of the interlaminar stiffness – resulting in an incorrect flexural stiffness. The correct reproduction of this behaviour is clearly important in the overall success of composite tubular models. Consequently, effort will be given to the development of a delamination technique which accounts for the interlaminar stiffness. Furthermore, this technique will be validated through a series of tube

crush simulations, the focus of which is the correct inclusion of the pertinent crush features.

## **3 Materials and Characterisation**

Chapter Two identified the importance of material selection in vehicular crash structures and highlighted the advantages of employing composite materials in such a role. It was found that a particular area requiring attention was the cost effective manufacture of composite components, which in combination with improved computational simulation techniques, could allow the automotive industry to employ such materials in widespread crash structures. This chapter presents specific data on the composite materials which are employed throughout this work.

### **3.1 Material Types**

---

In this study, tubular profiles of two materials are compared;

- Continuous Filament Random Mat (CFRM) glass/polyester, and,
- Toray G83C carbon/epoxy pre-preg,

These materials were selected primarily for their inherent differences. The aim of the finite element modelling work presented later in Chapters Five, Six, Seven and Eight is to develop a general methodology that is applicable to many material types. As such, the differences in the chosen materials allow the generality of the modelling work to be assessed. These materials are discussed in detail below;

CFRM is an inexpensive alternative to carbon/epoxy composites, which is capable of absorbing high levels of energy, making it a likely candidate for use in the automotive industry. CFRM is a thermoplastic composite comprised of

Unifilo U750-450 continuous filament glass matting, held together by an 8% thermoplastic binder. The pre-accelerated polyester resin matrix, Crystic 701 PA, was initiated with a 1% MEKP (Methyl Ethyl Ketone Peroxide) Butanox M50 initiator.

Toray G83C carbon fibre reinforced pre-impregnated composite is a recently developed material whose modified resin formulation was developed in the interests of rapid curing [110]. The thermosetting material was supplied by Toray Composites (USA) and is available in several fibre forms, all of which utilise this advanced resin. Three types of fibre reinforcement were used, 5-harness satin weave, designated T700S 12K 5HS/G83C (370gsm and 40% resin content), 2x2 twill, designated T700S 12K 2x2 Twill/G83C (370gsm and 40% resin content), and uni-directional material, designated T600S/G83C (190gsm and 38% resin content).

### **3.2 Material Characterisation**

---

Material characterisation tests described here were designed to satisfy the input requirements of the FE modelling methodology described in Chapters Five, Six, Seven and Eight. This methodology utilises a typical composite material model which considers only the in-plane behaviour, necessitating the anisotropic properties listed in Table 3.1, be defined. Further detail on the material model can be found in Chapter Five.

Table 3.1. Material properties required by LS-DYNA's material 58.

<b>Symbol</b>	<b>Property</b>
$\rho$	Density
$E_1$	Young's modulus in the longitudinal direction
$E_2$	Young's modulus in the transverse direction
$\nu_{12}$	Poisson's ratio in the 1-2 direction
$G_{12}$	Shear modulus in the 1-2 direction
$G_{23}$	Shear modulus in the 2-3 direction
$G_{31}$	Shear modulus in the 3-1 direction
$\sigma_{11t}$	Ultimate tensile strength in the longitudinal direction
$\sigma_{11c}$	Ultimate compressive strength in the longitudinal direction
$\sigma_{22t}$	Ultimate tensile strength in the transverse direction
$\sigma_{22c}$	Ultimate compressive strength in the transverse direction
$\sigma_{12s}$	Ultimate shear strength in the 1-2 plane
$\epsilon_{11t}$	Tensile strain at failure in the longitudinal direction
$\epsilon_{11c}$	Compressive strain at failure in the longitudinal direction
$\epsilon_{22t}$	Tensile strain at failure in the transverse direction
$\epsilon_{22c}$	Compressive strain at failure in the transverse direction
$\epsilon_{12s}$	Shear strain at failure in the 1-2 plane

Extensive CFRM characterisation tests were performed at the University of Nottingham and all required material property data has been published previously. Detail on the CFRM characterisation tests and additional material properties not discussed herein can be obtained in reference [55]. All material data used herein can be found in Appendix Two.

### 3.2.1 Specimen Preparation

A single fibre-form of Toray G83C (12K 2x2 twill) was characterised here, and all work was undertaken at Deakin University. Samples were manufactured on a flat mould plate. Care was taken to ensure the surface was clean and a release agent, Frekote 44-NC was applied. Samples were laid up with a number of material layers before a 'WL5200' perforated release film (produced by

Airtech), ‘airweave N10’ breather and ‘Wrightlon 7400’ vacuum bag (supplied by Airtech) were applied over the sample. Two thermocouples were inserted between the sample and mould plate, at opposing ends, to monitor the cure temperature. During lay-up, subsequent to the application of 2 layers of material, samples were placed under vacuum to debulk for 20 minutes. For the 6 layer samples used predominantly in testing, a total debulk time of 60 minutes was employed.

Samples were cured in the standard Quickstep clamshell mould using the manufacturer suggested cure cycle which held the part at a dwell temperature of  $\sim 100^{\circ}\text{C}$  for at least 5 minutes before a 3 minute period at  $\sim 155^{\circ}\text{C}$  before being returned to ambient temperature. Using the standard Quickstep™ cure chamber, the cure cycle typically took 45-60 minutes depending on sample thickness and position in the clamshell mould.

Once cured, the required specimen dimensions were marked on the panel and cut using a carbide blade tile saw. To ensure parallelism, on occasion, sample edges were lightly sanded using a linisher. All samples were dried in an oven at  $100\text{-}105^{\circ}\text{C}$  for an hour prior to testing. Special manufacture/preparation requirements for any particular test can be found in the sections below.

### **3.2.2 Digital Speckle Photography (DSP)**

A recent technology for accurately monitoring strain paths in samples called Digital Speckle Photography (DSP) was investigated in this work. This process, reported by Vacher *et al.* [111], requires only the existence of a well-defined pattern on the surface of the sample. Images taken during the test are then analysed with the appropriate software and the displacement relationships between various distinguished points are calculated to provide accurate strain

values. This process can provide strain information right up to failure, unlike some extensometer apparatus which must be removed well-before failure to avoid damage. For the small strain testing typical of composite materials (such as those described herein), samples were marked with matt grey and matt white spray paint simultaneously (from generic pressure pack aerosol cans). Additionally, specimens were given a coat of Molybond which accentuated the speckled surface shown in Figure 3.1.

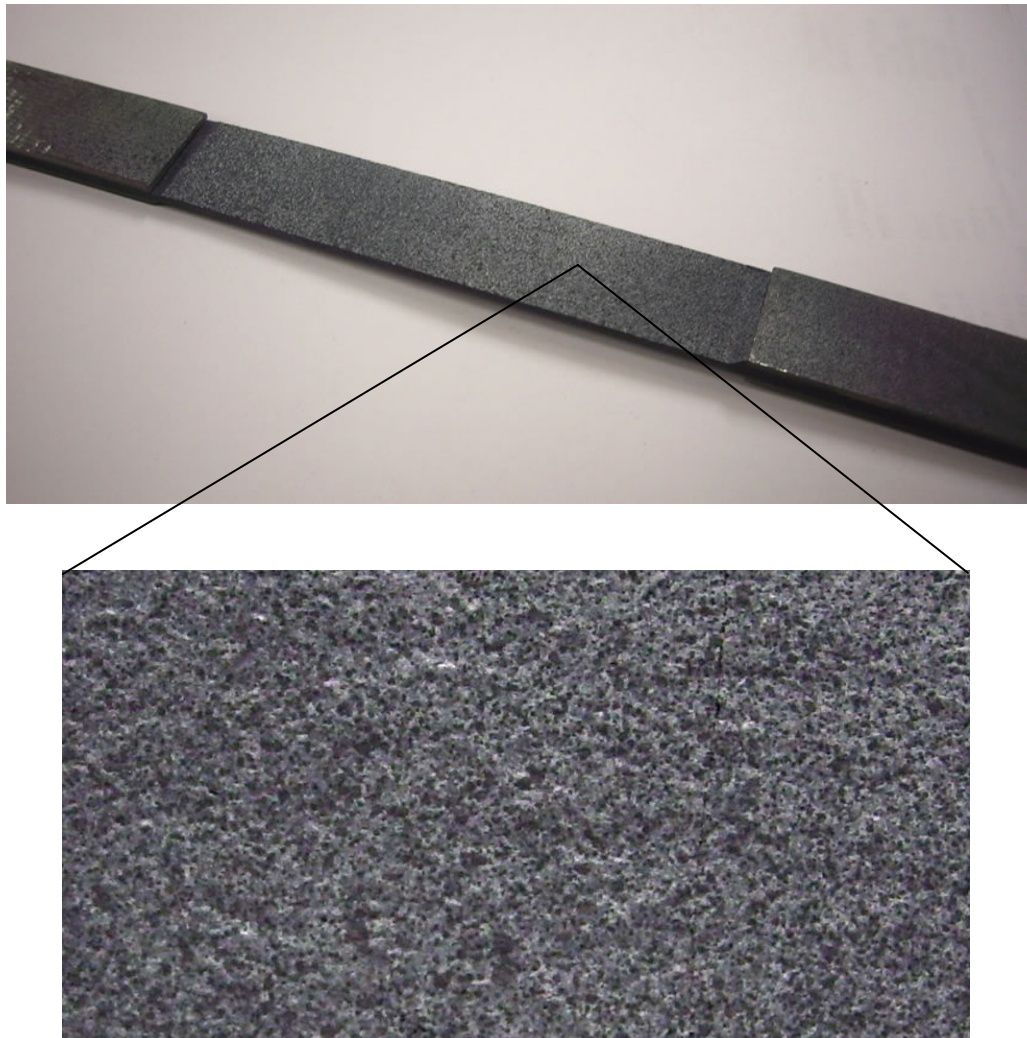


Figure 3.1. Typical speckle pattern observed in this testing. (photos taken by M.Silcock, 2006)

Images were taken by a Nikon D50 6.1 Megapixel digital SLR camera fitted with an 18-55mm lens mounted on a tripod. The software used to analyse the images was ICASOFT (version 4.5), developed by TechLab.

Typically, one photo was taken every 0.5mm of crosshead displacement. The output data from the load cell provided the specimen stress at the point each photo was taken. Once the software had calculated the strains, the values could be correlated and graphed giving the required stress-strain relationship.

A potential source of error with this approach was the manual activation of the camera during the tests. This produced a degree of error when the speckle strains were compared with stress data from the testing rig at a given crosshead displacement. Though minimal, slightly non-linear responses were often produced and hence, for clarity, trendlines have been used to display the majority of the data below and calculate the required properties. The material properties have been tabulated and are shown in Table 3.2, together with the test from which they were obtained.

Table 3.2. Toray G83C 2x2 twill mechanical properties for use with LS-DYNA's material 58. Note: Range of stated Poisson's ratio values taken from literature [96, 112, 113].

Test Type	Property	Value	
<b>In-plane Tension</b>	$E_{11t} = E_{22t}$	52.2 GPa	
	$\nu_{12} = \nu_{21}$	0.028-0.075	
	$\sigma_{ult}$	1.037 GPa	
	$\epsilon_{ult}$	1.98 %	
<b>In-plane Compression</b>	$E_{11c} = E_{22c}$	55.4 GPa	
	$\sigma_{ult}$	560 MPa	
	$\epsilon_{ult}$	1.01 %	
<b>Through-Thickness Compression</b>	$E_{33c}$	7.52 GPa	
<b>Shear</b>	$G_{21} = G_{12}$	8.84 GPa	
	<b>Mode 1,2</b>	$\tau_{ult}$	95.3 MPa
		$\gamma_{ult}$	3.51 %
	<b>Mode 2,3</b>	$G_{23} = G_{13}$	3.98 GPa
	<b>Mode 3,1</b>	$G_{31} = G_{32}$	1.10 GPa

### 3.2.3 In-plane Tensile Tests

Tensile testing was conducted in accordance with ASTM 3039D. Specimens of 250mm in length, 25mm wide and 2.7mm thick (6 layers) were manufactured by the aforementioned process. A screw-driven MTS 20/G press was used with a 100kN load cell controlled by Testworks 4 (V.4.01) at a crosshead speed of 2mm/min. Hereafter, this apparatus will be referred to only as the 'MTS'. Difficulty with the jaws slipping on the sample was eradicated by bonding tabs to the samples using 5 minute Araldite. 200gsm E-glass and R180 resin were used to manufacture the 60mm long, 1.5mm thick tabs.

DSP was used during this test and images were taken every 0.5mm of crosshead displacement. Stress-strain curves for the Toray material are given in Figure 3.2.

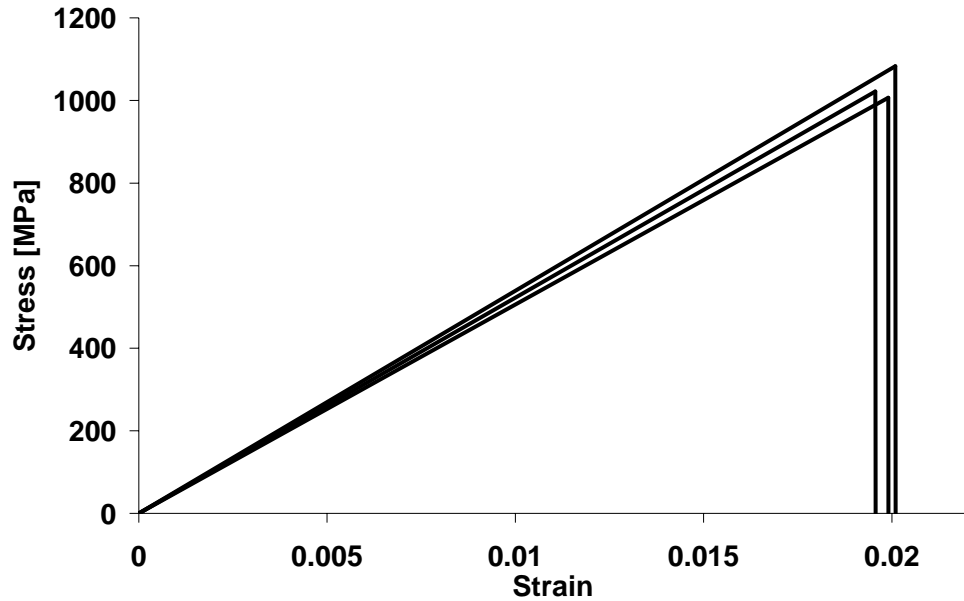


Figure 3.2. Three stress-strain curves for in-plane tensile tests of Toray G83C 2x2 twill based on trendline data.

All in-plane tensile tests failed within the gauge length. In each case, a close-to-linear loading region exists before a sudden, brittle failure at  $\sim 70$  kN. Samples failed at an average 1.98% strain with a failure stress of 1.037 GPa, giving a Young's modulus ( $E_{1t}$ ,  $E_{2t}$ ) of 52.2 GPa.

Difficulty was encountered with extracting reliable data in the transverse direction from the speckle tests. The output strain values from the speckle software varied significantly in magnitude and from positive to negative. No such difficulty was found for longitudinal strains and repeatable values were produced in this direction. The software developer could not resolve the issue and no explanation could be given, making it impossible to accurately determine the Poisson's ratio. A literature search revealed a range of values between 0.028 and 0.075 for similar  $[0^\circ/90^\circ]$  woven carbon/epoxy laminates [96, 112, 113]. The importance of accurately determining this value in the context of the FE modelling work, will be explored in Chapter Five.

### 3.2.4 In-plane Compressive Tests

Compressive testing was conducted in accordance with ASTM 6641D. Specimens of 140mm in length, 12mm width and 3.4mm thick (8 layers of material) were placed into a combined loading compression rig produced by Wyoming test fixtures a loaded into the MTS. This rig can be seen in Figure 3.3. The rig's design ensures that no bending stresses are placed on the sample. A test specimen, with strain gauges applied to both sides, was loaded and the variation between each side was monitored, confirming the absence of bending loads. Samples were compressed quasi-statically at 1.3mm/min.

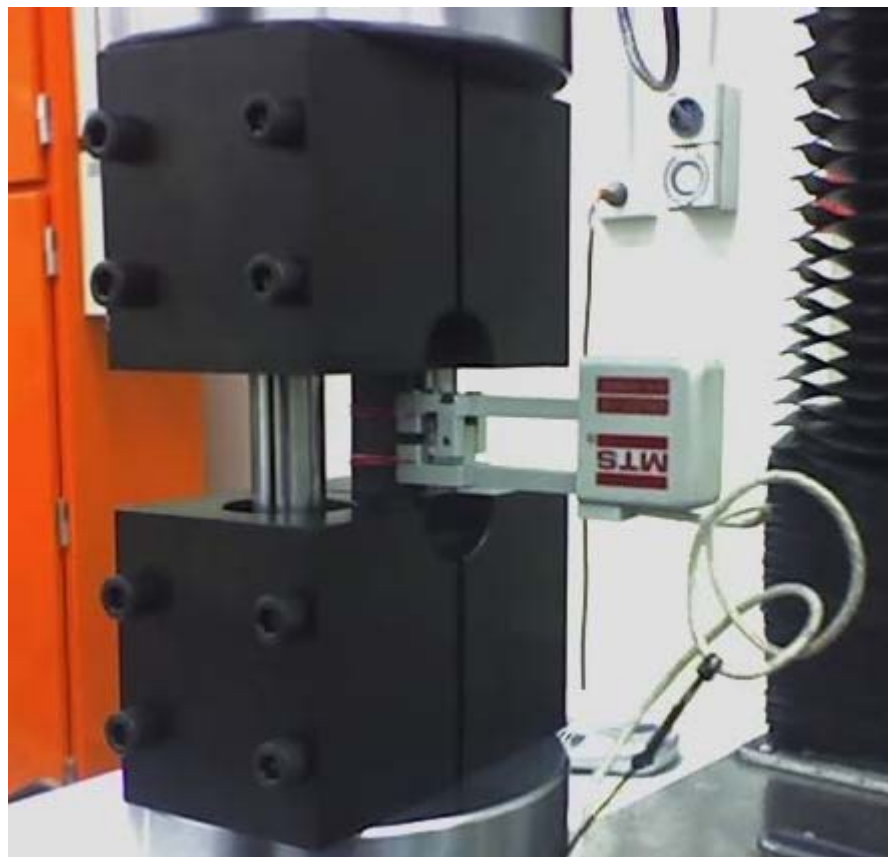


Figure 3.3. In-plane compression rig with extensometer attached.

Due to the design of the rig, images of the coupon could not be taken which meant that DSP could not be employed. Instead, an extensometer was employed to monitor strains during the first portion of the test. The extensometer was then removed (to avoid damaging the sensitive unit) and the

test completed. The data from the extensometer was extrapolated linearly to the failure stress. It has been acknowledged that this approach was not ideal as the slight reductions in load (a result of individual fibres breaking and the matrix cracking) near the failure stress was not captured. Given the very small load reductions shown, it was assumed that this effect was insignificant though a fractionally lower failure strain will likely have been produced. An image of a failed sample is shown in Figure 3.4. Load-displacement curves for the Toray material are given in Figure 3.5 while the stress-strain curves are shown in Figure 3.6.



Figure 3.4. Failed specimen from in-plane compression testing.

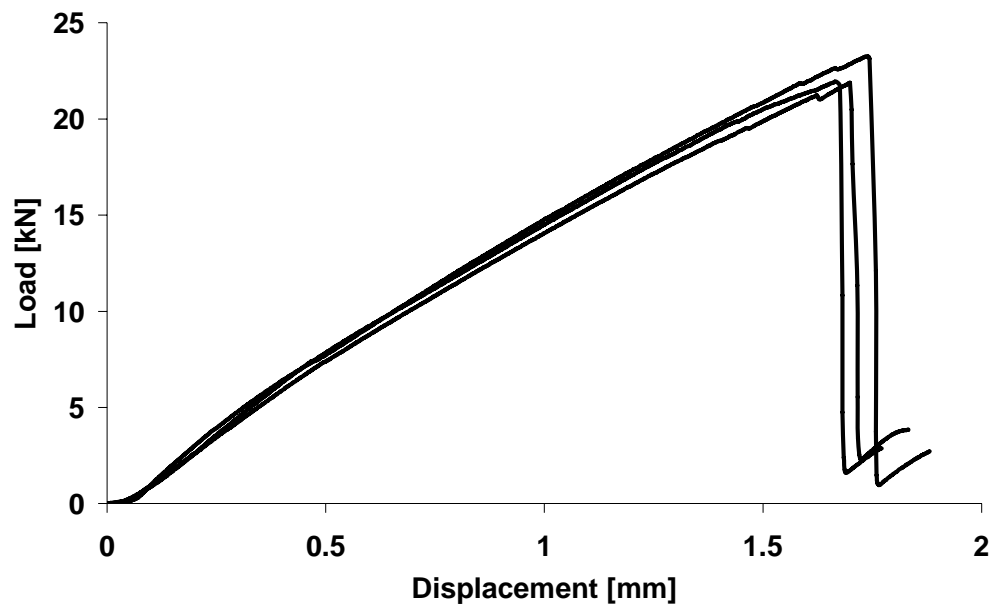


Figure 3.5. Load-displacement response of Toray G83C 2x2 twill during in-plane compression.

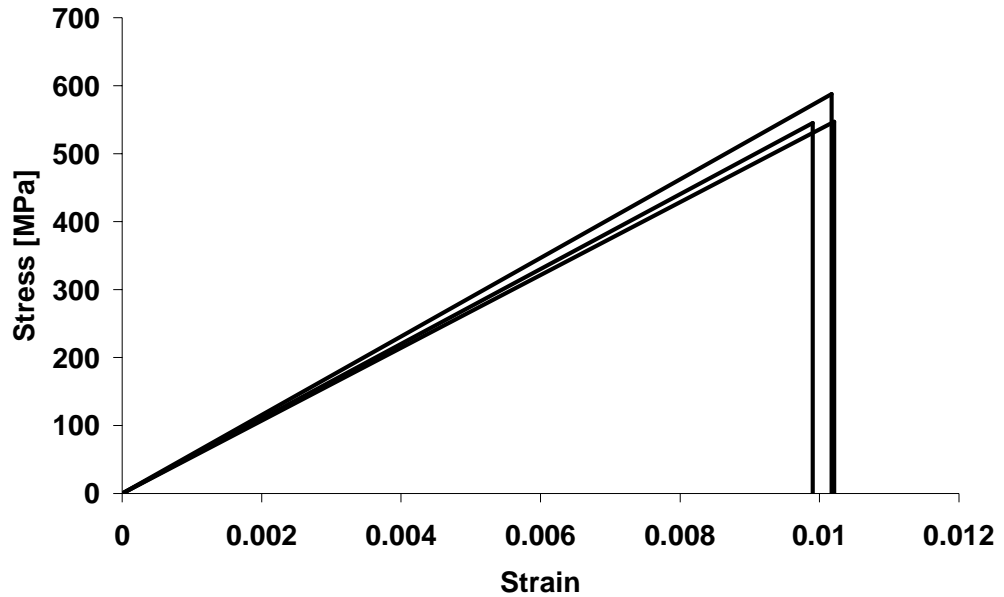


Figure 3.6. Stress-strain response of Toray G83C 2x2 twill during in-plane compression.

All in-plane compressive tests failed within the gauge length of the sample. In each case, a linear loading region can be seen before a sudden brittle failure at  $\sim 22\text{kN}$ . The average failure stress is  $560\text{MPa}$  corresponding to an average failure strain of  $0.0101$ , giving a Young's modulus of  $55.4\text{GPa}$ .

During the test, despite samples being end- and shear-loaded, some specimen slippage was observed, evident by the presence of longitudinal scratches on the sample close the gauge section. The length of these scratches increased toward the gauge section of the sample. This could not have affected the results from the extensometer. However, if speckle photography had been employed, using the rig's gauge length to calculate the strain would be inaccurate as the sample was observed to strain outside this section. This would result in a calculated strain value that would be too high, effectively providing a soft material response.

### 3.2.5 Shear Tests

Shear tests were conducted in accordance with ASTM 5379D which uses specimens of 76mm in length, 20mm wide and 4.5mm thick. A carbide tile saw was used to cut V-notches in the specimens which were sandwiched to minimise delamination caused by the cutting process. Samples were loaded into the Iosipescu test rig manufactured by Wyoming test fixtures, and placed in the MTS. A crosshead displacement rate of 2mm/min was used and DSP was employed. Images of samples at the point of failure can be seen in Figure 3.7 and Figure 3.8. Stress-strain curves for the Toray material in both the 1-2 and 1-3 directions are given below in Figure 3.9 and Figure 3.10.  $G_{31}/G_{32}$  properties were obtained from neat resin testing performed by Toray Composites (America) Inc.

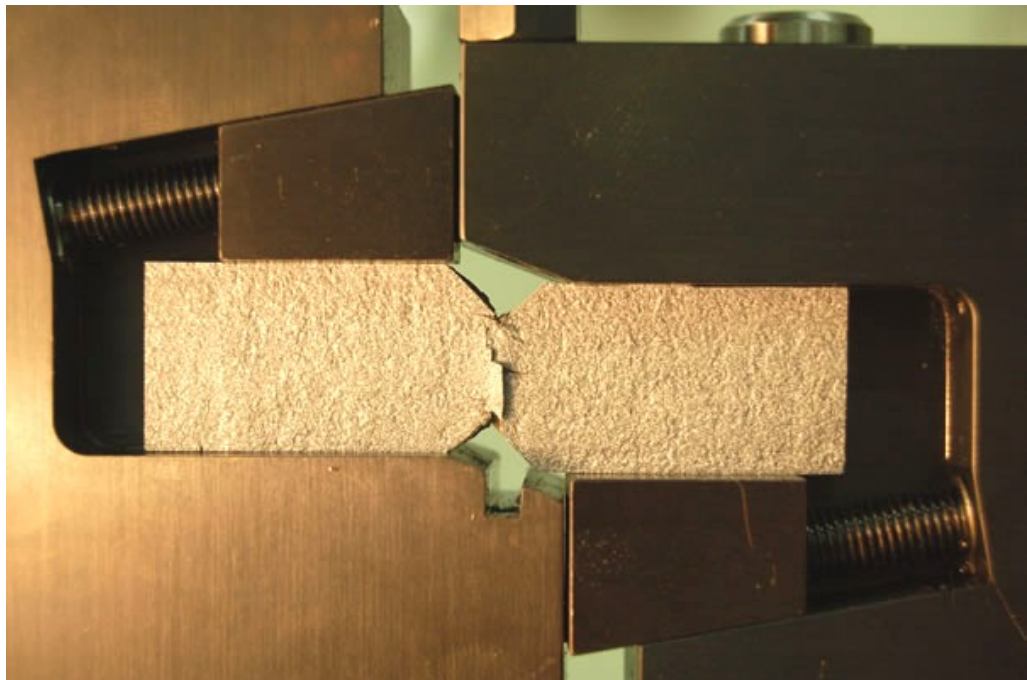


Figure 3.7. Shear ( $G_{12,21}$ ) test showing a sample at the point of yield.

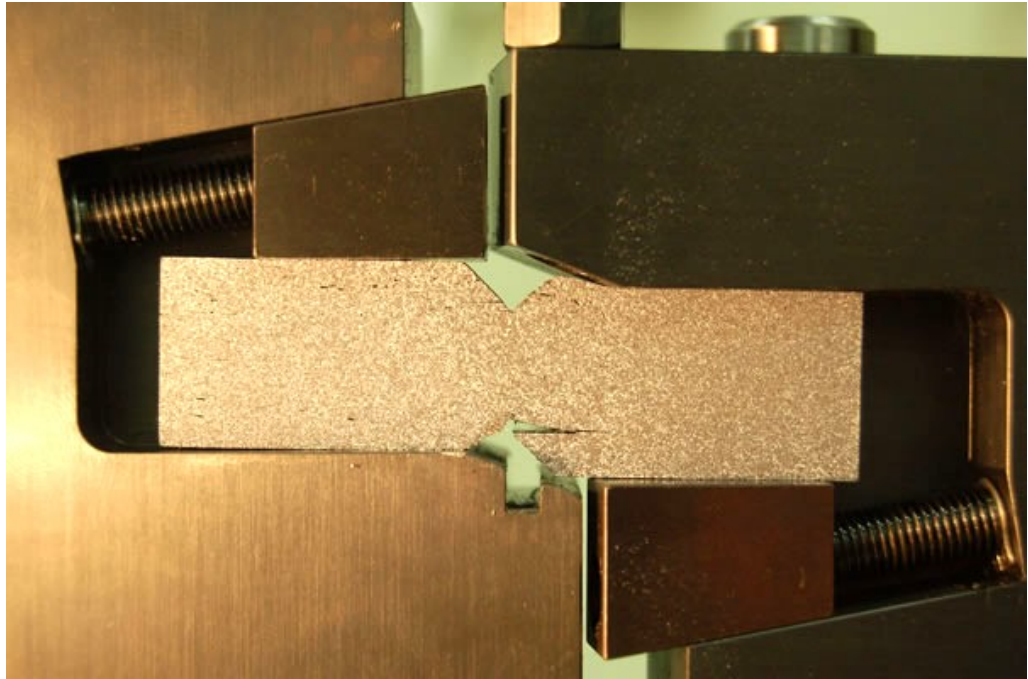


Figure 3.8. Shear ( $G_{13,23}$ ) test showing a sample at the point of yield.

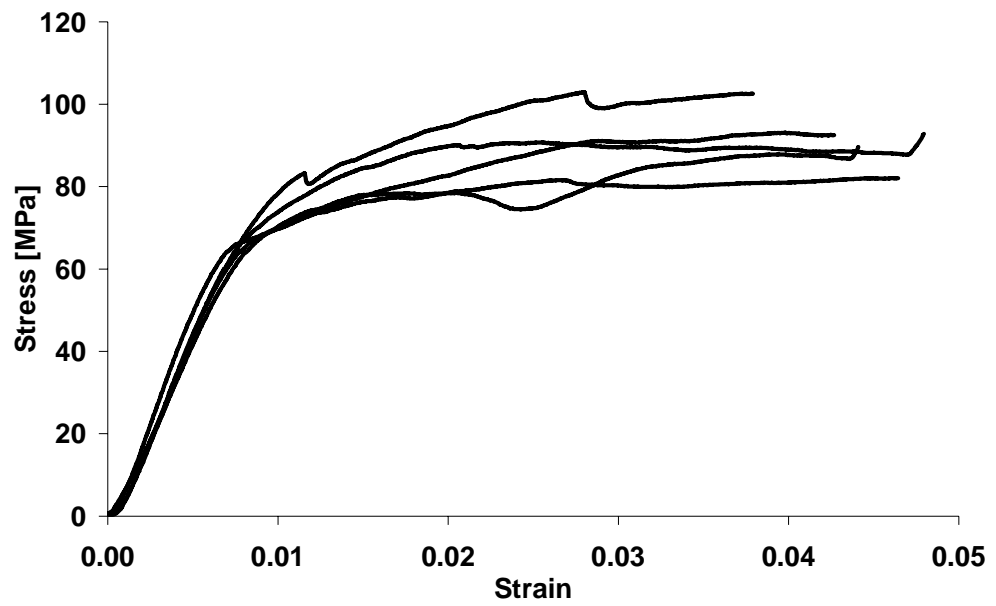


Figure 3.9. Stress-strain relationship for shear test ( $G_{12,21}$ ).

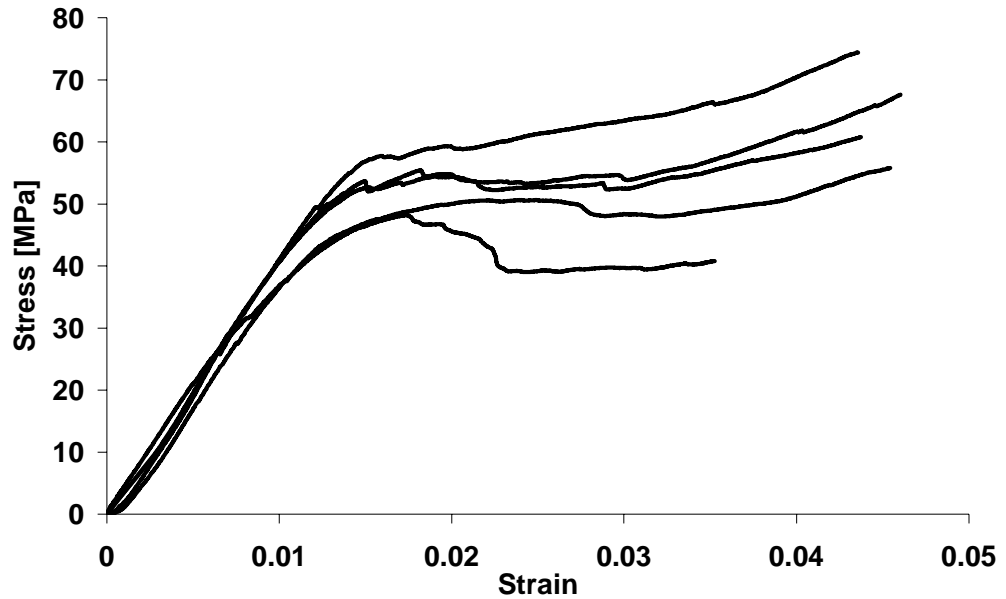


Figure 3.10. Stress-strain relationship for shear test ( $G_{13,23}$ ).

The increase in load near the end of each test is a consequence of the rig reaching its maximum travel. In Figure 3.7 and Figure 3.8, this can be foreseen as contact between the displaced portion of the sample, and the rig below the sample.

These tests showed a linear increase in load giving moduli of 8.84 and 3.98GPa for  $G_{12,21}$  and  $G_{13,23}$  respectively. The average ultimate shear stress was determined to be 95.3MPa at a strain of 0.0351.

### 3.2.6 Through-Thickness Compression Tests

This test was conducted in accordance with ASTM 695. Specimens 18.7mm high (52 layers) and 13mm square were compressed between the flat-platens of the MTS at a loading rate of 1mm/min. Specimens were loaded elastically as failure data was not required for the modelling work. DSP was employed and images were taken every 0.05mm of crosshead displacement. The stress-strain graphs can be seen in Figure 3.11.

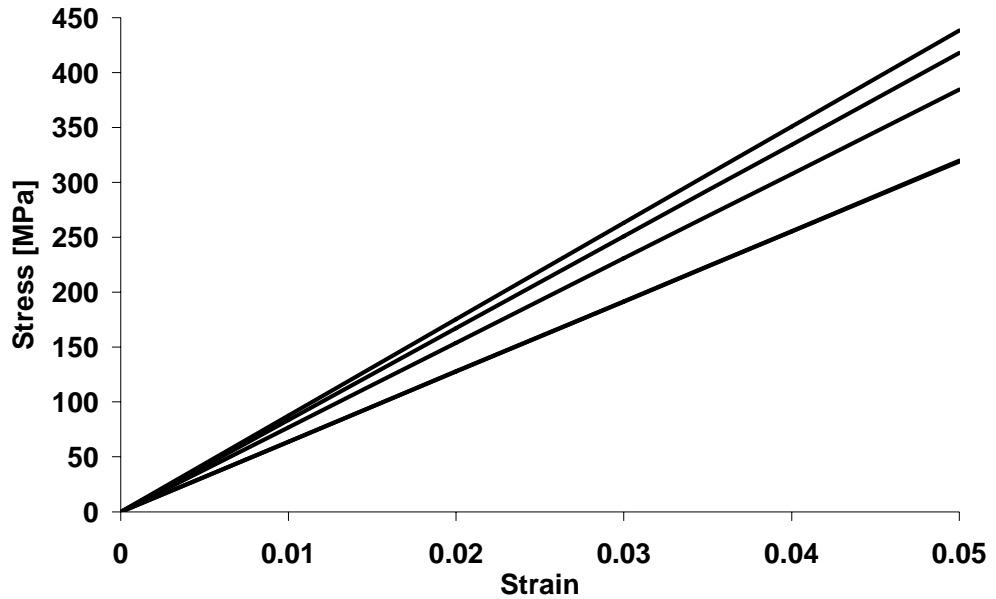


Figure 3.11 Stress-strain curves for through-thickness compression of Toray G83C.

These tests produced an average through-thickness Young's modulus of 7.52GPa.

### 3.2.7 3-Point Bend Tests

As was the case with the through-thickness testing, in 3-point-bend tests, only an elastic flexural response was required. Specimens 140mm long, 20mm wide and 2.7mm thick (6 layers) were displaced 1.5mm over a span of 80mm in the Lloyd LR30K testing frame using LrLrxCon controller software and 'Batch' (version 4.5.1 Issue 3) data capture software, both developed by Nexygen MT. Hereafter, this apparatus will be referred to as the 'Lloyd'. The load-displacement of this test can be seen in Figure 3.12.

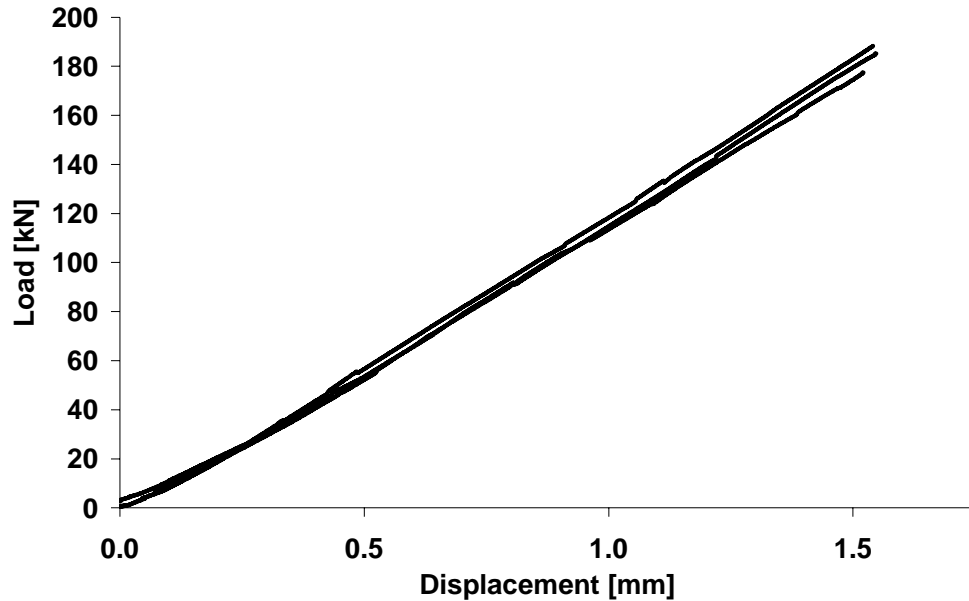


Figure 3.12. Load-displacement response taken from Lloyd rig during 3-point bend testing.

### 3.2.8 Double Cantilever Beam Tests

Mode I delamination behaviour is found by DCB testing. These tests were performed in accordance with the European Structural Integrity Society's (ESIS) "protocol for interlaminar fracture testing of composites". Specimens were 125mm long, 20mm wide and 2.7mm thick (6 layers). A pre-crack of 62.5mm was created by the insertion of a layer of unperforated peel ply (nominal thickness 0.03mm) which was inserted between the third and fourth layers during lay-up. 25mm long aluminium blocks were bonded to the samples such that during the test, the load was applied 12.5mm from the end of the specimen, creating an effective pre-crack length of 50mm. Specimens were loaded at 2mm/min in the Lloyd tensile testing frame fitted with a 1kN load cell. A photo taken during the test can be seen in Figure 3.13. The load-displacement response can be seen in Figure 3.14.



Figure 3.13. DCB test in progress on the Lloyd testing frame.

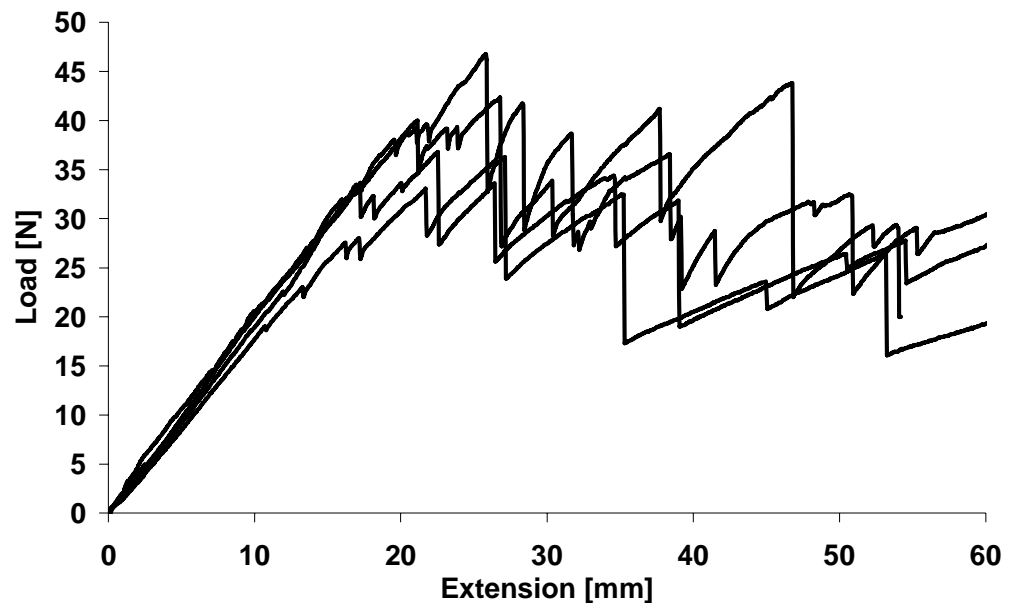


Figure 3.14. Double Cantilever Beam (DCB) test results taken from the Lloyd.

This test showed a steady rise in load until at between 18-25mm (and a load of 25-45N), the first obvious drop in load was observed, followed by the typical ‘stick-slip’ response. Interestingly, at ~12mm of extension in each test, the first crack was visually recorded, followed by continual loading to the point described above. The relatively high degree of variation in the behaviour can

be attributed to the material type where the crack propagation may be either hindered or assisted by the change in fibre orientation from  $0^\circ$  to  $90^\circ$  due to the weave.

### 3.2.9 End Notch Flexure Tests

Mode II delamination behaviour is found by ENF testing. While no standard currently exists for Mode II testing, this test was conducted in accordance with the ESIS's "protocol for interlaminar fracture testing of composites". Specimens measured 120mm in length, 20mm wide and 2.7mm thick (6 layers) with a 35mm pre-crack (created by the method described in 3.2.8 above). Specimens were loaded in a 3-point bending rig with a 100mm span on the Lloyd testing frame using a 10kN load cell as shown in Figure 3.15. The crack-tip was aligned 25mm from the support pin and 25mm from the load pin. The response can be seen in Figure 3.16.

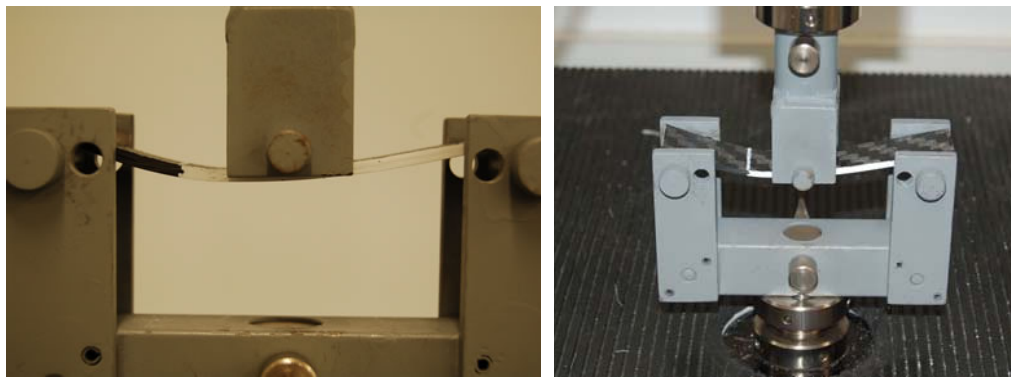


Figure 3.15 Images taken during ENF testing.

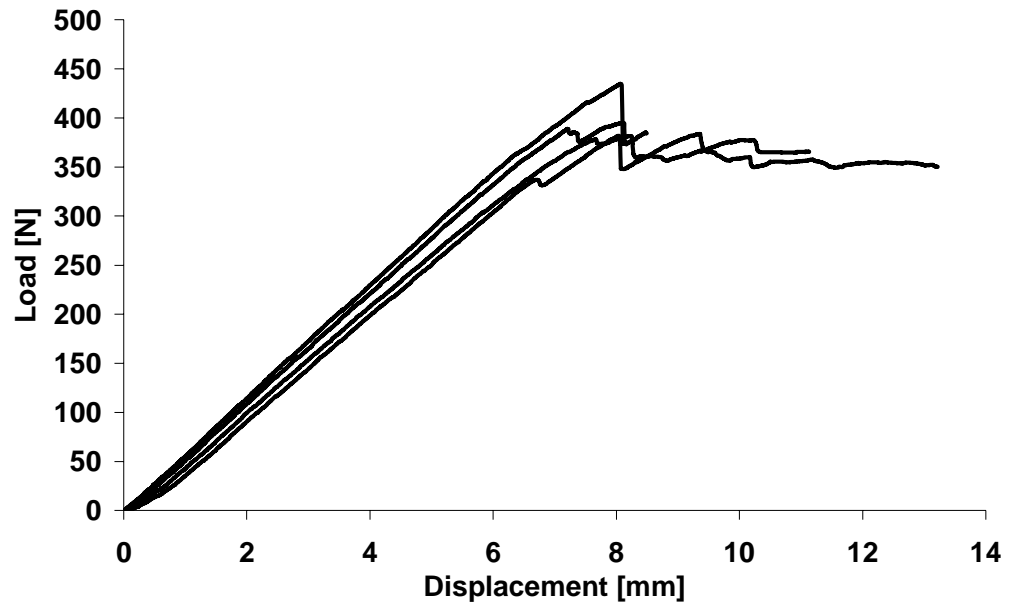


Figure 3.16. Load-displacement response of End Notch Flexure tests.

These tests showed a linear increase in load before a slight taper at around 6mm at which point the coupon began sliding inside the loading pins. No crack propagation was observed until the failure load at which point, the crack would instantly extend to some distance after the loading pin, signifying failure. This was observed between 7-8mm of crosshead displacement at a load of 380-430N.

### 3.3 Discussion

This chapter presented the results of coupon tests conducted on Toray G83C, a rapid curing resin formulation. The tests conducted here were chosen to satisfy the requirements of a typical FE composite material model based on plane-stress conditions; that is, with no through-thickness effects. The general purpose code LS-DYNA contains several such material models; in particular the tests were chosen to satisfy the input requirements of material 58 ('laminated composite fabric'), listed in Table 3.1.

In general, repeatable results were achieved and the values were in the expected range. The tensile modulus calculated by Rule Of Mixtures (ROM [114]) was 70.36GPa, some 18.16GPa above the experimentally reported 52.2GPa. This is largely due to the fibre kinking typical of woven materials. Subsequently, as the fibres straighten under the tensile strain, the modulus is affected by the support of the matrix.

In some cases, the use of DSP was successful while in others it was clearly unsuccessful. Subsequently, a high degree of care must be taken when using DSP to ensure accurate results are produced by the software. Until these issues are resolved, DSP is not recommended for measuring the very small strains in composite materials. However, modification of the approach may improve the correlation. To this effect, it is suggested that a coarse spray-pattern is adopted in future testing. The spray-painted surface used in DSP testing herein was shown in Figure 3.1, showing the fine resulting pattern. This made the task of selecting several distinguishable features difficult.

All forms of shear testing reached the limits of the testing rig. It was not possible to modify the rig without removing the locating pin position. As will be discussed in later chapters, the behaviour of materials beyond the yield point is of significant interest, particularly to computational modelling of the post-failure response.

## **4 Rapid Composite Tube Manufacture**

Chapter Two described the potential benefits of employing composite materials in the crash structures of modern vehicles. Two particular areas of focus were identified – reducing the cost of manufacture (which could be achieved primarily through shorter cure cycle times), and the provision of computational methods which accurately reproduce the crushing behaviour of such materials. This chapter presents the specific processing details of a novel method of manufacturing composite tubular profiles. Additionally, the results of an extensive investigation into cure-cycle, lay-up and fibre-orientation optimisation are presented. This work was accomplished using the recently released Toray G83C carbon/epoxy in various fibre forms.

Development of this process has shown that this manufacturing method is capable of producing fully cured, high performance composite tubes with a cure cycle of 7 minutes – a 95% reduction in time over the equivalent autoclave cycle. Furthermore, the optimisation study included an investigation into SEA and subsequently, the overall performance of Toray G83C as a crashworthy material is shown.

### **4.1 The Process**

---

A prototype mandrel was constructed from 6061-T6 aluminium. The design utilises a 1200mm long, 60mm OD circular tube section, capped at one end, with a 10mm thick flange with eight M6 bolts, at the other. The capped end employs an aluminium plate insert, which was welded in place before being machined to ensure a smooth outer surface. Mating to the flange is a 10mm

thick plate, which holds the Quickstep™ inlet/outlet connections as shown in Figure 4.1 and Figure 4.2. The inlet pipe extends 1100mm through the inside of the mandrel, unlike the outlet, which extends only to the reverse side of the flange at the connection point. The ends of the connectors utilise cam-lock, quick-release hose connectors allowing the mandrel to be disconnected and moved easily. Though the prototype is circular, it is expected that any near-symmetrical cross-section can be used.

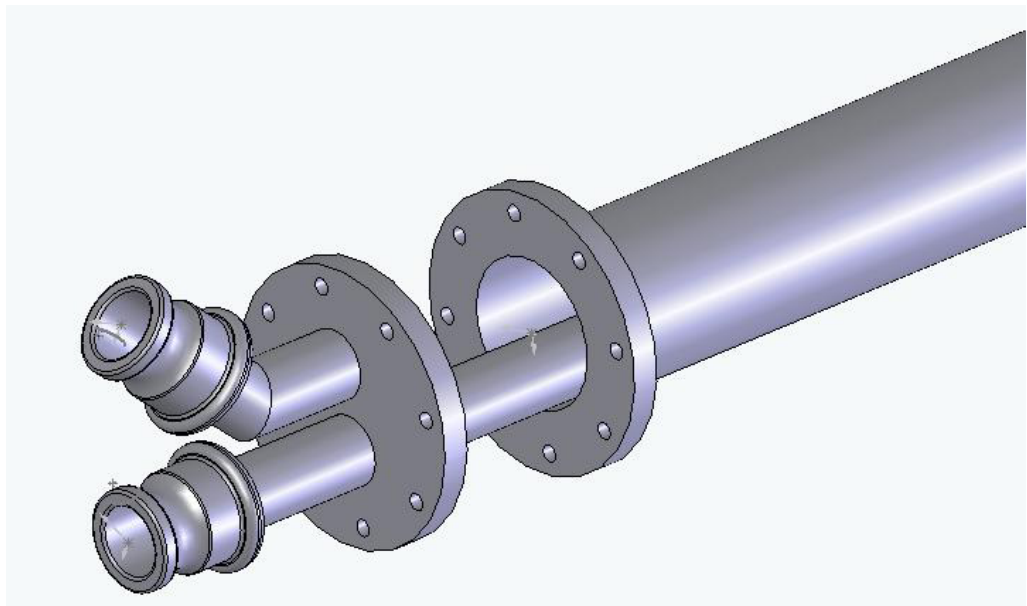


Figure 4.1. 3D design of prototype tube tool showing Quickstep connectors, flanged attachment and inlet pipe extension.



Figure 4.2. Actual prototype tube tool.

Prior to each wrapping process, the surface of the mandrel was cleaned and then treated with a release agent, Frekote 44-NC, to ensure that no surface contaminants were present. A section of pre-impregnated carbon fibre was then cut and rolled onto the mandrel by hand with care taken to avoid the entrapment of air between the layers. This was facilitated by the use of a heat-gun on the material during application, ensuring a high degree of tack. This method of application produced a 4-layer ‘Swiss roll’ type lay-up as can be seen in Figure 4.3. Thermocouples were inserted between the material and the mandrel at each end for monitoring component temperatures during the cure. One of several lay-up configurations (described shortly) was then applied and the tubes were left under vacuum (where possible) to debulk for at least 30 minutes prior to curing. The temperature and flow rate of the fluid in the Quickstep™ was controlled manually.



Figure 4.3. 'Swiss roll' lay-up produced by wrapping a single layer of material onto the mandrel.

During the lay-up process, application of both the perforated release film ('WL5200' produced by Airtech) and breather bag involved wrapping a single layer over the composite tube's surface. Two thicknesses of breather bag were used, the thicker was 'airweave N10' produced by Airtech, the thinner was 'Airbleed 120' from Aerovac. Airtech's shrink tape product 'A575RC' was used which specifies a 20% shrink at 149°C. Shrink tape application was achieved with the use of a lathe with the mandrel's connector end supported by a nylon ring inside the lathe's steady with the capped end held inside a three-jaw self-centring chuck as shown in Figure 4.4. Shrink tape rolls were held in a four-way tool-post and the required overlap of 3-4mm was achieved using the auto-feed. The shrink tape rolls were pressed between two plates, forced together with springs by which, altering the compression on the springs (hence plates) would alter the tension of the shrink tape being applied, shown closely in Figure 4.5. Vacuum bag application involved sealing a rectangular shaped bag across the top of the mandrel (between the Quickstep™ connector flange and composite tube) and extending approximately 300mm past the end of the

mandrel/tube for inclusion of a vacuum port. ‘Wrightlon 7400’ obtained from Airtech, was used. A ready-to-cure tube apparatus is shown in Figure 4.6.

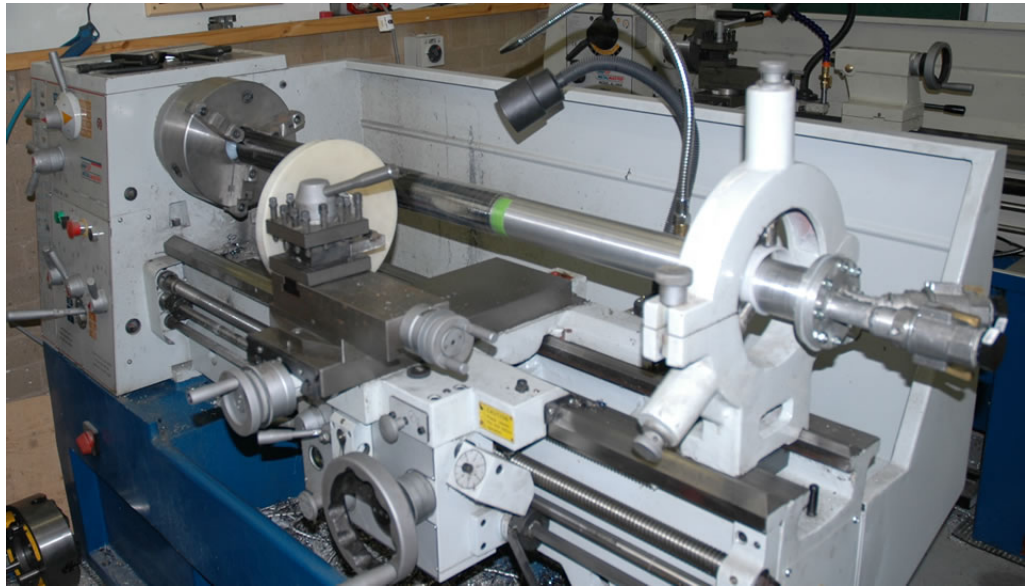


Figure 4.4. Shrink-tape application showing tube tool support and general layout.



Figure 4.5. Close-up of shrink-tape application showing shrink tape roll holder and tensioning system.

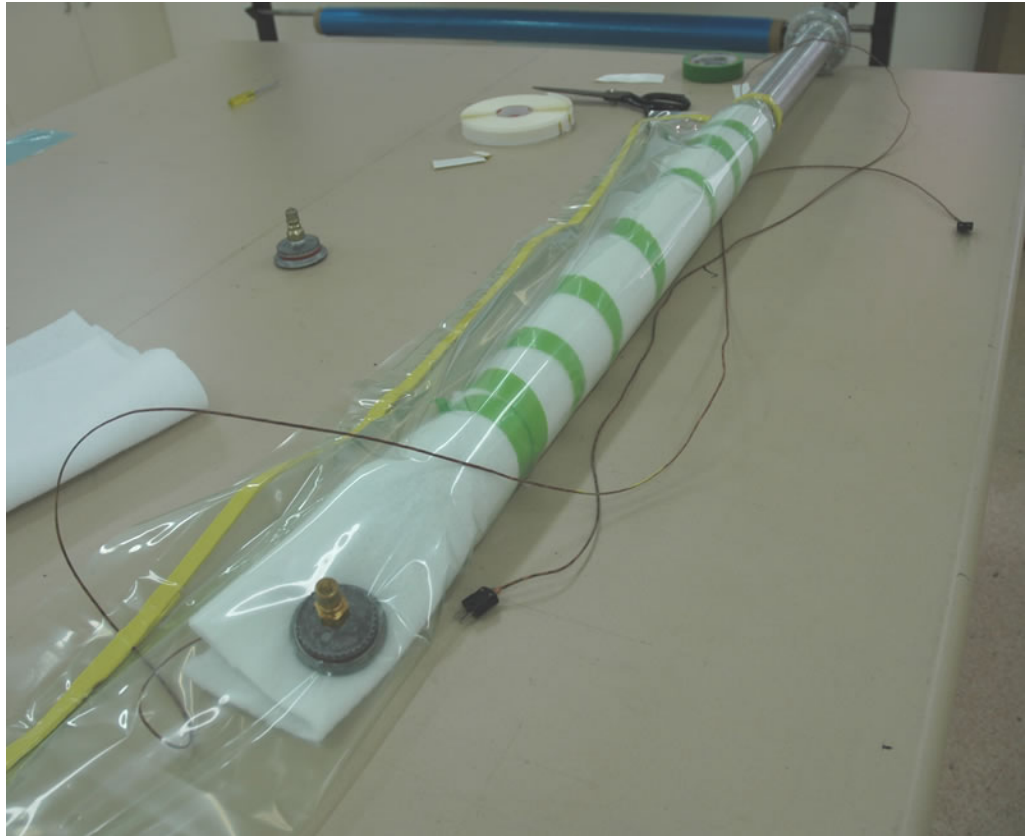


Figure 4.6. A tube with all preparation complete ready to be debulked and cured.

In following the manufacturer's recommended cure cycle [110], temperatures of up to 155°C were used, causing the aluminium to expand, applying outward pressure to the tube. Once the epoxy cured, the mandrel was flushed with ambient fluid, allowing the aluminium to shrink back to its original size. The difference in thermal expansion coefficients of the two materials (carbon/epoxy and aluminium) facilitated the removal of the cured tube. This produced tubes of ~1000mm in length. The tube's ends were removed prior to cutting the remainder into nine or ten samples. These smaller samples were of 100mm length, 60mm ID, ~2mm thick and weighed 50-55 grams.

The manufacturer recommended autoclave cure cycle for Toray G83C [110] suggests a dwell at 150°C for 5 to 10 minutes, followed by cooling to 45°C. Assuming a 2.5°C/minute ramp-rate, the resulting cure cycle time is 130 minutes [109]. Based on the manufacturers recommendations [110], a standard

Quickstep™ cure cycle was established which consisted of a 5 minute dwell at 100°C followed by a 3 minute dwell at 150°C before being cooled to less than 45°C, shown schematically in Figure 4.7. This cure cycle was optimised as described in 4.3.1 (Cure Cycle Optimisation). This cure cycle takes a total of 14 minutes – an 88% reduction in time over the equivalent autoclave cure cycle. A benefit of using the aforementioned aluminium mandrel was its low latent heat and high thermal conductivity, which resulted in remarkable ramp rates (average 40°C/min on ramp-up for the 14 minute cure cycle and 70°C/min during ramp-down for all cycles).

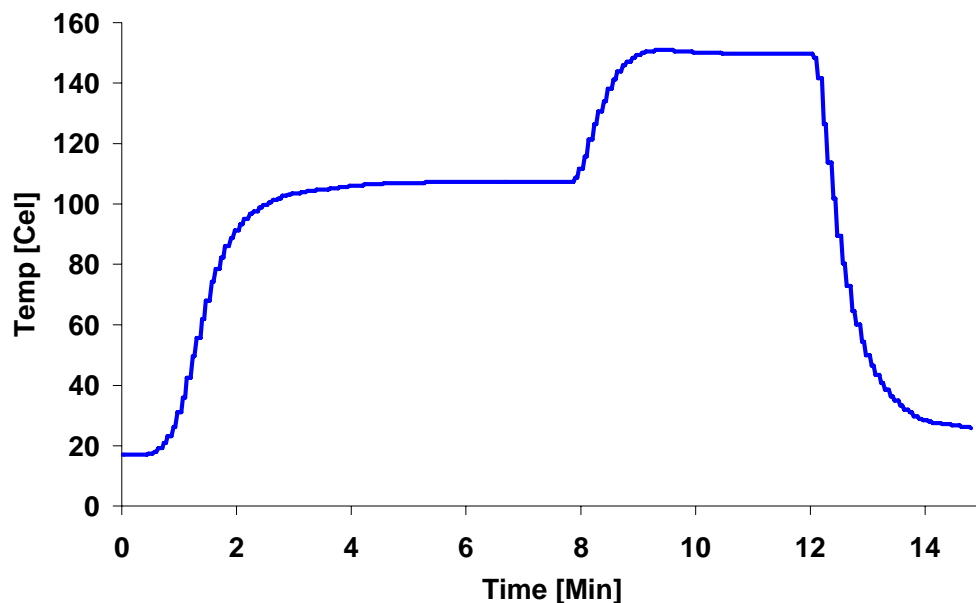


Figure 4.7. Actual temperature profile of 14 minute cure (cure cycle A).

## 4.2 Test Specifications

In order to establish the effect of the cure cycle, lay-up configuration and fibre orientations, several tests were conducted. Each tube manufactured was approximately 1 metre in length allowing for at least nine samples for compression testing; typically five samples from various positions on the mandrel were tested. Tubes TSP-1, 2, 3 and 4 were crush tested in a

hydraulically driven 385kN MTS with Teststar 2s control software utilizing a 385kN MTS load cell. All following tubes were crushed in a screw-driven 100kN MTS 20/G with Testworks 4 (V.4.01) control software with a 100kN MTS load cell. The change in MTS was deemed necessary due to the accurate range of the 385kN being  $>50\text{kN}$  in compression (average loads of 45-55kN were observed). A control test was performed to confirm the accurate calibration of both machines. A sequence of a Toray tube compression test is shown in Figure 4.8. A quasi-static compression rate of 10mm/min was used on all Toray specimens.

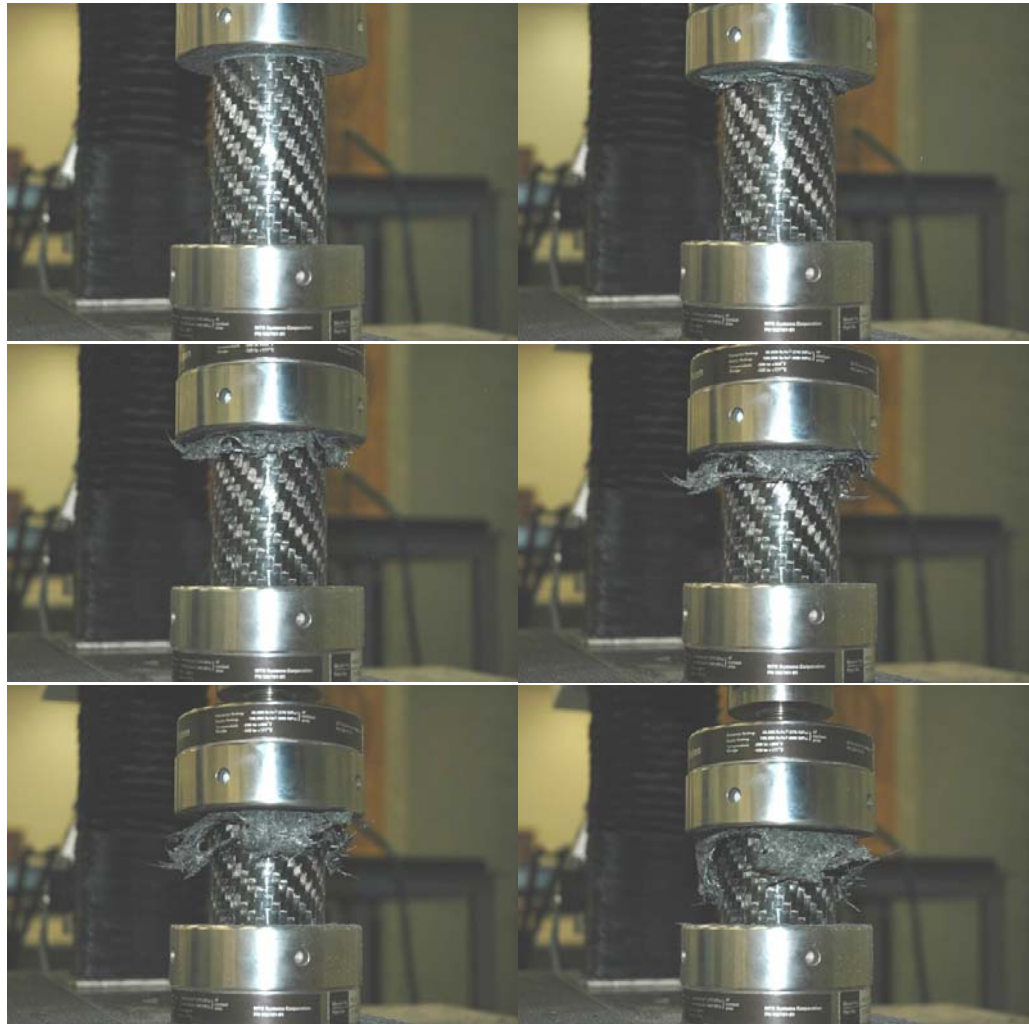


Figure 4.8. Sequence of images during axial crushing of Toray tube between flat-platens. (sequence taken by B.Smith, 2005)

Prior to compression testing, each tube had a 45° chamfer turned into one of the ends which ensured a progressive failure mode was produced. Each tube was weighed and crushed with the recorded load-displacement data used to calculate the SEA. As expected, all crushed tubes failed progressively, most of them in the splaying mode, an example of which can be seen in Figure 4.9. A minor variation in the failure mode was observed between the 5-harness satin weave (shown below) and the 2x2 twill used in later testing. Though predominantly a splaying mode, the 2x2 twill produced a degree of transverse shearing.



Figure 4.9. Example of the splaying mode of failure observed experimentally produced by Toray 5-harness satin weave.

Early developmental work raised concerns about a potential temperature differential along the length of the 1 metre long tube and the effect of temperature gradients on the energy absorption. To determine whether this adversely affected energy absorption, the third tube manufactured was cut into 10 separate samples and these were crushed with excellent reproducibility.

Therefore the lengthwise location of the tube sample prior to testing was shown to be inconsequential.

Dynamic Mechanical Thermal Analysis (DMTA) was conducted on a Rheometrics Scientific IV. The instrument was computer controlled and the proprietary software used is known as “Orchestrator”. All samples were run on a large frame in dual cantilever mode. A multi-frequency analysis was undertaken at 1, 10, 50 and 100Hz, over a temperature range of 25 to 250°C, at a heating rate of 5°C/minute. Glass transition temperatures ( $T_g$ ) were derived by the  $\tan \delta$  peak position at 1Hz.

Differential Scanning Calorimetry (DSC) analyses were conducted on a Mettler Toledo 821 with “Star Software” version 6. Samples were run with a heating rate of 10°C/minute under nitrogen. A sample size of between 10 and 30mg was used. DSC was used to identify whether the samples had reached the highest attainable degree of cure.

For porosity testing, 10 samples were chosen as representative of each tube, 5 central specimens and 5 from an end. Samples were set in resin and polished to 1 micron. Images were taken by an Olympus BX51M microscope at a magnification of 100x and analysed by OLYSIA m3 imaging software.

### **4.3 Results**

---

The results are separated into three sections; cure cycle optimisation, lay-up optimisation and specific energy absorption optimisation sections. Additionally, a brief discussion on the observed failure modes is presented.

### 4.3.1 Cure Cycle Optimisation

During cure cycle optimisation, tubes were prepared with a perforated release film, N10 breather and vacuum bag. A fibre-orientation of  $[0^\circ/90^\circ]$  was used and all tubes experienced identical treatment and debulk times. In discussion concerning fibre-orientation, it should be noted that the  $0^\circ$  follows the axial direction while an orientation of  $90^\circ$  is wound around the tubes' circumference.

Four variations of the Quickstep™ cure cycle were tested, these are shown schematically in Figure 4.10. One particular cycle held the part at full temperature for the minimum 3 minutes, excluding the intermediate dwell period used in the standard cure cycle. This resulted in a 7 minute cure (cure cycle B), a 95% reduction in time over an equivalent autoclave cycle. The two longer cures, cycles C and D, tested the effectiveness of the dwell and full-temperature times of the standard, 14 minute cure (cure cycle A). A post-cure was performed on four tubes manufactured by the 7 and 14 minute cure cycles (two from each cycle). Tubes were post-cured for 2 hours at  $150^\circ\text{C}$  in an oven.

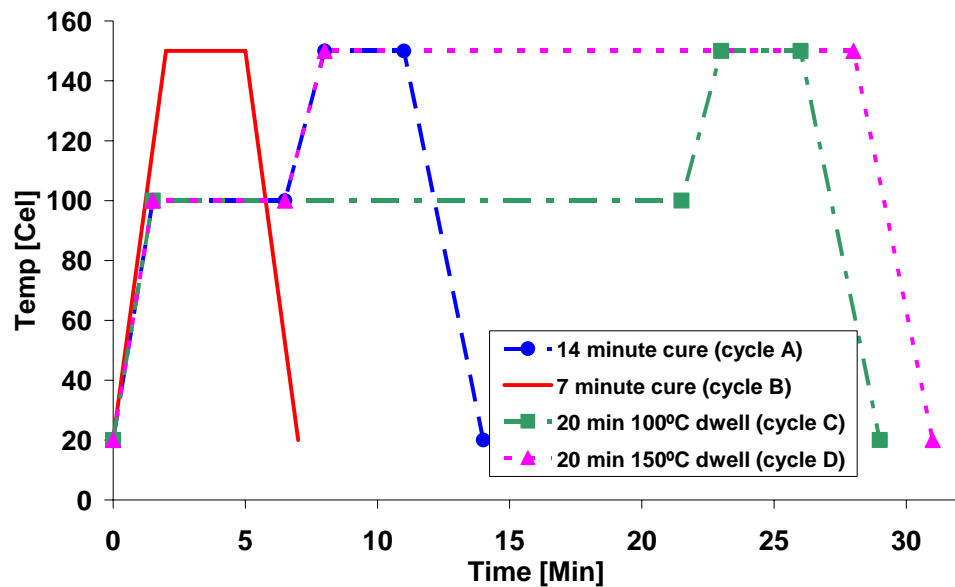


Figure 4.10. Various cure-cycles used in optimisation study.

Altering the cure cycle had very little effect on the appearance of the tubes, other than some light pitting was evident on tubes cured in 7 minutes – a result of the ‘snap cure’, which did not have an intermediate dwell at 100°C. Further testing confirmed a slight increase in the porosity of the tubes manufactured by the 7 minute cure (cure cycle B) compared with those from the 14 minute cure (cure cycle A) with average void contents of 5.2% and 4.2% respectively. Examples of typical optical microscope analysis specimens can be seen in Figure 4.11. In an attempt to reduce the tube porosity further, a 3-layer  $[0^\circ/90^\circ]$  tube was manufactured where each layer was debulked after being applied to the mandrel and cured with cycle A. The porosity values for this specimen averaged 6.0%. No reduction in porosity was observed with the longer cure cycles. Despite the varying porosity levels, the effect was not evident in compression testing as all cure cycles produced tubes of very similar SEA values, as shown in Figure 4.12.

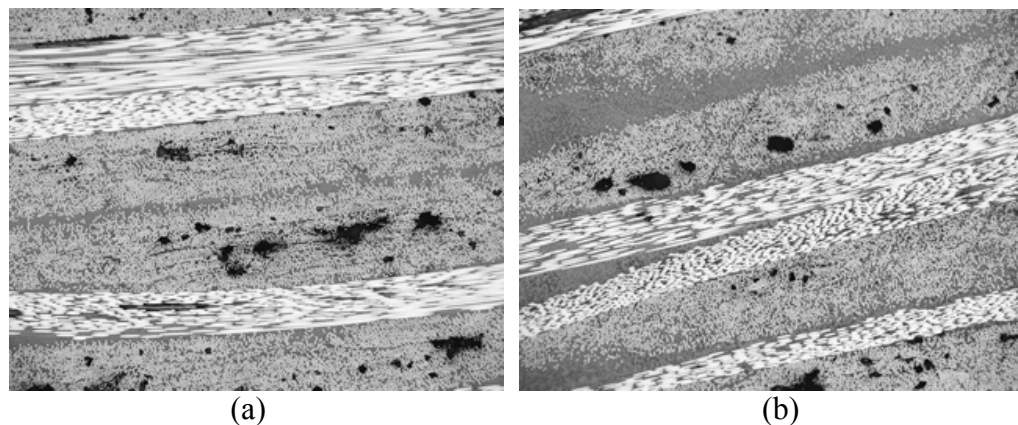


Figure 4.11. Typical porosity images for (a) 7 minute and (b) 14 minute cure cycles (100x).

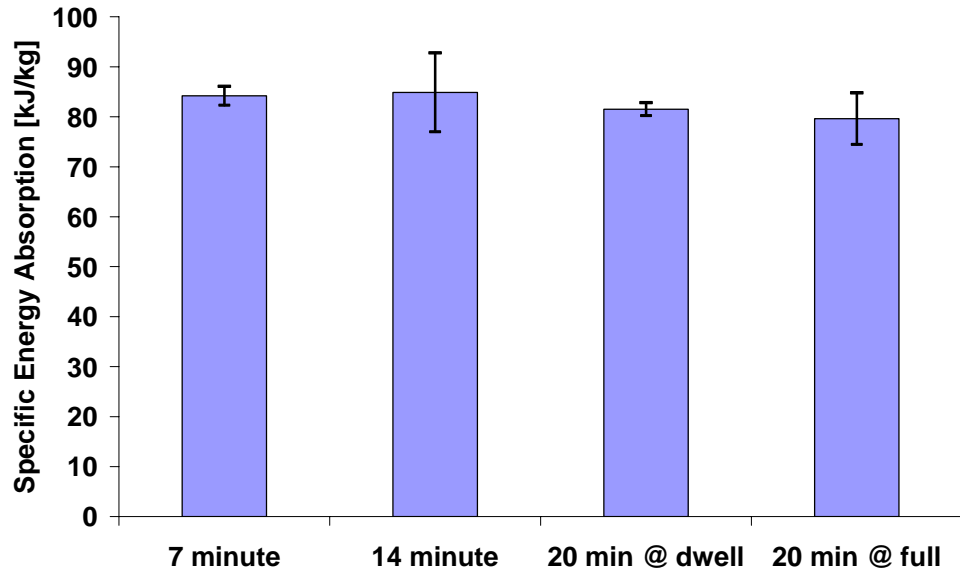


Figure 4.12. SEA values produced from the various cure cycles.

While the energy absorption of the tubes is similar for all cure cycles, there is a noticeable trend in the glass transition temperatures as measured by DMTA. The average  $T_g$  for tubes cured with the 14 minute cycle (cure cycle A) was 174°C whereas the average  $T_g$  for tubes cured with the 7 minute cycle (cure cycle B) was 183°C. The same trend may be observed even after the tubes have been post-cured, as can be seen in Figure 4.13. The author attributes the increased  $T_g$  associated with the shorter cure cycle to be a result of the higher heating rates associated with this cycle, being 65°C/min compared with 40°C/min in cycle A. The effect of high temperature ramp rates during cure on the glass transition temperature of composites has also been observed in a study by Fang *et al.* [115]. This comparison of thermal and microwave cure processes found higher  $T_g$  was observed in microwave cured composites, where the heating rate was much higher than in the autoclave cured composites. The  $T_g$  values in this study were measured using  $\tan \delta$  peaks (at 1Hz and 10Hz) and increases of up to 15°C were observed when composites were cured using microwave processing. In the current study, a small reduction in  $T_g$  was observed for post-cured tubes from the 14 minute cure cycle,

although this was most likely experimental error as the same trend was not apparent for the post-cured 7 minute cure cycle tubes. Post-cured tubes demonstrated no detectable variation in crush performance.

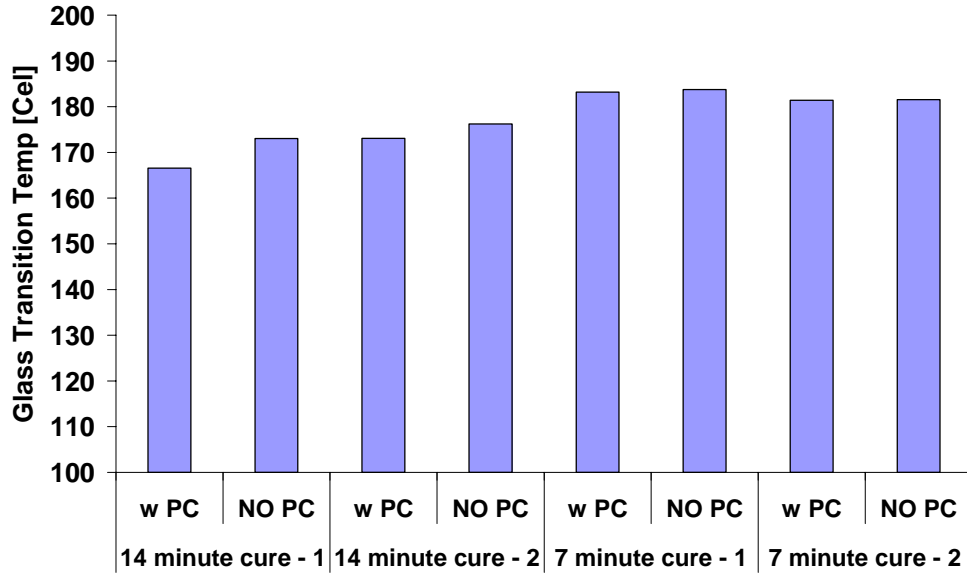


Figure 4.13. Glass transition temperatures for 7 and 14 minute cure cycles with post-cure (w PC) and without post-curing (NO PC). Values are obtained from tan  $\delta$  peaks from DMTA.

DSC testing showed no difference between samples cured by cycle A or B, either with or without post-cure. Comparison of the enthalpy curves (for the  $T_g$  transition) showed only straight lines with no apparent peaks (making calculation of the exact degree of cure extremely difficult), confirming that the highest possible degree of cure had been reached with the 7 minute cycle.

### 4.3.2 Lay-up Optimisation

Several lay-up configurations were tested in order to improve the manufacturability, performance and appearance of the tubes. The first five tubes were wrapped with a layer of perforated release film, N10 or N4 breather and a conventional vacuum bag. This approach resulted in light axial ridges along the length of the tubes and a rough, grainy appearance, which was deemed unacceptable for production purposes and likely to affect the

mechanical properties. Shrink tape was then employed to counteract this problem and provide consolidation pressure. Several tubes were then manufactured using only shrink tape but the surfaces (both inner and outer) of these tubes exhibited pitting, therefore N10 breather and vacuum bags were applied over the shrink tape. This was adopted as the standard procedure. The various lay-up configurations can be seen in Table 4.1.

Table 4.1: Variations of lay-up configuration.

	<b>Lay-up</b>	<b>Cure Time</b>	<b>Lay-up configuration</b>	<b>Surface finish/appearance</b>
<b>TSP-1</b>	[0°/90°] <sub>4</sub>	14 min	Perforated Release Film Breather (N10) Vacuum Bag	<b>Poor</b> External-Coarse & grainy, light axial ridges. Internal-Light pitting.
<b>TSP-2</b>	[0°/90°] <sub>4</sub>	14 min	Perforated Release Film Breather (N4) Vacuum Bag	<b>Poor</b> External-Rough, light axial ridges. Internal-Light pitting.
<b>TSP-3</b>	[0°/90°] <sub>4</sub>	14 min	Shrink Tape only	<b>Acceptable</b> External-Smooth, noticeable pitting. Internal-Light pitting.
<b>TSP-4</b>	[0°/90°] <sub>4</sub>	14 min	Shrink Tape Breather (N10) Vacuum Bag	<b>Excellent</b> External-Excellent, smooth. Internal-Extremely light pitting.

Tubes manufactured with the various lay-up configurations displayed very little difference in energy absorption despite several samples possessing flaws. During the manufacture of TSP-1 and TSP-2, axial ridges formed along their lengths, as can be seen in Figure 4.14. Interestingly, this had little effect on the crush performance of the tubes suggesting that they possess a degree of damage tolerance. Ribeaux and Warrior [65] studied the effect of pre-existing damage and found the response varied depending on the damage type.

The introduction of shrink tape removed these defects. An example of a shrink tape tube is shown in Figure 4.15. The introduction of shrink tape, as well as

improving appearance, increased the energy absorption fractionally (as can be seen in Figure 4.17) and reduced sample porosity slightly.



Figure 4.14. Image of large defect produced in preliminary process development. This ridge did not affect the energy absorption capability of the tube nor the behaviour.



Figure 4.15. An example of the surface finish produced from shrink tape application.



Figure 4.16. Image of 3 tubes of various fibre-forms showing the surface finish and product quality. (L-R: 2-layer [0°/90°] plain weave, 3 layer [±45°] 2x2 twill, 4 layer [0°/90°] 2x2 twill)

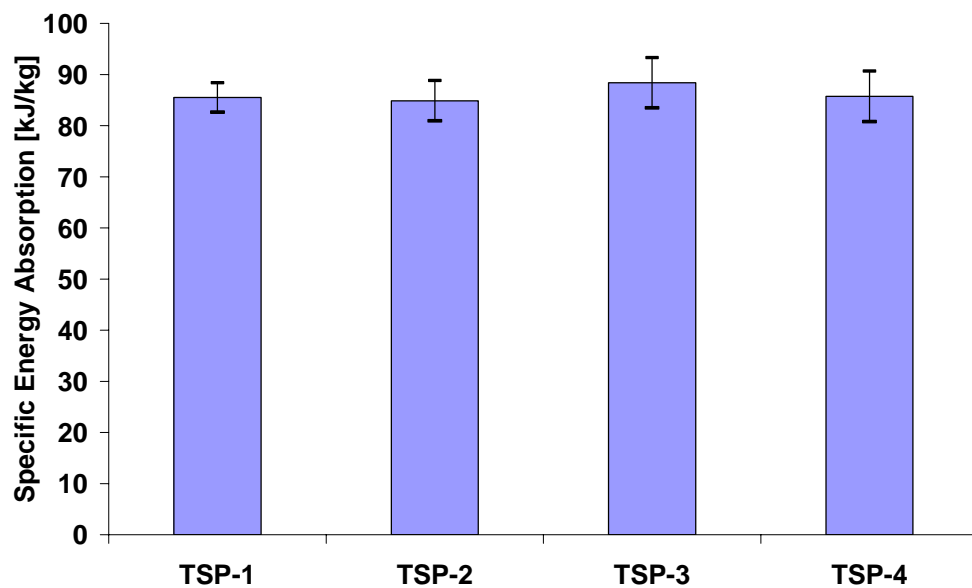


Figure 4.17. SEA figures for various lay-up configurations ( $\pm 2\sigma$ ).

### 4.3.3 Specific Energy Absorption Optimisation

The following sections discuss the results of a parametric study on the optimisation of the SEA through alterations in fibre-orientation and initiator type.

#### 4.3.3.1 Initiator Optimisation

Two forms of crush test were used in this work; flat-platen and plug initiators. Flat-platen crush testing simply involved crushing samples between two smooth flat steel surfaces with a 45° chamfered initiator included on one end of the tube. Plug initiators provide a means to facilitate attachment of tubular

crash structures in vehicular applications, simultaneously providing a failure initiator. Plugs were manufactured from billet steel and three radii were tested, 5, 7.5 and 10mm. The selection of the radii was based on Cooper's [54] CFRM testing which demonstrated significant changes in failure mode, combined with equally substantial changes in load and SEA (see Appendix Two). Additionally, a 45° chamfer was employed, consistent with the CFRM plug initiator testing. The geometry of the plugs and the radii tested can be seen in Figure 4.18 and Figure 4.19.

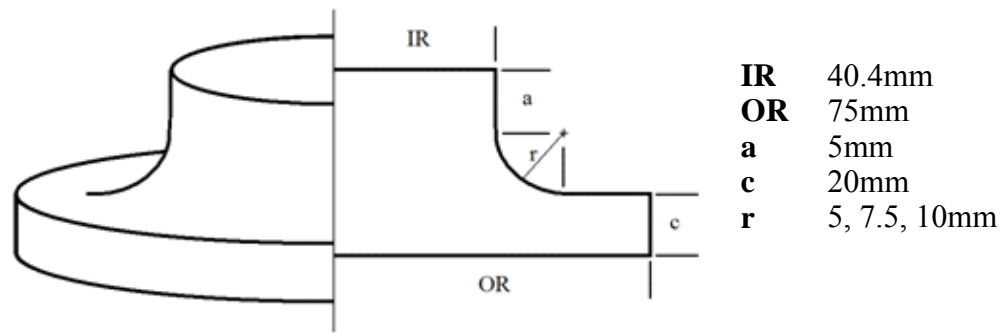


Figure 4.18. Plug-initiator geometry.



Figure 4.19. Image of 5mm radius plug initiator used in testing.

All of the plug initiated tubes showed extremely similar crush behaviour. In general, a splaying type failure mode was observed with axial tears separating the tubes into 8, 6 and 6 fronds for the 5, 7.5 and 10mm plugs, respectively. Likewise, the curvature of the fronds decreased for each of the radii. Images of the crushed samples can be seen in Figure 4.20.



Figure 4.20. Images of the tubes crushed on (L-R) 5mm, 7.5mm and 10mm plug initiators showing the increased curvature of the fronds for the reducing plug radius.

Inspection of the crushed tubes showed little indication of damage on the material in contact with the plug for any radius, with each frond appearing extremely glossy. However, the outermost material did show evidence of damage with highly compressed material visible. Breakage of the  $0^\circ$  fibres together with matrix cracking between the fibres oriented at  $90^\circ$  (cracks running circumferentially) were observed. The fibres oriented at  $90^\circ$  only failed due to the production of axial tears. The degree to which the fronds are damaged correlates directly to the radius of the plug with the smaller radii causing higher levels of damage.

Consistent with the lower degree of material damage, the average loads produced in these plug-initiated crush tests were a fraction of the loads produced in flat-platen crushing. Average loads of 19.3, 15.4 and 13.85kN were produced for the 5, 7.5 and 10mm plugs respectively, as can be seen in Figure 4.21. Consequently SEA values of 38.7, 30.7 and 27.7kJ/kg were produced for the respective plugs.

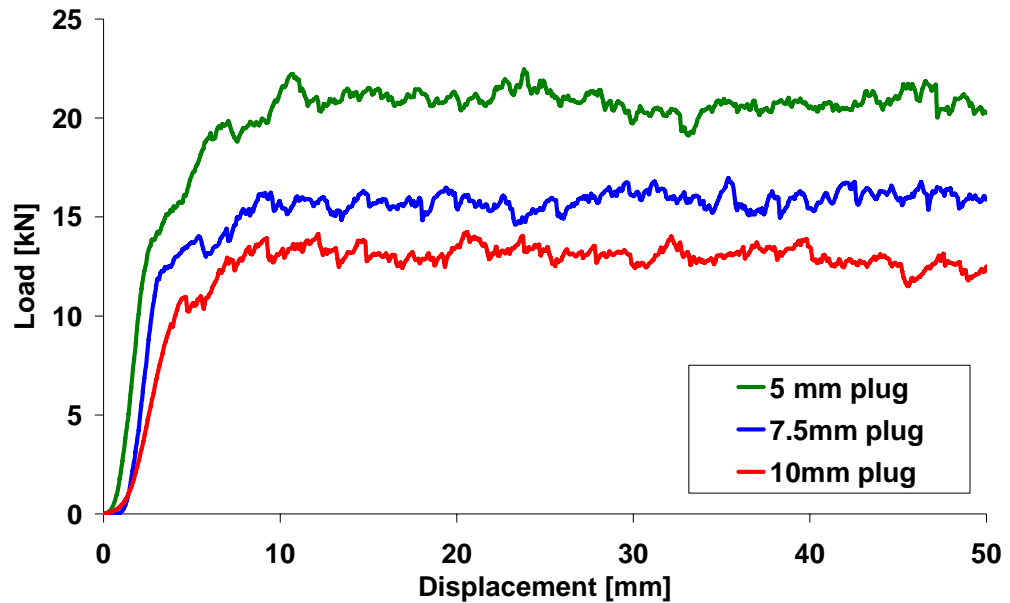


Figure 4.21. Example load-displacement responses of Toray tubes crushed on 5, 7.5 and 10mm radius plug initiators.

Interestingly, in the tubes tested here, the degree of material damage correlated directly to the curvature of the crush zone. However, in CFRM testing, this trend was not true. Reportedly, in CFRM testing, increasing the plug radius resulted in an increase in SEA up to 5mm, after which, significant reductions were reported. These results imply that the level of damage imparted on the tube material as it passes through the crush zone is significantly less in flat-platen tests than for the 5mm plug initiator tests. This behaviour is worthy of further investigation as it opposes logic which suggests that a tighter crush radius will cause higher levels of damage.

#### 4.3.3.2 Fibre Orientation Optimisation

To aid in the early development of the process, a single length of woven prepreg was wrapped onto the mandrel, resulting in tubes with a 4-layer,  $[0^\circ/90^\circ]$  configuration without seams. This produced average SEA values of 86kJ/kg at an average steady-state load of 46.4kN. Work by Farley [44] has shown that this is the least effective fibre orientation for energy absorption and significant improvements in Specific Energy Absorption (SEA) are possible with

orientations of  $[0^\circ/\pm 15^\circ]$  – see Section 2.4.3.2. However, Farley does not discuss the tube geometry, stacking arrangement or material type. As a result, it was not possible to replicate the lay-ups. The relationship between energy absorption and fibre-orientation reported by Farley can be seen in Figure 2.17, shown earlier in Chapter Two. Here, effort is given to improving the SEA of the tubes through testing a range of fibre-orientations.

A variety of lay-ups were tested which included orientations based on the reported work. The various orientations crush tested are shown in Table 4.2 including the specific form of the material used. For ease of manufacture, sections of woven pre-preg material were cut and rotated such that the required orientation was produced (for instance, in TFO-2,  $[0^\circ/90^\circ]$  material was rotated to produce a resulting orientation of  $[\pm 15^\circ/\pm 75^\circ]$ ). It should be noted that all tests were performed using the various forms of Toray G83C, cured with cycle A and prepared with shrink tape and vacuum bag.

Table 4.2: Fibre orientations tested

	<b>Layers</b>	<b>Fibre Orientation</b>
<b>TFO-0</b>	4	$[0/90]_H$ (standard – 1 piece)
<b>TFO-1</b>	4	$[0/90]_H$ in 4 separate pieces
<b>TFO-2</b>	4	$[+15/-75, -15/+75]_{S T}$
<b>TFO-3</b>	4	$[\pm 45, 0, 0, \pm 45]_{T \& U}$
<b>TFO-4</b>	4	$[\pm 45, 90, 90, \pm 45]_{T \& U}$
<b>TFO-5</b>	3	$[0/90, \pm 45, 0/90]_T$

Subscripts ‘S’, ‘H’, ‘T’ and ‘U’ denote (S)ymmetric, 5-(H)arness, (T)will and (U)nidirectional respectively.

No significant improvement in SEA was achieved by altering the fibre orientation as can be seen in Figure 4.22. TFO-1 was designed to experiment the effect of fibre discontinuities with 4 layers applied in separate pieces so that their seams were  $90^\circ$  apart. This effectively isolated the influence of these

seams, an important consideration as the following tubes were to be manufactured in separate pieces. Five samples were crushed with SEA values of within 3.4% of the average SEA produced by the ‘Swiss roll’ tubes demonstrating that further lay-ups would be unaffected by separation of the layers.

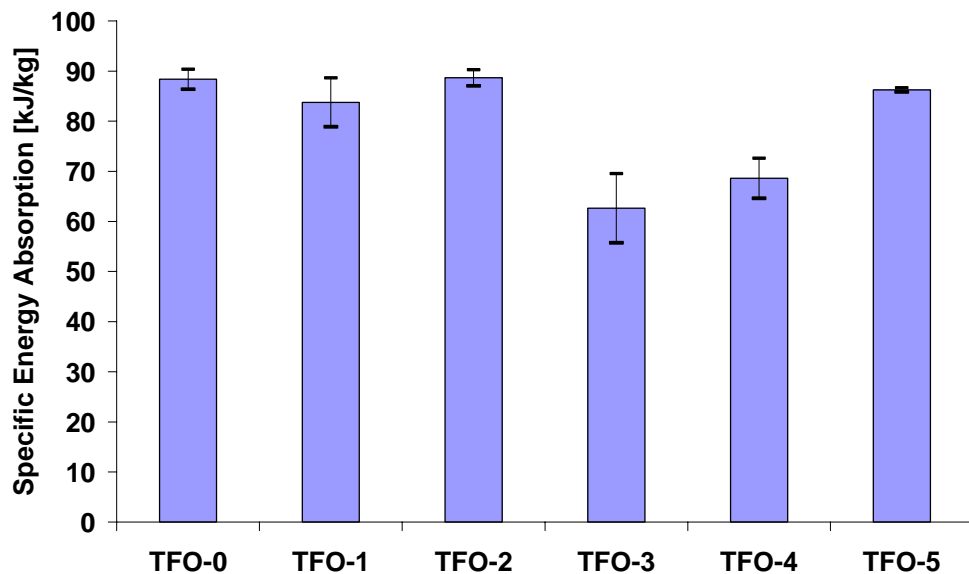


Figure 4.22. SEA values produced from tubes with various fibre-orientations ( $\pm 2\sigma$ ).

In the remaining tests, a range of failure modes were observed. The failure mode observed in the crushing of TFO-2 possessed several key differences when compared to the splaying mode. A key attribute of the splaying mode is the formation of several fronds where material splits axially forming fronds, as shown in Figure 4.9. The failure of TFO-2 showed the failed material of both the inner and outer layers turns through a very tight radius of curvature. The typical axial tears were not produced and the failed material slid along the outer surface of the tube. In all cases, a single tear could be found on the material folding outwards at the location of the seam on the outer-most layer. An example of this failure mode is shown in Figure 4.23.



Figure 4.23: Failure mode produced during crush testing of TFO-2.

The variation in failure mode produced by tubes TFO-3 and TFO-4 can be seen in Figure 4.24 and Figure 4.25, respectively. Tubes of designation TFO-3 produced multiple fronds from the  $0^\circ$  fibres, which are clearly visible, along with an uncharacteristic concertina mode developed by the central layers. In this case, the folded material increased the resistance to axial load in the latter part of the test. TFO-4 failed in what appears to be transverse shearing. There are no clearly defined fronds and there is evidence of cracks developed in the hoop direction.



Figure 4.24. Failure mode observed in TFO-3 showing external fronds and internal concertina buckling.



Figure 4.25. Failure mode observed in TFO-4 showing the transverse shearing failure mode.

Notable reductions in SEA values were observed in tubes TFO-3 and TFO-4, the purpose of which was to identify whether axial or hoop fibres had a greater contribution to the energy absorption. As demonstrated, hoop fibres (TFO-4) contributed the most by resisting axial tears although, an interaction between the hoop and axial fibres is required to produce much greater SEA values.

As some of the preceding discussion relates to the failure modes observed, it should be noted that slight variations in the failure behaviour of the standard tubes were observed when crushed on flat-platens. The variations were effectively observed only between the two types of woven material used.

Early production work employed a 5-harness satin weave. This material produced the almost ideal example of a splaying mode shown in Figure 4.9. For convenience and material availability, the 2x2 twill was subsequently employed. Flat-platen crushing of this material essentially showed a splaying mode but included a degree of transverse shearing. An example of this failure mode can be seen in Figure 4.26. No effect on the load-displacement response or resulting SEA values was observed. It should be re-iterated that the characterisation testing performed in Chapter Three was on the 2x2 twill, not the 5-harness satin weave.



Figure 4.26. Image of a 2x2 twill Toray tube crushed on a flat-platen showing a variation in the failure mode with some transverse shearing.

## 4.4 Discussion

---

The aim of this chapter was two-fold; to develop a manufacturing method for accelerated curing of composite tubular structures, and, characterise the experimental crashworthiness of Toray G83C.

### 4.4.1 Rapid Tube Manufacture

A novel technique for manufacturing composite tubes which took advantage of the Quickstep's fluid heat transfer medium has been described and the effect of key processing parameters was investigated. Specifically, the effect of the cure cycle, lay-up configuration and composite fibre-orientation were tested by axial crush testing, DMTA, DSC and porosity analysis. Most significantly, this process has shown the ability to reduce cure cycle times dramatically by eliminating the lengthy heat-up periods typical of composite curing. As a result, a process has been developed which shifts the rate-limiting step to the lay-up process, potentially reducing production costs.

A standard cure cycle of 14 minutes was employed and validated by testing several similar variations. One variation eliminated the dwell period, resulting in a 7 minute cure cycle; 95% quicker than the autoclave cure. DSC testing concluded that all cure cycles left an undetectable amount of uncured material suggesting that they had reached the highest attainable degree of cure, while a marginal increase in porosity was observed for the 7 minute cure cycle.

In general, relatively high levels of porosity were found. This could be a result of either the wrapping process or the faster cure cycles which may not have allowed sufficient time for the voids to be extracted by vacuum. Given that a test cure was performed in which the part was held at the dwell temperature for 20 minutes, showing no improvement in porosity, it is clear that the wrapping

process largely determined the porosity level. The hand-wrapping introduced a degree of inconsistency in the manufacture of the tubes. Subsequently, the use of an automated rolling/winding process could alleviate this inconsistency and lower the porosity. However, it must be noted that no observable trend in the energy absorbency of the tubes was observed for varying levels of porosity.

DMTA results indicate that the shorter 7 minute cure achieved distinctly higher  $T_g$  values, potentially a result of the increased heating rate and rapid reduction in resin viscosity. Heat-up rates of up to 160°C/min were observed in testing, 98% higher than those seen in autoclave processing. This rapid reduction in resin viscosity caused by the heating rate has been shown to improve several mechanical properties in recent work [73, 74].

No improvement in SEA,  $T_g$ , porosity or degree of cure was observed from extended periods at intermediate dwell or full temperature or when a post-cure was employed.

The use of shrink tape resulted in tubes with none of the flaws that were observed prior to its introduction improving their appearance markedly. Despite the removal of these flaws from the process, only marginal improvements in SEA and porosity were observed. Subsequently, the process was shown to be fairly robust given that large defects did not significantly alter the crush performance. The application of the composite material in separate layers, producing several seams, resulted in an insignificant difference to the performance of the tubes.

Further development of the mandrel has resulted in the design of an improved tooling system. Initial specifications called for a 0.5mm lengthwise taper and assumed a perfectly round tube stock, yet subsequent measurements showed

the tube not to have either of these. The tube was shown to be out-of-round by ~0.5mm and to increase in diameter to the mid-point before tapering very slightly. Development of a tool for use in the manufacture of Formula SAE ([www.fsae.com](http://www.fsae.com)) driveshafts successfully demonstrated a significant drop in tooling cost, easier handling during the lay-up process and easier removal of the cured tubes. However, this design is not suitable for full-scale production as removal of the cured tube requires disconnection of the Quickstep™ fluid hoses which can be a messy, time consuming task. A full image of this mandrel can be seen together with a close-up of the cam-lock end connector below in Figure 4.27. Additionally, the final product, a 40mm ID 4 layer  $[\pm 45^\circ]$  driveshaft can also be seen in Figure 4.27.

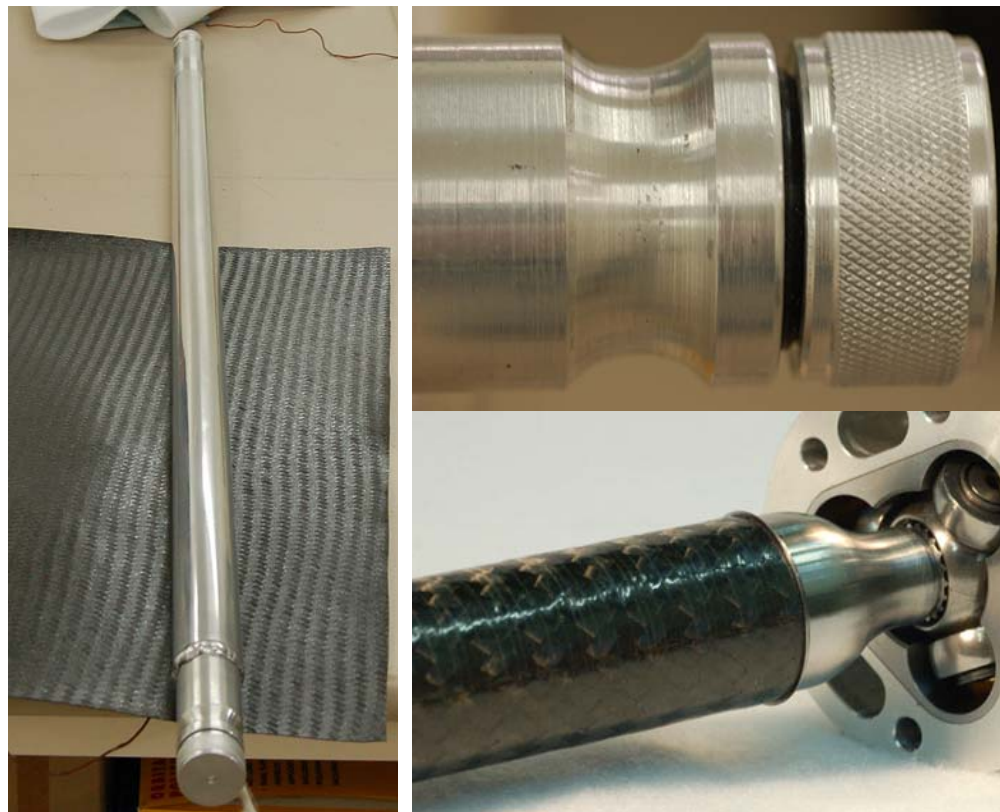


Figure 4.27. Clockwise from left – full 1.2m, 40mm OD tube tool; close-up of cam-lock connector and screw-in plug (removed when connected to Quickstep); and finished driveshaft connected to the CV joint. (photos taken by B.Adamson, 2006)

#### 4.4.2 Toray G83C Crush Performance

A large number of samples with various geometric properties, fibre-orientations, fillings, initiator types and fibre forms were tested. Accordingly, the crashworthiness of Toray G83C can be compared to other materials.

The development of this resin system was aimed at reducing the cure cycle duration by accelerating the reaction time. Hence, reducing the time required at dwell and full temperatures. In combination with this novel curing process, the cure cycle was shortened dramatically. While this curing process could reach the required temperature quicker than existing technologies, the Toray G83C required a fraction of the time to cure as other resin systems.

A baseline average SEA figure of 86kJ/kg was obtained for several tubes of 4-layer  $[0^\circ/\pm 90^\circ]$  lay-ups in either 5-harness satin weave or 2x2 twill with a slight variation in the observed failure mode being the only difference. Other materials commonly used in automotive crash applications are aluminium and steel whose typical SEA values are 20 and 30kJ/kg, respectively [36].

No further improvements were made by altering the orientation of the fibres, though this is contrary to Farley's findings which suggests a lay-up of  $[0^\circ/90^\circ]$  possesses the lowest energy absorption capability [44]. Simultaneously, notable SEA reductions for tubes of  $[\pm 45^\circ/0^\circ/0^\circ/\pm 45^\circ]$  and  $[\pm 45^\circ/90^\circ/90^\circ/\pm 45^\circ]$  indicate that interactions between the hoop and axial fibre components are vital for higher degrees of energy absorption. For instance, in a uni-directional  $[0^\circ/90^\circ]$  plug crush, if all the hoop fibres were on the inner layers, then they will have no restraining effect on the axial fibres, allowing them to easily separate from the tube. The woven material used here ensured a great deal of restraint as the intralaminar cracks, which would otherwise

separate a unidirectional lamina, were arrested at the next junction with the perpendicular fibres. Additionally, in the optimisation testing described, the hoop fibres were observed to contribute more than axial fibres. This indicates that the use of a higher hoop:axial fibre ratio may improve the SEA results. However, work by Hull [42] has shown that under quasi-static conditions, optimum results are achieved for a H:A fibre ratio of approximately 1:1 suggesting that the H:A ratio of the  $[0^\circ/90^\circ]$  tubes tested here was close to ideal.

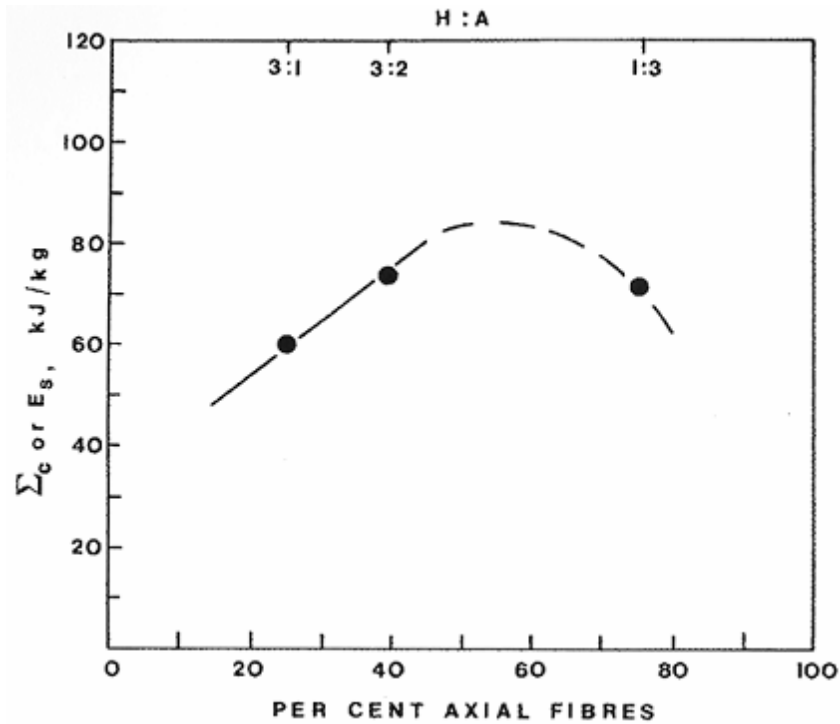


Figure 4.28. Graph showing the relationship between average crushing stress and Hoop:Axial fibre ratio at quasi-static rates [42].

Additional efforts to improve the SEA were made by including two forms of tube filling; aluminium foam and Nomex honeycomb. Both filling materials caused a significant reduction in SEA and consequently, no further combinations were investigated. Initiating failure with various radius plugs resulted in SEA values of less than 50% of the flat-platen value. Examination of the crushed forms showed a link between the degree of deformation caused

by the crush radius and the SEA value – a decreasing crush radius causes more damage and consequently, higher SEA values. In the 10mm plug initiated test, very little damage was observed other than the development of the axial tears. Additionally, material in contact with the smooth plug was not damaged, suggesting a small frictional contribution. Subsequently, most of the energy in this test was absorbed through tensile fibre fracture. The highest SEA value produced in testing was 94.5kJ/kg.

## **5 Finite Element Modelling**

The prohibitive cost associated with the implementation of composite components has relegated composites to the ultra-high performance automotive sector. Chapter Three presented material characterisation detail on a material designed specifically for accelerated curing. This material was used in the development of a production process, presented in Chapter Four, capable of producing high performance composite tubes in a matter of minutes. This process has the potential to shift the rate-limiting step in composite production to the lay-up process, reducing production times and lowering part cost. However, further cost reductions are possible with the provision of modelling methodologies capable of reproducing the post-failure behaviour of these materials in crash conditions, therefore reducing the need for prototyping.

Chapter Two identified four typical approaches used in modelling composite structures. The inability for single shell and bi-shell models to include all the required failure mechanisms has been shown in previous work. Additionally, the high computational cost of solid elements makes their use in full-scale vehicle simulations unlikely [64]. It has been suggested that a realistic representation of the crush behaviour is best captured by a multi-shell modelling approach [16].

Herein, a multi-shell approach has been adopted, the development of which was focussed on the correct inclusion of all the necessary failure mechanisms typical of composite crush. As a consequence, correct representation of the interlaminar material is extremely important. To this effect, a variation of the

spotweld modelling methodology, which correctly represents the interlaminar material, has been adopted.

The “spotweld” modelling methodology has been used, with reasonable success, in past studies and is favoured due to its easy implementation. However, the typical approach of ‘tying’ lamina, can result in an incorrect transfer of shear stiffness. The approach adopted herein, sought to ensure the correct shear stiffness and consequently, laminate stiffness.

Additionally, while the development of a predictive FE solution for composite materials would be ideal, realistically, it is unlikely that such a feat could be achieved given that the comparatively simple metallic crash models still require a degree of calibration. Subsequently, the intention is to develop a methodology which best captures the features pertinent to the crushing process; in doing so, reproducing the correct failure mode and steady-state crush load. This, it is hoped, will allow manufacturers to study the behaviour of composite crash structures without comprehensive prototyping.

## **5.1 Composite Tube Models**

---

LS-DYNA (v.970), an explicit general purpose code, was chosen as it is widely employed by industry in crash simulations, potentially allowing users of other codes to benefit from the findings herein. Circular tubular profiles were developed for analysis through the MATLAB code developed by the author (see Appendix Three) which created input decks of the required syntax. The tube models were formed by concentric layers of shell elements, each placed at the mid-plane of the material layer they represent. It was not possible to test this exact configuration experimentally. However, by applying the material to

the mandrel in separate layers, it was shown that the number of seams did not have a significant affect on the crush behaviour or performance of the tubes. Consequently, exclusion of the seams in the simulations should not have an effect. Each layer of shell elements was fixed to the next by beam elements, using a force-based spotweld delamination modelling methodology. These attributes will be discussed in detail in the following sections.

### 5.1.1 Model Geometry and Mesh Specification

Model geometries mimic those described in Chapter Three and Appendix Two for Toray and CFRM tubes respectively. Toray models were created from four layers of shells to an Outer Diameter (*OD*) of 64mm with a wall thickness (*t*) of 2mm resulting in a 0.5mm shell thickness. Six layer CFRM tube models had an *OD* of 89mm and a wall thickness of 4mm resulting in each shell element being 0.667mm thick.

Where possible, a 35mm length of tube was modelled to minimise unnecessary computational expense but still allowing adequate time for a steady-state crush to develop. Furthermore, provided the same failure mode is observed<sup>3</sup>, the length of tube tested makes no difference to the behaviour. A difference in the failure mode was observed in two instances and for these cases alone, full-length 100mm simulations were employed – these will be addressed later.

Each shell element in the tube used a fully integrated formulation (shell element formulation #16 in the LS-DYNA library [87]) which distributes integration points in a 2x2 pattern across the element face. Reduced elements (in which calculations are performed at the centre of the element face) were

---

<sup>3</sup> Long, slender tubes can fail by Euler buckling [115].

investigated by the author, but were shown on occasion to produce considerable hourglass effects necessitating varying degrees of hourglass control – an undesirable inconsistency. This was believed to be caused by the attachment of the beam elements to the shell centroids, at the integration point, which has been previously reported to cause such problems [116]. Additionally, earlier work by the author with these reduced integration elements, in modelling the collapse of metallic tubes, resulted in the incorrect prediction of the failure mode and a correspondingly poor load correlation (see Appendix One). Finally, the added computational expense incurred by the use of fully integrated formulations was deemed an acceptable compromise for the added repeatability and accuracy they produce. All simulations used 3 through-thickness integration points, spaced equally, to account for element bending. Very similar performance was observed for between 2 to 5 through-thickness points but a significant reduction in average crush load was observed where a single through-thickness integration point was tested.

Unless stated, tubes were formed with a shell element size of close to 1mm x 1mm for consistency. Due to the changing circumference of each layer, this varied slightly. Consequently, there were 280 shell elements circumferentially and 35 elements longitudinally per layer in the CFRM tube and 202 x 35 shell elements per layer in the Toray tube models. An image of the CFRM tube model is shown in Figure 5.1.

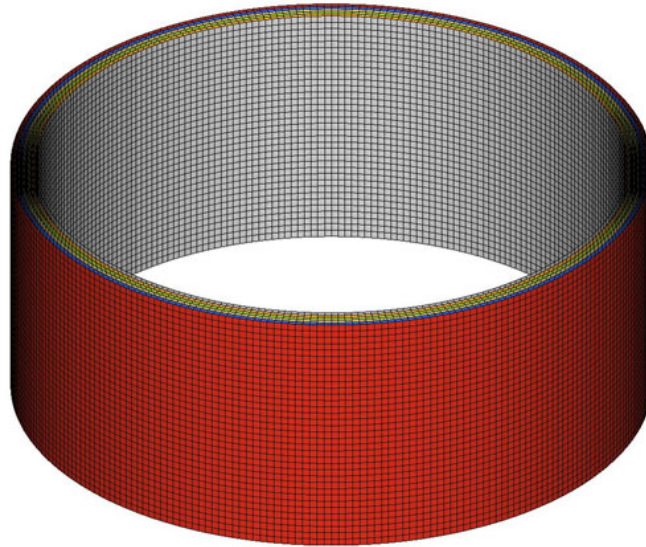


Figure 5.1. Image of tube model showing the multiple shells and element size.

Two forms of tube simulation were completed; flat-platen and plug initiated crushing. Both simulations used an upper ram which was displaced downwards, crushing the tubes. This was modelled using shell elements with a reduced integration element formulation and a rigid material model. Even though it is rigid, LS-DYNA requires elastic material data in order to calculate the contact forces. The material properties of bulk steel were used ( $E=205\text{GPa}$ ,  $\nu=0.3$ ). In flat-platen simulations, solid elements were used to represent the lower crush platen as contact issues were encountered during development; tube elements would penetrate the contact surface, terminating the simulation. Although this was likely due to the contact cards in use at the time, no further problems were encountered and the solid elements were retained with no adverse affect on simulation time. Again, a rigid material model was used with the properties of steel. Likewise, plug initiators were modelled with shell elements using the properties of steel. Figure 5.2 shows examples of the crush platens and plug initiator geometry with the tube removed.

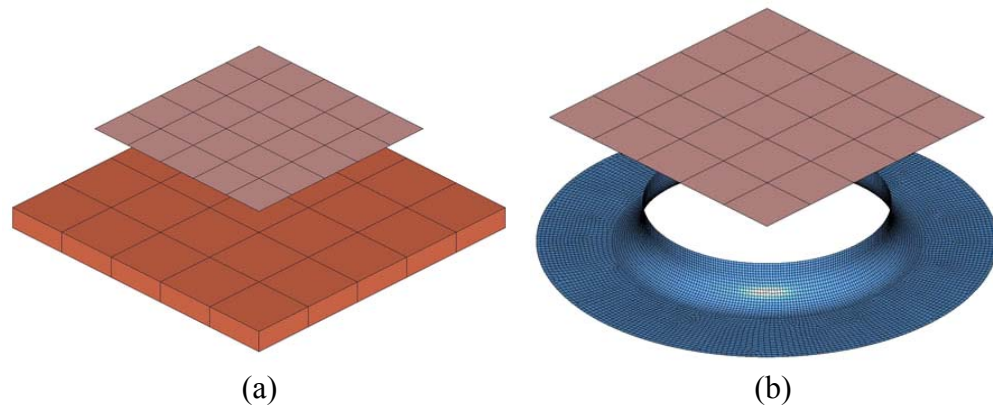


Figure 5.2. Model geometry of the experimental crush apparatus in (a) flat-platen and (b) plug initiated simulations.

No constraints were placed on any nodes of the tube. However, the lower crush platen was constrained in all directions while the upper platen was only free to displace vertically.

It should be noted that model development was focussed on achieving accurate behaviour in flat-platen simulations and unless stated, flat-platen simulations were used to test the effect of parametric changes.

### 5.1.2 Initiator Modelling

Preliminary initiator testing showed that representation of the experimental chamfer with shell elements caused global buckling in flat-platen simulations. This agrees with tests conducted by Lourenco [89] (using PAM-CRASH) and Xiao *et al.* [100] (using LS-DYNA) but contradicts work by Curtis [56] (using PAM-CRASH). The shell element is interpreted to have a rectangular profile when viewed side-on resulting in a stepped chamfer profile, effectively nullifying any initiator effect (see 2.6.2.3). Consequently, elevated wall loads lead to a global buckling mode of collapse. Likewise, pre-splaying two rows of nodes, such that the lower elements were at 45° to the crush platen, yielded the same global buckling failure.

It has been acknowledged that the debris wedge is a characteristic of the failure mode observed in experimental testing, like that described in Chapter Four. Consequently, for completeness, the debris wedge must be included in the model as it contributes to the collapse. To the best of the author's knowledge, no model has successfully reproduced the development of a debris wedge as such a task would require the conversion of failed finite elements into rigid bodies [56]. As a result, a pre-defined debris wedge was used to ensure the inclusion of all the necessary failure mechanisms, while simultaneously initiating the required failure mode.

The debris wedge was created during model initialization and placed on the lower crush platen, below the tube. Debris wedge geometry is the same for both materials and was taken from micrographs of the CFRM crush zone (shown in Figure 5.3) as it was not possible to set the Toray samples in resin while under compression. This allowed the fronds to relax giving incorrect frond angles and wedge dimensions. The simulated wedge, shown in Figure 5.4, is modeled by a spire of solid elements. Preliminary testing showed that the debris wedge must maintain a smooth curvature since representing the wedge curvature with 2 or 3 elements resulted in a global buckling mode; the sudden change in wedge angle would cause tube elements to 'catch', producing high axial wall loads.

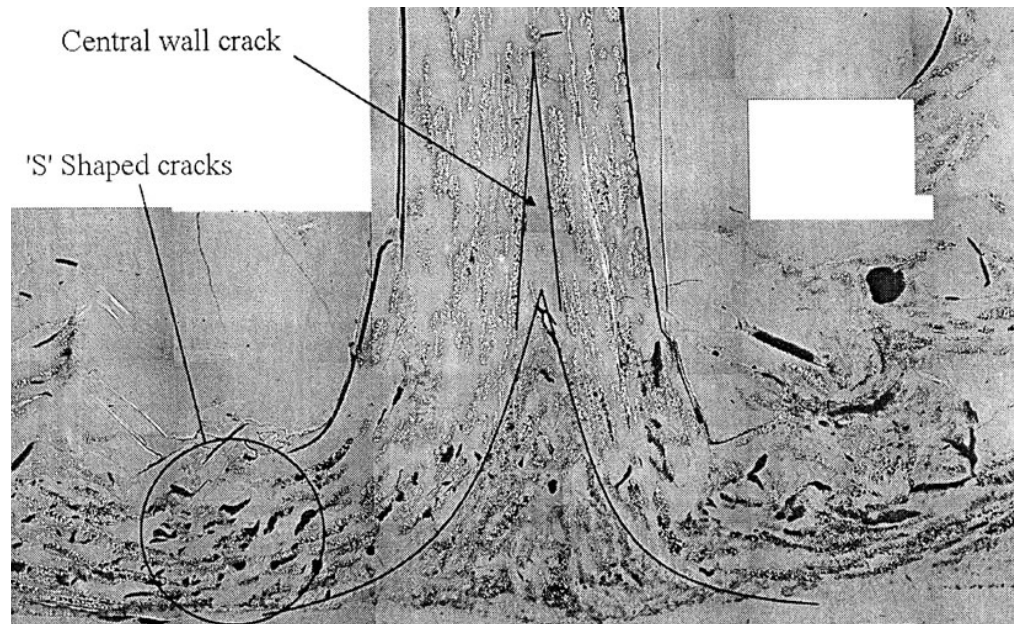


Figure 5.3. Micrograph of CFRM cross-section clearly showing the debris wedge profile [54].

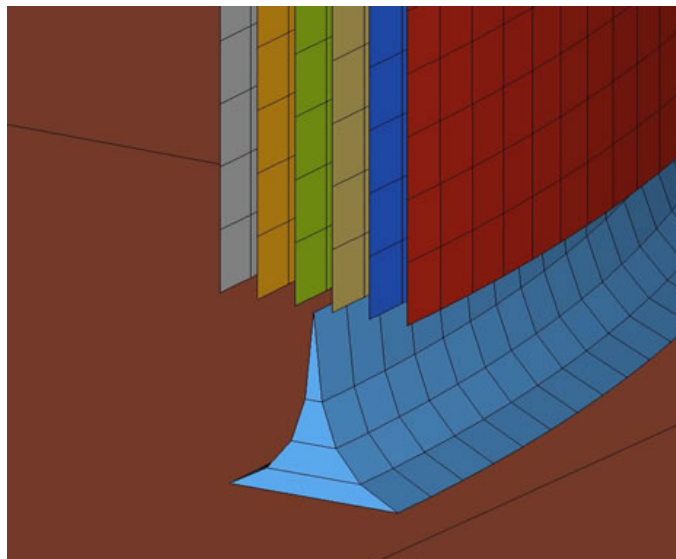


Figure 5.4. Image of simulated CFRM debris wedge cut-away profile showing its placement and shape.

The tip of the wedge was aligned with the centre of the tube's wall. A rigid material model was used with the elastic properties of the respective material (CFRM or carbon/epoxy). Constraints were applied to restrict motion in the  $z$ -direction but as the experimental debris wedge is held only by the fronds, the simulated debris wedge was able to move across the platen ( $x$  and  $y$ -directions remained unconstrained). The number of elements used around the

circumference of the tube matched the number of divisions around the debris wedge.

### **5.1.3 Material Modelling**

LS-DYNA offers several composite specific material models, most of which were investigated during model development (materials 22, 54/55, 58 and 59 were investigated). Material 22, the easiest to implement allows definition of an orthotropic material with failure defined by longitudinal and transverse, tensile and compressive strengths, in addition to the shear strength. Once failure occurs, element elimination is immediate resulting in a brittle material response. Such behaviour is undesirable for two reasons; sudden changes in load should be avoided in the interests of numerical stability and the inability to invoke any post-failure strength can lead to a significant underestimation of the absorbed energy, as is discussed in the following paragraph.

Under an in-plane compressive load, an experimental coupon develops a crack signifying the failure load has been reached, yet under further compression, damaged material would continue to resist the compressive load. In the simulation of such a scenario, once the failure load is reached (at a strain of 2.1% for CFRM), the failed elements are deleted allowing the undamaged material to travel the remaining distance (97.9% of the original element length) unrestricted. Similarly, in simulating an in-plane tensile test, post-failure strengths are not needed to match the correct behaviour. However, when this failure occurs in a tube crush simulation (or similar), the volume of material eliminated is significantly more than in reality, leading to a similar underestimation of the absorbed energy. Consequently, post-failure strengths are

introduced to account for this lost energy. Materials 54/55 and 58 allow these factors to be included.

Simple single element loading simulations highlighted a fundamental difference between the performance of materials 54/55 and 58. The tensile test shown in Figure 5.5 (no post-failure behaviour defined) demonstrates how material 58 smooths the material response, avoiding the sudden load changes which can cause numerical instability. In addition, despite attempts to employ material 59, difficulty was encountered in achieving the desired behaviour, the tensile response for which has been included in Figure 5.5. For the reasons described above, Material 58 was selected to represent the tube material.

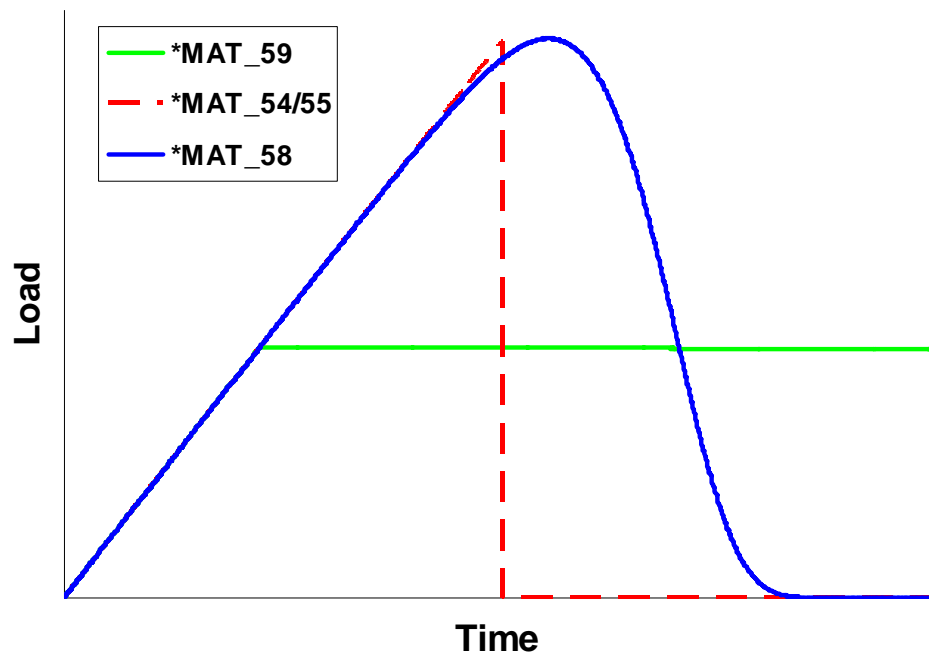


Figure 5.5. Observed tensile response of Materials 54/55, 58 and 59.

#### 5.1.3.1 LS-DYNA's Material 58

Material 58 (\*MAT\_LAMINATED\_COMPOSITE\_FABRIC) was originally developed by Matzenmiller *et al.* [117] and later modified by Schweizerhof *et al.* [118]. This material was used to good effect by the Automotive Composites Consortium (ACC) in various single shell applications [92, 119, 120].

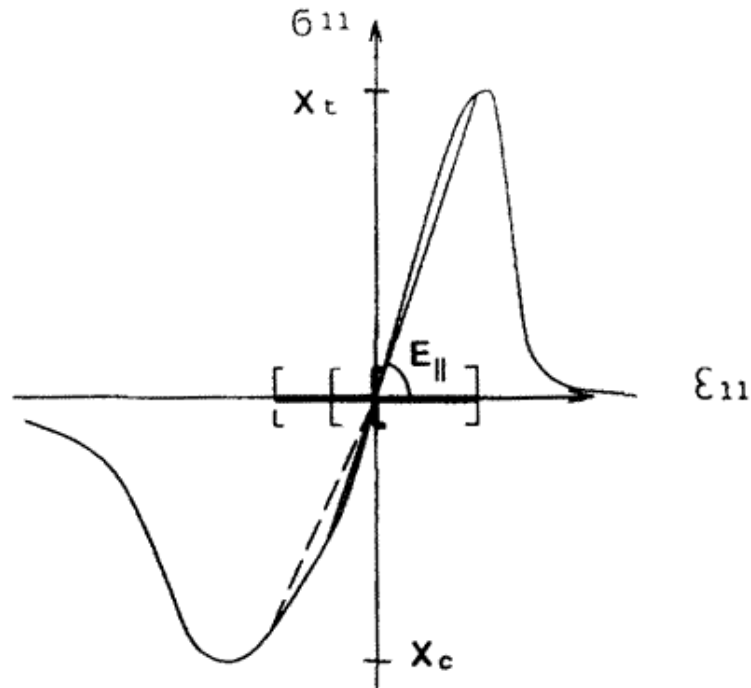


Figure 5.6. Stress-strain response of material 58 showing the different response under compression/tension [117].

Material 58 is an elastic-damage material model in which it is thought that deformation causes micro-cracks weakening the material and degrading the stiffness. It is only available for use with shell elements as the formulation is based on plane stress conditions, reducing the number of elastic constants required to  $\rho$ ,  $E_1$ ,  $E_2$ ,  $\nu_{21}$ ,  $G_{12}$ ,  $G_{23}$ ,  $G_{31}$ . All these parameters (except  $\nu_{21}$ ) were taken directly from the experimental data presented in Chapter Three or Appendix Two (for Toray and CFRM, respectively). As mentioned previously (in 3.2.3), difficulty was encountered in determining the experimental Poisson's ratio for the Toray material. Literature on similar woven carbon/epoxy laminates reported a range of values between 0.028 and 0.075. Values of 0.025, 0.05 and 0.075 were used in a tube simulation and no discernable variation in the output response was observed. Consequently, a value of 0.05 has been adopted in all Toray simulations. All other elastic values were taken directly from the experimental data.

Numerous values were required for precise control of the material failure, the criterion for which was based on the suggestions of Hashin [121]. For each of the five loading directions (longitudinal and transverse, tension and compression together with shear) the stress and strain at the point of failure must be defined. These values again, were taken directly from the experimental data.

Schweizerhof *et al.* [118] included the ability for a combined failure surface, as shown in Equation 5.1, which is for use with quasi-isotropic laminates/fabrics. If required, failure can still be defined independently.

$$f_{11} = f_{22} = \frac{\sigma_{1,22}^2}{X_{c,t}^2} + \frac{\tau^2}{S_c^2} = 1 \quad (5.1)$$

Once an experimentally determined ultimate strength value is reached, the material then maintains the post-failure strength defined by the ‘*SLIMxx*’ factors. The importance of this attribute was described previously. Lourenco [89] adopted a compressive post-failure strength of 1.0 (‘*SLIMCx*’), and tensile and shear post-failure strengths of 0.5 (‘*SLIMTx*’ and ‘*SLIMSx*’ respectively) for CFRM models using the software code PAM-CRASH. However, LS-DYNA recommends post-failure strengths in both compression and shear of 1.0 as lower values can cause numerical instability problems. A tensile post-failure strength of 0.5 was selected based on the work of Lourenco [89]. The load-displacement response of a single element tensile simulation is shown in Figure 5.7 with the tensile post-failure strength limited to 0.5 of the original strength. It is difficult to determine these values experimentally – to the best of the author’s knowledge, only one publication exists where effort has been

given to capturing the post-failure behaviour [122]. Fundamentally, the selection of these values provides the modeller with a degree of tunability.

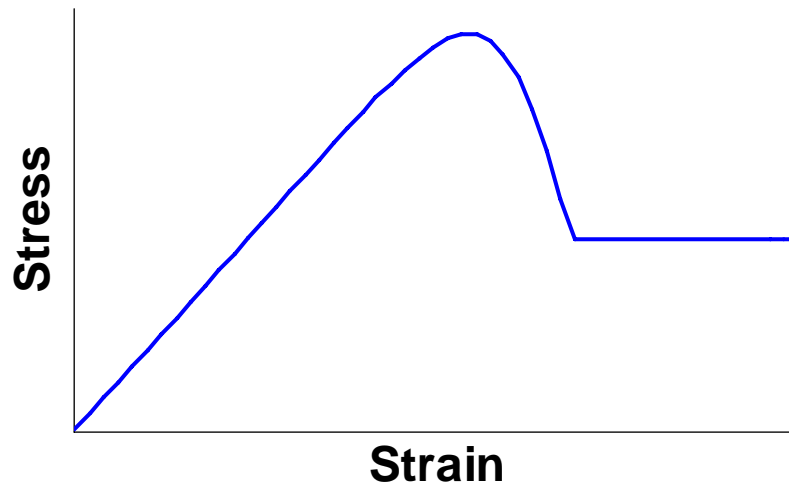


Figure 5.7. Tensile response of material 58 with '*SLIMITx*' = 0.5.

Initial modelling work established that the chosen values resulted in unrealistic failure behaviour. Significant levels of deformation, with no element elimination (representative of crack propagation) typified this response, which was caused essentially by the material being too tough. Subsequently, an investigation was undertaken which sought to improve the chosen post-failure values in order to induce the experimentally observed failure behaviour. The investigation focussed on the behaviour of the flat-platen simulations, however, identical material cards were adopted for all simulations of the respective material. To this effect, values of 0.2, 1.0 and 1.0 were used for the tensile (longitudinal and transverse), compressive (longitudinal and transverse) and shear post-failure strengths respectively, for both materials. The chosen values achieved a practical degree of element elimination leading to the production of axial tears, which increased the failure mode correlation with the experimental flat-platen tests. The response of material 58 with these parameters in the various loading scenarios can be seen in Figure 5.8 below for Toray G83C.

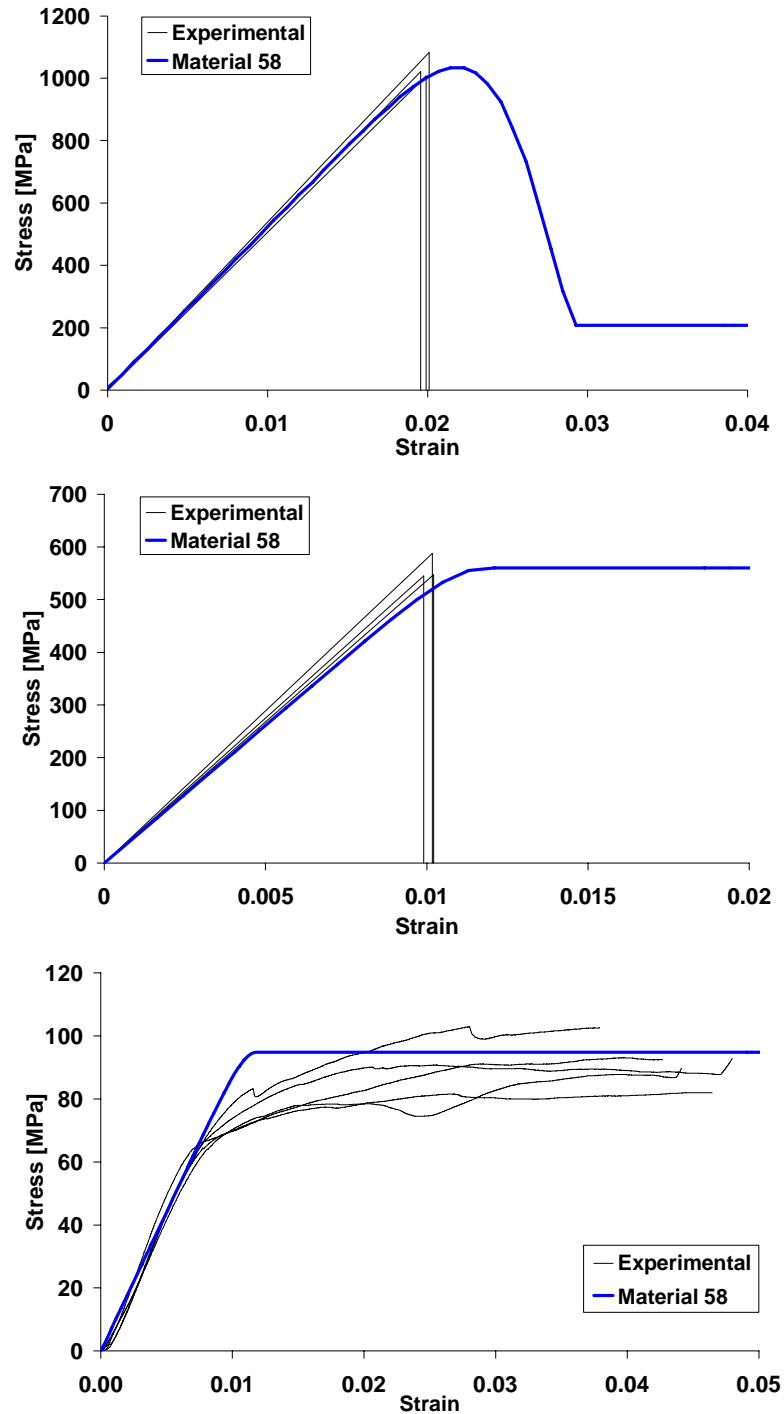


Figure 5.8. Graphs of the stress-strain response of material 58 under in-plane tension (top), in-plane compression (middle) and shear (bottom) for Toray G83C.

Additionally, the sensitivity of the steady-state crush load was used to compare changes in the compressive and tensile post-failure factors. A similar trend was observed for variations to each value. As either factor increased, large increases in predicted steady-state load were observed which gradually levelled out at higher values. This trend is shown in Figure 5.9. Altering the shear post-

failure strength allowed the failure mode to change from splaying to transverse shearing as the value approached 0.0, but showed little influence on the steady-state load.

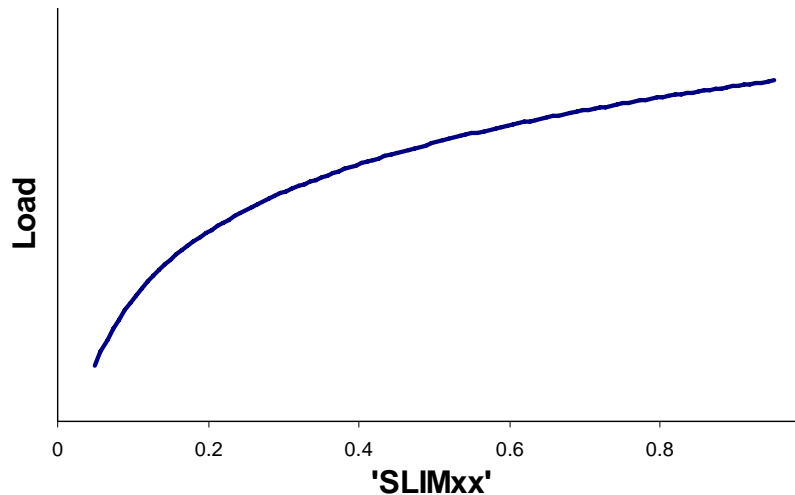


Figure 5.9. Trend produced by altering '*SLIMTx*' or '*SLIMCx*' on average tube crush load.

Once failed, the post-failure strength is limited by the '*SLIMxx*' values allowing elements to continue straining. Elements are eliminated only when the strain reaches the maximum effective strain, defined by '*ERODS*'. Based on the work of Lourenco [89], a relatively high maximum strain of 90% ( $ERODS=0.9$ ) was selected. However, as was the case with the post-failure strength factors ('*SLIMxx*'), this was found to be too high for the materials in this work. Subsequent to a brief investigation, maximum strain values of 0.6 and 0.4 were adopted for the CFRM and Toray materials respectively. The difference in the value selected for each material can be attributed to the variation in their experimental behaviour - CFRM tends to show higher strains at the point of ultimate strength suggesting a higher ductility, hence the maximum strain limit is higher.

The sensitivity of the model to changes in the maximum strain limit, '*ERODS*', was investigated. Altering the value between 0.75 and 1.0 showed an almost

insignificant difference in average crush load but below 0.75, the load began reducing rapidly in addition to the presence of an increasing number of fronds as shown in Figure 5.10.

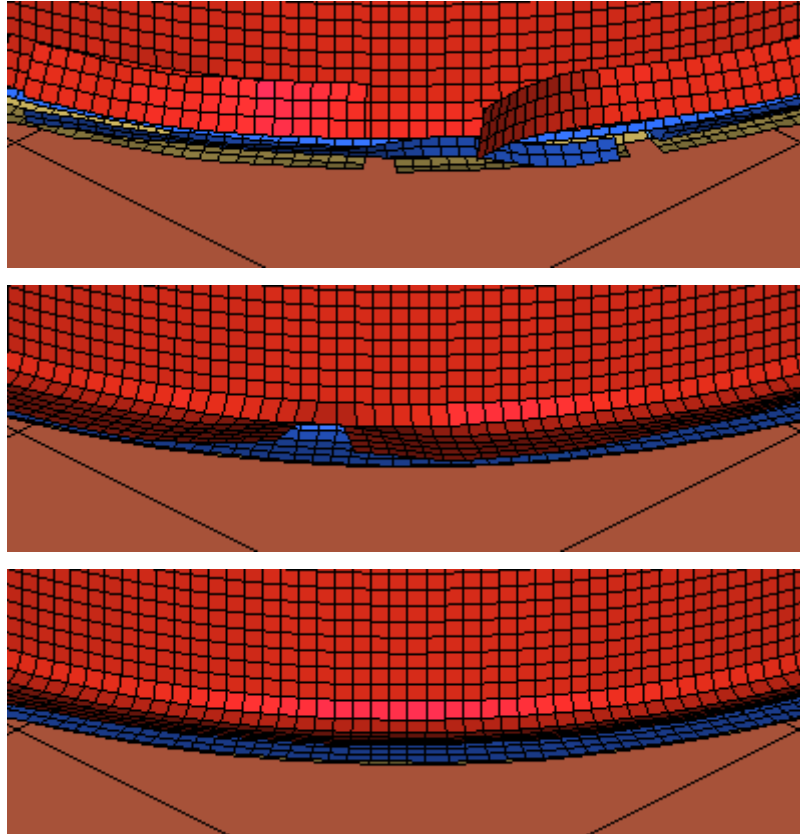


Figure 5.10. External layers of a simulated CFRM tube showing the effect of ‘*ERODS*’ varying from 0.25 (top) to 0.5 (middle) to 1.0 (bottom).

In addition, material 58 (along with materials 54/55 and 59) offers crashfront softening which can reduce the strengths of crashfront elements. This is controlled by the parameter ‘*SOFT*’ and is only activated once ‘*TSIZE*’, the timestep for automatic element deletion, is set. The minimum timestep can be used to effectively limit compressive strains, removing highly compressed elements as their timestep reduces below the defined value. Efforts were made to initiate ‘*TSIZE*’ in this work, although massive element deletion occurred either during initialisation or upon initial contact regardless of the ‘*TSIZE*’ selected. Consequently, neither ‘*SOFT*’ nor ‘*TSIZE*’ were used in the work

herein. The material cards for CFRM and Toray are shown below in Table 5.1 and Table 5.2.

Table 5.1. Material 58 control card with the material parameters used in CFRM simulations.

*MAT_LAMINATED_COMPOSITE_FABRIC								
\$\$	MID	RO	EA	EB	(EC)	PRBA	TAU1	GAMMA1
	1	1200	10.1E09	10.1E09	6.49E09	0.296		
\$\$	GAB	GBC	GCA	SLIMT1	SLIMC1	SLIMT2	SLIMC2	SLIMS
	4.25e09	1.76e09	1.68e09	0.2	1.0	0.2	1.0	1.0
\$\$	AOPT	TSIZE	ERODS	SOFT	FS			
			0.6		1.0			
\$\$	XP	YP	ZP	A1	A2	A3		
\$\$	V1	V2	V3	D1	D2	D3	BETA	
\$\$	E11C	E11T	E22C	E22T	GMS			
	0.0214	0.0151	0.0214	0.0151	0.02			
\$\$	XC	XT	YC	YT	SC			
	221E06	153E06	221E06	153E06	87E06			

Table 5.2. Material 58 control card with the material parameters used in Toray simulations.

*MAT_LAMINATED_COMPOSITE_FABRIC								
\$\$	MID	RO	EA	EB	(EC)	PRBA	TAU1	GAMMA1
	1	1500	52.2E09	52.2E09	7.52E09	0.050		
\$\$	GAB	GBC	GCA	SLIMT1	SLIMC1	SLIMT2	SLIMC2	SLIMS
	8.84e09	3.98e09	1.10e09	0.2	1.0	0.2	1.0	1.0
\$\$	AOPT	TSIZE	ERODS	SOFT	FS			
			0.4		1.0			
\$\$	XP	YP	ZP	A1	A2	A3		
\$\$	V1	V2	V3	D1	D2	D3	BETA	
\$\$	E11C	E11T	E22C	E22T	GMS			
	0.0101	0.0198	0.0101	0.0198	0.01075			
\$\$	XC	XT	YC	YT	SC			
	560E06	1037E06	560E06	1037E06	95E06			

### 5.1.4 Delamination Modelling

The critical task of fusing the layers of shell elements is performed by the chosen interlaminar modelling approach. Incorrect representation of the matrix stiffness/strength can lead to significant inconsistencies in a multi-shell model, or essentially any model in which delamination is considered. Detail on the delamination approach adopted, and its development is presented in Chapter Six.

### 5.1.5 Contact and Friction

Upon delamination, shell offsets maintained the correct material thickness ensuring friction processes at the interlaminar interfaces are considered. This was accomplished through the use of ‘automatic’ contact cards which consider the shell offsets set in the \*section\_shell cards in the input deck. Depending on the model configuration, a number of contact cards were required which in the CFRM models, would vary between 23 and 29 individual cards. Typical contact interfaces under consideration were; each tube layer to the crush platens, each layer to the next and self contact as the material curls back onto itself. The contact cards employed were:

\*contact\_automatic\_surface\_to\_surface

\*contact\_automatic\_single\_surface

\*contact\_automatic\_nodes\_to\_surface

These contact cards all allow the input of friction coefficients for both static and dynamic conditions, based on the Coulomb formulation. Values of 0.3 and 0.28 respectively were employed in this work, based on work by Mamalis [123] which suggested that the coefficient of friction lies within 0.3-0.7. The friction values were varied by 25% and compared through changes in the average crush load. The results showed a marginal increase in steady-state crush load with increased friction, but a significant reduction for the 25% lower friction case. This sensitivity is not surprising given that experiments have shown friction to be responsible for approximately 50% of the crush energy and hence load [47, 48]. Additionally, it is expected that interlaminar friction, between delaminated plies and between the fronds and debris wedge, will be of a significantly higher coefficient than is presented here, but the actual value is

difficult to quantify [47]. Consequently, the same values have been adopted between all contact interfaces.

## 5.2 Modelling Detail

Due to the apparent difficulty in experimentally characterising the behaviour of composite materials, all simulations here have been conducted at quasi-static rates. In tube crush simulations, the upper platen was displaced downward at a maximum of 4m/s according to the velocity profile shown in Figure 5.11(a) below. Quasi-static conditions were confirmed by comparison of the total and kinetic energies with the latter remaining under 1% of the total energy. A comparison of the energies can be seen in Figure 5.11(b) below. This rate allowed completion of the simulations in an acceptable time. Additional improvements were made through mass-scaling in which the densities of all parts were increased four-fold.

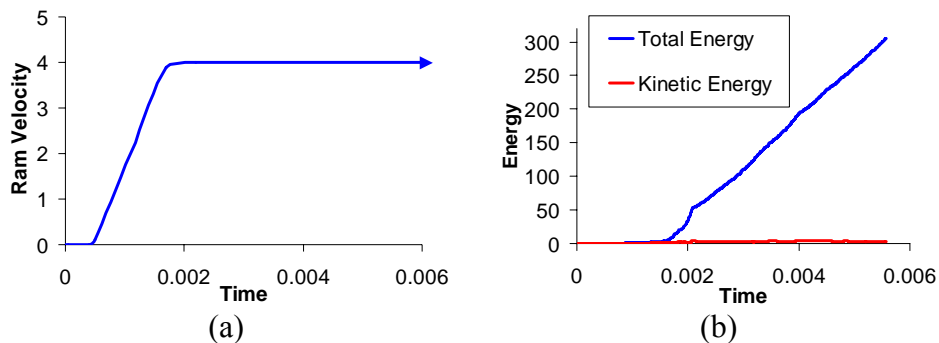


Figure 5.11. (a) Ram velocity profile and (b) corresponding total and kinetic energies.

For consistency, all simulations were performed in SMP mode (Symmetric Multiprocessing) using one node (2 CPU's) on 'Wexstan', a 64-bit Opteron Linux Cluster. Each node consists of Dual Opteron 256 @ 2Ghz, with 4Gb RAM and 36Gb SCSI HDD. This system is available through the Victorian Partnership for Advanced Computing (VPAC). The double precision possible with these machines meant that very few numerical instabilities were

encountered from highly deformed elements or contact issues. Such difficulties were encountered when simulations were run on local PC's in the default single precision mode. All post-processing was performed using Altair Hypermesh [124].

### **5.3 Summary**

---

This chapter presented the details of a holistic modelling methodology whose development sought to include all of the features relevant to the composite crushing process. The multi-shell methodology uses a force-based delamination model to represent the interlaminar material and its ability to correctly reproduce the interlaminar stiffness is investigated in the following chapter. Later, this methodology is applied to model a range of tube crush experiments and the results are presented.

## **6 Delamination Modelling**

Cost is the fundamental reason for the minimal use of composite materials in the automotive industry. This problem exists in the high cost of component manufacture and the inability to predict the performance through computational methods. Accordingly, Chapter Four introduced a novel method of manufacturing composite tubular profiles which could lower the component cost through substantially reduced cure cycle times. Chapter Five introduced a modelling methodology for the representation of composite materials in crush simulations. Here, the interlaminar modelling methodology adopted is verified with DCB and ENF simulations, before application in full-tube simulations in the subsequent chapter. It is shown that the presented methodology appears well-suited to the task of modelling delamination in composite materials as a good correlation in both failure behaviour and laminate stiffness was observed.

### **6.1 Delamination Modelling Methodology**

---

The critical task of fusing the layers of shell elements is performed by the chosen interlaminar modelling approach. Incorrect representation of the matrix stiffness/strength can lead to significant inconsistencies in a multi-shell model. Preliminary work saw the investigation of several basic approaches including springs and contact definitions which tied the layers.

The use of springs, with a defined force/displacement relationship, allowed the elastic stiffness and failure to be defined. However, a combined failure surface between the normal and shear forces was not achieved, leading to an over-estimation of the strength in a mixed-mode loading. Furthermore, visualisation

of the interlaminar behaviour was difficult as the springs were not removed from the model, despite having failed. This meant that if, under some type of deformation, the spring shortened to within its original length, it could self-heal and its strength/stiffness would return.

LS-DYNA has numerous contact type cards which can be used to achieve the ‘tying’ approach, in which two modelled parts are attached by a contact definition. Two such contact types were briefly investigated in this work; type a3 (‘automatic surface to surface tiebreak’) and 8 (‘nodes to surface tiebreak’). The former could consider shell offsets (giving it a contact thickness) but upon a single nodal connection reaching the defined failure force, the entire surface would simultaneously fail. On the other hand, the latter contact card (type 8) could consider the failure at each node independently and consequently delaminate in a physically realistic manner though it does not consider shell offsets. A requirement of the holistic modelling approach was the preservation of the realistic material thickness once delaminated. Though no further testing was performed with these approaches, they are classified as a ‘tying’ technique which has shown to incorrectly transfer the shear stiffness between the laminae they join [56, 91]. Instead, a solution was found in the use of beam elements.

The beam elements attach to the centroids of the shell such that in the event of a shell element being eliminated, so too is the interlaminar connection. A sample section of tube wall can be seen Figure 6.1 showing the spotweld connections.

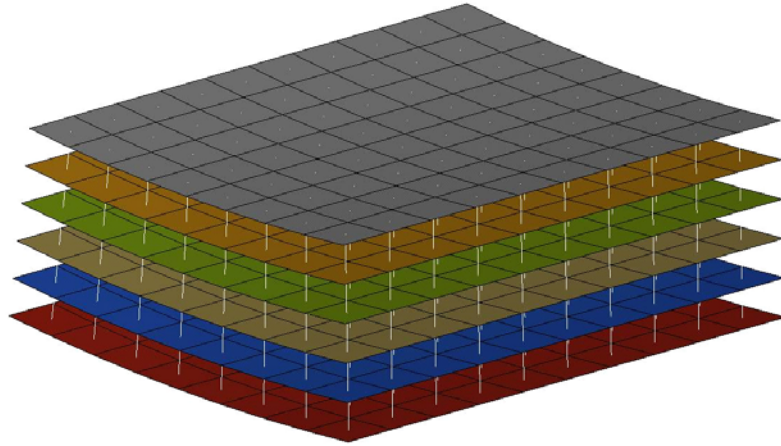


Figure 6.1. Sample cross-section of tube wall showing spotweld connections.

To create these beams, a superfluous node is created in between the shell planes and the node set is listed in a `*part` card. Additionally, all the shell layers are listed in a separate `*part` card, which are then tied using `*contact_tied_shell_edge_to_surface` card. This connects all the shell layers, through the redundant node. The beams are assumed to be circular in profile and are 0.9mm in diameter, to ensure that during laminate bending, beam elements are unable to interfere with each other. A schematic of a beam, connecting two single shell elements is shown in Figure 6.2.

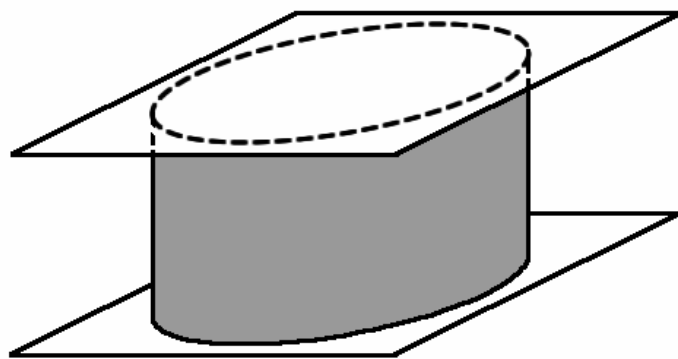


Figure 6.2. Schematic of a beam joining two shell elements showing the assumed profile.

The spotweld material model, material 100 (`mat_spotweld_OPTION`) in the LS-DYNA library [87] was used in conjunction with the beam elements. This model was developed primarily for modelling metallic spotwelds such as those

in automotive car bodies. It allows an isotropic representation of the elastic material properties of the interlaminar layer. The elastic properties required are  $\rho$ ,  $E$  and  $\nu$ . Inclusion of the optional command ‘\_damage-failure’ to the material card introduces the failure control. Definition of the failure can be performed in a number of ways. In this work, a simple force based criterion is used though it is possible to use stress or effective strain. With this approach, failure is defined in terms of normal and shear forces which, under a combined loading, must satisfy Equation 6.1.

$$\left(\frac{N_{rs}}{N_{rsF}}\right)^2 + \left(\frac{N_{rt}}{N_{rtF}}\right)^2 = 1 \quad (6.1)$$

It was not possible to alter the exponent values and the default of 2 was used. While it is acknowledged that this failure surface may not be ideal for mixed-mode loadings, it has been used to link the loading directions where the ‘tying’ approach to spotweld modelling has been adopted [56, 99].

In order to ensure the correct interlaminar material behaviour and laminate stiffness, the following methodology was adopted. Firstly, it should be noted that the specified beam diameter throughout this work was 0.9mm, largely to avoid spotweld-to-spotweld contact which was found to cause cessation of the given simulation. Consequently, the cross-sectional area of each spotweld is much smaller than the representative laminate area that it joins (whose area is  $1\text{mm}^2$ ). In order to ensure an accurate representation of the interlaminar material, an effective beam modulus was calculated which compensated for the reduction in the volume of interlaminar material. Where the experimentally determined Young’s modulus was employed in the interlaminar material

model, the simulation predicted a considerably lower flexural modulus than shown experimentally.

The through-thickness compression test was used to calculate the effective stiffness of the spotweld elements. Given that the fibres make little contribution to the stiffness in the through-thickness direction, it was assumed that the fibre layers were infinitely thin, making the stiffness in this direction, purely the response of the matrix. Fundamentally, the experimental through-thickness Young's modulus is hypothesised to be controlled by numerous interlaminar springs – the length of one interlaminar region. Using the interlaminar thickness, the hypothesised spring length is known together with the sample cross-sectional area. Subsequently, it is possible to calculate the stiffness (' $k$ ') of the matrix with the simple formula  $k = \frac{EA}{L}$ . In so doing, this stiffness can be used to modify the Young's modulus of the spotweld elements given that the area and beam length are already known. The calculated value for CFRM tube modelling was found to be 10.3GPa and for Toray, a value of 9.96GPa was used. An example calculation can be found in Appendix Four.

In these 3D delamination models, two layers of shell elements, each representative of half the coupon thickness, were used and connected with these beam elements. The correct width was used as there are known to be edge effects in such tests, which, if not considered, can lead to an over-estimation of the strength [125]. In all cases, an elastic material model (material 1 in the LS-DYNA library - an isotropic elastic material) was employed as coupon failure was not expected.

As a consequence of the two layer approach, the longer beam elements required re-calibration of the beam's Young's moduli. In CFRM coupon

simulations, the Young's modulus used was 30.92GPa and in Toray G83C simulations, the value was 26.89GPa. The values chosen were compared through a series of 3-point bend simulations in which the use of the experimental Young's modulus ( $E_3$ ) resulted in a distinctly softer coupon response. Altering the Young's modulus to 25% above and below the calculated value demonstrated no effect on the behaviour in DCB tests and little effect on 3-point bend and ENF tests. Experimental data was only available for Toray and comparison of the values showed the equivalent Young's modulus to achieve the best correlation when tested against the experimentally determined value.

Importantly, the flexural stiffness was shown to be unaffected by the interlaminar friction values employed. A range of values were tested but no changes were observed. This is significant as it shows that the interlaminar material is represented entirely by the beams and their given properties. Furthermore, this friction, that will play a role once the coupons have delaminated, should not affect the elastic behaviour or alter the failure values determined through the following calibration tests.

Once the elastic behaviour of the interlaminar material was validated, failure behaviour was then considered. For this purpose, Double Cantilever Beam (DCB) and End Notch Flexure (ENF) simulations were completed in which a pure Mode I or Mode II loading is placed on the interlaminar material. This would provide an empirical method of determining the required failure force in the normal and shear directions, respectively.

The CFRM and Toray material cards used in the tube simulations are shown in Table 6.1 and Table 6.2. Preliminary testing showed that the values '*SIGY*'

(yield stress) and ‘*EFAIL*’ (effective plastic failure strain) were required for the material to behave correctly and consequently were set high to ensure the failure was controlled solely by the failure forces. The values ‘#’ will be covered in the subsequent sections. A force filtering option, ‘*NF*’ was employed to reduce spurious forces which were produced upon failure as the spotwelds were removed abruptly.

Table 6.1. Material 100 control card used for CFRM tube simulations.

*MAT_SPOTWELD_DAMAGE-FAILURE								
\$\$HMNAME		PROPS	100spotweld					
\$\$	MID	RO	E	PR	SIGY	ET	DT	TFAIL
	100	120010.3E+009	0.3050	4.00E+008				
\$\$	EFAIL	NRR	NRS	NRT	MRR	MSS	MTT	NF
	0.5	#	#					25.0
\$\$	RS	OPT	SIGKF					
		0.0						

Table 6.2. Material 100 control card used for Toray tube simulations.

*MAT_SPOTWELD_DAMAGE-FAILURE								
\$\$HMNAME		PROPS	100spotweld					
\$\$	MID	RO	E	PR	SIGY	ET	DT	TFAIL
	100	15009.96E+009	0.0500	6.00E+008				
\$\$	EFAIL	NRR	NRS	NRT	MRR	MSS	MTT	NF
	0.5	#	#					25.0
\$\$	RS	OPT	SIGKF					
		0.0						

## 6.2 Delamination Modelling Results

### 6.2.1 Double Cantilever Beam Simulations

Having confirmed the correct specimen stiffness, attention was given to ensuring the correct delamination behaviour. The spotweld material model (material 100 in the LS-DYNA library) provides several choices for failure control. Here, forces in the normal and shear directions were used and combined for mixed-mode loading by Equation 6.1.

DCB tests apply a pure Mode I loading to the specimen, translating to a purely axial force in the beam elements. This allowed empirical calibration of the axial failure force without interference by other force components.

Initially, the simulation was completed without a defined spotweld failure force giving a purely elastic coupon response. Analysis of the load response revealed the point at which the crack tip should propagate (first row of spotwelds eliminated) in order to match the experimental response. Analysis of the spotweld forces at the crack tip yielded the necessary failure force. In the case of CFRM, an axial failure force of 38N provided the correct response. Toray G83C required an axial failure force of 78N. These values were input and the simulations re-run. An image of the simulation can be seen in Figure 6.3.



Figure 6.3. Image of CFRM DCB simulation underway.

Preliminary tests showed the sudden failure of the spotwelds could create stress-waves, resulting in the premature elimination of neighbouring elements. To reduce this effect, a degree of global damping was applied to this simulation only. This was in addition to spotweld force filtering option described earlier. Evidence of the aforementioned edge effects was apparent in these simulations and can be seen in the curved delamination front shown in Figure 6.4. The experimental and simulated DCB results are shown below in Figure 6.5 and Figure 6.6.

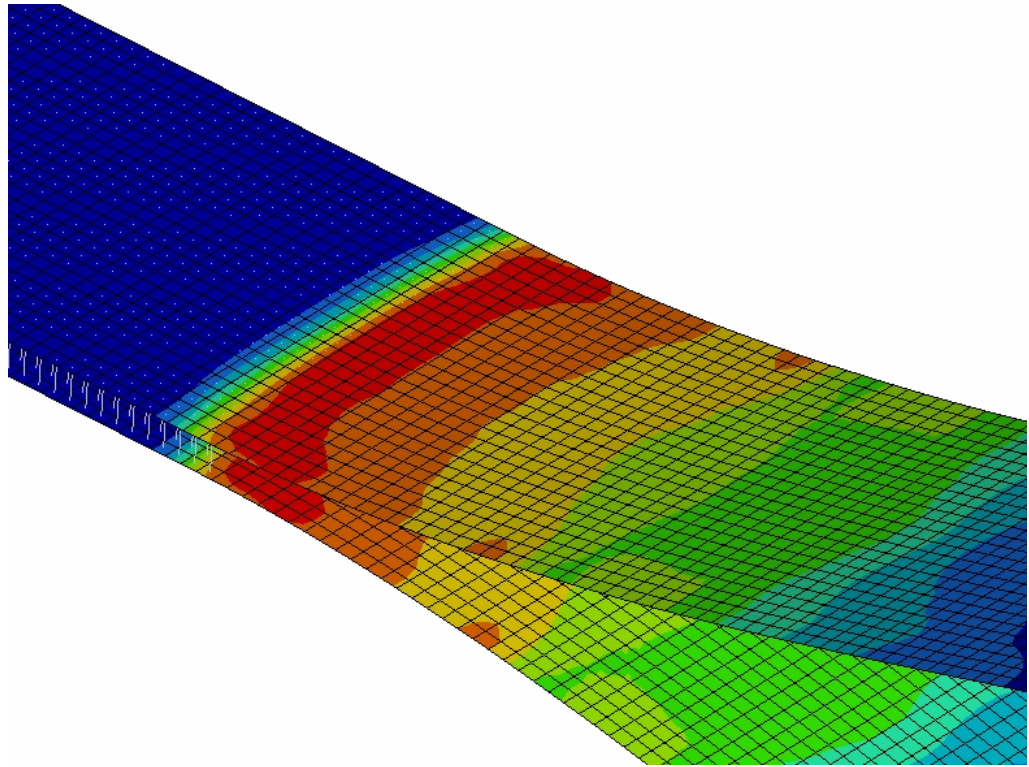


Figure 6.4. Von Mises stress distribution in DCB test of CFRM, demonstrating edge effects.

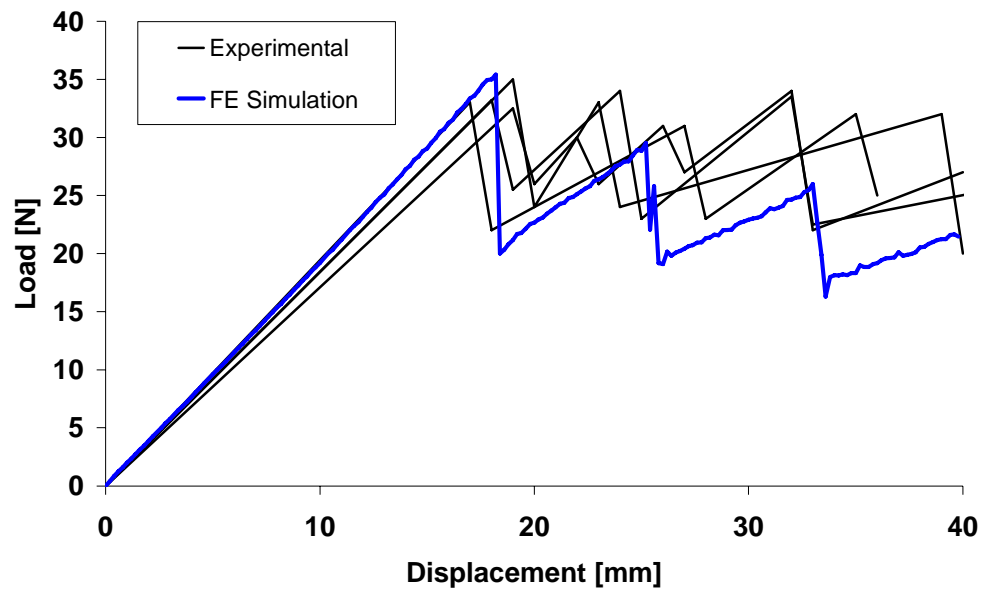


Figure 6.5. Comparison of experimental and simulated DCB response of CFRM.

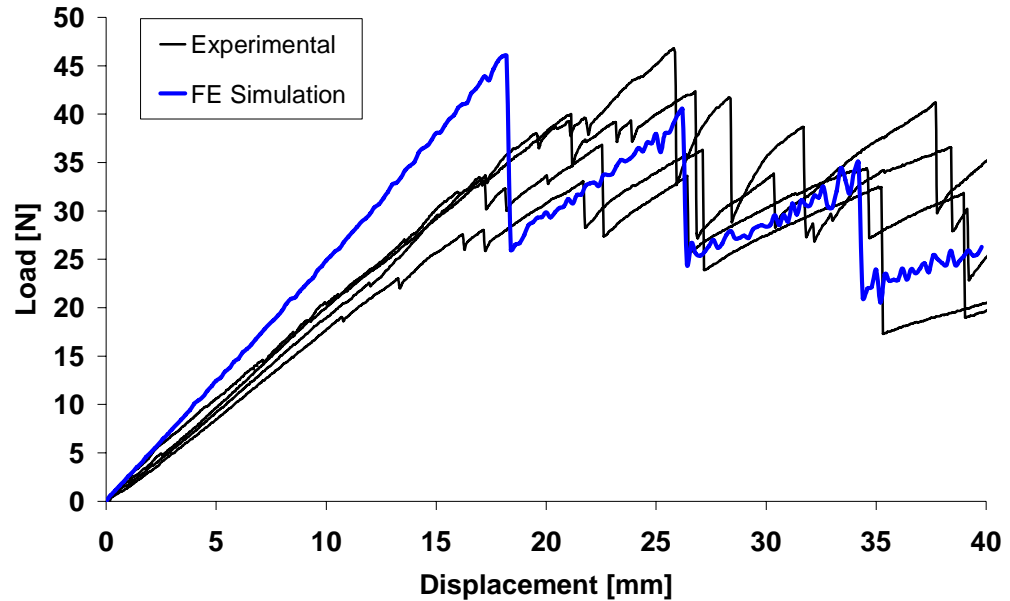


Figure 6.6. Comparison of experimental and simulated DCB response of Toray G83C.

Both simulations reproduced the ‘stick-slip’ behaviour observed during experimental testing and the crack propagation during each ‘slip’ process correlates well with the experimental tests. As can be seen for CFRM, a very high degree of correlation was demonstrated. However, the Toray simulation displayed a reduced correlation with a much stiffer response throughout the initial portion of the test, leading to an over-estimation of the load at the point of failure. This response is solely due to the flexural stiffness of the shell elements. Exploration of the cause of the incorrect stiffness prediction identified the primary source of error. Prior to testing, experimental Toray DCB samples were measured to be an average 2.7mm thick. However, the peel ply used to create the pre-crack caused a large variation in the specimen thickness on each of the two halves of the coupon. The thickness variations can be seen in Figure 6.7.

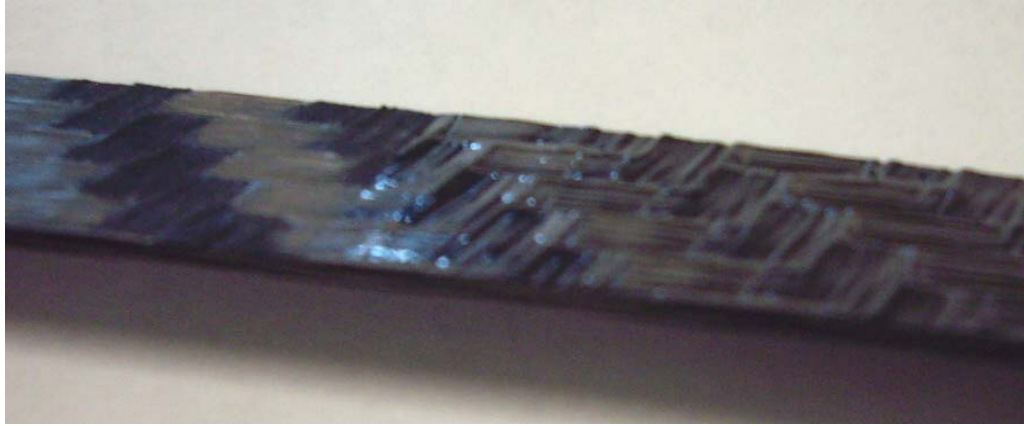


Figure 6.7. An image of the pre-cracked portion of the Toray DCB test on the right, with a delaminated section on the left. The significant thickness variations, which affect the FE simulation's correlation, can be seen on the right.

The value used in the simulated response shown above was 1.35mm (half the original 2.7mm). Measurements were taken at numerous intervals on the specimens (after separation) on half of the coupon and values as low as 1.1mm were recorded. The incorrect coupon thickness caused the simulation to over-estimate the bending stiffness. In order to include these imperfections, the average thickness was found (1.25mm) and used in a repeat of the simulation. This gave the greatly improved response shown below in Figure 6.8. It should be noted that the selected failure force did not change, but the failure displacement was affected.

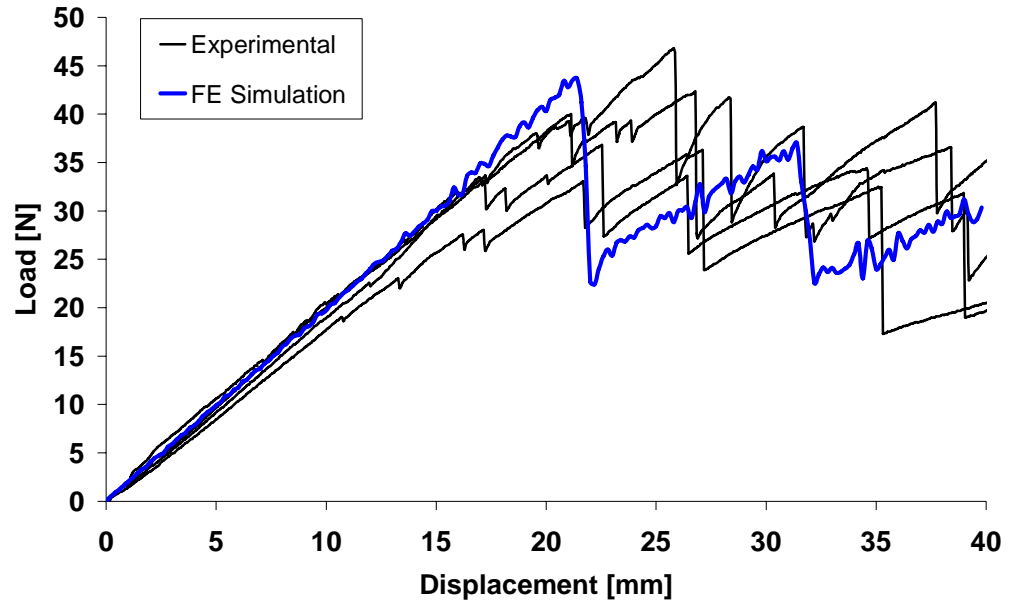


Figure 6.8. Simulated response of Toray DCB test with corrected specimen thickness, displaying a significantly improved correlation.

### 6.2.2 End Notch Flexure Simulations

ENF tests were utilised in order to load the sample in pure Mode II, a sliding shear loading scenario. However, as a consequence of selecting the beam/spotweld combination, together with the requirement of maintaining shell element thicknesses, under this type of loading a partial mixed-mode response is observed. This situation can be visualised as shown in Figure 6.9.



Figure 6.9. A schematic of a beam element connecting two shells in the undeformed (left) and deformed (right) positions demonstrating the beam elongation that occurs under pure shear loading.

Under a shear loading it is clear that for any large deflection, the beam connecting the shell elements will be required to elongate. Despite the loading being largely in shear, a degree of axial force is introduced - the higher the stiffness of the beams, the less axial contribution is developed. It was suspected

that this behaviour would also be subject to the frictional forces between the laminates/shells (in theory, larger shear displacements increase larger axial forces, and consequently contact force). However, as mentioned earlier, a range of friction coefficients were tested and no discernable change was observed, leading to the conclusion that the behaviour of the interlaminar material response is unaffected by changes in friction.

As a consequence of the elongation of the spotwelds under shear loading, it is essential that the axial failure force be known prior to calibration of the shear failure force. Therefore, using the pre-determined axial failure forces (from the DCB simulations described previously), the ENF simulations were run and the shear failure forces determined. The shear failure force determined from CFRM and Toray ENF simulations was 70.81 and 75N respectively. An image of the simulation can be seen in Figure 6.10. The load-displacement responses of these simulations can be seen in Figure 6.11 and Figure 6.12.



Figure 6.10. Image of CFRM ENF test underway.

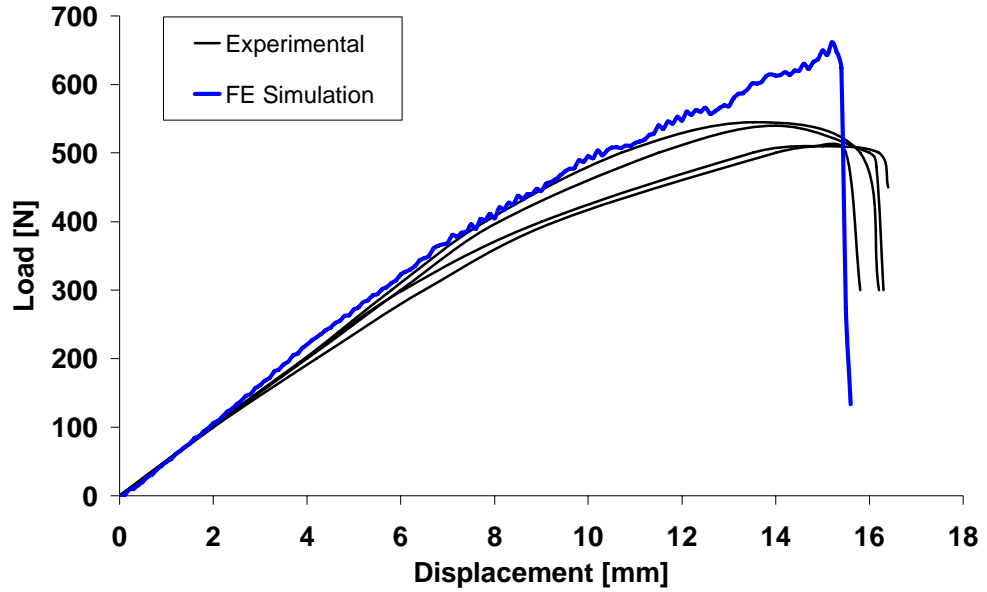


Figure 6.11. Load-displacement response from CFRM ENF test.

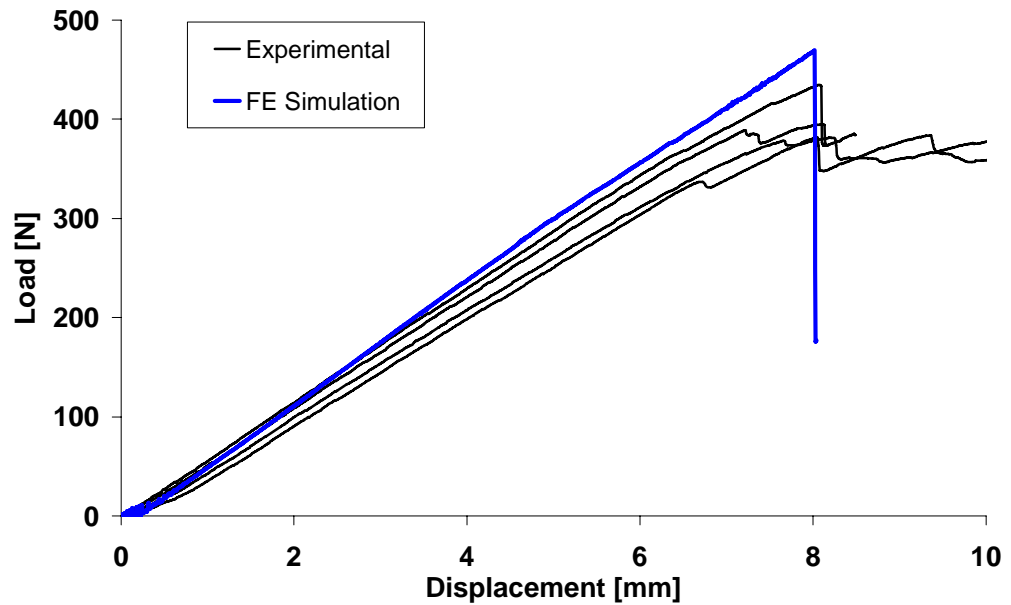


Figure 6.12. Load-displacement response from Toray ENF test.

Here, the flexural response of the beams is of primary concern and the results show that the stiffness has been reproduced well. These results are significant as it shows that this variation of the force-based approach, can accurately reproduce laminate stiffness, potentially enhancing the predicted correlation of further tests.

In the case of the CFRM test, an almost identical response can be observed from 0 to 12mm displacement. At this point, it can be seen that the CFRM experimental load begins to taper-off while the simulation predicts a continued rise to 661N. Examination of the simulated stresses on the upper and lower surfaces of the sample at the failure displacement shows it to have exceeded both the in-plane compressive strength (221MPa), and the in-plane tensile strength (153MPa) respectively. If a material model with failure was used, the simulation would have predicted the coupon to fail well before the experimental displacement or force (this was verified by employing material 58). Therefore, it is thought that a complex bending deformation occurs in the experimental testing. However, no discussion was given by Duckett [55] on the response observed during this test and consequently, no conclusion can be drawn here. In any case, this response could not be captured in the FE model.

As was the case with the Toray DCB simulations, the thickness variation over the pre-crack surface of the ENF tests caused an over-prediction of the coupon stiffness. Setting the shell offsets to 1.25mm, the average thickness (rather than the 1.35mm used originally) gave the response shown in Figure 6.13. Presumably, a similar effect could be observed in CFRM samples although, no conclusion can be drawn without careful measurement of the experimental samples.

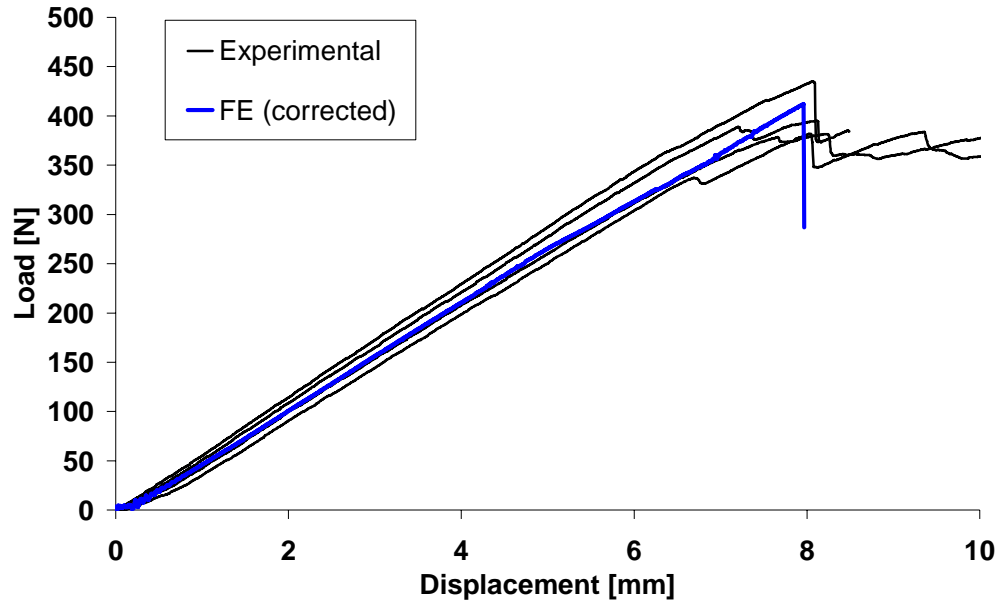


Figure 6.13. Simulated response of Toray ENF test with corrected specimen thickness displaying a significantly improved correlation.

### 6.3 Summary

The purpose of this chapter was to present and validate a delamination modelling methodology which could accurately transfer the shear stiffness.

A typical approach to the ‘spotweld method’ of modelling composite delamination involves tying lamina using a constraint type definition which restricts nodal displacement until the failure force is reached. Morthorst and Horst report that in LS-DYNA, this approach can result in the incomplete transfer of the shear stiffness resulting in an incorrect laminate response [91]. Curtis [56] encountered such difficulties while using the explicit software PAM-CRASH, suggesting that this issue is not software specific. Herein, deformable beam elements have been used to connect adjacent layers at the shell centroids using a material model which provides an isotropic-elastic response prior to failure, which can be defined anisotropically.

Using a calculated equivalent Young's modulus, the flexural stiffness correlation was found to be excellent, accurately transferring the shear stiffness between laminae. Additionally, in the tests reported here, once calibrated, the delamination behaviour of this approach correlated very well with experimental tests. The inability to capture the complex bending deformation resulted in an over-estimation of the failure load in the ENF simulation for CFRM alone. From the tests performed here, this method appears suitable for use in large scale multi-shell models where delamination is expected.

## **7 Force-Based Delamination - Tube Modelling**

Having the ability to successfully predict the performance of composite materials in crash situations could substantially reduce the need for prototyping and allow automotive manufacturers to exploit the benefits of such materials, particularly in crash structures. A step in this direction was reported in Chapter Six where a modified spotweld delamination methodology was introduced and validated. It was shown that this approach to delamination modelling accurately reproduced the delamination response of both the CFRM and Toray materials in 3-point bend, DCB and ENF simulations. Interlaminar failure was governed by normal and shear interface forces.

Here, the aforementioned methodology is applied to tube crush simulations of various forms. Model development concentrated on achieving a holistic representation of the crushing process by including the features pertinent to the crushing process. In particular, effort was focussed on achieving an accurate reproduction of the behaviour of flat-platen tests. In general, a good visual correlation is achieved with changes in the experimental failure mode mimicked by the FE simulations. However, comparison of the steady-state loads was less encouraging. Examination of the contributing mechanisms highlights the inadequacies of the delamination model. Consequently, valuable conclusions are drawn on the limitations of the current methodology and recommendations are made to further improve this approach.

## 7.1 Results

---

As model development focussed on the reproduction of flat-platen crush tests, these results will be presented first.

### 7.1.1 Flat-Platen Simulations

As expected, inclusion of the pre-defined debris wedge in flat-platen simulations resulted in an unrealistic response during the initial loading portion of the simulation. Consequently, analysis of the crush behaviour and the associated steady-state loads was of primary interest. The loading portion of several plug initiated simulations was similar to the experimental behaviour and this will be discussed where relevant.

#### 7.1.1.1 Interlaminar Material Loads in Flat-Platen Simulations

A benefit of FE analysis is the ability to examine the exact loading conditions experienced at various points of a structure. To this effect, a multi-layer CFRM simulation was performed and the loads on crashfront beam elements were monitored. Of primary interest, was the loading experienced at each interlaminar region as it approached the crush zone. The loads in 5 interlaminar regions, taken from the same point in the tube are presented in Figure 7.1.

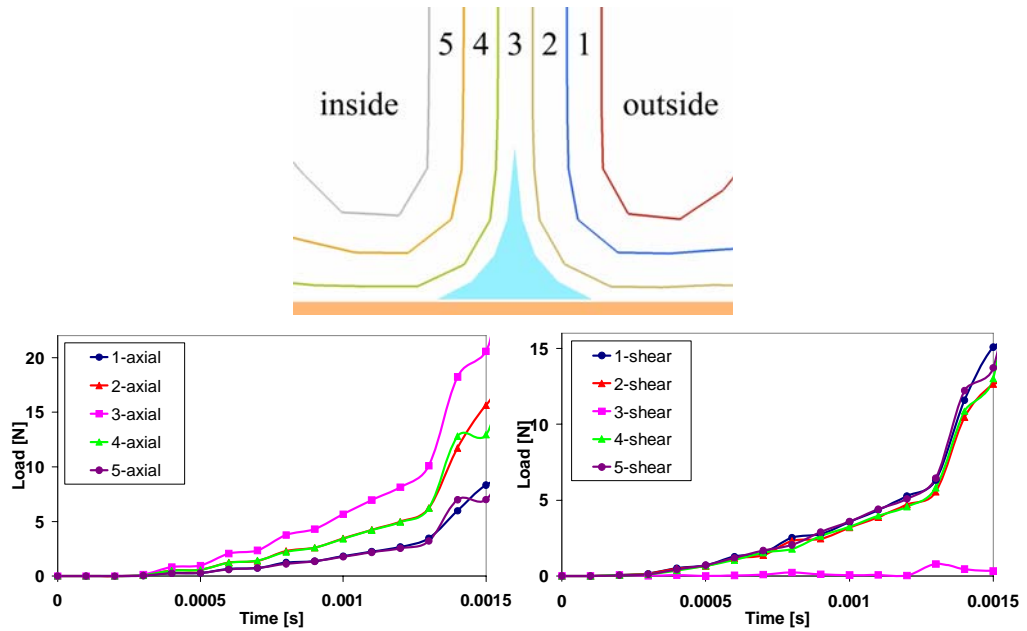


Figure 7.1. Axial and shear load components on interlaminar spotweld elements of a CFRM simulated tube, as the spotwelds approach the crush zone. The regions are numbered from the outside of the tube wall, to the inside.

During the loading period shown, the spotwelds in the centremost region (3-axial) are under the greatest axial load, with little shear loading, confirming a Mode I loading of spotwelds in this region (the central wall crack). The axial loads reduce for the regions either side of the central crack (2, 4), and again for the outer and innermost regions (1, 5). However, the shear loads in all these regions straddling the central wall crack are approximately equivalent, indicating that the through-thickness shear stress distribution is constant. Furthermore, as the axial force to shear force ratio varies for each region, it is clear that the mixed-mode loading ratio will vary. It should be noted that the performance of the adopted delamination modelling approach has not been tested under a variety of mixed-mode loading conditions; an area for further work.

#### 7.1.1.2 CFRM

In flat-platen CFRM tests, a very good agreement was observed between the failure modes produced experimentally and those in the FE simulation. Images of the experimental specimens, together with the simulated equivalent can be

seen in Figure 7.2. The experimental debris wedge is visible as the ring on the upper surface (blue ring in Figure 7.2) while internal material bunching, axial tears and fronds can also be seen in both images.

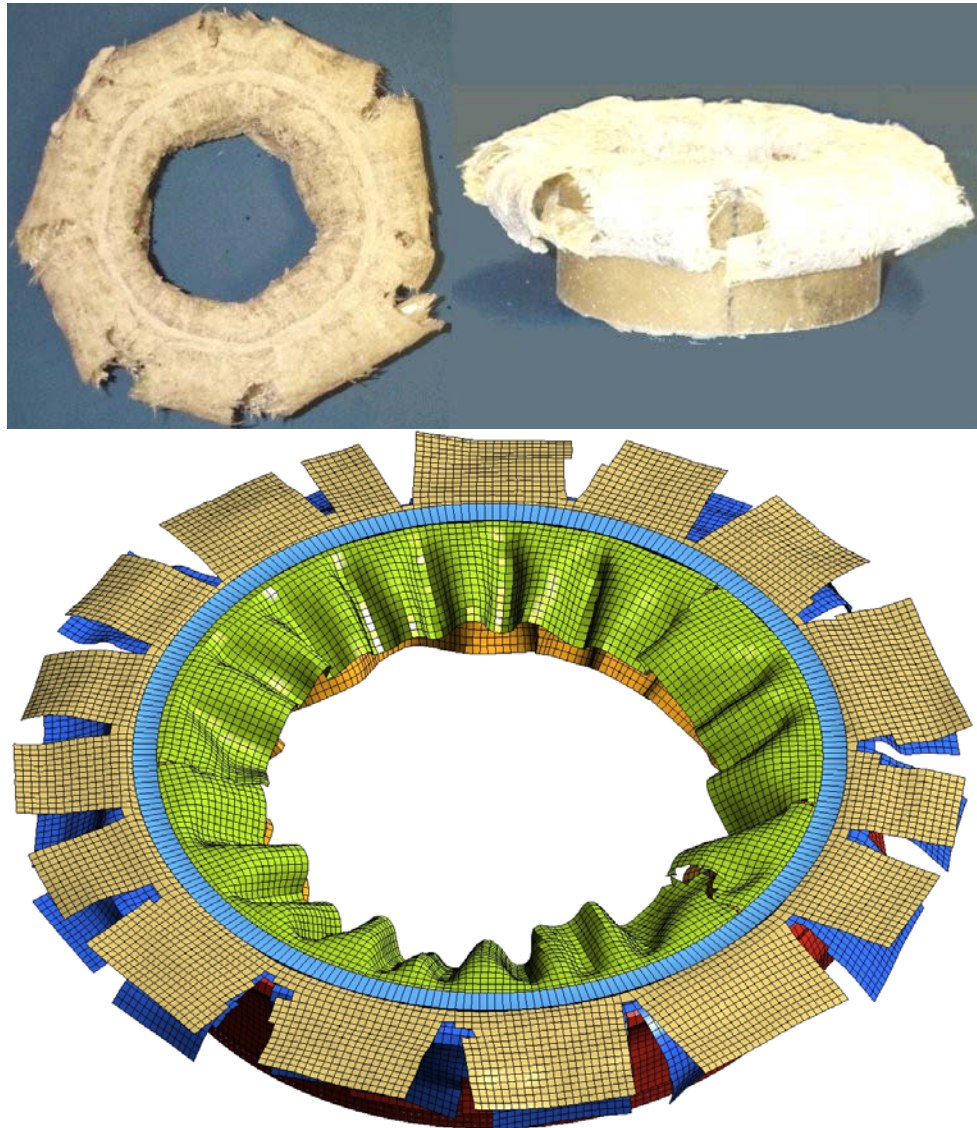


Figure 7.2. Images of experimental (above) and simulated (below) CFRM tubes crushed on flat-platens showing similar formation of fronds and internal material bunching. Additionally, the debris wedge can be seen in both images. (Experimental image supplied by the University of Nottingham)

As the simulation begins, the first several layers were shown to splay correctly as the independent layers separate over the debris wedge. As the spotwelds approach the crush zone, those in the centremost region were removed, representative of the central wall crack propagation. Throughout the simulation, the central spotwelds were eliminated ahead of those in

neighbouring regions. All remaining spotweld elements were eliminated as they came level with the tip of the debris wedge. Material layers which curled inwards were placed under circumferential compression stresses. The innermost layer curled through an extremely tight radius which caused a large number of elements in this layer to fail. All inward folding material eventually buckled, resulting in a good reproduction of the material bunching observed experimentally. Examples of the FE material bunching can be seen in Figure 7.3 and Figure 7.4. Figure 7.3 includes the stress gradient showing that the ultimate compressive strength (221MPa) was reached, causing this behaviour.

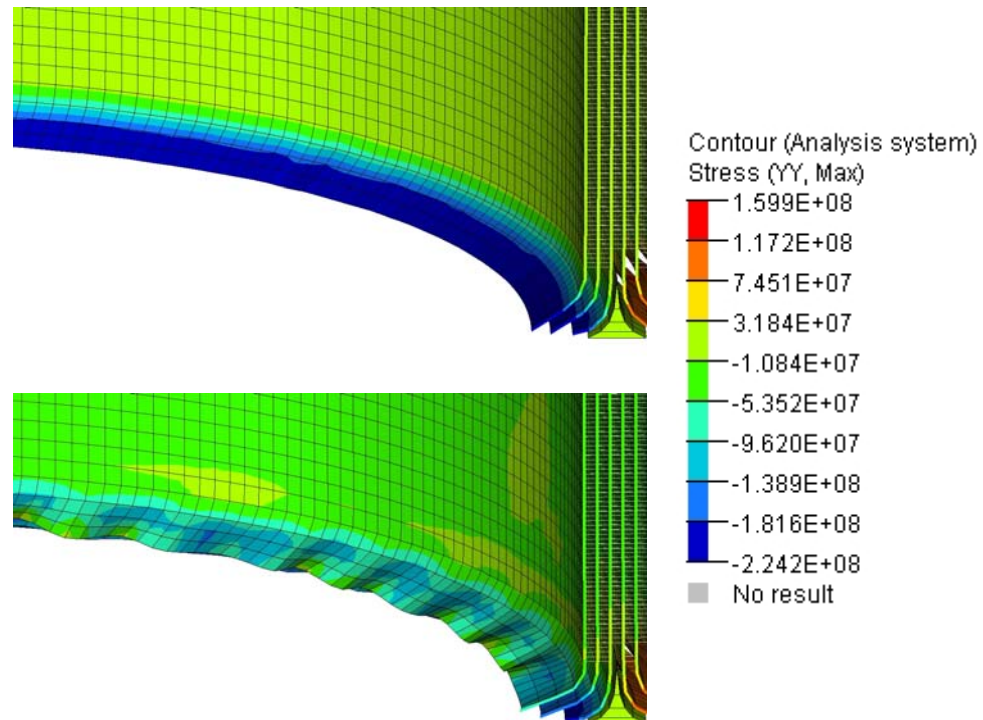


Figure 7.3. Circumferential compressive stresses (compressive hoop stresses) on the tube's inner layers which cause bunching in CFRM flat-platen simulations. NOTE: The stress required to induce this behaviour is equivalent to the in-plane compressive strength (221MPa).

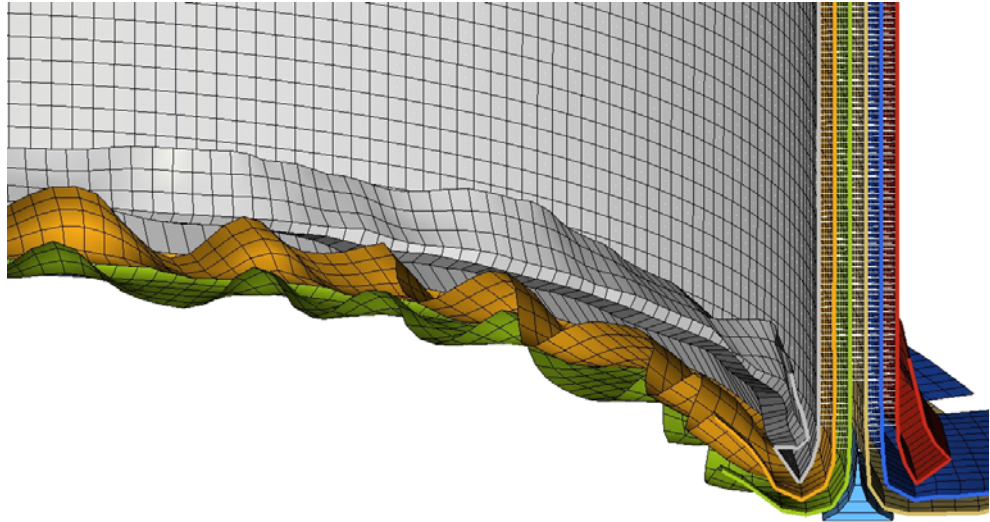


Figure 7.4. Internal material bunching during the CFRM flat-plate simulation.

The material observed to fold externally behaved in a similar manner to the experimental tests with the production of numerous axial tears, producing fronds. The number of fronds formed during the simulation was higher than shown experimentally, with the greatest number in the layer closest to the debris wedge. The outermost layer was largely undamaged with very few tears formed. Instead this layer curled up, contacting the undamaged tube wall.

Analysis of the simulated crush zone shows the deformation to be similar to that observed experimentally. Comparison of these images can be seen in Figure 7.5. Analysis of these images reveals that as the simulated material entered the crush zone, all of the spotwelds reached the defined failure force and were eliminated. This allowed the fronds to behave independently as they passed through the crush zone. This behaviour was not observed in the experimental test and no evidence of complete delamination between the fronds was observed. In the simulation, this essentially reduced the bending stiffness of the fronds, and hence the axial crush load.

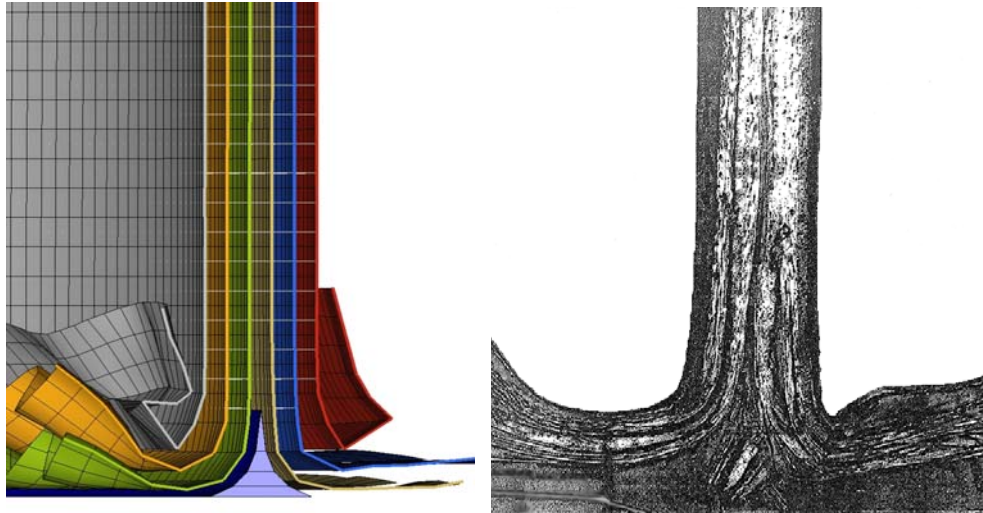


Figure 7.5. Images of simulated (left) and experimental (right) crush zones in CFRM flat-platen tube crush tests. Experimental image taken from reference [55].

The average steady-state load (measured between 9-22mm displacement) during this simulation was 25.5kN, well below the experimentally produced steady-state load of 94.5kN. The comparative load-displacement responses can be seen in Appendix Five. Repeating the simulation without the spotwelds showed a reduction to 21.2kN indicating that the spotwelds were not having a significant effect on the crush load.

### 7.1.1.3 Toray G83C

In general the simulated shape matched the experimental tests reasonably well. The externally folding material showed a degree of transverse shearing while internally, compressive cracks formed, both of which were observed in the experimental testing of the Toray G83C 2x2 twill. Images of an experimental specimen, together with the simulated equivalent can be seen in Figure 7.6. In addition, a sequence of the simulated crush is shown in Figure 7.7.

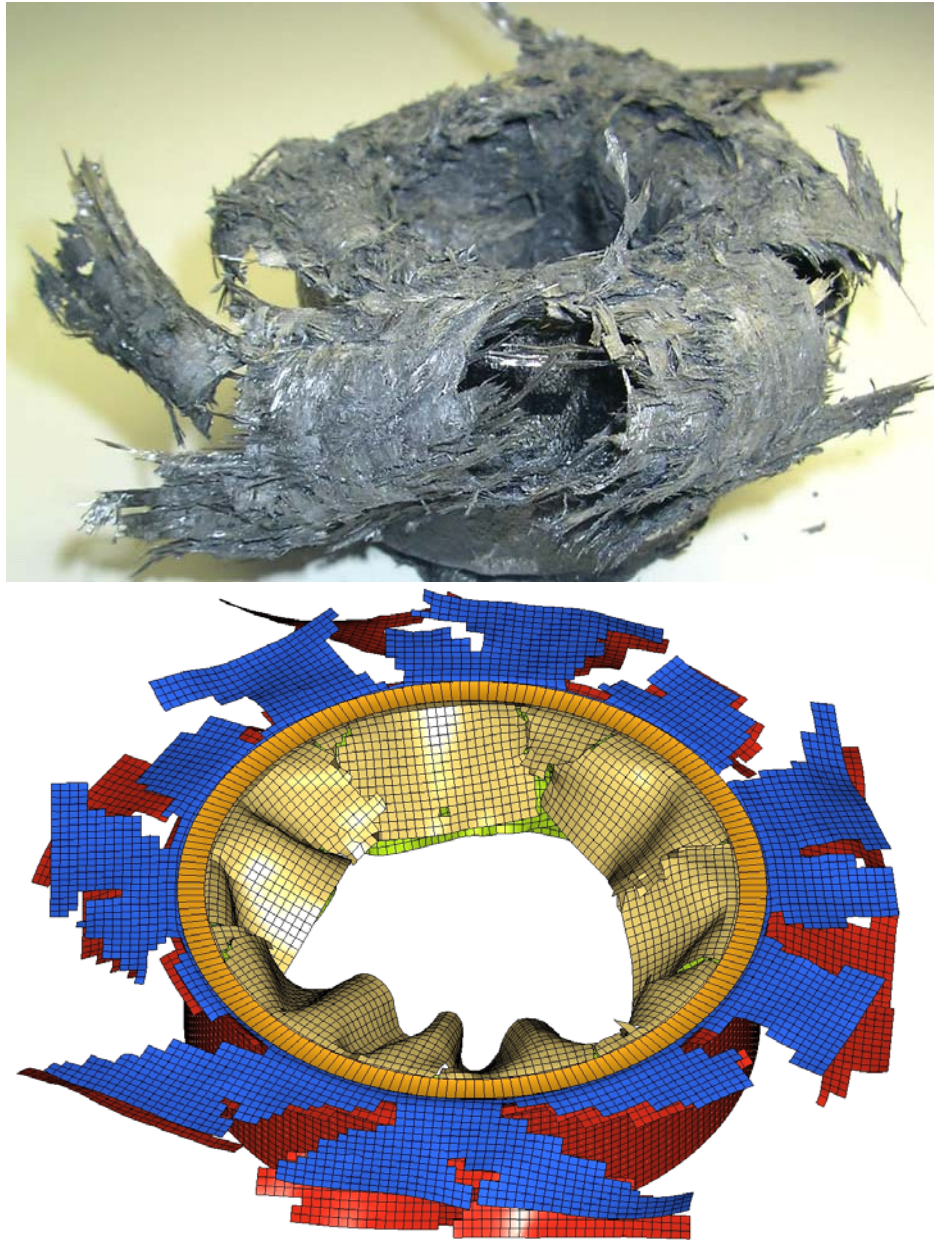


Figure 7.6. Image of experimental (above) and simulated (below) Toray flat-platen simulation showing internal cracks, transverse shearing and bunching.

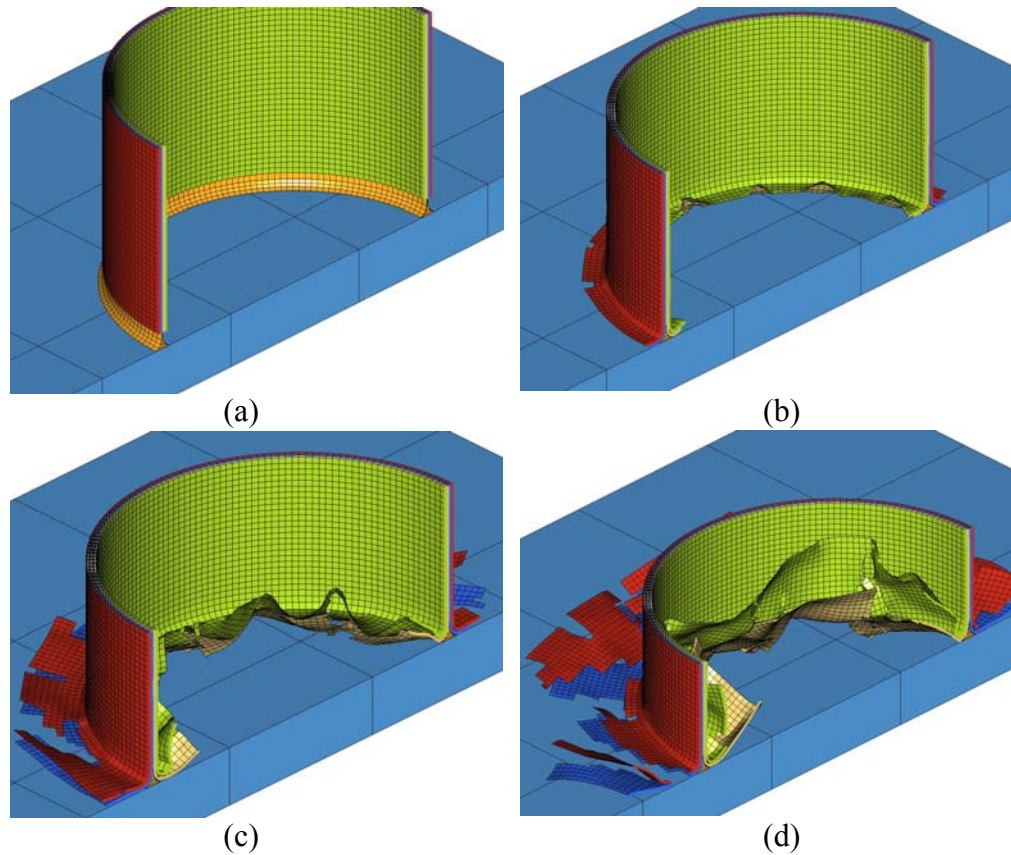


Figure 7.7. (a)-(d) Sequence of cut-away images taken from simulation of Toray tube crushed on flat-platen.

The spotweld behaviour in the Toray simulations was very similar to that observed in CFRM simulations. Spotwelds in the regions either side of the central wall crack were observed to fail as they became level with the debris wedge tip. No spotwelds remained once the material had passed the crush zone signifying complete delamination. Conflictingly, a small degree of localised delamination existed in the experimental specimens, leaving the fronds primarily laminated and intact. Figure 7.8 shows a comparison of the experimental and simulated crush zones for the Toray flat-platen test. It should be noted that upon removal of the crush load from the experimental specimen, the fronds would spring back elastically. This is visible in Figure 7.8 which shows the internal and external fronds having returned beyond the level of the crush platen. Unfortunately, it was not possible to set the sample in resin while under load in order to observe this phenomenon.



Figure 7.8. Images of simulated (left) and experimental (right) crush zones from Toray flat-platen tube crush tests.

The comparison between the experimental load-displacement results and the simulated response can be seen in Appendix Five where a poor correlation was observed. The average steady-state load (measured between 9-22mm displacement) was predicted to be 25.4kN compared to the experimentally produced 46.6kN.

### 7.1.2 Plug Initiator Simulations

All flat-platen simulations were based on a 35mm section of tube. However, the 7.5mm and 10mm CFRM plug-initiated simulations uncovered a geometrical dependence with this type of test. It was expected that the tube material would simply slide down the plug wall and through the radius smoothly. Instead, as the plug is designed to force the bottom of the tube outwards, there was an equal and opposite force on the top portion of the tube pushing it inwards; causing the tube wall to rotate as shown in Figure 7.9. This meant the tube contacted the plug part way through the radius, causing the accelerated propagation of the axial tears, which extended well ahead of the crush zone. This caused catastrophic failure as the tube wall split completely. This was first noticed during analysis of the reaction force on the upper crush platen which showed the outermost material layer to be transferring all of the crush force at the end of the simulation. This effect was not apparent in flat-

platen simulations due to symmetry within the crush zone, or in Toray simulations where the tube was sufficiently stiff.

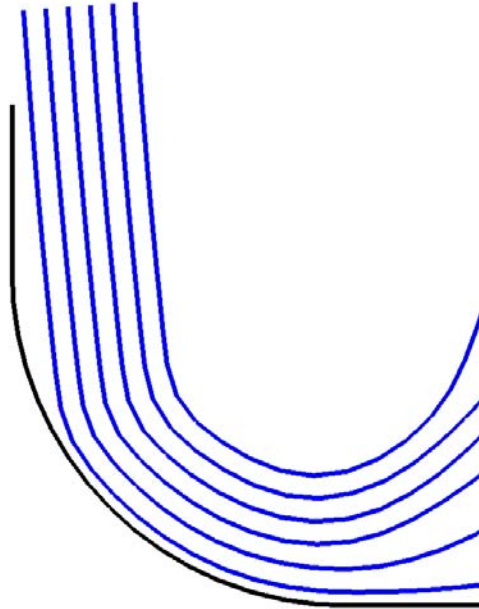


Figure 7.9. Image of 10mm plug initiated crush simulation showing the rotation of the 35mm length tube wall.

Two models were tested to try to correct the problem; a 35mm length tube modelled with appropriate constraints, and, a full length (100mm) tube section without constraints. The first test constrained the uppermost nodes of a 35mm length tube in the x and y directions. Surprisingly, this reduced the simulated steady-state load considerably, presumably a result of the reduced work required to deform the tube wall due to over-constraining. As a result, the 100mm length models have been presented, without constraints, for the CFRM 7.5mm and 10mm radii plug initiated simulations only. Similar tests were performed on the 5mm radius CFRM and Toray plug simulations but no variation in the behaviour was observed.

#### **7.1.2.1 Interlaminar Material Loads in Plug-Initiated Simulations**

Like flat-platen simulations, the forces on 5 spotwelds at the same point on a CFRM tube were tracked as they entered the crush zone. These are shown in

Figure 7.10, numbered 1 to 5 from the outermost spotweld to the innermost spotweld.

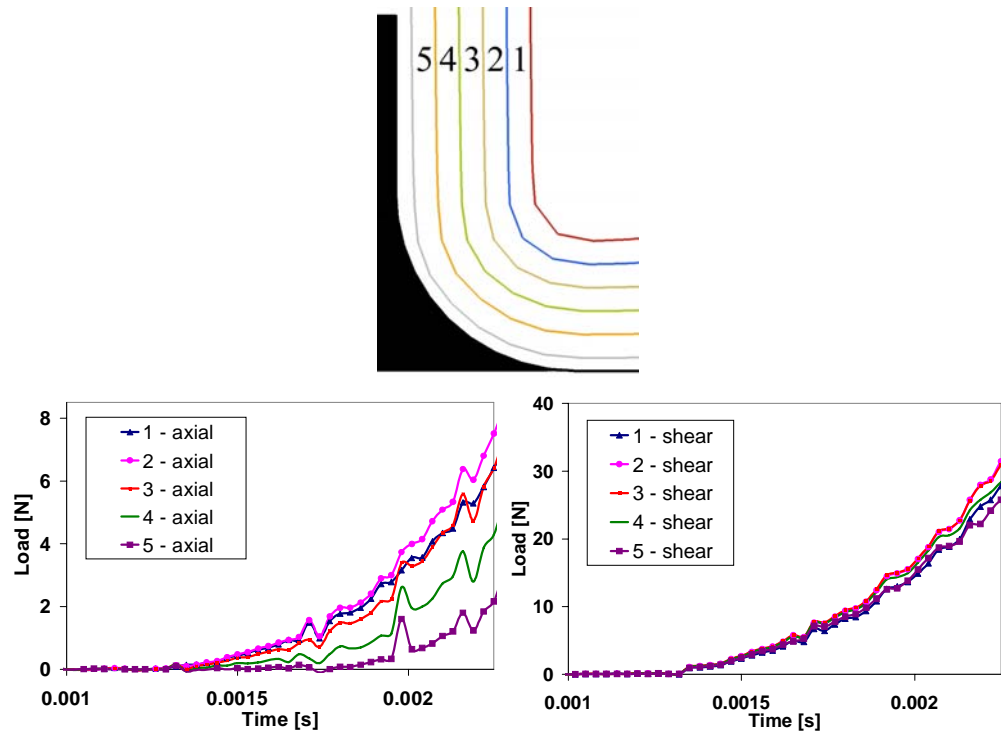


Figure 7.10. Axial and shear load components on interlaminar spotweld elements of a CFRM simulated tube, as the spotwelds approach the crush zone of a plug-initiated crush. The regions are numbered from the outside of the tube wall, to the inside.

During the period shown, shortly before element elimination, the axial force is greatest in the second (2 - axial) interlaminar layer from the outside of the tube. The axial forces in the first (1 - axial) and third (3 - axial) regions are very similar and are only slightly below the region they straddle. The normal forces reduce equally for the following fourth and fifth regions. For the same period, the shear forces through the interlaminar regions are very similar. However, the outlying regions (1 and 5) are observed to be under the smallest shear loads while region 2 is under the greatest combined load.

**7.1.2.2 CFRM***5mm Radius*

Simulation of the 5mm radius plug initiated CFRM crush test reproduced the experimental failure behaviour to a reasonable degree. A sequence of images, taken from the simulation, can be seen in Figure 7.11.

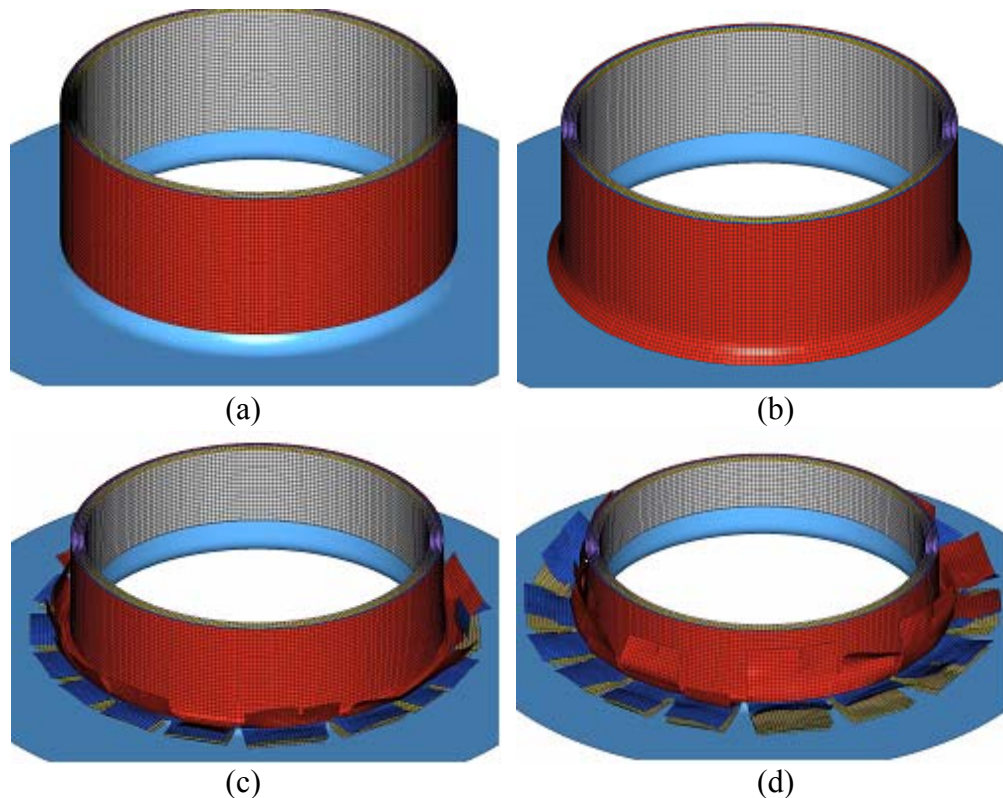


Figure 7.11. (a)-(d) Sequence of images taken from simulation of CFRM tube crushed on 5mm radius plug initiator.

The tighter radius of this plug meant that higher levels of material deformation were observed and a large number of fronds were produced. It should be noted that in the experimental test, it was difficult to determine the number of fronds as there were few distinct axial tears. Rather a high degree of damage occurred within the material, evident in its opaque appearance. As was the case experimentally, the simulated fronds tended to splay along the plug base. Images of the experimental and simulated test specimens can be seen in Figure 7.12.

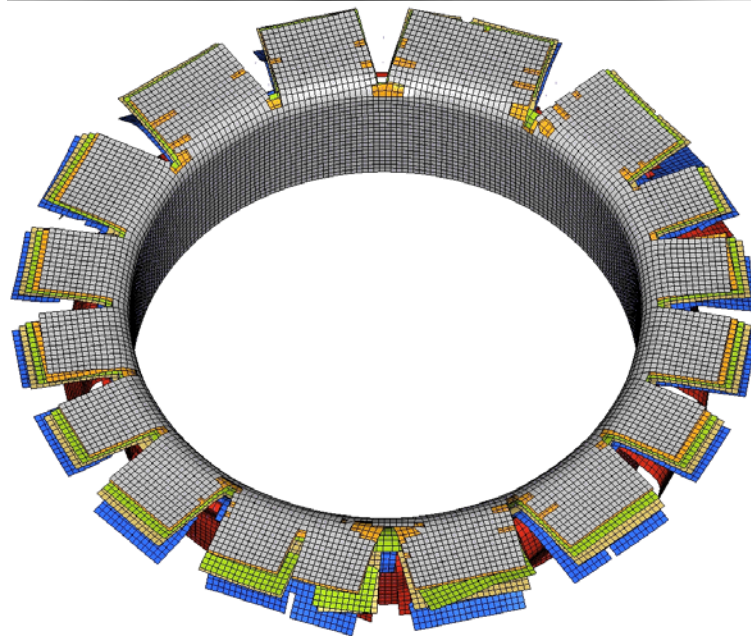


Figure 7.12. Images of experimental (above) and simulated (below) tubes at completion of test on 5mm plug initiator. Experimental image taken from [126].

Examination of the cross-section of the simulated crush zone shows a diagonal delamination front, which perfectly mimics the damage initiation site in the experimental test, as shown in Figure 7.13. However, almost every spotweld element is eliminated at this point, prior to entering the plug radius, indicating complete delamination of the fronds. Evidently, this is incorrect as the experimental test shows only a single complete delamination on the far right of the image.

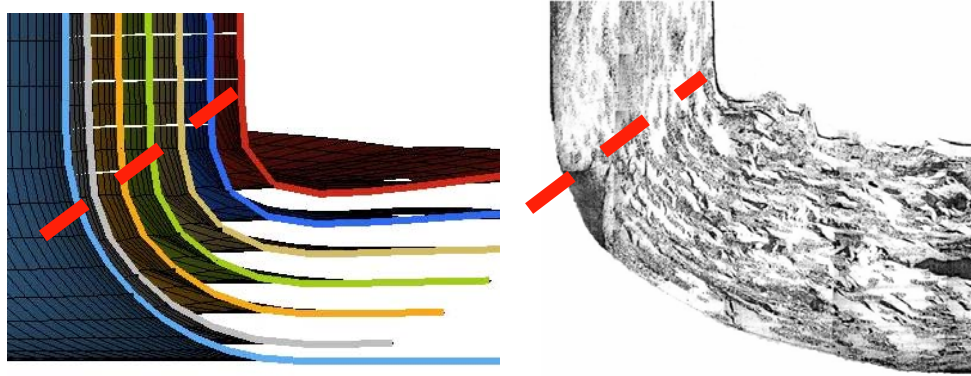


Figure 7.13. Simulated (left) and experimental (right) crush zones of a CFRM tube crushed on a 5mm radius plug initiator showing the matching deformation fronts. Additionally, the experimental image shows a high level of shear deformation with a single delamination. Experimental image taken from [54].

The predicted steady state load was well below the experimentally determined value of 145kN, being just 18.4kN (measured between 13-22mm displacement). Load-displacement graphs can be seen in Appendix Five. It is interesting to note that the loading portions of this test, together with the 7.5mm radius CFRM plug and 10mm radius CFRM plug tests (presented hereafter) all reproduce the initial portion of the experimental load-displacement plots well. This suggests that in these cases only, removal of the leading rows of spotwelds accurately reproduces the behaviour of the chamfer as it breaks down. Such a similarity was not evident in the Toray tests.

#### *7.5mm Radius*

Experimental CFRM crush tests on the 7.5mm radius plugs showed the formation of more distinct fronds than were produced with the 5mm radius plug. These fronds extended a short distance across the plug before curling upward. A total of 9 fronds were predicted, which compares well with the 8-10 distinct fronds produced experimentally. The simulation captured this response well, as shown in Figure 7.14.

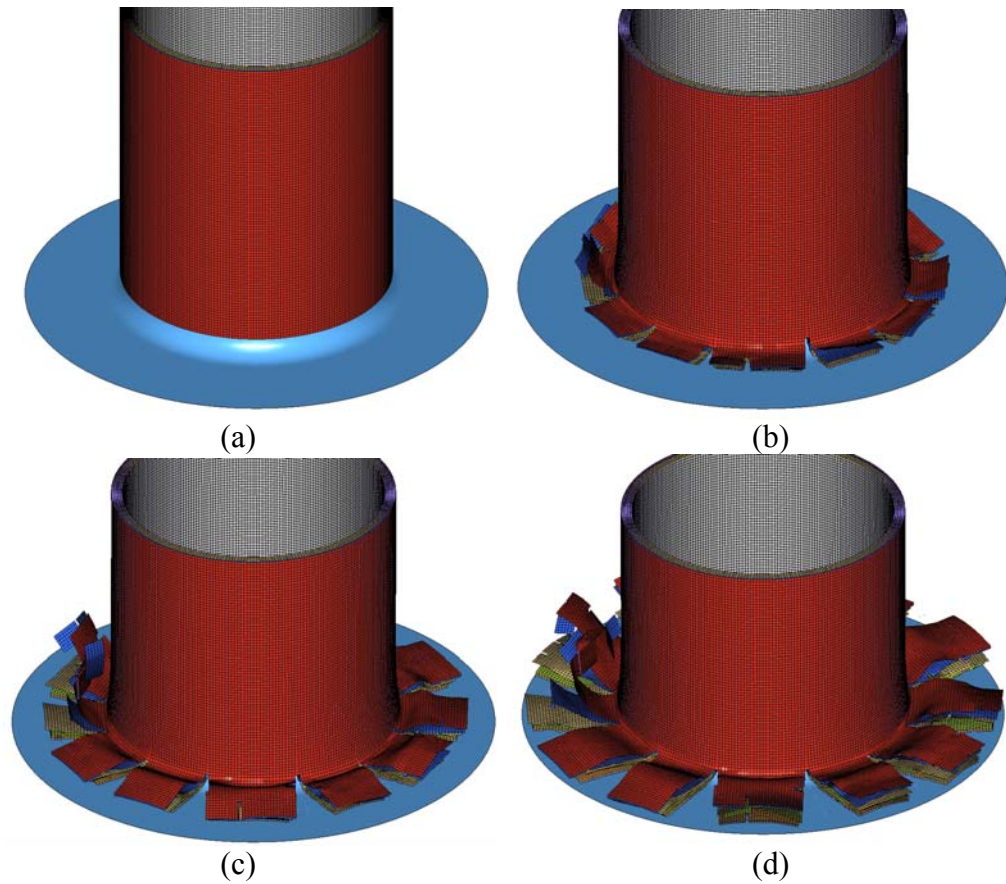


Figure 7.14. (a)-(d) Sequence of images taken simulation of CFRM, tube crushed on 7.5mm radius plug initiator.

Like the 5mm plug simulations, the axial tears extended only to the base of the radius. Additionally, unlike previous tests, a small number of spotwelds remain after the crush zone, the majority of which attach the two laminae nearest the plug. This is not surprising as it was previously shown that this interlaminar region is under the lowest stress. Comparison of the experimental and simulated failure behaviour can be seen in Figure 7.15 and Figure 7.16.

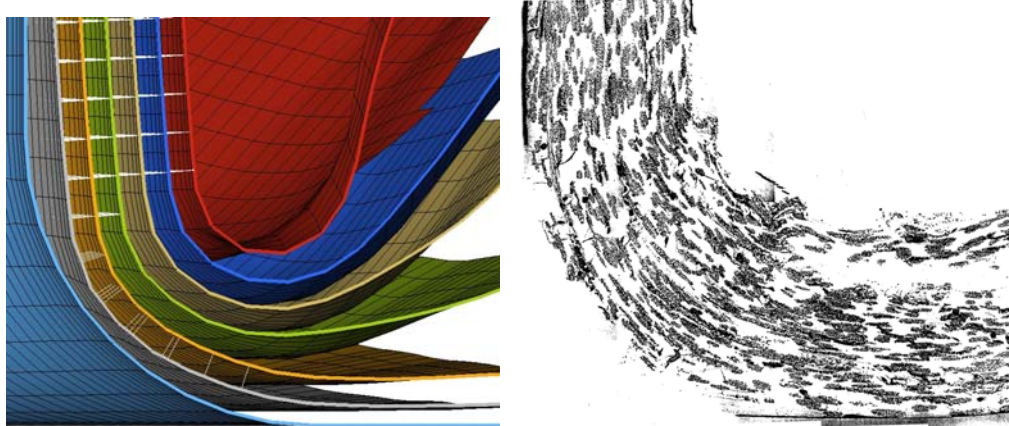


Figure 7.15. Simulated CFRM crush zone (left) showing a region in which spotwelds had passed the crush zone, and experimental crush zone (right) with an interlaminar crack visible. Experimental image taken from [54].

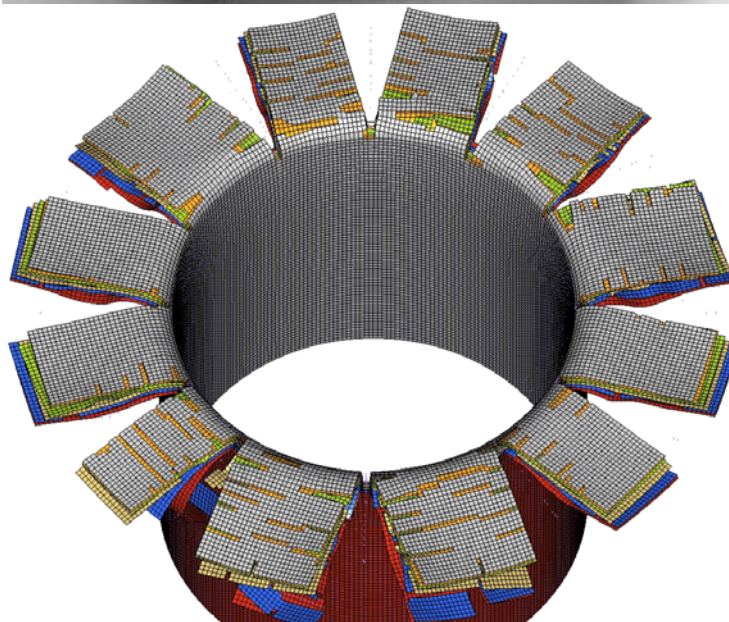


Figure 7.16. Images of experimental (above) and simulated (below) CFRM tubes at completion of test on 7.5mm plug-initiator. Experimental image taken from [126].

The delamination front was difficult to determine from the experimental micrographs. However, a single clear delamination can be observed on the far right of Figure 7.15. According to the FE analysis discussed earlier in 7.1.2.1, this interlaminar region is under the highest stress, explaining the presence of the only visible delamination.

Predicted steady-state load for this simulation was 18.2kN (measured between 20-40mm displacement), compared to the experimentally determined 79.5kN. Comparative load-displacement curves can be seen in Appendix Five.

#### *10mm Radius*

Experimental crushing of CFRM tubes on a 10mm radius plug initiator showed a change in the observed failure behaviour compared to the previous two plugs. Rather than splay in the same manner as the 5mm and 7.5mm tubes, the 8-10 axial tears were observed to propagate well above the plug initiator's radius. In several places, circumferential tears would join at the tip of the axial tears, allowing several large sections of tube wall to detach. This material would not pass through the crush zone, resulting in a significantly lower crush force than for the 5mm and 7.5mm plug-initiated crush tests.

This change of failure mode was extremely well-captured by the FE simulation, which showed extended axial tears, separating the tube into 9 fronds. The fronds began sliding along the plug radius but would not conform to its shape causing a bending stress at the point where the axial tears stop. Consequently, the fronds 'snapped' at this point, simultaneously causing a drop in the axial load. Images of the experimental and simulated tubes are shown in Figure 7.17 below. Additionally, a sequence of the simulated response is shown in Figure 7.18.

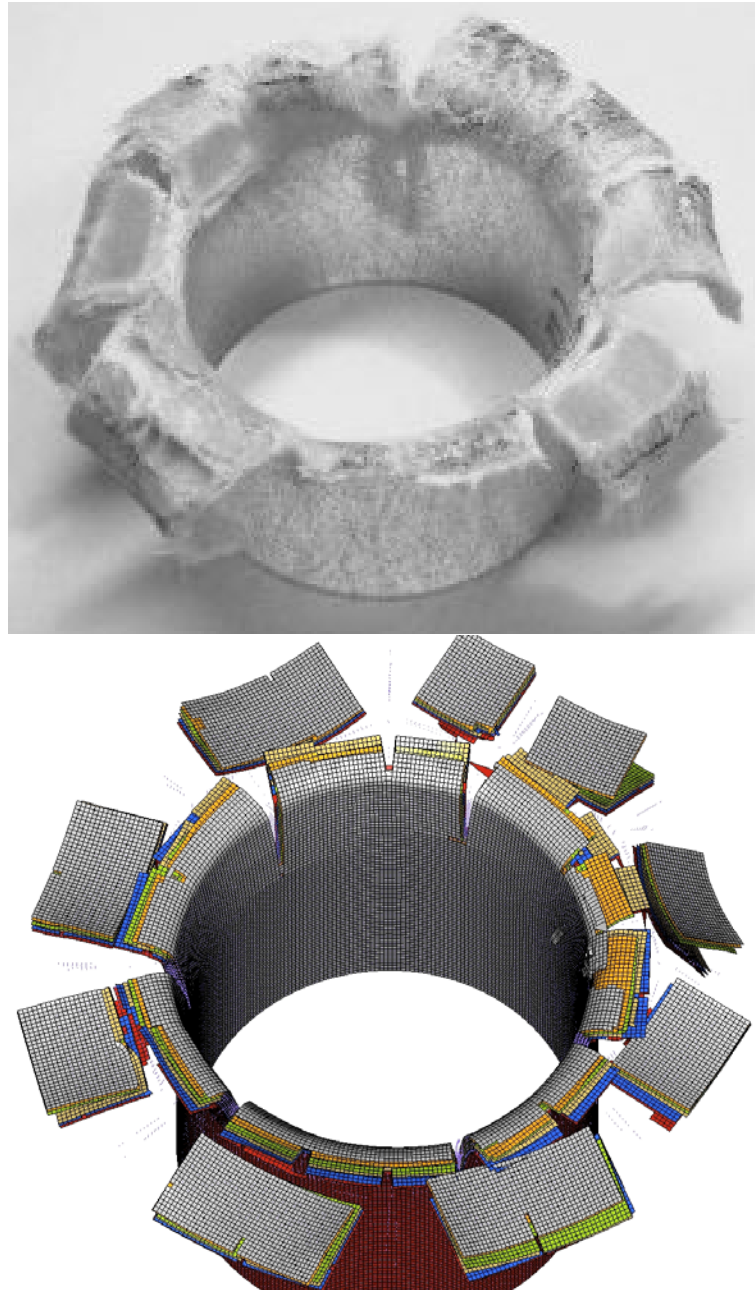


Figure 7.17. Images of experimental (above) and simulated (below) CFRM tubes at completion of test on 10mm plug-initiator. Experimental image taken from [126].

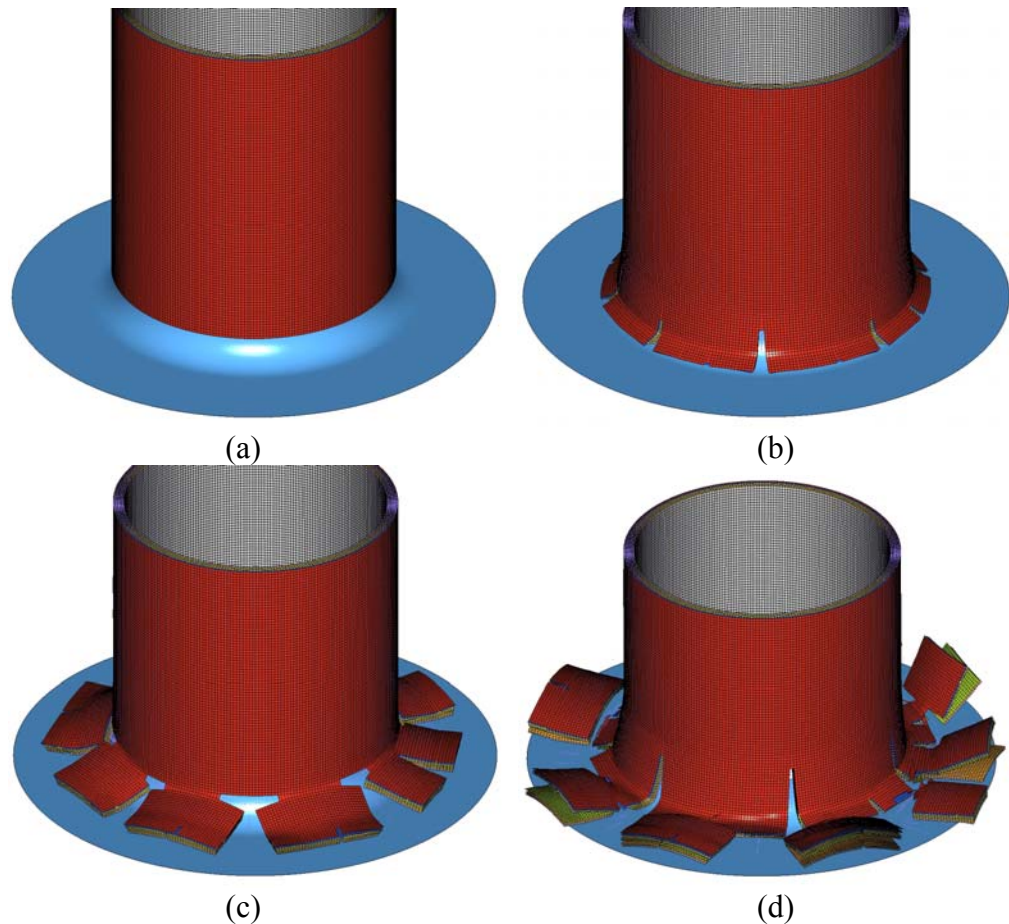


Figure 7.18. (a)-(d) Sequence of images taken from simulation of CFRM tube crushed on 10mm plug initiator.

A large number of spotwelds remain in the material as the fronds do not conform to the plug radius, hence, a low level of interlaminar damage occurred in the tube material. Interestingly, when the simulation was re-run without the spotwelds, the failure mode changed, becoming a splaying type of failure as seen in the 7.5mm plug simulation. Evidently the spotwelds add a great deal of stiffness to the tube material.

A steady-state load for the simulation was unobtainable as the loads varied significantly for each cycle as the fronds failed. However, taking the average gives a crush load of 10.1kN (measured between 20-40mm displacement), compared to the experimentally determined 42kN. Comparative load-displacement curves can be seen in Appendix Five.

### 7.1.2.3 Toray G83C 5mm Radius

The Toray 5mm radius plug-initiated simulation showed the formation of distinct fronds which were observed experimentally. 8-9 simulated fronds (exact number is difficult to determine) correlates well with the 8 experimental fronds. As was the case experimentally, the axial tears extend only to the base of the plug radius. However, the curvature of the experimental fronds was not captured, due largely to the removal of every interlaminar spotweld prior to entering the plug radius. Experimentally, a moderate degree of interlaminar cracking was observed, though a high frond bending stiffness was maintained. Further analysis indicated that the interlaminar cracks were arrested at the next fibre-bundle junction, leaving a reasonable portion of the matrix and fibres intact. An image of the experimental crush-zone can be seen below in Figure 7.19. Note that samples could not be set while under compression, exacerbating the interlaminar cracks.



Figure 7.19. Image of experimental crush-zone produced from Toray tube crushed on a 5mm plug-initiator.

Early elimination of the spotwelds is the likely cause of the under-predicted load. As the simulated fronds could slide independently, very little damage occurred in the upper lamina where experimentally, the compressive stresses caused a high degree of fibre fracture and consequently, through-thickness

shearing. Additionally, through-thickness shearing is an out-of-plane loading which cannot be considered by shell elements. This resulted in an over-estimation of the strength of the upper laminae. The simulated average steady-state load was 14.4kN (measured between 13-22mm displacement) compared to the experimental average of 20.3kN. A sequence of the simulated crush response can be seen in Figure 7.20. A comparison of the experimental and simulated tubes can be seen in Figure 7.21. The comparative load-displacement curves can be found in Appendix Five.

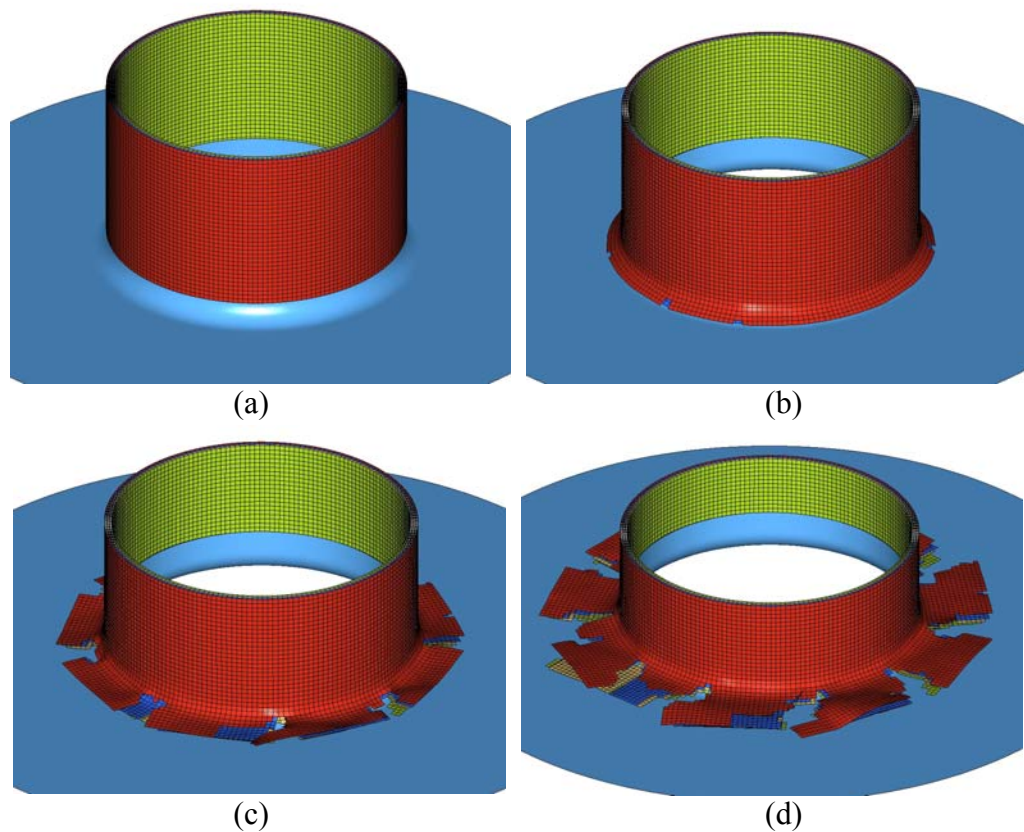


Figure 7.20. (a)-(d) Sequence of images taken from simulation of Toray tube crushed on 5mm plug initiator.



Figure 7.21. Images of experimental (above) and simulated (below) Toray tubes crushed on 5mm plug initiator.

### *7.5mm Radius*

The 7.5mm plug radius simulation demonstrated a good visual correlation. Rather than perfect axial tears, a small degree of circumferential cracking (or transverse shearing) was captured. Nine fronds were predicted, compared to the six fronds produced experimentally. These can be seen in the comparison of the deformed tubes shown in Figure 7.22. A sequence taken from the simulation is shown in Figure 7.23.

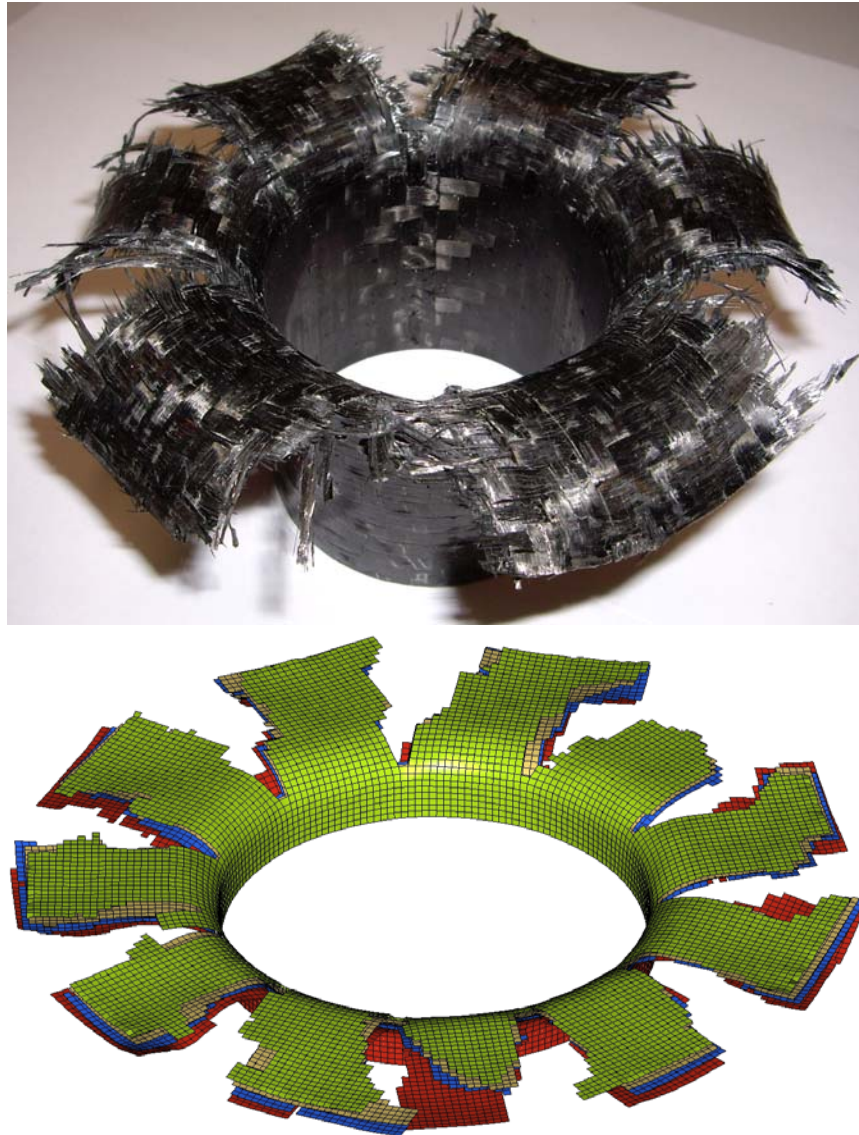


Figure 7.22. Images of experimental (above) and simulated (below) Toray tubes crushed on 7.5mm plug initiator.

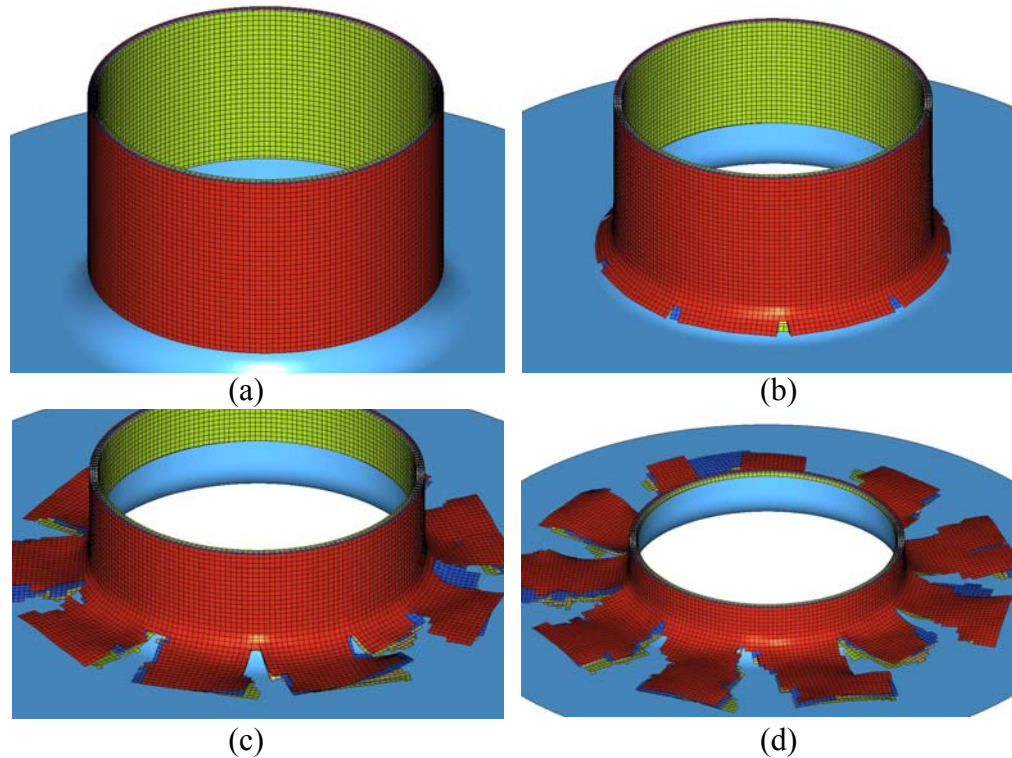


Figure 7.23. (a)-(d) Sequence of images taken from simulation of Toray tube crushed on 7.5mm radius plug initiator.

As the material entered the radius of the plug, every interlaminar spotweld was removed allowing each lamina to move independently through the crush zone. Figure 7.24 below shows the level of delamination observed experimentally which is considerably less than predicted in the simulations. As with the 5mm plug crush-zone, small cracks can be seen with an occasional larger delamination.



Figure 7.24. Image of experimental crush-zone produced from Toray tube crushed on a 7.5mm plug-initiator.

The load-displacement response showed the load increasing to ~22kN before reducing as the tube began tearing. An average steady-state load of 13.8kN was recorded (measured between 16-30mm displacement). This compares well with the experimentally observed value of 15.4kN. The comparative load-displacement responses can be seen in Appendix Five.

#### *10mm Radius*

The simulated failure mode adequately resembled the experimentally observed behaviour with clear axial tears separating 11 fronds. 6 fronds were produced in physical testing with the axial tears extending to near the top of the plug radius. This crack development was captured by the model. As a consequence of the extended axial tears, the hoop constraints on the fronds are much lower in this test. This meant that the laminae were not forced through the exact plug radius, reducing the stress on the interlaminar material. This suggests that the interlaminar material behaviour does not affect the energy absorption significantly. A number of spotwelds remain after the crush zone in this model, particularly in the regions nearest and furthest from the plug. Examination of the experimental crush-zone shows a relatively low degree of cracking and deformation. Some through-thickness shearing is apparent in this test, which was again not considered by the use of shell elements. A comparison of the experimental and simulated tubes can be seen in Figure 7.25 while a sequence of the simulation can be seen in Figure 7.26.

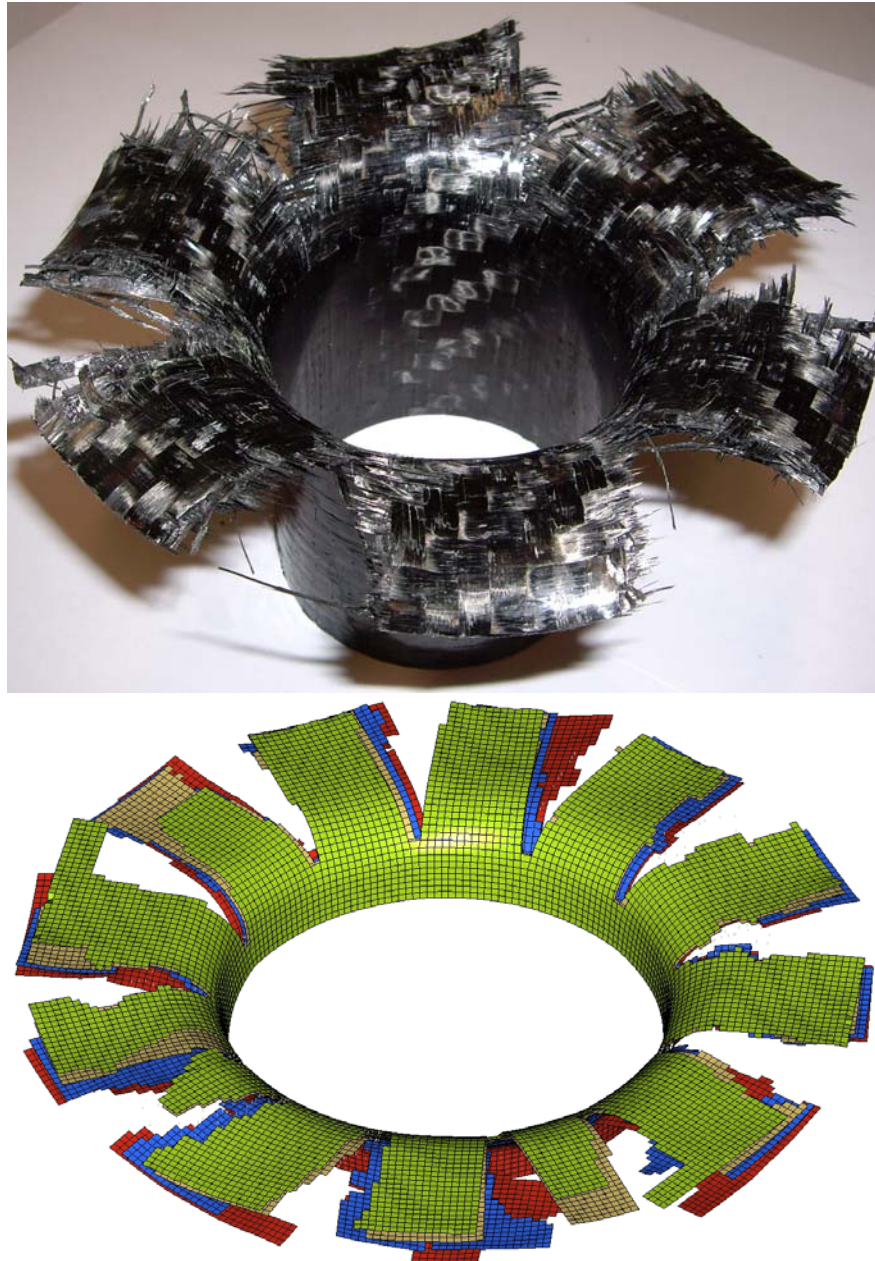


Figure 7.25. Images of experimental (above) and simulated (below) Toray tubes crushed on 10mm plug initiator.

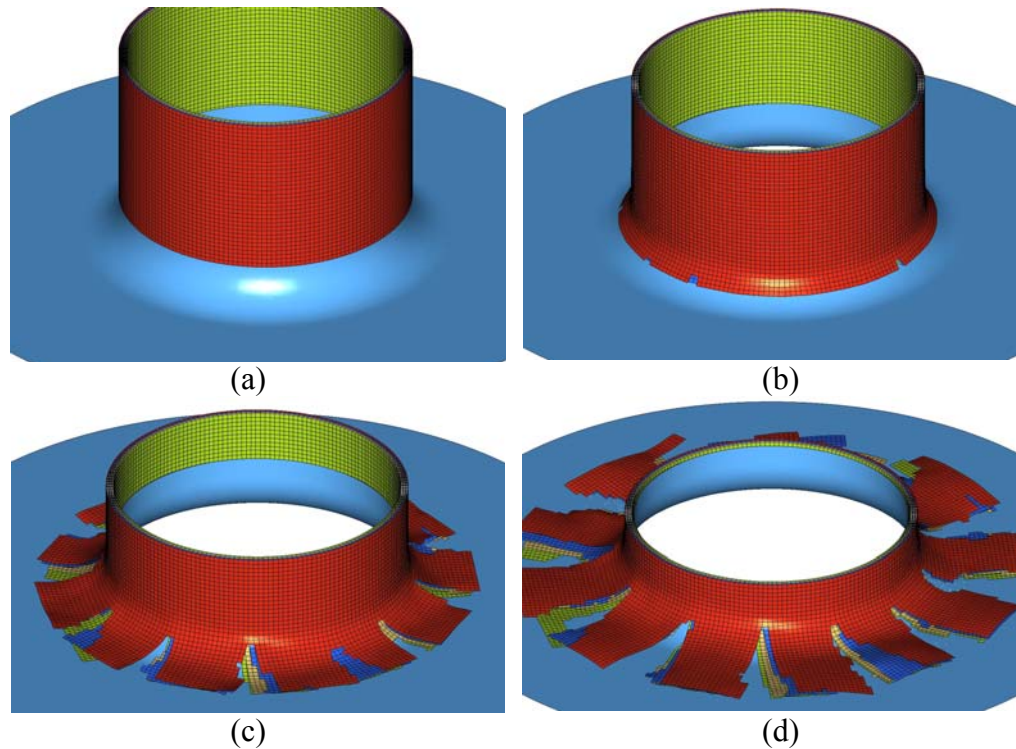


Figure 7.26. (a)-(d) Sequence of images taken from simulation of Toray tube crushed on 10mm radius plug initiator.

Given the similarly low degree of interlaminar deformation in the simulated and experimental tests, it is not surprising to learn that the predicted steady-state load was 13.3kN (measured between 16-30mm displacement), just 5% below the experimentally recorded load of 13.9kN. Comparative load-displacement curves are shown in Appendix Five.

## 7.2 Discussion

Chapter Six presented a modified force-based delamination model which could accurately transfer the shear stiffness between lamina, producing the correct flexural stiffness. In this chapter, the elastic force-based delamination model was applied to full-tube crush simulations. Emphasis was placed on the inclusion of the features pertinent to the crushing process and an accurate reproduction of the behaviour observed in flat-platen tests.

In general, the failure behaviour of the simulations correlated well with experimental testing. The simulation reflected the change in failure mode between the 7.5mm and 10mm plug-initiated CFRM crush tests. However, despite the good visual correlation, predicted loads were extremely low for all CFRM tests together with the Toray flat-platen test. Similar under-predictions of the load have been previously observed (using a force-based approach) but the cause of the error was not identified [56, 64]. On the other hand, simulations of Toray plug-initiated tests resulted in reasonable predictions of the load. This may be due to the over-estimation of the tube wall strength, resulting from the inability to predict through-thickness shear with shell elements. A summary of the results can be seen in Figure 7.27. In this plot, the experimental load is included together with 2 simulated loads; 1) with the spotwelds included as presented above, and 2) with the spotwelds removed from the input deck before initialisation.

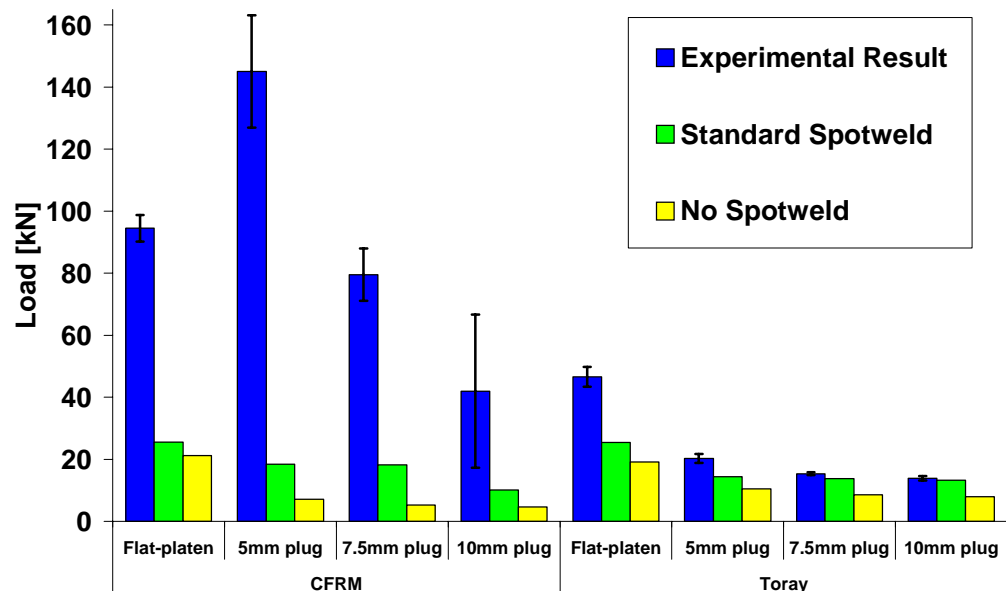


Figure 7.27. Summary of simulated results, with and without interlaminar spotwelds, compared to the experimentally recorded values for various tests and materials.

If we consider each material independently, the simulations display a logical trend – as the crush radius decreases, the amount of material deformation, and

hence load, increases. The effective crush radius in flat-platen simulations is approximately 2mm, leading to the highest simulated load. However, in the case of the CFRM 5mm plug-initiated test, a large degree of deformation is inaccurately captured by the model. An attempt was made to try and achieve the correct load by increasing the post-failure strength and strain values however, beyond a certain point, such efforts only resulted in a change of failure mode, and a marginal increase in the steady-state load. The inability to reproduce the experimental behaviour was probably due to the premature removal of the spotwelds, leaving each lamina unattached which allowed them to slide freely, finding the path of least resistance. An image of this type of failure can be seen below in Figure 7.28.

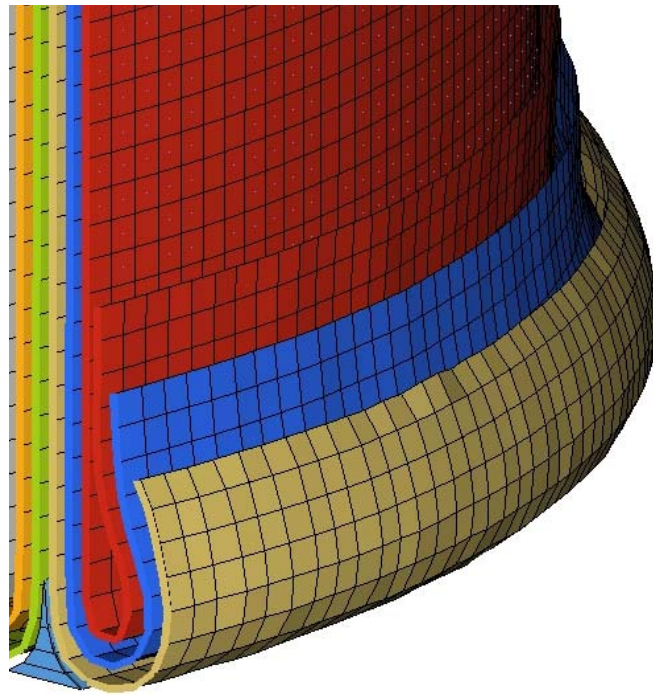


Figure 7.28. Cut-away image of simulated CFRM flat-platen tube behaviour with an increased maximum strain limit showing the resulting incorrect failure mode.

The wall thickness of the CFRM tubes was approximately double that of the Toray tubes. Therefore, it was no surprise to find that the influence of the interlaminar material was more significant in the CFRM samples than for the Toray specimens, as higher levels of shear deformation were expected. This

was evident from repeat simulations in which the spotwelds had been removed, where a larger drop in steady-state load was observed in CFRM tests, as shown above in Figure 7.27.

The selection of a 1mm x 1mm mesh density is likely to have affected the response but the degree of influence cannot be quantified. The 1mm<sup>2</sup> mesh density was selected early during the modelling work. Consequently, calibration of the behaviour of both the material and the spotweld failure forces requires the mesh density remain the same or at least, similar. Re-calibration of these values for a finer mesh would most likely result in a similar steady-state load, such is the effectiveness of the post-failure strength controls. However, a finer mesh provides more locations for tears to develop, making the selection of the post-failure values increasingly critical. Additionally, modelling of metallic crush members has shown that plastic folds are more accurately reproduced when the shell length approaches the shell thickness [127]. If this effect is similar in composite crush, then the influence of the selected mesh density would be more significant in Toray simulations where the shell thickness:length ratio is much smaller than the CFRM simulations. Selection of an optimum ratio for reproducing composite crush behaviour is an area worthy of further consideration. In addition, it is known that strain-softening material models are mesh sensitive, a result of localisations causing single elements to strain-soften [15]. The mesh dependence of this approach is undesirable but is unavoidable given the moderate level of calibration that is required for any given mesh size.

Having considered the above discussion points, it appears that the general trend for the CFRM simulations (and the flat-platen Toray simulation) to under-predict the steady-state is likely to be a result of either;

- 1) the shell thickness:length ratio (mesh density),
- 2) inadequate consideration of the post-failure behaviour of the material, or,
- 3) the premature removal of the spotwelds,

It is difficult to gauge whether the post-failure material parameters selected in material 58 are accurate, although, the visual correlation offers a good indication. In all simulations (except the 5mm plug-initiated CFRM tube), the failure mode was close to the experimentally observed result suggesting that the selected values were close to optimum. In general, the number of fronds predicted was too high allowing relaxation of the hoop stresses. This inaccuracy could be removed with further calibration, though the small changes needed to the post-failure strength would only account for a small portion of the under-predicted load.

In all simulations, a much higher level of delamination was predicted than was observed experimentally. This allowed the laminae within the fronds to behave independently, reducing the bending stiffness and hence crush load. In addition, had the spotwelds continued to keep the lamina intact, it is anticipated that the fronds would curl outwards through a larger radius, causing increased levels of material deformation and the absorption of higher levels of energy through interlaminar shear. Subsequently, this behaviour was investigated.

Photographs of the crush zone of flat-platen simulations revealed that only Mode I loading would repeatedly result in the complete separation of the

lamina. This type of loading is typically only observed in the central wall crack, and was confirmed earlier in 7.1.1.1. It has been shown experimentally, that the central wall crack consumes very little energy in a flat-platen tube crush test [45]. Application of basic fracture mechanics theory on the CFRM flat-platen test (with a  $G_{IC}=661\text{J/m}^2$  [55]) indicates that 0.2% of the total 4.725kJ is absorbed through the propagation of the central wall crack. During this process, very little damage occurs in the material ahead of the crack, indicating that failure is sudden, as observed during a DCB test. The use of a force-based failure, as used here, appears to adequately represent all the facets of this form of crack propagation. Such an approach can therefore be used in any simulation (axisymmetric, multi-shell and solid element) where a Mode I delamination is expected.

With reference to the images of the experimental crush zones, analysis showed that Mode II interlaminar loads in the fronds typically resulted in interlaminar shear cracking and cracking at the fibre-matrix interface, yet seldom resulted in the complete separation of the lamina. Indeed, shear loading is known to result in hackles, an indication of shear damage [117]. These are clearly evident in the CFRM crush-zones. A schematic of this form of damage can be seen in Figure 7.29.

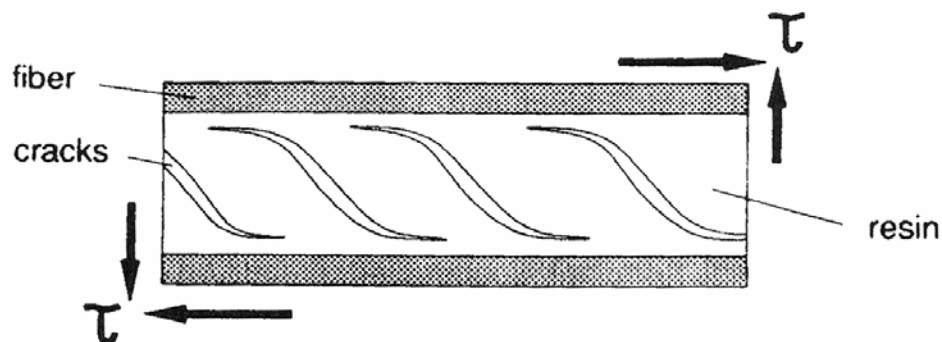


Figure 7.29. Schematic of hackles which form within the interlaminar regions of composite materials under shear loading [117].

Toray crush-zones displayed numerous small interlaminar cracks running parallel to the fibres. By comparison, a larger degree of interlaminar cracking was observed in Toray tubes than CFRM tubes. However, despite the degree of cracking, the fronds remained largely intact in all tests. In addition, the experimental fronds were observed to maintain an extremely high bending stiffness – further suggesting that most of the interlaminar region remained intact following the crush zone.

It would appear that the spotwelds did not adequately reproduce the behaviour of the experimental matrix material since complete delamination was predicted in almost every simulation. Given that an accurate representation of the Mode II behaviour was predicted in Chapter Six, it must be questioned whether the ENF test is a suitable representation of the loading experienced by the interlaminar material in a tube crush scenario. Due to the largely symmetric loading and the inclusion of a pre-crack, neither of which exist in a tube crush experiment, ENF testing is unlikely to be representative of the Mode II deformation which occurs in tube crush experiments. This suggests that validation of a delamination model with an ENF test is not an accurate indication of its ability to successfully represent the interlaminar material in a crush simulation.

In any case, very little Mode II interlaminar deformation was considered by the spotwelds in this elastic force-based failure form. Effort must be given to the inclusion of the effect of micro-cracking that occurs within the interlaminar regions under Mode II loading.

## **8 Strain-Controlled Delamination - Tube Modelling**

The ability to successfully predict the performance of composite materials in crash situations could substantially reduce the need for prototyping and allow automotive manufacturers to exploit the benefits of such materials. A step in this direction was reported in Chapter Six where a modified spotweld methodology to modelling delamination, using a force-based approach, was introduced and validated using simulated coupon tests. When employed in a tube crush simulation, the Mode I behaviour was shown to be reproduced accurately. However significant discrepancies between the experimental and simulated Mode II behaviour, and predicted load, were observed. This raised questions about the representative validity of ENF testing for the Mode II loading experienced within the fronds of an experimental tube. Subsequently, it was confirmed that a significant underestimation of the crush energy was caused by the premature removal of the spotwelds which predicted complete delamination in most cases.

Here, the aforementioned delamination modelling methodology is further modified by adopting a strain-controlled approach. This ensures the appropriate influence from the interlaminar material by maintaining a user-defined post-failure strength. Significant improvements in predicted load were observed. However, a need to recalibrate the material behaviour for each test scenario was encountered, reducing the attractiveness of this methodology.

## 8.1 Strain-Controlled Spotweld Behaviour

---

The principle of composite materials being weakened by micro-cracking has been covered previously [15, 64]. This synopsis has been used to explain the need for the post-failure control of the shell elements in the past. However, the results of the force-based failure suggest that such an approach must be adopted for the interlaminar spotwelds to accurately consider the shear deformation during a tube crush simulation. Essentially, it has been shown that under a shear loading, micro-cracks form (also known as hackles) which reduce the stiffness and strength of the matrix material [117]. Due to the degree of correlation in the ENF simulations presented in Chapter Six, this phenomenon was not identified as an issue.

In order to account for this deformation, the spotwelds were modified to strain elastically until a prescribed stress (the actual values used will be discussed shortly). At this point, it is hypothesised that the matrix may develop micro-cracks, which cause a reduction in stiffness. Accordingly, the elastic stiffness of the spotwelds is reduced to zero. The spotwelds are then free to continue straining until a prescribed strain limit is reached. In effect, the aim is to provide an elastic-perfectly plastic response, thus ensuring the correct degree of interlaminar deformation is considered (hence energy) before complete laminate separation.

Due to the formulation of material 100 (discussed in detail in Chapter Six), the spotweld material model, which was intended for metallic spotwelds and hence isotropic materials, many of the elastic material input parameters must be isotropic. Subsequently, the only way to consider the micro-cracking damage is to define an isotropic yield stress and maximum strain limit. Once the yield stress is reached, in any direction (normal or shear), the stiffness of the beam is

reduced to zero and the beam will continue deforming until the prescribed maximum plastic strain. It should be noted that ideally, the Young's modulus should also be specified anisotropically as the normal and shear response of the matrix is unlikely to be identical.

Difficulty was encountered in selecting an appropriate yield stress given the anisotropic response of the materials. The calculated values of normal and shear interfacial failure force had to be converted into a single isotropic yield stress. In the Toray simulations, the values of the normal and shear interlaminar failure forces were very similar (75 and 78N respectively), yet in CFRM, the optimum values were further removed (38 and 70N respectively). Previous discussion highlighted that the energy absorbed by a Mode I delamination could be accurately reproduced by a force-based approach (and little deformation occurred prior to failure). This implies that the majority of the interlaminar energy is absorbed through the Mode II deformation and that the yield stress should be derived from the shear failure force alone. However, as discussed in Chapter Six, under a pure Mode II loading, the spotweld experiences both normal and shear loads. Using either the normal or shear failure force alone to derive the yield stress would be erroneous, particularly when the opposite load case was encountered. Consequently, a compromise was found by averaging the normal and shear failure forces. This value was then converted to stress – in this case, the yield stress. For CFRM, the yield stress was 85.48MPa while for Toray, a value of 117.89MPa was used.

As mentioned, under a Mode II loading, both axial and shear loads are placed on the spotweld. An investigation into the relative contribution of the axial component on a pure Mode II loading showed that a perfectly plastic response (no plastic hardening/softening) provided the best response. An arbitrary strain

limit of 50% was selected for both the CFRM and Toray materials. Like the post-failure strength and strain controls in material 58, this value must be calibrated and a value of 0.5 is designed to simply demonstrate the concept. The input deck for material 100 used in the CFRM and Toray simulations are shown in Table 8.1 and Table 8.2, respectively. The values ‘*NRR*’ and ‘*NRS*’ must be input for the spotwelds to initialise, and are set very high. Note that ‘*FS*’ is now set to 1.0 denoting a stress-based failure.

Table 8.1. Material 100 control card for CFRM with strain-control values.

*MAT_SPOTWELD_DAMAGE-FAILURE								
\$\$HMNAME PROPS 100spotweld								
\$\$	MID	RO	E	PR	SIGY	ET	DT	TFAIL
	100	120010.3E+009	0.3050	85.48E+06				
\$\$	EFAIL	NRR	NRS	NRT	MRR	MSS	MTT	NF
	0.5	400E+06	400E+06					25.0
\$\$	RS	OPT	SIGKF					
		1.0						

Table 8.2. Material 100 control card for Toray with strain-control values.

*MAT_SPOTWELD_DAMAGE-FAILURE								
\$\$HMNAME PROPS 100spotweld								
\$\$	MID	RO	E	PR	SIGY	ET	DT	TFAIL
	100	15009.96E+009	0.0500	117.8E+06				
\$\$	EFAIL	NRR	NRS	NRT	MRR	MSS	MTT	NF
	0.5	400E+06	400E+06					25.0
\$\$	RS	OPT	SIGKF					
		1.0						

## 8.2 Results

As was the case earlier, the focus of this work was on achieving the correct behaviour in the flat-platen simulations; these results are again presented first.

### 8.2.1 Flat-platen

#### 8.2.1.1 CFRM

The results of this simulation are significantly improved. Large portions of the spotwelds now remain in the simulation following the crush zone leading to a higher bending stiffness in the fronds and consequently, higher loads are required to continue the crushing process. As the spotwelds are not included in

a contact card, they are able to pass through other elements in the model (all except other spotwelds; such a penetration causes the simulation to cease). The central wall crack spotwelds are only removed approximately 0.8mm from the crush platen, or approximately midway through the height of the debris wedge.

The overall visual behaviour changed noticeably on the outer and innermost layers only. In these layers, the tight radius of curvature through the crush zone, combined with the added stiffness from the now present spotwelds, causes a significant degree of material failure and element elimination. The selection of a finer mesh would be likely to have allowed a better representation of the curvature. This would have allowed a larger number of shell elements to remain through the crush zone and the number of spotwelds joining these regions would have remained high. The behaviour of the remaining laminae are near-identical to that observed in the original simulation. The spotwelds between various layers can be seen easily in Figure 8.1, taken at the completion of the simulation.

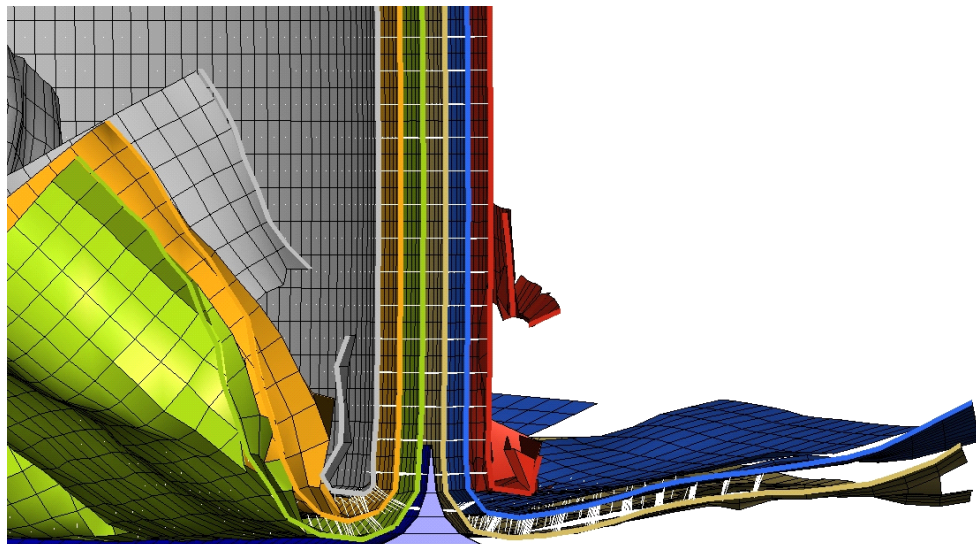


Figure 8.1. Image of simulated CFRM crush zone at completion showing the number of spotwelds remaining after passing the crush zone.

The improvements made to the spotweld response were clearly evident in the load-displacement response. The simulation predicted a steady-state load of 85.8kN compared to the experimentally obtained 94.5kN (the original model predicted a value of 25.5kN). The load-displacement responses are shown in Appendix Six.

### 8.2.1.2 Toray

Again, the results of this simulation have been significantly improved. A significant number of spotwelds pass through the crush zone leading to a higher degree of material deformation, visible as deformed shell elements. Other than this, the overall visual behaviour did not change noticeably from that shown earlier in Figure 7.6. Figure 8.2 shows an image taken at the completion of the FE simulation.

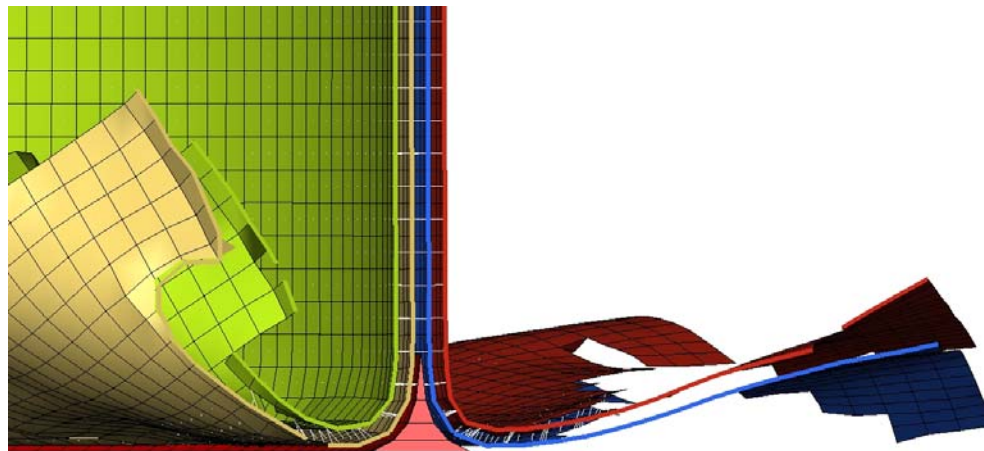


Figure 8.2. Image of simulated Toray crush zone at completion showing the number of spotwelds remaining after passing the crush zone.

The increased front stiffness and material damage resulted in a predicted steady-state load of 45.8kN, compared to the experimentally obtained 46.6kN, a 2% error. The load-displacement responses are shown in Appendix Six.

## 8.2.2 Plug Initiator Simulations

### 8.2.2.1 CFRM

#### *5mm Radius*

Implementation of the strain-controlled spotweld approach did not improve the observed failure mode in this test. However, as was discussed previously, it was not possible to achieve the experimental failure mode, despite repeated attempts. The failure mode produced here closely resembled the simulated failure mode reported earlier in 7.1.2.2, with the exception that the fronds were observed to curl, due to them remaining laminated. This resulted in a large degree of damage in the laminae closest to the plug. This behaviour was not observed experimentally. The simulated load increased from 18.4kN to 59.3kN. However, this is still well below the experimentally recorded value of 145kN, demonstrating the importance of predicting the correct failure mode. An image of the failure mode produced by the strain-controlled spotweld response can be seen in Figure 8.3.

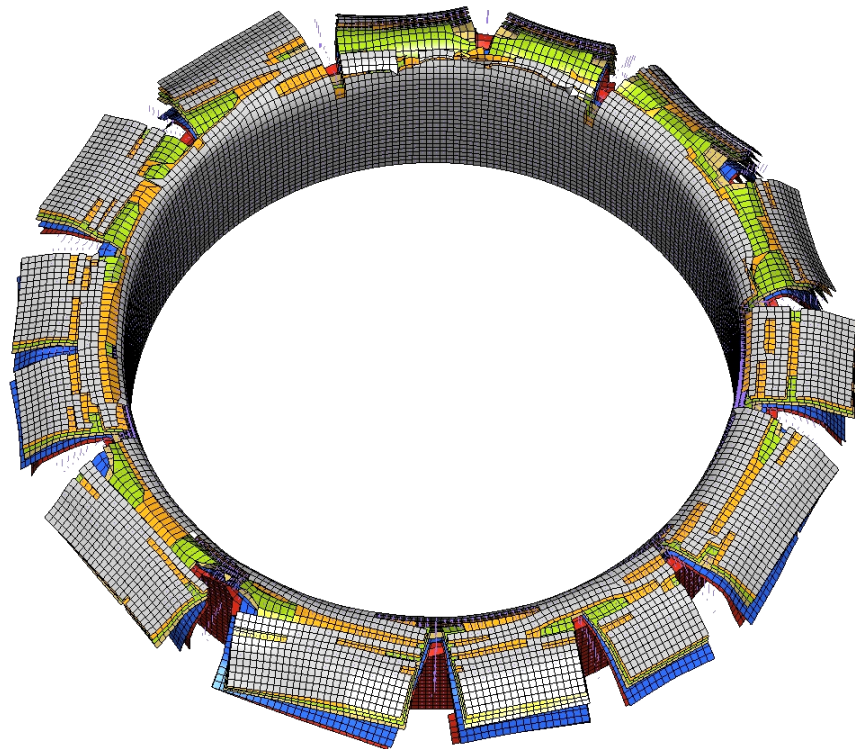


Figure 8.3. Image of simulated response of CFRM tube crushed on 5mm plug initiator with the strain-controlled spotwelds.

It is unclear what can be done to reproduce the experimental failure mode. However, in order to achieve the steady-state load of 145kN, there is a need for the majority of shell elements to strain under circumferential tension. Unfortunately, in the simulation, some elements reach the strain limit and are eliminated allowing surrounding elements to relax. To avoid this, the post-failure strength was increased to 90%, forcing all the elements to strain. Likewise, the strain to failure was increased to 90% to maximise the energy absorbed. However, this resulted in a change of failure mode, as shown in Figure 8.4. These changes did increase the steady-state load to 103.8kN.

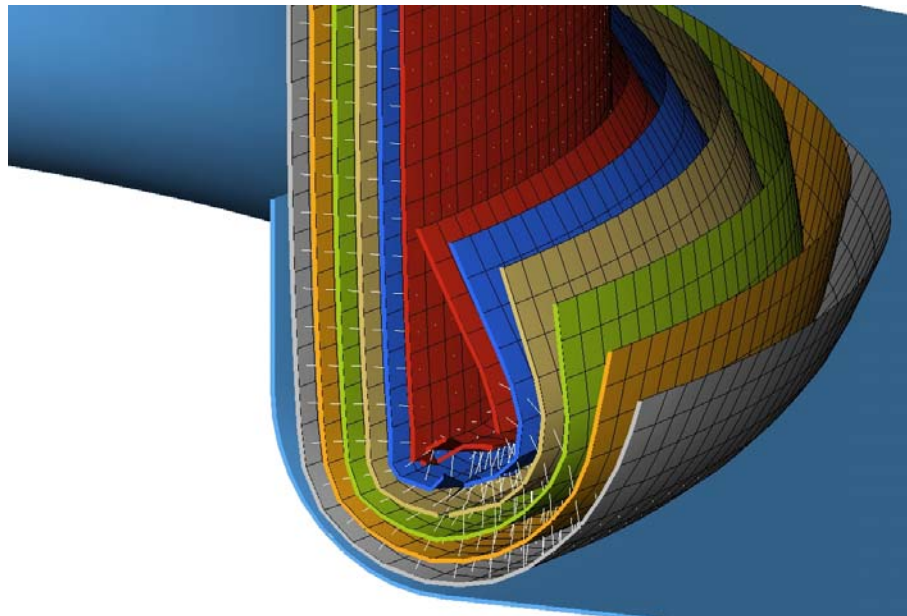


Figure 8.4. Cut-away image of the simulation of a CFRM tube crushed onto a 5mm radius plug initiator in which an attempt was made to achieve the experimental failure mode and/or steady-state crush load.

#### *7.5mm Radius*

The strain-controlled spotweld behaviour resulted in a change in the failure mode of this simulation. Rather than develop clear axial tears and fronds, this simulation produced a failure mode near-identical to that shown for the CFRM tube crushed on a 10mm radius plug initiator. Sections of the tube wall would snap off causing the large oscillations that can be observed in the load-

displacement response, the curve for which can be seen in Appendix Six. This resulted in an average load of 22.7kN. An image of this behaviour can be seen in Figure 8.5.

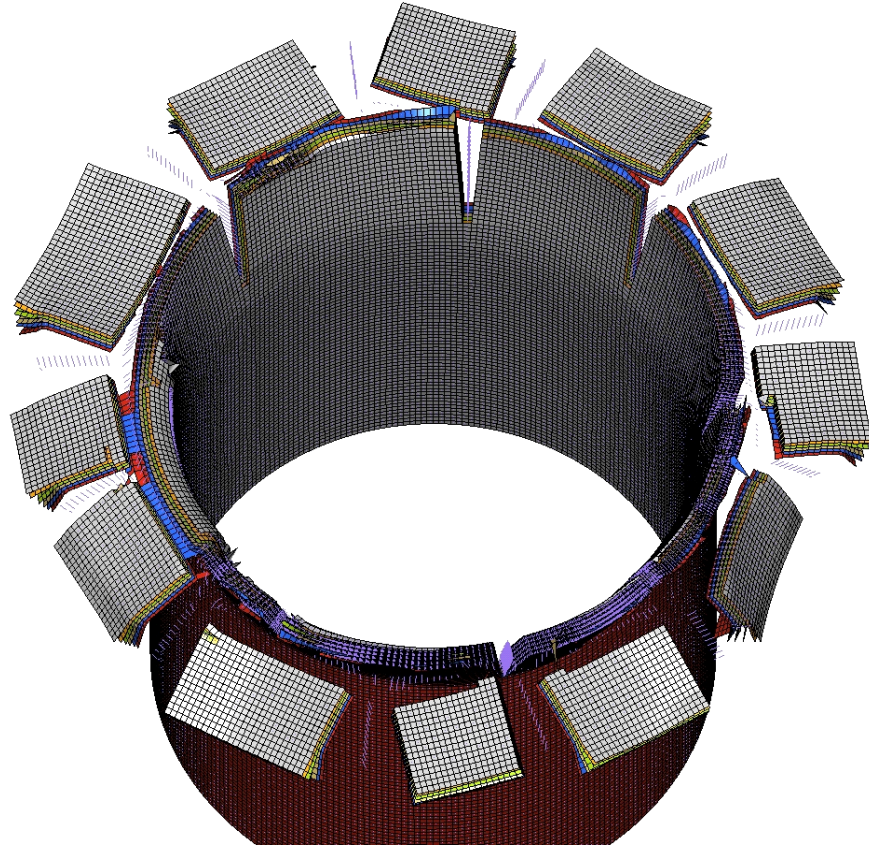


Figure 8.5. Image of the simulated response of a CFRM tube crushed onto a 7.5mm plug initiator showing the change in failure mode.

Given the increased frond strength (due here to the strain-controlled spotwelds not being removed immediately), the change in failure mode was almost certainly a result of the tensile post-failure properties (post-failure hoop strength) being lower than occurred experimentally. This caused the axial tears to propagate rapidly, resulting a large bending moment on the fronds which ultimately lead to them snapping. In order to achieve the correct failure mode in this simulation, the tensile post-failure strength must be increased in order shorten the axial tears and develop higher hoop stresses which force the material to deform through the plug's radius. A simulation was run to this

effect (with '*SLIMTx*' set to 0.7 instead of 0.2) and the steady-state load rose to 51.2kN with the failure behaviour shown in Figure 8.6. With a further increase in the tensile post-failure strength, it is likely that the desired behaviour and load could be achieved.

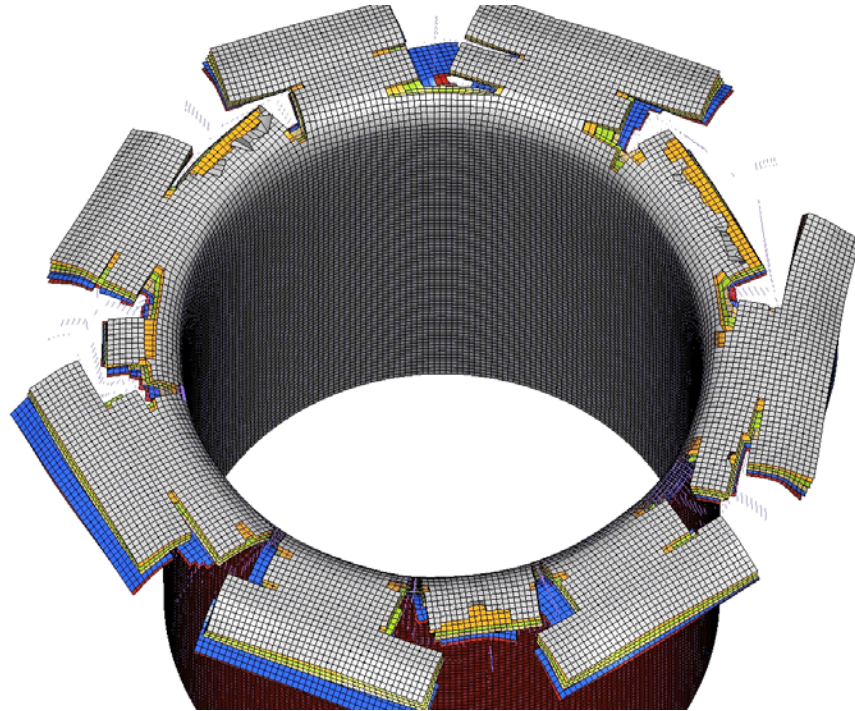


Figure 8.6. Image of the simulated response of a CFRM tube crushed onto a 7.5mm plug initiator showing the improved failure mode with '*SLIMT*', the post-failure strength in tension, equal to 0.7.

### *10mm Radius*

This simulation maintained the failure behaviour observed in the earlier test. Accelerated axial tearing caused bending of the fronds which initiated circumferential tearing. These tears allowed the fronds to snap away from the tube without passing through the crush zone. As was suggested earlier, very little interlaminar damage occurs during this failure mode and consequently, improvements made to the spotweld behaviour had little effect on the axial crush load. An image of the simulated failure mode can be seen in Figure 8.7.

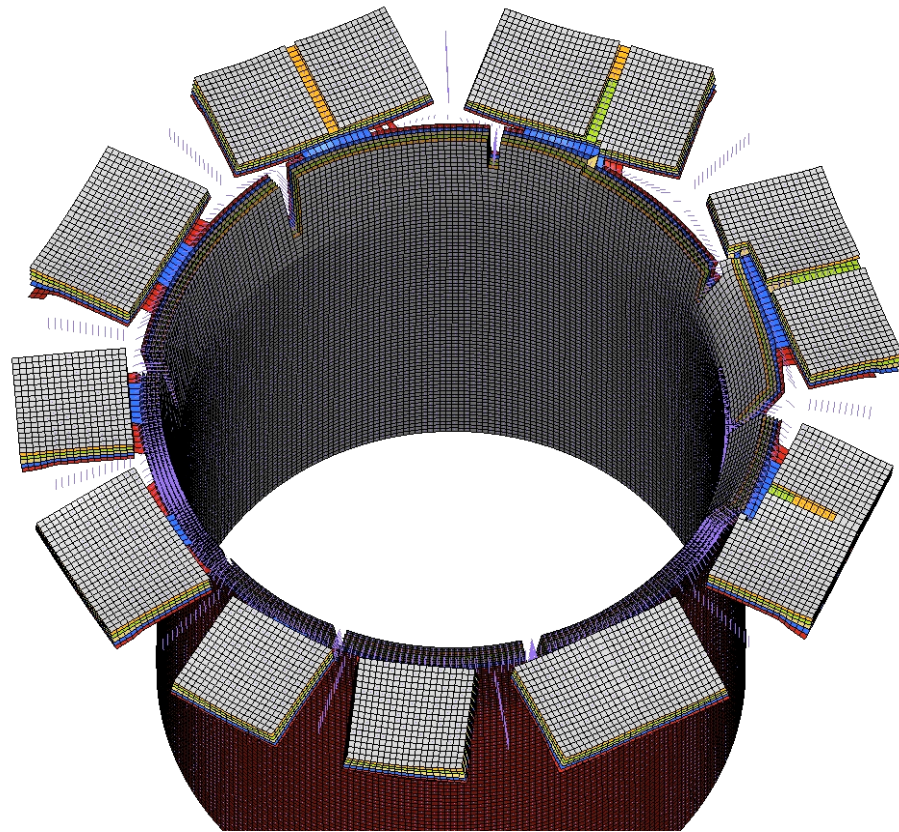


Figure 8.7. Image of the simulated response of a CFRM tube crushed onto a 10mm plug initiator.

Re-examination of the experimental failure mode showed that several of the experimental fronds appear to remain partially intact and possess a degree of curvature. This suggests that while several fronds do separate from the tube, a small amount of damage does occur in the remaining fronds. In the essentially ‘perfect’ simulation, the axial tears and circumferential tears propagate at a similar speed regardless of the position around the tube. As a result, the load reaches such a point that all the fronds fail simultaneously, and a corresponding reduction in load is observed. The imperfections inherent to experimental testing allow several fronds to separate while others, now under lower stress due to the removal of the aforementioned fronds, can deform through the crush zone. It is unclear whether this experimental failure mode could be achieved given the perfect nature of the FE model.

In any case, predicted average load rose to 10.46kN (for the period 20-40mm). Comparative load-displacement curves can be seen in Appendix Six.

### 8.2.2.2 Toray *5mm Radius*

A similar behaviour was observed in this simulation as was reported for the original spotweld approach presented earlier in 7.1.2.3. After bending through the plug radius, the material splayed into 10-12 fronds with a degree of transverse shearing evident. A significant number of the spotwelds remain in the model subsequent to passing the crush zone, although most of the elements within the central region were removed. Figure 8.8 shows a cross-section of the crush zone and the experimental and predicted delamination. The simulation predicts a single large delamination while a high degree of deformation can be observed in the surrounding interlaminar regions.

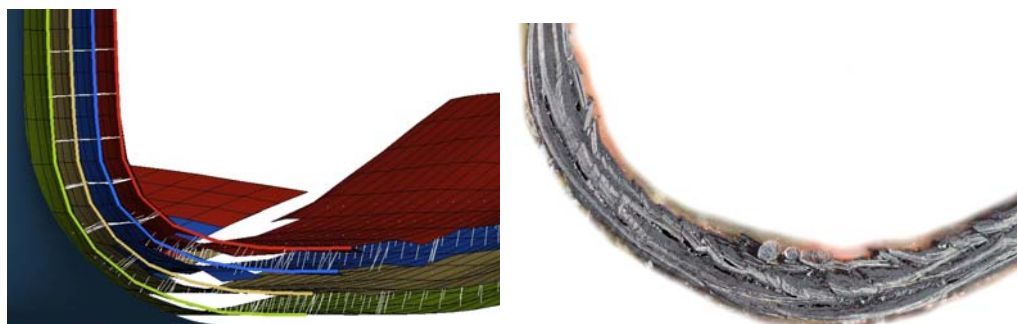


Figure 8.8. Simulated (left) and experimental (right) cross-sections of Toray tube crushed on 5mm radius plug initiator showing the improvement in the predicted delamination response.

Close examination of the experimental sample showed a reasonable degree of compressive damage on the outermost layer while little damage was observed on the layer nearest the plug. Likewise, the simulation shows that the compressive stress on the outermost layer exceeds the ultimate strength, while internally, the stresses are a fraction of the ultimate strength. This can be seen in Figure 8.9 and was not evident in the earlier simulations which utilised the standard force-based spotweld methodology.

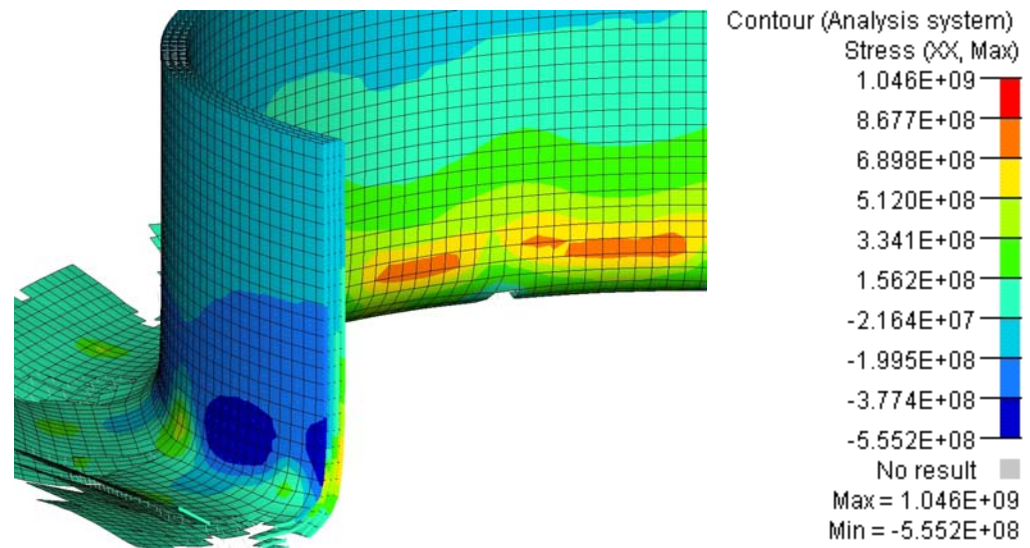


Figure 8.9. Simulated cross-section of Toray tube crushed on 5mm radius plug initiator showing the axial stress levels which caused damage on the external layer in experimental tests.

The strain-controlled spotweld simulation increased the steady-state load to 25.2kN, 4.9kN above the experimental figure of 20.3kN.

#### *7.5mm Radius*

Improvements made to the spotweld methodology resulted in this simulation predicting a significant change in the failure mode. A much higher degree of transverse shearing was predicted here than in the original simulation. An image of the failure mode can be seen in Figure 8.10.

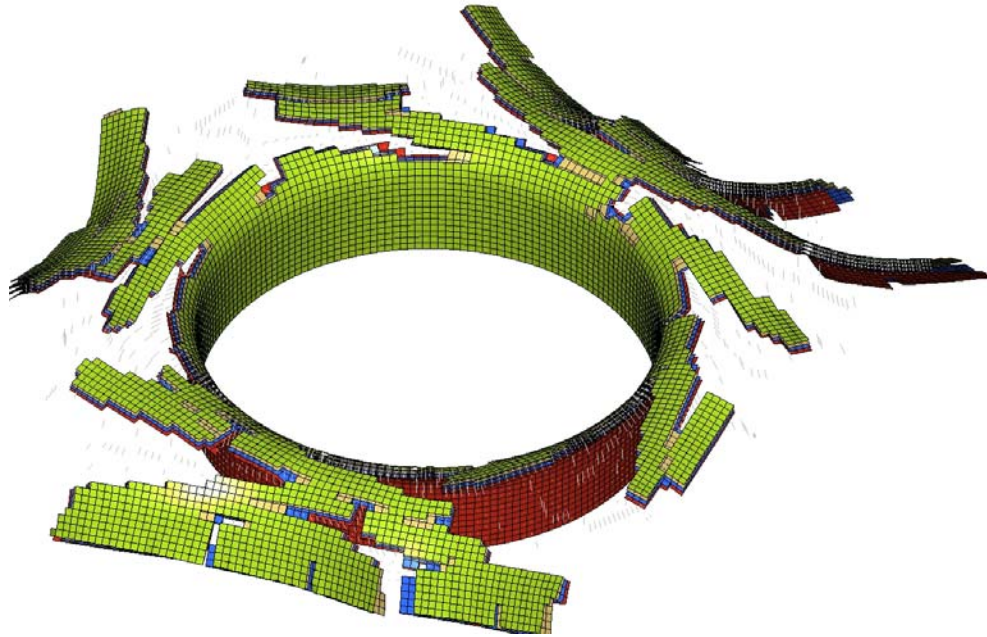


Figure 8.10. Image of the simulated response of a CFRM tube crushed onto a 7.5mm plug initiator showing the high degree of transverse shearing and the change in the predicted failure mode.

As the leading elements reach their strain limit, small axial tears develop allowing the neighbouring elements to draw away, relaxing the stress. In doing so, a shear load is introduced on the elements along the diagonal from the location of the eliminated elements. Evidently, the increased hoop stresses produced by the increased interlaminar strength has resulted in the shear ultimate strength, and subsequently the strain limit being reached which lead to the damage pattern observed. In any case, the strain-controlled spotweld behaviour increased the predicted steady-state load to 19.3kN.

It is unclear what steps could be taken to avoid the behaviour produced here as the post-failure strength in shear was already 100%. As a result, the question must be raised as to whether the characterisation testing, reported in Chapter Three, captured the correct shear behaviour of the woven Toray material. If the experimental shear strength reported in Chapter Three was lower than the material is capable of, then the high degree of shear failure observed in the simulations would be expected. In order to demonstrate this effect, a simulation

was completed with the ultimate shear strength increased 50% over the experimentally recorded value reported in Chapter Three (150% = 142.5MPa). This simulation showed a noticeable improvement in the failure mode correlation, as can be seen in Figure 8.11. Importantly, this change reduced the steady-state load to 17.9kN (compared to 15.4kN produced experimentally) indicating that a lower degree of material deformation occurs when the correct failure mode is produced.

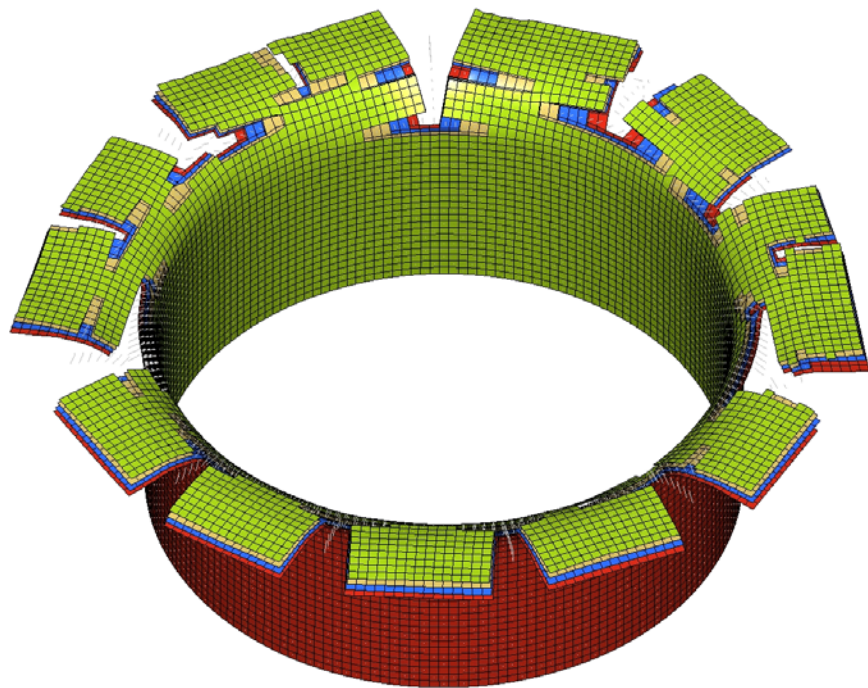


Figure 8.11. Image of the simulated response of a CFRM tube crushed onto a 7.5mm plug initiator showing the improvement in the predicted failure mode by increasing the ultimate shear strength by 50%.

It is unclear, why or even if the experimental shear performance was incorrectly captured. One hypothesis is that during the experimental Iosipescu shear test (1-2 direction), the initial yield and subsequent sustained stress is primarily a result of matrix cracking. Examination of the sample following the test shows the  $0^\circ$  fibres remain almost completely undamaged with matrix cracking running parallel to the  $0^\circ$  fibres. These cracks extend only until the subsequent junction with  $90^\circ$  fibres in the weave. Given that the cracks are

arrested by the 90° fibres, it is expected that the shear stress would have continued to rise as the axial load on the 0° fibres increased, had a larger displacement been possible. As discussed in 3.2.5, the testing rig repeatedly reached its maximum travel. Subsequently, given that the tube crush experiments showed high levels of fibre breakage, yet the coupon test did not, it can only be assumed that the shear strength values employed in the simulations were distinctly lower than they should have been.

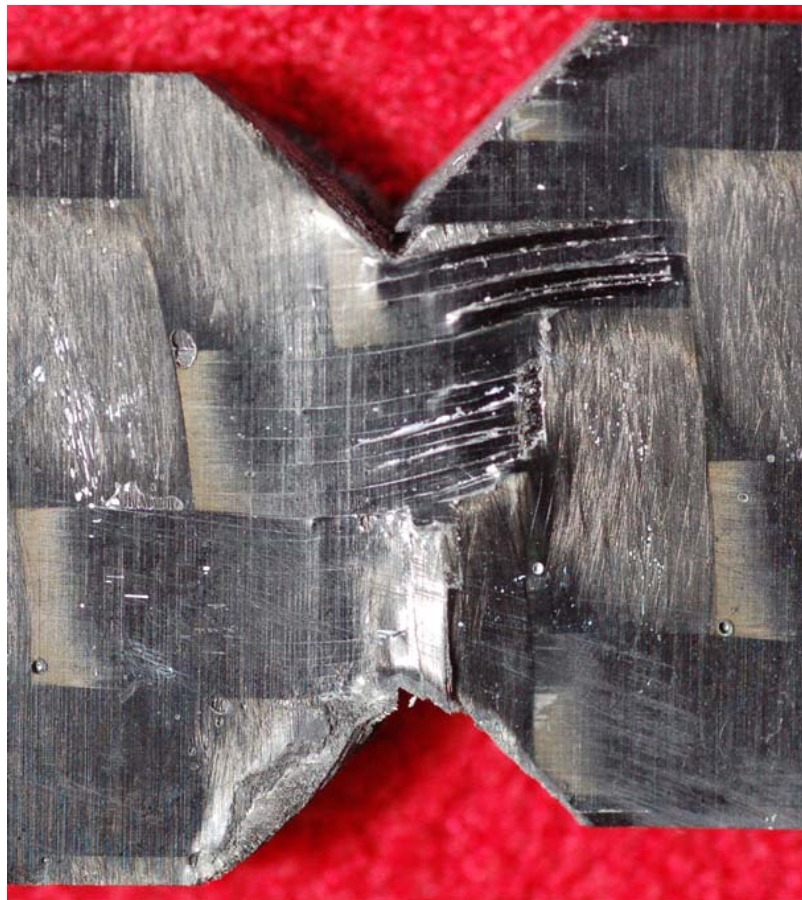


Figure 8.12. Image of shear 1-2 sample following test showing matrix cracking and altered longitudinal fibre alignment. No signs of longitudinal fibre breakage can be seen.

### *10mm Radius*

Improvements made to the spotweld methodology caused this simulation to predict a significant change in the failure mode, similar to that presented in the Toray 7.5mm radius plug crush. As was the case above, rather than splay into numerous fronds with a small degree of transverse shearing, this simulation

developed a much larger degree of transverse shearing. An image of the behaviour can be seen in Figure 8.13.

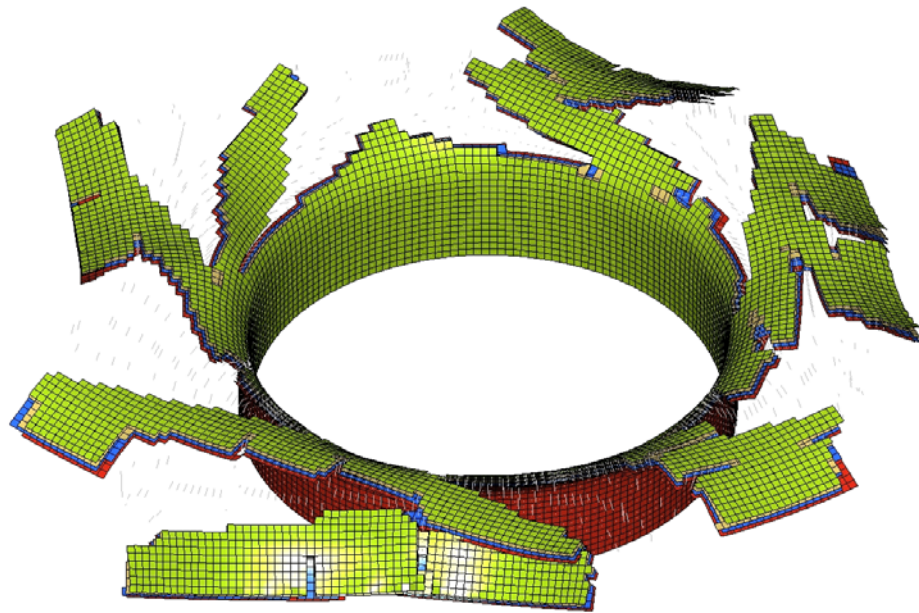


Figure 8.13. Image of the simulated response of a CFRM tube crushed onto a 10mm plug initiator showing the change in the predicted failure mode.

It is likely that the principal determinant for the change in failure mode is identical to that proposed for the Toray 7.5mm radius plug initiator simulation presented above. However, no additional simulations were run to confirm this.

The strain-controlled spotweld response resulted in an increased steady-state load of 15.9kN, 2.0kN above the experimental value of 13.9kN. Like the 7.5mm radius plug simulation, if the correct behaviour had been predicted, the steady-state load would be closer to the experimental value.

### 8.3 Discussion

In Chapter Seven, a deficiency in the force-based delamination modelling methodology was highlighted. Despite correlating well in ENF simulations, complete delamination within the fronds was repeatedly predicted. Analysis of the experimental crush zones showed that while high levels of cracking were

observed, complete separation was rare. It was concluded that a similar strain-softening approach, similar to that used in material 58, be used for the interlaminar material.

The purpose of this chapter was to further develop the delamination modelling approach to account for the micro-cracking and deformation that occurs throughout the fronds in tube crush experiments. To do this, a yield stress and plastic strain limit were defined such that an elastic-perfectly plastic response was achieved. The results of the strain-controlled spotweld response are shown graphically in Figure 8.14.

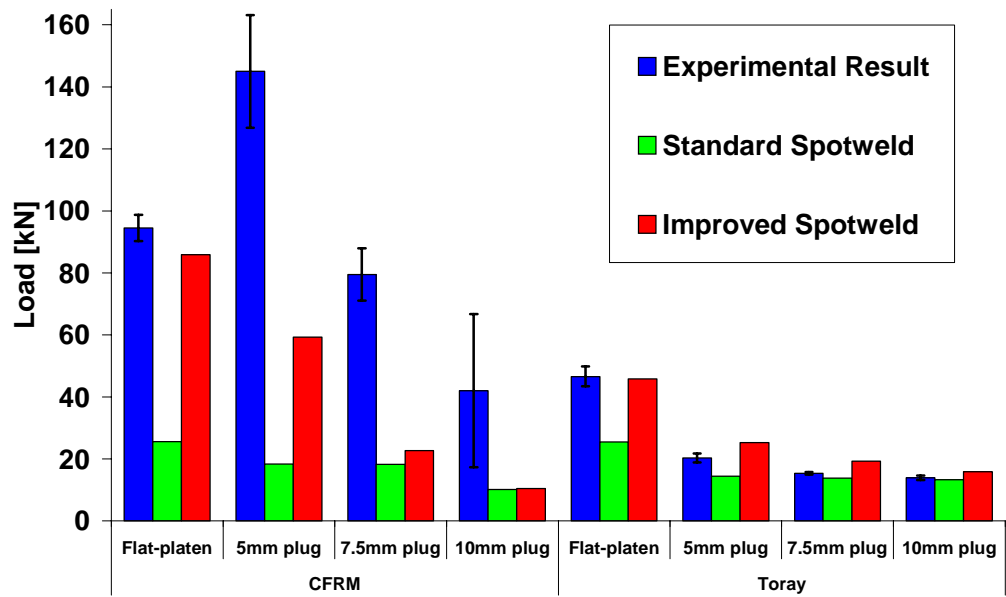


Figure 8.14. Summary of simulated results, with force-based interlaminar spotweld behaviour and strain-controlled interlaminar spotweld behaviour, compared to the experimentally recorded values for various tests and materials.

It should be reiterated that model development focussed on achieving accurate behaviour in flat-platen simulations in particular. The selection of a spotweld strain limit of 50% was arbitrary.

If we again consider each material independently, we see the same trend in the steady-state loads, despite significant changes in the failure mode in several of

the simulations. Significantly, it was not possible to achieve the experimental failure mode observed in the CFRM 5mm radius plug initiated tube crush, nor was it possible to achieve the required steady-state load. The defining characteristics of the failure modes observed in the remaining tests were reproducible. However, the changes made to the spotweld behaviour uncovered a need for the material parameters to be recalibrated in order to correct the failure behaviour in several cases.

In the case of the flat-platen simulations, a good estimation of the steady-state load was produced. Likewise, a reasonable visual correlation was produced in both cases suggesting that the relative contributions of the energy absorbing mechanisms were approximately correct.

For the Toray plugs, the steady-state load was generally over-estimated suggesting that the response of either the material or the spotwelds has been overestimated; in fact, it appears likely that both are true. As mentioned previously, through-thickness shear cracks were observed in the outermost layers of the experimental Toray specimens. This loading cannot be considered by the shell elements, resulting in an over-prediction of the tube wall strength. This was evident in the high steady-state loads shown in Chapter Seven. Additionally, it is likely that the strain-controlled spotweld behaviour is over-estimating the strength of the interlaminar material, causing the change in failure mode for the 7.5 and 10mm plugs, further evidenced by the good visual correlation achieved in Chapter Seven. Subsequently, comparison of the experimental matrix failure strains of the selected materials indicates that the CFRM matrix is more ductile than the Toray matrix. The CFRM matrix yielded at 2.2% compared to 0.79% for the Toray. Consequently, assuming the spotweld strain limit of 50% is approximately correct for the CFRM, it can be

suggested that the Toray strain limit should be 18.25%. Repeating the Toray simulations with this spotweld strain value resulted in the correct prediction of the failure behaviour in all cases. Likewise, a slight drop in the steady-state load was predicted improving the correlation in all but the flat-platen test. A comparison of the 10mm radius plug initiated simulations can be seen below in which the only change was the reduction in the spotweld strain limit from 0.5 to 0.1825.

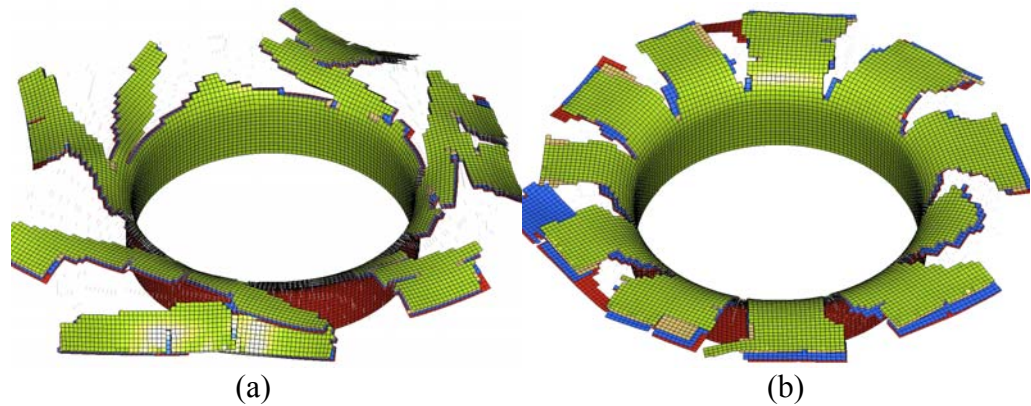


Figure 8.15. Comparison of simulated failure modes produced by Toray tubes on a 10mm radius plug initiator with a spotweld strain limit of (a) 0.5 and (b) 0.1825.

A similar scrutiny of the CFRM simulations indicates that the energy absorbed during the post-failure behaviour of either the tube material or the spotwelds was underestimated. It was necessary to increase the tube material's post-failure strength in the CFRM 7.5mm radius plug simulations (with strain-controlled spotwelds), in order to achieve the desired failure behaviour. Subsequently, given that these plugs failed in an incorrect failure mode once the interlaminar strength was increased, it is thought that the post-failure strength of the material was underestimated.

In all cases, the improvements made to the spotwelds more closely represent the behaviour of the interlaminar material. Large numbers of spotwelds are now maintained throughout the crush zone, keeping the fronds intact, adding to

the bending stiffness and consequently providing, on occasion, a significant increase in steady-state load. Small areas of localized delamination are now clear, together with occasional interlaminar separation, as shown in Figure 8.16 below.

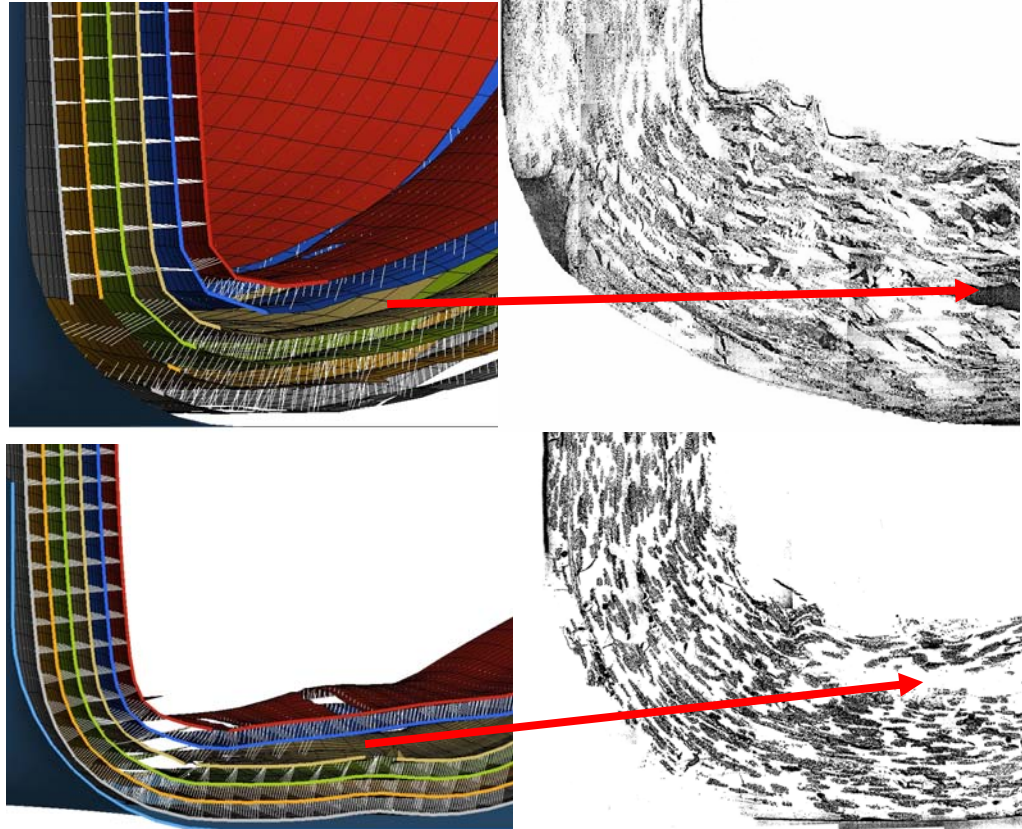


Figure 8.16. Images of simulated (left) and experimental (right) crush zones of CFRM tubes crushed on 5mm (above) and 7.5mm (below) radius plug initiators. Comparable delaminations can be seen (regions devoid of spotwelds in the simulation). Note: crush zone for 7.5mm radius plug was taken from simulation using higher '*SLIMIT*' to induce improved failure behaviour – refer to 8.2.2.1. Experimental images taken from [54].

As a consequence of the strain-controlled spotweld method being based on an isotropic approach, it should be noted that the energy absorbed by the central wall crack is heavily over-estimated. In the case of CFRM, given the  $G_{IC}$  value of  $661\text{J/m}^2$ , the spotwelds which form the central wall crack would only be required to strain approximately 2.4%. This could not be avoided with the current material model (material 100). However, the ability to include

anisotropic stiffness and failure values, including maximum plastic strain limits would allow more realistic control of the interlaminar material behaviour.

A high degree of calibration must be exercised with the approach presented, which allows a modeller to tune each model for the specific failure type that is expected; making this methodology non-predictive. It remains to be seen whether a set of values for a given material, will work in a variety of loading scenarios. The CFRM simulations presented here suggest that this is not the case while Toray simulations indicate that it is possible.

This methodology was relatively computationally expensive. The numerous, stiff spotweld elements resulted in a smaller timestep which, when combined with highly deformed shell elements, resulted in simulation durations of up to 124 hours for 40mm of crush displacement on the full-length CFRM tubes crushed on 10mm plug initiators with the yield-based spotweld failure. However, typical simulations took between 3 hours (no spotwelds in a Toray tube crush on a 5mm radius plug) and 30 hours (strain-controlled spotwelds in a 35mm section CFRM flat-platen crush). It should be noted that only minimal effort was given to expediting the simulations as the highest possible degree of accuracy was a priority. Furthermore, no results have been filtered, standardised or normalised and are presented in an ‘as-received’ state.

The simple approach to delamination modelling used in this work has successfully included the interlaminar shear stiffness and demonstrated an accurate reproduction of the failure behaviour in coupon tests and, after modification, tube crush simulations. The final methodology presented, allows FE modellers to calibrate the failure behaviour to any requirements, allowing a

detailed FE examination of the failure behaviour, inclusive of the failure mechanisms pertinent to the crushing process.

## 9 Conclusions and Further Work

The ability of composite materials to form the crash structures in modern vehicles has been clearly demonstrated, yet very few manufacturers have exploited their benefits. Fundamentally, this has been due to the associated cost of producing composite components – both in terms of manufacturing cost and the inability to reproduce the experimental crush behaviour through computational methods. Hence, the aim of this thesis was to develop enabling technologies that can reduce the associated cost of composite component manufacture. This aim was achieved by;

- Reducing the cost of manufacture through shorter cure cycles,
- Providing industry with further information on the performance of composite materials in crash structures,
- Providing advanced techniques for the simulated reproduction of the behaviour of composite materials in crash structures.

These goals were accomplished by completing the following tasks;

- Develop a manufacturing method for accelerated curing of composite tubular structures,*
- Characterise the experimental crush performance of Toray G83C,*
- Develop a force-based delamination modelling methodology that accurately reproduces the interlaminar stiffness,*
- Develop a holistic modelling methodology of axial tube crush which includes the features pertinent to the crushing process,*

*-Validate the performance of the combined delamination and tubular modelling approaches through simulation of experimental axial tube crush tests.*

## **9.1 Thesis Summary**

---

A review of related literature resulted in the formation of several conclusions;

- The experimental behaviour of composite materials is difficult to capture as many of the controlling mechanisms are interactive. This makes classification of the response to a specific variable subjective.
- The advantages of the Quickstep™ process over traditional curing techniques are significant. The enhanced heat-transfer and temperature control together with lower running costs make it an obvious area for further development.
- A number of modelling approaches, aimed at the accurate simulation of composite crush, have been investigated in the past but many are incapable of capturing all aspects of the true experimental behaviour. The approach best suited to this task relies heavily on the chosen delamination modelling approach.
- The simple force-based methodology offers the best delamination modelling solution, given the computational cost and material characterisation issues of comparable approaches. However, calibration of the behaviour is required.

The two materials that were selected in this work were Toray G83C carbon/epoxy and CFRM glass/polyester. Chapter Three presented specific information on these materials, together with the results of a characterisation

study in which the mechanical properties of the Toray G83C 2x2 twill were presented. The chosen tests were required to satisfy the input requirements of the subsequent modelling study. The properties of CFRM are readily available through numerous publications from the University of Nottingham. A new technology, DSP, was tested and found to produce inconsistent and sometimes erroneous results, despite contribution from the software developer. Future users must be sure to examine the software the software output to ensure reasonable results have been produced.

A tooling system, developed for use specifically with the Quickstep™ process demonstrated the reduction in curing time possible with higher heating rates. Using Toray G83C, a typical autoclave cure cycle would take around 130 minutes while Quickstep™ completed the cure cycle in just 7 minutes, simultaneously increasing the glass transition temperature. Similar reductions in curing time can be achieved for any appropriate composite material. Significantly, this process has demonstrated that the curing activity can be removed as the rate-limiting step, moving the focus to the development of quicker lay-up techniques. This technology will provide automotive manufacturers with the capacity to prototype or implement such structures in vehicles more economically.

The relatively high porosity values observed in the tubes could be reduced through the use of automated material wrapping, or as a minimum, through increased pressure during material application. The use of a single curing tool has limitations on the production rate and steps to develop a larger-scale production approach are underway. This work has resulted in the submission of an international patent application [128].

Toray G83C carbon/epoxy, in general, is well-suited to applications in crashworthy structures. The SEA values observed in testing within the expected range for carbon/epoxy composites. However, a clear benefit is the significantly shorter cure times required by this material (3 minutes at full temperature).

LS-DYNA, an explicit software code, was used to develop a holistic modelling methodology which included the features pertinent to the composite tube crushing process. With the multi-shell approach selected, it was evident that the performance of the delamination model would be critical to the success of the model. The literature review revealed that the popular ‘tying’ approach to the force-based methodology, though highly attractive due to its easy implementation, was unable to consider the interlaminar shear stiffness. A solution was found in the combination of beam elements and a metallic-spotweld material model, inclusive of anisotropic force-based failure.

This approach was utilised in Chapter Six and a high degree of correlation was demonstrated in simulations of the experimental 3-point bend, DCB and ENF tests. Consequently, this approach was deemed suitable for further application in larger structures as it adequately satisfied the requirements of accurate representation of the shear stiffness and the correct failure behaviour, and so, this delamination modelling approach was adopted in the multi-shell tube models. The inability to uncouple the normal and shear responses, under a pure Mode II loading, made calibration difficult.

Upon application in the multi-shell tube models, surprisingly poor results were observed given the correlation achieved in the coupon simulations. Comparison of the experimental and simulated crush-zones revealed that while

only small regions of localised delamination typified the experimental behaviour, the simulations generally predicted complete delamination even before the material passed the crush zone. It was concluded that the elastic force-based delamination model could adequately account for the small portion of energy absorbed through Mode I crack propagation. However, this same approach could not account for, nor reproduce the behaviour of, the interlaminar material under a Mode II loading where high levels of deformation lead to high levels of absorbed energy. In CFRM tests in particular, this deformation displayed the presence of only small shear cracks and an occasional complete delamination.

Since the ENF test indicated that this approach could accurately reproduce the Mode II failure, it must be suggested that the ENF test does not provide an adequate reproduction of the deformation experienced by the composite material as it passes through the crush zone. Effort was given to improving the Mode II behaviour by introducing a yield stress and plastic strain limit, in order to capture the effect of the shear hackles and micro-cracks, ensuring the correct delamination energy is absorbed. This modification displayed a considerable improvement in the predicted delamination behaviour and steady-state loads but also exposed the need for the material parameters to be recalibrated for the increased interlaminar strength.

Development of the rapid curing process for composite tubular structures, together with the findings of the simple, holistic modelling methodology, has provided further insight into the potential for these materials to form the crash structures in modern vehicles. With further development, faster cure times and higher production rates will be achieved, resulting in a significant drop in the end part cost. Similarly, a variation of the simple spotweld delamination

modelling approach was shown to provide a good reproduction of the experimental interlaminar behaviour, potentially reducing the need to prototype designs.

## **9.2 Conclusions**

---

Two main areas of work presented in this thesis were the manufacture and modelling of composites. Here, the conclusions of this work are presented.

### **9.2.1 Manufacture**

Work on the adaptation of the Quickstep™ process to curing tubular profiles showed that:

*This novel manufacturing technique can significantly shorten the cure cycle for any composite material system. The significant heat transfer rates can be achieved regardless of the material in use, leading to shorter heat-up and cool-down times.*

Work on demonstrating the experimental crashworthy capability of Toray G83C showed that:

*The combination of this quick-cure resin and the accelerated heating provided by the Quickstep™ curing process, demonstrated clear advantages for manufacture, yet no significant disadvantages in performance. The SEA results of this material were as-expected for a carbon-epoxy.*

### **9.2.2 Modelling**

The FE results show that;

1. *Provided appropriate steps are taken to dampen the resulting oscillations, a force-based spotweld method is a suitable representation of the delamination that occurs within the central wall crack or within any pure Mode I interfacial delamination.* The spotwelds accurately reproduced the DCB behaviour but more importantly, they reproduced the experimental central wall crack behaviour, which partly governs the failure mode in composite tube crushing.
2. *A force-based spotweld method to delamination modelling is not suitable to represent the interlaminar deformation observed in the experimental tube crushing work.* The fronds of experimentally crushed tubes display a high degree of interlaminar deformation together with shear micro-cracking, which were not reproduced by the force-based spotwelds, despite the accurate inclusion of the interlaminar shear elasticity. Instead, near-complete delamination was predicted before the crush zone. Subsequently, it was found that;
3. *The deformation observed in the fronds of experimentally crushed composite tubes is not equivalent to the Mode II loading produced in ENF tests.* The common method of validating a delamination modelling methodology through simulation of the ENF test is erroneous. Despite an accurate reproduction of the failure being achieved in the ENF simulations herein, significant flaws were observed in the Mode II interlaminar material response in tube models. It is suggested that a more representative test should be used to examine the validity of a delamination model before its application in tube crush simulations.

4. *Simple strain-control of the spotweld failure behaviour provides a good qualitative and quantitative correlation of the experimentally observed delamination.* Modification of the spotweld behaviour to account for the shear micro-cracking that occurs in tube crushing experiments resulted in a substantial improvement in the predicted steady-state loads in several tests. Note that a low level of interlaminar damage was observed in the remaining tests. Additionally, in the instances where the simulated failure mode was approximately correct, so too was the steady-state load. However a high degree of calibration was required. Ideally, the response should be determined from an experimentally obtained material property. The most obvious is the Mode II fracture toughness, though given point 3 above, the use of this property in delamination modelling, particularly where the energy absorption is a concern, should be carefully considered.
5. *While material 58 (an elastic damage model) has already demonstrated its usefulness in single shell models, here it was used successfully in a multi-shell model.* All but one failure mode was reproduced, and in that case, an extremely high level of deformation was evident. The input parameters give adequate control of the material.
6. *The holistic modelling methodology presented here requires a reasonably high degree of calibration, particularly in ascertaining appropriate post-failure strengths and strain limits.* In order to reduce the necessary calibration, effort must be given to developing experimental testing methods which can capture the post-failure properties of materials. Only one publication exists where an attempt has been made at characterising this response.

7. *Material 100, developed for metallic spotweld modelling, possessed several limitations in representing a composite material. More specifically, the limitations were the inability to specify the anisotropic elastic properties of the matrix ( $E_1, E_2, E_3$ ), and the inability to define anisotropic yield stresses and strains for the strain-controlled spotwelds.*
  
8. *Simulations of the axial crushing of composite tubes appear scarcely influenced by the accurate inclusion of the interlaminar stiffness. Far more critical is the realistic and accurate inclusion of deformation within the fronds and crush zone. The typical ‘tying’ approach to delamination modelling is unsuitable for representing the Mode II interlaminar deformation within the fronds, as the necessary degree of deformation is not considered.*

### **9.3 Further Work**

---

Preliminary validation work on the tube manufacture process has been performed here and the concept and its details have been presented (see also patent application [128]). However, for this process to achieve reasonable production rates and make it commercially viable, effort must be given to the design of a system in which multiple mandrels can be in operation simultaneously. Furthermore, attention must be given to minimising change-over time between cured and un-cured tubes.

The accelerated heating rates achieved with the Quickstep™ tube manufacture process, together with the shorter cure times needed for Toray G83C, and its ability to efficiently absorb energy in a simple  $[0^\circ/90^\circ]$  lay-up demonstrate the gains that can be achieved in this area. It is feasible that with further

development, even higher heating rates, shorter cure cycles and higher levels of energy absorption can be achieved, further improving the cost-to-benefit equation for automotive manufacturers.

The multi-shell modelling methodology presented includes the features pertinent to composite crushing, and its effectiveness was demonstrated. Furthermore, a good reproduction of the delamination behaviour can be achieved. Subsequently, the success of this approach in various applications, such as damage prediction in plates or tube bending, would be of interest.

Significant discrepancies were observed between the loading produced in the ENF tests and that observed in the fronds of the tube crush experiments; both Mode II delaminations. The representative nature of another testing method, such as the double-lap shear test, should be investigated. In this test, no pre-crack is present and matrix damage and deformation occur before complete delamination, a response akin to the loading within the tube's fronds.

Under a Mode II loading, the spotweld response is influenced by both the shear and axial components, making calibration difficult. Subsequently, attention should be given to developing a modelling approach in which these components can be uncoupled such that the shear properties exclusively control the Mode II response. Likewise, control of the interlaminar material behaviour must be uncoupled for best results. Ideally, a force-based Mode I failure, together with a strain-controlled Mode II failure should be considered. This can only be achieved if the uncoupling step is taken, allowing the strain-controlled shear material properties to control the Mode II response without influence from the axial component.

Finally, there remains a clear need to understand the post-failure response of composite materials, given that in these simulations, the majority of the energy absorbing deformation takes place in this regime. The ability to specify these values, based on experimental data would be invaluable.

## **A1 Finite Element Modelling of Metallic Tubular Crash Structures with an Explicit Code**

This paper was accepted by the 'International Journal of Vehicle Safety' in May, 2006 and the content presented here is 'as-submitted' with the format modified to be consistent with this thesis.

### **A1.1 Authors**

---

M. SILCOCK, W. HALL AND B.L. FOX

School of Engineering and Technology, Deakin University, Victoria, 3217, Australia

N. WARRIOR

School of Mechanical, Materials, Manufacturing Engineering and Management, University of Nottingham, Nottingham, NG7 2RD, UK

### **A1.2 Abstract**

---

Numerous experimental studies have been carried out to investigate the collapse of tubular metallic crash structures under axial compression. Some simple theoretical models have been developed but these often assume one type of progressive collapse which is not always representative of the real situation. Finite Element (FE) models, when further refined, have the potential to predict the actual collapse mode and how it influences the load-displacement and energy absorption characteristics. This paper describes an FE modelling investigation with the explicit code LS-DYNA. An automatic mesh generation program written by the authors is used to set-up shell and solid element tube

models. Mesh specification issues and features relating to the contact and friction models are discussed in detail. The crush modes, load-deflection characteristics and energy absorption values found in the simulations are compared with a reasonable degree of correlation to those observed in a physical testing programme; however improvements are still required.

### **A1.3 Introduction**

---

In recent years, automobiles have been required to satisfy strict legislation in relation to occupant safety and as a result, tubular crash structures are now commonly employed to absorb kinetic energy in frontal impact events. The most common structures currently in use are metallic (usually mild steel) tubes, which absorb energy by progressive plastic folding during the post-buckling phase of the collapse. Numerous experimental studies have been carried out on the post-buckling behaviour of these thin-walled structures under axial compression [30-34, 37] and some simple theoretical models have been developed [30, 32, 33]. These simple theoretical models often assume one type of progressive collapse which is not always representative of the actual behaviour. In parallel with these simple models, there has also been a recent shift towards simulating the crash behaviour by the Finite Element (FE) method [129-131].

One reason behind the move towards FE models is their potential to show how the structure collapses and how this influences the load-displacement characteristics, and hence, energy absorption. The move to FE has been made possible by recent developments made in commercial software codes and the dramatic improvements in computational power. Such developments have meant the successful simulation of the progressive collapse of tubular

structures can now be attained within a reasonable amount of computational time, and at a fraction of the cost of physical tests. Explicit FE codes differ from traditional implicit codes in that they do not require the frequent inversion of large stiffness matrices to evolve simulations in the time domain and therefore the number of calculations per time step (and computational cost) is significantly reduced.

In this paper the explicit code LS-DYNA [87] is used to simulate the crushing behaviour of mild steel tubular crash structures with a circular cross-section. This code was selected as it is widely recognised as one of the leading explicit codes. The findings, however, will be of interest to all FE crash analysts, not just LS-DYNA users. The intention of this paper is to evaluate the performance of the LS-DYNA code for predicting the crush modes of circular tubes, and associated load-displacement characteristics under quasi-static loading conditions. Both shell and solid element tube models are employed and the results discussed. A suitable modelling approach is developed and discussed in which both shell [129-131] and solid element tube models are considered and compared. Furthermore, the influence of various modelling parameters are tested and discussed. Future research will consider the collapse of composite tubular structures - for example, Continuous Filament Random Mat (CFRM). To benchmark the performance of the FE tube simulations, the numerical results are compared to those observed in a physical testing programme carried out at the University of Nottingham [31].

#### **A1.4 Physical Testing Programme**

---

Tubular test specimens were fabricated from commercially available circular section EN3B mild steel. Four different tube sizes and three specimens at each

size were considered resulting in a range of  $t/D$  (0.0239-0.0567) and  $D/L$  (0.253-0.632) ratios being tested. No noticeable defects were observed in the tubes, and the dimensional tolerances were as expected from such ‘off-the-shelf’ materials. The tubes were cut to 100mm lengths, and the top and bottom surfaces were machined flat to ensure that they were parallel. The specimen dimensions (wall thickness and diameter) were measured at three equidistant points around the perimeter of each tube. The mean dimensions were then calculated - see Table A1.1. In the table, the Specific Energy Absorption (SEA) measurements for each tube are also given and were calculated as the mean crush load divided by the mass per unit length of the specimen, *viz*

$$SEA = P_m \left( \frac{L}{m} \right) \quad (A1.1)$$

where  $P_m$  is the mean crush load,  $m$  is the mass and  $L$  is the length of the tube before crushing.

Physical tests were carried out on an Electronic Servo Hydraulic (ESH) frame with Instron 8500 control. The tubes were placed in vertical alignment between two horizontal platens in the test frame. The specimens were then quasi-statically loaded under axial compression at 10mm/min. Each specimen was crushed for at least half the tube length. This testing methodology ensured steady-state crushing was achieved. Load and displacement measurements were recorded during each test and results were stored electronically in ASCII-format data files.

Table A1.1. Specimen geometry for EN3B mild steel tubes.

<b>Tube Size (Designation)</b>	<b>Specimen</b>	<b>Outer Diameter, OD[mm]</b>	<b>Wall Thickness, t[mm]</b>	<b>SEA [kJ/kg]</b>
<b>(ST01)</b>	1	25.3	1.43	28.37
	2	25.2	1.41	28.08
	3	25.2	1.42	27.58
<b>(ST02)</b>	1	37.9	1.65	47.44
	2	37.8	1.70	47.24
	3	38.0	1.67	47.53
<b>(ST03)</b>	1	50.6	1.44	24.45
	2	50.6	1.43	23.38
	3	50.6	1.43	22.94
<b>(ST04)</b>	1	*	*	*
	2	63.2	1.51	18.34
	3	63.2	1.51	18.94

\* Data unavailable

The range of geometries used ensured that various crush modes were observed. Concertina (axisymmetric), diamond (asymmetric) and Euler buckling (catastrophic collapse) crush modes were observed in the physical testing.

### **A1.5 Finite Element Modelling**

Circular tube models were developed for analysis using the explicit software package LS-DYNA [87], a large deformation structural analysis code. One model was developed for each tube designation, i.e. tubes ST01(2), ST02(2), ST03(2) and ST04(2). The number in the brackets represents the specimen that was modelled given in Table A1.1. This identification method is used throughout this article. It was not deemed necessary to model every specimen as the variations in the wall thickness and diameter for each tube size were insignificant to the outcome of the simulations.

The LS-DYNA model descriptions were generated automatically using a MATLAB [132] program developed by the authors. The mesh generation program creates a tubular circular structure with a user-defined geometry and mesh specification which reduced the risk of any discrepancies between models and allowed rapid creation of the input decks for the various parametric studies. Two surfaces are routinely created to represent the horizontal platens in the test frame together with the relevant contact data. An example of the MATLAB input screen used to create a shell element tube (such as those presented in references [129-131]) is given in Figure A1.1. After selecting whether to use a shell or a solid tube model, a total of twenty five inputs are required. As a result, a ready-to-run ‘input deck’ can be created in less than one minute.

```

*****
ans =
*****TUBE MODELLING*****
ans =
*****
What is the DIAMETER of the tube [m]? 37.8e-3
What is the tube wall THICKNESS [m]? 1.7e-3
What is the LENGTH of the tube [m]? 100e-3
How many NODES around the the tube CIRCUMFERENCE? 49
How many LAYERS OF NODES in the LENGTH of tube? 41
ans =
Material Type 24, *MAT_PIECEWISE_LINEAR_PLASTICITY, with Strain Rate effects ignored.
What is the tube material? EN3B MILD STEEL
ans =
Shell Modelling, *SECTION_SHELL.
REDUCED [1] or FULLY INTERGRATED [2] shell elements? 2
ans =
FULLY INTEGRATED SHELL elements are assumed. HOURGLASS CONTROL is not needed
hourglass =
    0
How many INTEGRATION POINTS should be used?5
ans =
*****
ans =
*****CONTACT SURFACE MODELLING*****
ans =
*****
ans =
WIDTH and BREADTH of contact surface are taken to be 0.15 m
How many layers of NODES along WIDTH (x-axis) and BREADTH (y-axis) of surface? 16
ans =
Material Type 20, *MAT RIGID with full translational and rotational constraint
*****

```

Figure A1.1. MATLAB program input screen.

### A1.5.1 Mesh Specification and Material Properties

A number of element formulations were tried but fully integrated 4-node thin shells from the LS-DYNA [87] element library (shell element formulation 16) were found to be the most relevant. Shell elements were preferred to solid ones because they are computationally more efficient. Furthermore, no significant improvement was observed when solid elements were employed as discussed in ‘Results and Discussion’. Fully integrated shell elements were chosen instead of reduced integration shells (e.g. Belytschko-Tsay [133, 134]) because they were found to be more accurate in their representation of the crush modes seen in the physical testing programme. For example, the reduced integration shell elements incorrectly predicted that ST02(2) would fail in diamond mode whereas the fully integrated shell elements correctly predicted a concertina mode collapse, as shown in Figure A1.2. This is an important finding since reduced integration elements are often preferred for computational efficiency.

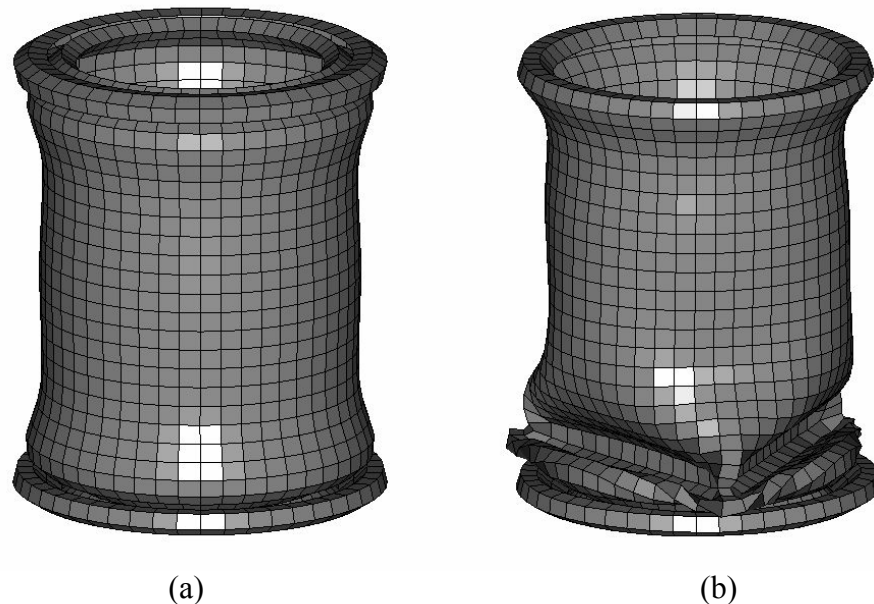


Figure A1.2. Comparison of the simulated crush modes of ST02(2) produced by; a) Fully-integrated shells (type 16) with piecewise linear material model (mat-24) – STANDARD; b) Reduced shells (Hughes-Liu & Belytschko-Tsay) with piecewise linear material model.

The shell elements were positioned at the mid-plane of the tubes' thin wall. Each tube is represented with elements of about 2.5mm square and, as a result, the number of elements and computational time are dependent upon the model dimensions. Larger elements (for example, 5mm square elements) were not able to accurately represent the curvature of the plastic folds seen in the post-buckling phase of the collapse. When 2.5mm square elements were used a realistic representation of the crushing behaviour was seen within an acceptable computational time. The issue of computational efficiency is an important one but must be balanced with the fact that the plastic folds are known to be more realistically simulated as the element length approaches the shell thickness – at the same point, the assumptions of standard shell theory are beyond their limits [127].

Two through-thickness Gauss integration points are usually sufficient to model a linear elastic material, while more points (typically 4 or 5) are recommended for simulation of nonlinear materials. Since progressive plastic folding is known to occur during the post-buckling collapse in metallic tubes, five through thickness Gauss integration points were specified in the tube models. The tubes' modulus of elasticity  $E$ , was assumed to be 205GPa with a Poisson's ratio  $\nu$ , of 0.3. The nonlinear strain (work) hardening characteristics of the circular tubes were taken from reference [131] and were simulated using the Piecewise Linear Isotropic Plasticity material model (material type 24) available in the LS-DYNA code. The use of the Plastic Kinematic material model (material type 3) resulted in a poor load-displacement correlation. The crush predictions become even worse when used with reduced integration shell elements. The combination of fully integrated shell elements and the bilinear

material model was also tested. Although the crush mode was similar to that shown in Figure A1.2 the load-displacement correlation was found to be poor.

The two horizontal platens were assumed to be rigid and were represented using material type 20 (Rigid material model). They were modelled as flat surfaces using 10mm square reduced integration Belytschko-Tsay shell elements [133, 134]. One surface was positioned above the tube model while the other was positioned slightly below it. This was done to allow simulation of the interaction between the tube and the two surfaces. The elastic constants of the horizontal platens were based on those of bulk steel, i.e.  $E = 205\text{GPa}$  with  $\nu = 0.3$ . This mechanical property data is required in the contact model to allow the sliding interface parameters to be calculated when the rigid body contacts the tube.

### **A1.5.2 Contact and Friction**

To simulate the crushing behaviour of the tubes, three contact regions need to be considered: two contact interfaces between the tube and horizontal platens; and a ‘single surface’ contact generated during collapse when elements of the tube wall contact each other.

The automatic nodes-to-surface model (contact type a5 in the LS-DYNA library) is employed to represent the tube to surface contacts, while the automatic single surface model (type 13) is used to simulate the self contacts of the tube wall. These contact models allow compression to be carried, thereby allowing two bodies to be either separate or in contact. The contact formulations are based on the penalty stiffness method [135]. For contact type a5, the slave nodes are defined on the tube and the master nodes on the surfaces. On initialisation, the master node nearest to each slave node is found

and the master ‘segments’, which are a four node element of the surface, attached to that node are checked for contact. For contact type 13, a master surface is not specified, thus resulting in slave nodes contacting slave segments. The contact definitions take into account the thickness of shell elements and friction modelling is based on the coulomb formulation, in which a distinction is made between the static  $\mu_p$ , and the dynamic  $\mu_s$ , coefficients of friction. Such a distinction is necessary in many situations since the static force necessary to cause sliding is often higher than that required to maintain the dynamic situation. The values for  $\mu_p$  and  $\mu_s$  used were 0.3 and 0.2 respectively [130], although, varying these values produced no significant differences in the load-displacements, crush modes or SEA values.

## **A1.6 Finite Element Simulations**

---

To simulate the quasi-static crushing behaviour of the steel tubes, under a monotonically increasing displacement of greater than 50mm, the upper horizontal surface was displaced vertically downwards at a constant rate of 100mm/s. Models were run over a ‘real time’ of 0.6s using the LS-DYNA default time step. This resulted in a maximum simulation time for the fully integrated shell element models of approximately 52 hours using one processor of a dual-processor XEON 2 GHz personal computer. An example of the plastic deformation stages – for tube ST03(2) - are shown in Figure A1.3. Figure A1.3(a) shows the cross-section at the start of the simulation, while Figure A1.3(b) to (d) show its progressive collapse with time at  $t=0.07s$ ,  $t=0.41s$  and  $t=0.60s$ , respectively.

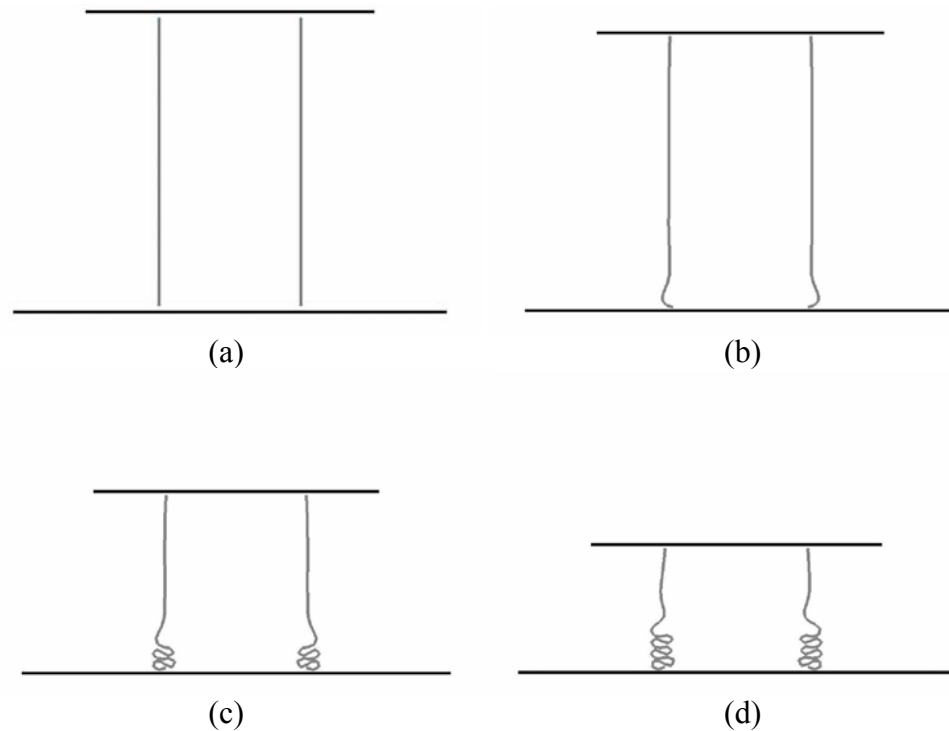


Figure A1.3. Deformation of cross-section for the tube ST03(2): a) undeformed ( $t=0.00s$ ); (b) first fold develops ( $t=0.07s$ ); (c) folding progresses ( $t=0.41s$ ); (d) simulation complete ( $t=0.60s$ ).

A displacement rate of 100mm/s satisfied the compromise between minimising computational expense and maintaining a quasi-static loading. A slower displacement rate mirroring that of the physical testing programme would be computationally too expensive. Therefore, in order to ensure the simulation rate was representative of quasi-static loading, the contact forces on the upper and lower platen were compared. The difference was found to be insignificant. Moreover, the kinetic energy was compared with the internal energy of the tube to ensure that no dynamic effect was evident in the simulation. The kinetic energy was found to be less than 1% of the total energy.

## A1.7 Results and Discussion

Crush properties and crush modes of metallic tubular structures are highly dependent upon the tube geometry  $D/L$  and in particular, the  $t/D$  ratio [30, 31, 34]. The three crush modes, concertina, diamond and Euler modes common to

metallic tubes were observed in the physical testing programme reported herein.

Simulations of the collapse of tubes are of special interest to vehicle crashworthiness engineers. If the crush characteristics of circular tubes with given geometric dimensions can be accurately predicted, then initiation of the preferred concertina mode (with the highest energy absorption values) can be guaranteed and the load-deflection characteristics can be obtained without the need for physical testing. Realistic load-displacement characteristics could then be represented in a computationally efficient manner in a full vehicle crash simulation using, for example, non-linear discrete springs. Similarly, these load-displacements characteristics can only be employed when users are certain that the crush mode has also been correctly predicted. Incorrect prediction of the crush mode can result in significant variations in performance.

Diamond and concertina collapse modes are seen in the numerical and experimental tests for sizes ST02, ST03 and ST04 – see Figure A1.2, Figure A1.4 and Figure A1.5. In the physical tests, a concertina mode was seen for all three ST02 tubes, whilst both diamond and concertina modes were seen for ST03 and ST04. In general, metallic tubes with lower  $t/D$  ratios when crushed produce a diamond mode collapse, above which a concertina collapse occurs [31]. However, the specific value of  $t/D$  is also dependent on the  $D/L$  (Diameter/Length) ratio of the tube. For tubes ST03 and ST04, the repeat tests did not yield the same crush mode, most likely due to the  $t/D$  ratios that falls closely to the diamond/concertina mode threshold. The failure modes produced experimentally and in FE simulations are shown in Table A1.2. The 4-node full integration shell elements correctly predict a concertina mode for ST02(2). The

simulation of ST03(2) fails with a concertina mode whilst that of ST04(2) exhibits a diamond collapse mode. In the case of ST04(2), the tested tube produced a 2-lobe diamond mode crush, compared to a simulated 3-lobe diamond mode as shown in Figure A1.4. Fully integrated shell elements were preferred to reduced integration elements [133, 134] because, as mentioned earlier, they more closely reproduced the failure modes expected and were shown to yield the best correlation with the experimental load-displacement data.

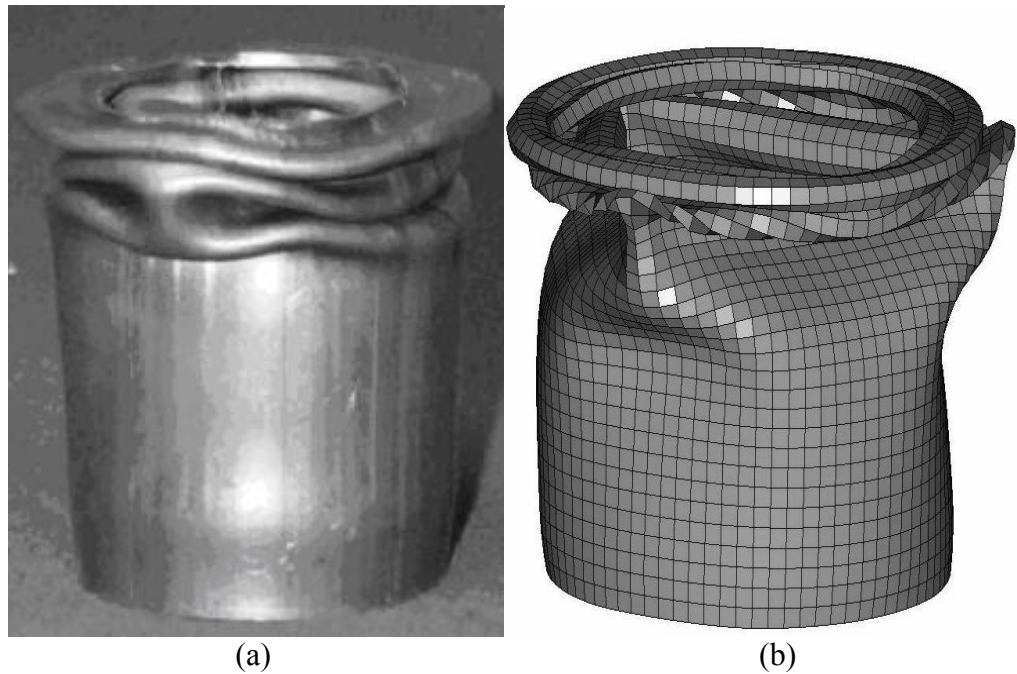


Figure A1.4. Diamond mode: (a) Experiment; (b) LS-DYNA simulation for the tube ST04(2).

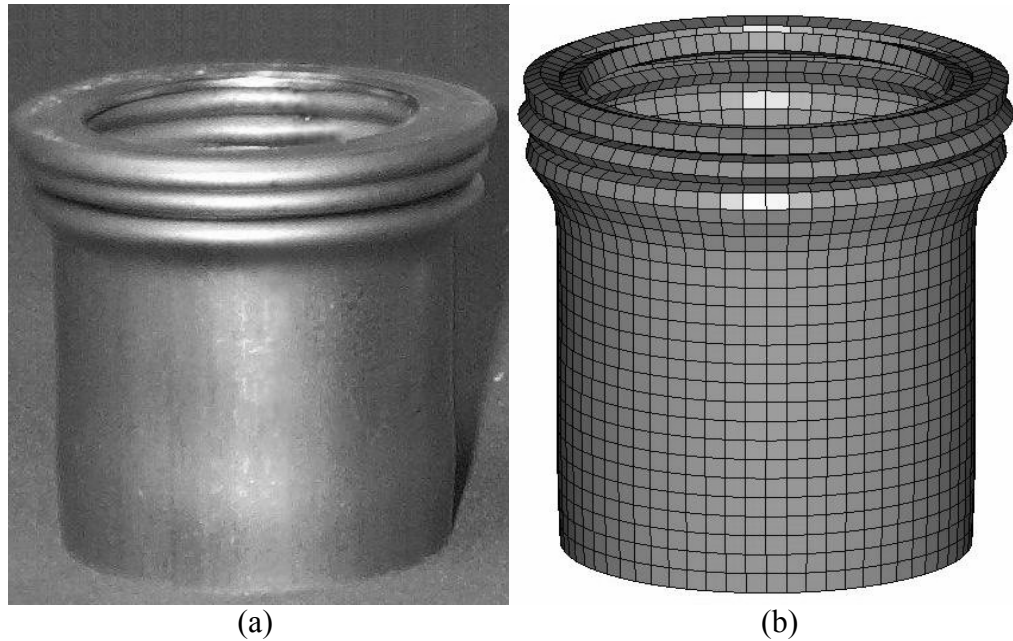


Figure A1.5. Concertina mode: (a) Experimental; (b) LS-DYNA simulation for tube ST03(2).

The folding mechanisms of the diamond and concertina progressive collapse modes result in a series of undesirable oscillations in the load-displacement characteristics as shown in Figure A1.6. In the case of Euler buckling, only a single peak is produced as the tube collapses. These load oscillations are effectively peak decelerations for the occupants of a vehicle in a crash. Consequently a bilinear response without oscillations is considered ideal for crashworthiness [28]. A comparison of the numerical and experimental load-displacement characteristics for ST02(2) is shown in Figure A1.7, exhibiting an example of the correlation achieved with this modelling methodology. The experimental curve for ST02(2) shows a higher initial peak (corresponding to the first fold) which is about 20kN above the value for the subsequent peaks (folds) of 95-100kN. In Figure A1.7, the FE simulation results give good agreement in peak loads for all but the first fold, and also show that the folds occur more frequently - five folds, in the simulation (over a 50mm crush) when compared to four in the corresponding physical test. This also indicates that the predicted "wavelength" of fold is different from that observed in the

test. Folds arise in the FE tubes via element rotations about the adjoining nodes. The shell element tubes fold more frequently due to the ease with which the elements can rotate. This is clearly evident when solid elements (type 2, Fully Integrated S/R Solid Elements [87]) are considered in a model which, in turn, predicts only three folds. An increased mesh density only served to exacerbate this issue and contributed to significant computational expense. Despite the load-displacement curve for ST03(2) (Figure A1.8) suggesting a change from concertina to diamond mode (commonly referred to as mixed-mode), the experimental test maintained the concertina mode during axially compressive crush. All results have been tabulated for comparison in Table A1.2.

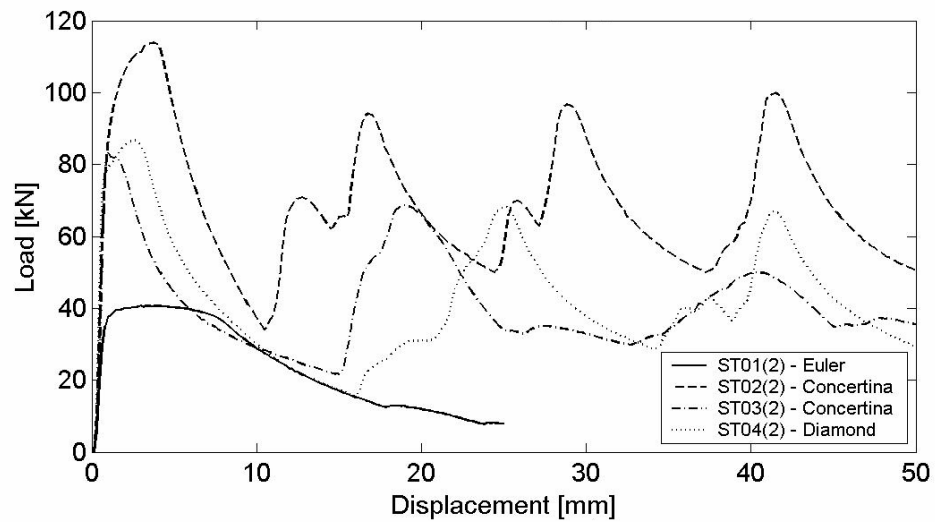


Figure A1.6. Experimental load-displacement curves for tubes ST01(2), ST02(2), ST03(2) and ST04(2).

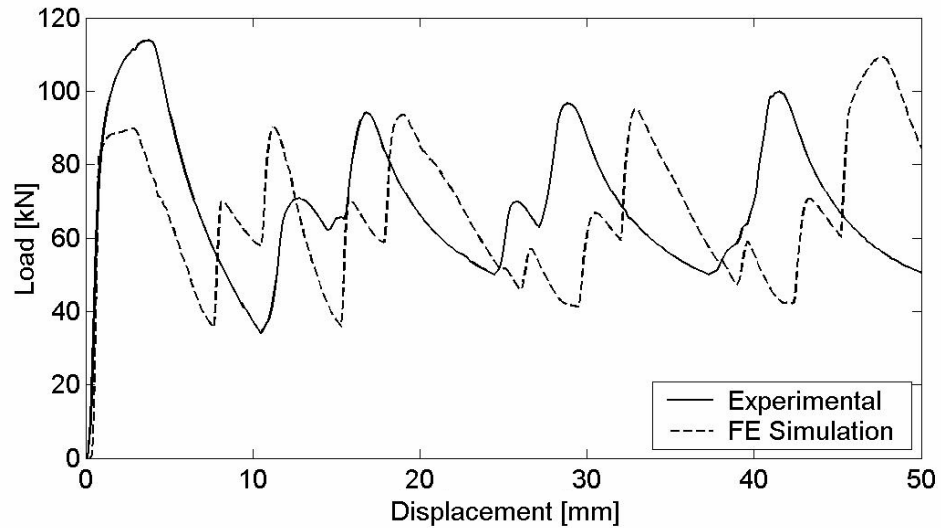


Figure A1.7. Numerical and experimental load-displacement curves for tube ST02(2).

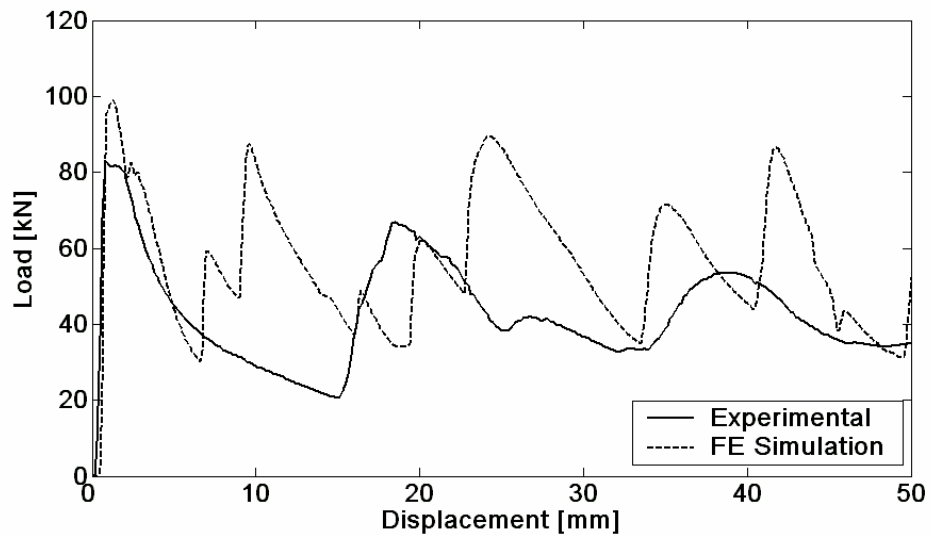


Figure A1.8. Numerical and experimental results for tube ST03(2) showing the variation in load-displacement for the same crush mode.

Table A1.2. Tabulated Experimental and FE results.

Tube	Experiment		Simulation		% difference		Experimental Crush Mode	Simulated Crush Mode	
	Peak	Mean	Peak	Mean	Peak	Mean			
(ST01)	1	40.7	23.9		84.6	53.9	Euler		
	2	40.7	23.7	75.3	36.8	84.6	55.2	Euler	Concertina
	3	37.7	23.4			100	57.8	Diamond	
(ST02)	1	114.0	69.9			4.1	20.1	Concertina	
	2	113.9	69.5	109.3	55.8	4.0	19.7	Concertina	Concertina
	3	113.7	69.9			4.0	20.1	Concertina	

	<b>1</b>	83.2	42.9			16.6	9.7	Diamond	
<b>(ST03)</b>	<b>2</b>	83.7	41.2	97.0	47.1	15.9	14.4	Concertina	Concertina
	<b>3</b>	83.5	40.0			16.2	17.6	Concertina	
	<b>1</b>	*	*			*	*	Concertina	
<b>(ST04)</b>	<b>2</b>	86.7	42.3	129.7	53.3	49.5	17.0	Diamond	Diamond
	<b>3</b>	86.6	43.7			49.7	22.3	Diamond	

In order to accurately predict load-deflection characteristics of metallic tubes it is essential that the crush mode is correctly captured by the model. The FE shell models here replicate the deformations of the two progressive collapse modes and therefore offer a reasonable approximation of the load-displacement responses and hence, specific energy absorption values. For ST02(2), ST03(2) and ST04(2), the predicted energy absorption values were found to be 37.13kJ/kg (21.4% to low), 27.34kJ/kg (16.9% to high) and 23.36kJ/kg (27% to high) respectively. Similarly, the predicted mean loads for these tubes were 19.7% below, 14.4% above and 17% above the respective experimental test figures. The FE model of ST03(2) produced the correct concertina mode but failed to reproduce the unusual experimental load-displacement results. This comparison can be seen in Figure A1.8. The unstable Euler mode [31, 34] which arises in the physical tests for tube ST01(2) was not repeated and, as a result, the correlation between the load-displacement curves and the energy absorption values were poor – the SEA value calculated for the simulation was 44.82kJ/kg which is significantly higher than the 28.08kJ/kg found in the physical test.

## **A1.8 Conclusions**

---

An automatic mesh generation program has been developed and used to create FE model descriptions of tubular structures with a user-defined geometry and mesh specification. Two horizontal surfaces were also routinely created by the program. The output of the program was a ready-to-run input deck making parametric studies and variations in the geometry quick and uncomplicated. This explicit LS-DYNA FE code used these input decks to simulate the progressive plastic folding of three thin-walled tubular structures of various geometries under axial compression. Diamond and concertina collapse modes seen in the physical tests were repeated in the corresponding simulations – for tubes ST02(2), ST03(2) and ST04(2). However, LS-DYNA model was unable to predict the unstable Euler mode seen in tube ST01(2). Discrepancies in the observed failure modes and corresponding load-displacement curves highlight the need for further improvements in this area.

In the models, fully integrated 4-node shells were preferred to reduced integration ones as they were found to better replicate the crush modes seen in the physical test programme. The experimental load-deflection and energy absorption characteristics were simulated with a reasonable degree of correlation when LS-DYNA correctly predicted a progressive collapse mode. With the exception of ST03(2), the FE simulations were found to predict realistic peak loads for the oscillations corresponding to folds as seen in the experimental curves. Folds occur in the FE tubes via element rotations about the adjoining nodes. When fully integrated 4-node shell elements were used to represent the tube, too many folds were predicted, while too few folds were predicted with solid elements. The shell tubes fold more frequently due to the ease at which the elements can rotate. A reduction in mesh density can achieve

a lower folding frequency though at the expense of load-displacement correlation.

The correlation between the numerical and experimental load-deflection characteristics (and energy absorption values) was much worse for tube ST01(2) where an Euler buckling mode was seen in the physical tests but not repeated in the corresponding FE simulation. It is therefore clear that in order to accurately predict the load-deflection and energy absorption characteristics of tubular crash structures, simulation of correct crush mode and wavelength of fold is essential.

## **A1.9 Acknowledgements**

---

The authors gratefully acknowledge the help and support of colleagues at the University of Nottingham and the Victorian Centre of Advanced Materials and Manufacturing (VCAMM).

## A2 CFRM Properties and Behaviour

### A2.1 CFRM Properties

CFRM is an inexpensive alternative to carbon/epoxy composites, which is capable of absorbing high levels of energy, making it a likely candidate for use in the automotive industry. Extensive CFRM characterisation tests were performed at the University of Nottingham. Detail on the CFRM characterisation tests and additional material properties not discussed herein can be obtained in reference [55]. The material properties that were required for the modelling methodology presented in Chapters Five, Six, Seven and Eight are shown in Table A2.1.

Table A2.1. CFRM material properties required for LS-DYNA's material 58.

Test Type	Property	Value	
<b>In-plane Tension</b>	$E_{11t} = E_{22t}$	10.1 GPa	
	$\nu_{12} = \nu_{21}$	0.296	
	$\sigma_{ult}$	153 MPa	
	$\epsilon_{ult}$	1.51%	
<b>In-plane Compression</b>	$E_{11c} = E_{22c}$	10.1 GPa	
	$\sigma_{ult}$	221 MPa	
	$\epsilon_{ult}$	2.14%	
<b>Through-Thickness Tension</b>	$E_{33t}$	6.49 GPa	
<b>Shear</b>	$G_{21} = G_{12}$	4.25 GPa	
	<b>Mode 1,2</b>	$\tau_{ult}$	87.0 MPa
		$\gamma_{ult}$	2.0%
	<b>Mode 3,1</b>	$G_{31} = G_{32}$	1.68 GPa
	<b>Mode 2,3</b>	$G_{23} = G_{13}$	1.76 GPa

## A2.2 Tubular Specimen Manufacture and Preparation

CFRM circular specimens were manufactured by Resin Transfer Moulding (RTM) at the University of Nottingham. Specific details on RTM production can be found in reference [55]. Tubular profiles were formed from 6 layers of glass matting with a high dimensional tolerance. Samples of 100mm in length were cut and a 45° chamfer was turned into one end. CFRM tubes were measured to have an average outer diameter of 88.56mm  $\pm$ 0.07mm with an average wall thickness of 3.87mm  $\pm$ 0.06mm.

## A2.3 Crush Testing

Two types of crush testing were performed on CFRM tubes; flat-platen and plug-initiator tests. Three radius plug initiators were tested; 5, 7.5 and 10mm. Plug initiator geometries are shown in Figure A2.1.

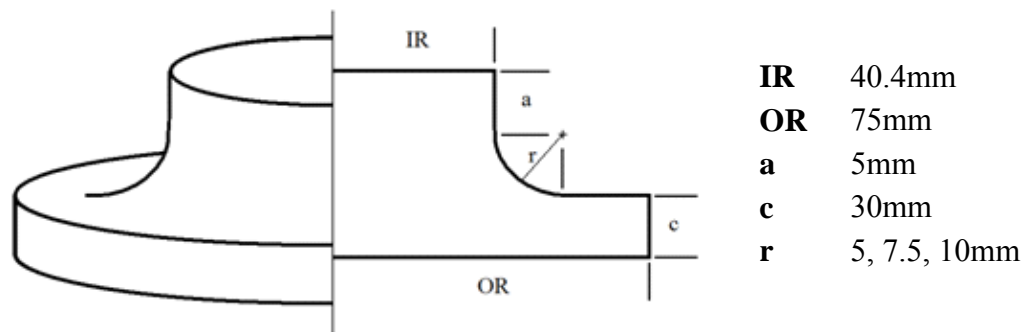


Figure A2.1. Plug-initiator geometry.

Flat-platen crush testing was conducted at 0.5mm/min in a servo-hydraulic press. Plug initiator tests were conducted at 10mm/min. Further details on the experimental testing conducted at the University of Nottingham can be found in references [54, 55]. Here, excerpts from the relevant reference, together with comments of the experimentally observed findings will be given.

### A2.3.1 Flat-platen Crush-Zone Analysis

On the observed failure mode and image of the crush-zone shown in Figure A2.2, Cooper [54] writes ‘[t]here is significant buckling of the inside frond and it is fragmented and broken. Within the fronds there is some shear damage. This is most noticeable in the frond on the left where a few dark “S” shaped cracks are visible. The principal modes of energy absorption are fracturing in the fronds, friction and crack growth (central wall and axial).’

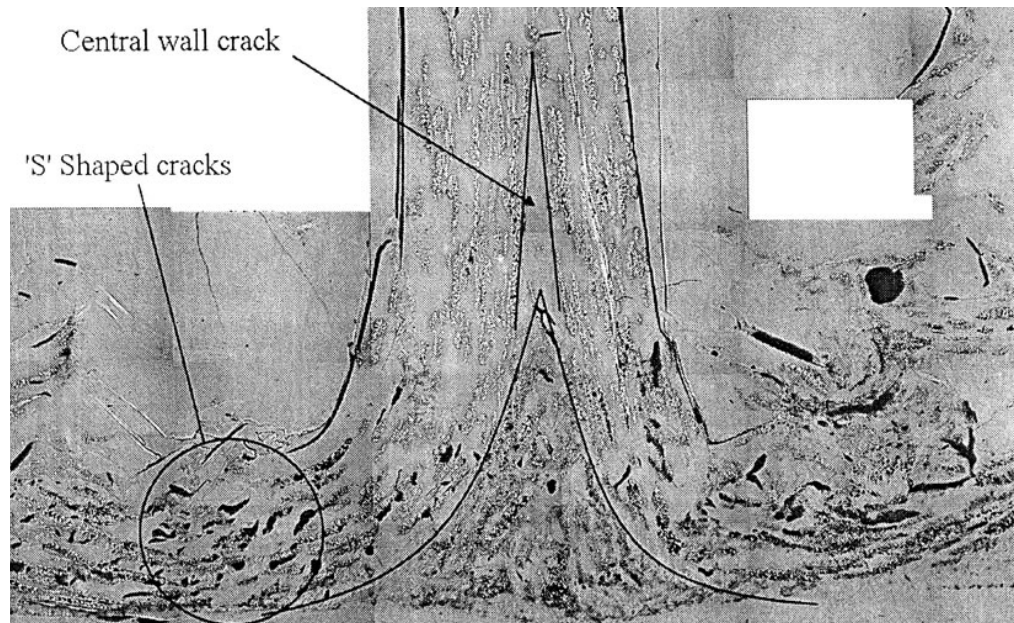


Figure A2.2. Image of CFRM flat-platen crush zone taken from Cooper [54]. The S-shaped interlaminar shear cracks can be observed.

### A2.3.2 Plug-Initiator Crush-Zone Analysis

#### *5mm Radius*

On the observed failure mode and image of the crush-zone shown in Figure A2.3, Cooper [54] writes ‘[t]he 5.0mm initiator gave the highest SEA of all the initiators tested. The shapes of the fronds for this initiator are significantly different to the typical curled fronds seen when crushing tubes against flat-platens. The fronds extended horizontally without curling [along the plug]. As they extended radially they tore and separated although the individual fronds were not well defined. The fronds also turned an opaque white colour

indicating a large amount of internal cracking and damage. The micrograph shows that considerable cracking occurred in the crush zone. The damaged material is full of dark “S” shaped cracks in the matrix. The shapes of the cracks suggest that the primary mode of failure was through-thickness shearing. The primary modes of energy absorption for the 5.0mm radius initiator were tensile cracking, through-thickness shear and friction.’

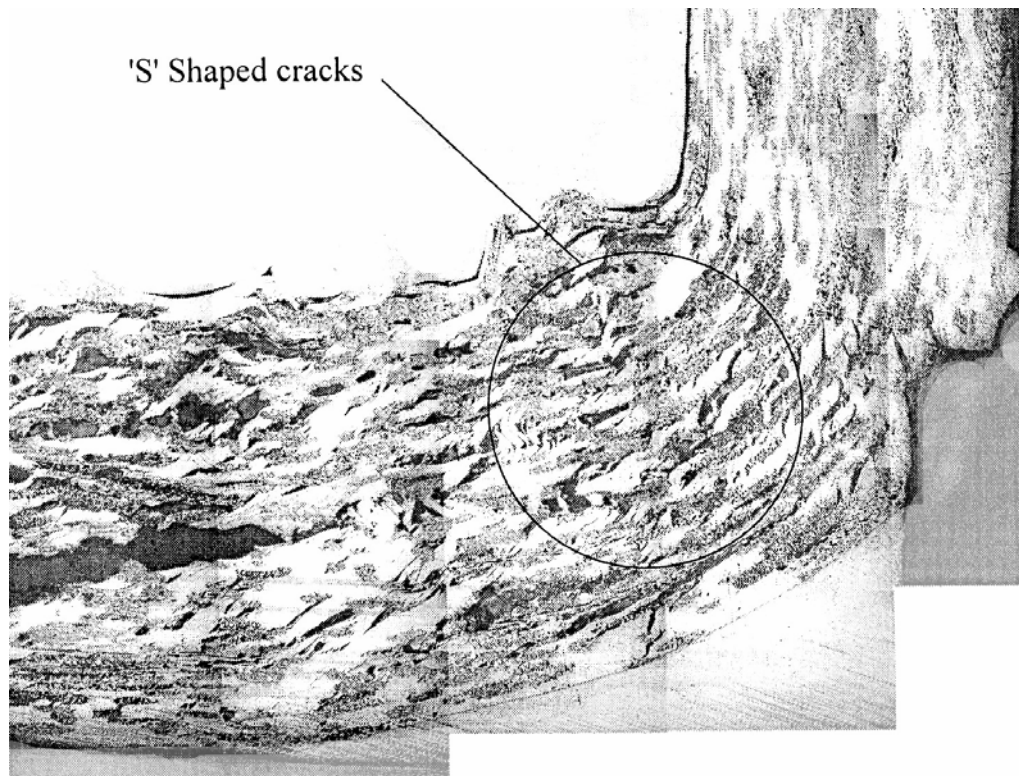


Figure A2.3. Image of CFRM tube crushed on 5mm radius plug initiator taken from Cooper [54]. A single clear delamination can be observed.

### *7.5mm Radius*

On the observed failure mode and image of the crush-zone shown in Figure A2.4, Cooper [54] writes ‘...axial cracks formed but did not propagate far ahead of the crush zone and...significant mode II fracture occurred in the fronds. In the micrograph...the tip of an interlaminar crack can be seen near the top surface of the frond on the left side of the picture. (The black bubble near the left edge of the image formed when the casting resin did not

completely fill the crack). Some tensile cracks can be seen on the bottom surface of the frond however there is little evidence of significant internal damage or cracking.’

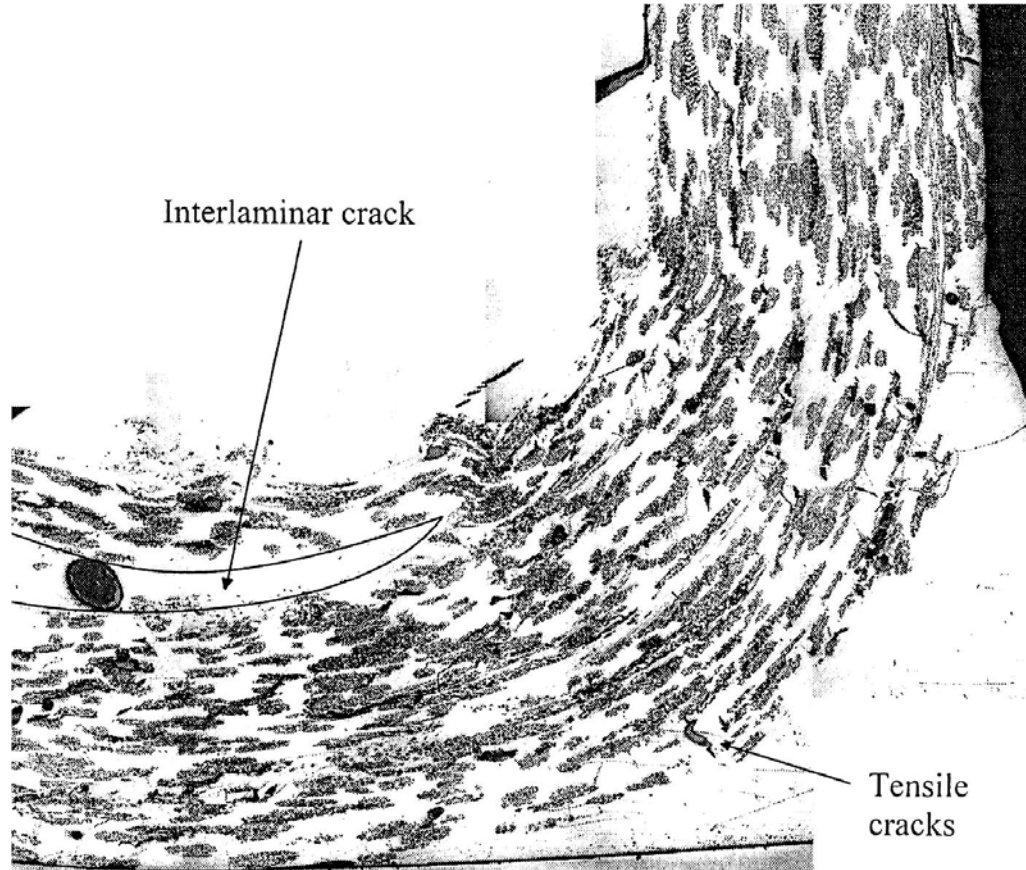


Figure A2.4. Image of CFRM tube crushed on 7.5mm radius plug initiator taken from Cooper [54].

### *10mm Radius*

On the observed failure mode and image of the crush-zone, Cooper [54] writes, ‘When the 10mm radius initiator was used the crush was stable but with low energy absorption. Axial cracks formed at regular intervals around the circumference of the tube. As crushing progressed the fronds formed by the axial cracks snapped resulting in chunks of undamaged material breaking away. This gave a low SEA with a significant fraction of the material left undamaged.’ No image of the crush zone of this specimen was available.

## **A3 MATLAB Input Deck Generator**

Throughout the FE modelling work discussed in Chapters Five, Six, Seven and Eight, numerous models of various geometries, compositions and approaches were tested. The solver software, in this case LS-DYNA [87], requires that all model information be submitted in an input deck - a text file of a specific syntax. Input decks submitted by this author range from just several lines to ~500,000 lines. Consequently, significant time can be spent constructing and modifying these input decks. Creation of such input decks can be a trivial exercise and reproduction can often lead to parameter inconsistencies. It is possible for a single incorrect number to render the results useless. To eliminate these issues, a MATLAB program was created to generate a complete, ready-to-run input deck of the required model geometry with all necessary information, in the correct syntax. This program allowed the creation of completely new input decks in less than one minute. While several variations now exist, the one of primary interest created a multi-layer composite shell element tube placed endwise under a ram and above either a debris wedge/crush platen or plug initiator.

An example of the MATLAB input screen used to create a 6 layer CFRM shell element tube is given below in Figure A3.1. Depending on the program variant selected, a number of user defined inputs are required and are requested by the program. Any values to remain constant between models can be assigned within the MATLAB code, eliminating the potential for inconsistency.

```

1 clear all
2
3 sprintf('%s','*****')
4 sprintf('%s','*****QUICKTUBE COMPOSITE TUBE INPUT DECK GENERATOR*****')
5 sprintf('%s','*****')
6 sprintf('%s','*****')
7 sprintf('%s','*****')
8
9
10
11 %*****
12 %*****Tube Mesh*****
13 %*****
14
15 OD = input('What is the OUTER DIAMETER of the tube [m]? ');
16 t = input('What is the tube wall THICKNESS [m]? ');
17 Thick_layers = input('How many LAYERS OF MATERIAL in the THICKNESS of the tube? ');
18 L = input('What is the LENGTH of the tube [m]? ');
19 Length_levels = input('How many NODES along the LENGTH of the tube? ');
20 nodes_circ = input('How many NODES around the the tube CIRCUMFERENCE? ');
21
22
23
24 %ORGANISE SPOTWELD NODAL NUMBERS AND POSITIONS
25 OD1 = OD;
26 degree_step = 360/(nodes_circ)*(2*pi/360);
27 level_step = L/(Length_levels - 1);
28 i=1;
29
30 for layer = 1:Thick_layers-1;
31     level_z = 0.00705 + (0.5*level_step);
32     for level = 1:Length_levels-5;
33         degrees = (0.5*degree_step);
34         for spotweld_no = ((level-1)*nodes_circ)+1+(layer*1000000):(nodes_circ*level)+(layer*1000000);
35             spotweld(i,1) = spotweld_no;
36             spotweld(i,2) = (OD1/2 - ((t/[Thick_layers]))*cos(degrees));
37             spotweld(i,3) = (OD1/2 - ((t/[Thick_layers]))*sin(degrees));
38             spotweld(i,4) = level_z;
39             degrees = degrees + degree_step;
40         end
41     end
end

```

Figure A3.1. Example screenshot of MATLAB automatic mesh generation code.

### A3.1 Software Operation

The nodes and elements of each material layer were numbered consecutively in the circumferential direction for a full 360° before moving up one row, until the required tube length was reached. The layers were numbered 1 to ‘n’ from the outermost layer such that node 10000X (the Xth node on the first layer) was adjacent with node 20000X (the Xth node on the second layer). The beam elements and their connections were routinely created. Where required, the ‘debris wedge’ was included such that the peak of the wedge was aligned with the centre-most point of the tube wall. An example of the wedge is shown in Figure A3.2 and further related discussion can be found in ‘Chapter Five –

Finite Element Modelling’. In all the necessary contact cards were also created routinely.

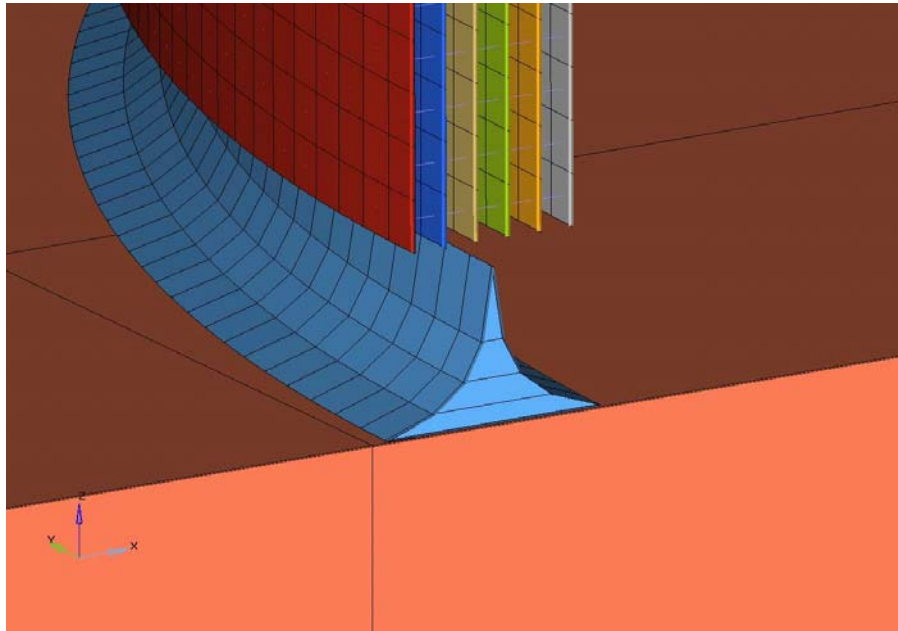


Figure A3.2. The simulated ‘debris wedge’ automatically created for the multi-layer flat-plate simulations.

### A3.2 Software Limitations

Although this software can save a significant number of work hours, it is important that the user remains aware of the limitations that exist. This software’s primary limitations lie in numbering restrictions. For instance, the node numbering system dictates that the tube’s first layer contains the nodes 100,001 to 199,999 and the second contains nodes 200,001 to 299,999. As such, the user must ensure that the product of the circumferential and lengthwise nodes does not exceed 99,999, which will result in duplicate node numbering (ie. a node on layer two numbered 300,001, the same as the first node of layer three). These same numbering procedures were applied to the tube’s shell elements where element 100,001, the first element on the first layer is adjacent to element 200,001, the first element on the second layer. Additionally, where the debris wedge is included, tubes must be created with

an even number of layers. While this will not cause a problem with the MATLAB program, it will undoubtedly produce meaningless FE results.

The interlaminar beam elements and their nodes are numbered from 10,000,001-99,999,999, where the first digit indicates the region in which the element lies (1-9). These are sequentially numbered such that beam element 10,000,001 connects the two shell elements numbered 100,001 and 200,001.

The ram and crush platen nodes can range from 1,000,001-1,999,999 (upper surface) and 2,000,001-2,999,999 (lower surface) respectively. Consequently, the number of material layers in a tube should not exceed 9 due to the 10th layer utilizing similar numbering to those of the ram, being 10‘00000’. Though the limitations on nodal numbering can be easily removed (eg. by allowing the range of ram nodes to start from 100,000,000,001), such efforts were unnecessary as the author’s work never breached these limits.

The most severe limitation of this code clearly relates to the inclusion of the debris wedge, and the resulting requirement to maintain an even number of layers.

### A3.3 Shortened MATLAB Code

```
clear all
sprintf('%s', '*****')
sprintf('%s', '*****QUICKTUBE COMPOSITE TUBE INPUT DECK GENERATOR*****')
sprintf('%s', '*****')

%*****
%*****TUBE MESH*****
%*****

OD = input('What is the OUTER DIAMETER of the tube [m]? ');
t = input('What is the tube wall THICKNESS [m]? ');
Thick_layers = input('How many LAYERS OF MATERIAL in the THICKNESS of the tube? ');
L = input('What is the LENGTH of the tube [m]? ');
Length_levels = input('How many NODES along the LENGTH of the tube? ');
nodes_circ = input('How many NODES around the the tube CIRCUMFERENCE? ');

%****ORGANISE SPOTWELD NODAL NUMBERS AND POSITIONS****
OD1 = OD;
degree_step = 360/(nodes_circ)*(2*pi/360);
level_step = L/(Length_levels - 1);
i=1;

for layer = 1:Thick_layers-1;
    level_z = 0.00705 + (0.5*level_step);
    for level = 1:Length_levels-5;
        degrees = (0.5*degree_step);
```

```

for spotweld_no = ((level-1)*nodes_circ)+1+(layer*1000000):(nodes_circ*level)+(layer*1000000);
    spotweld(i,1) = spotweld_no;
    spotweld(i,2) = (OD1/2 - (t/[Thick_layers]))*cos(degrees);
    spotweld(i,3) = (OD1/2 - (t/[Thick_layers]))*sin(degrees);
    spotweld(i,4) = level_z;
    degrees = degrees + degree_step;
    i=i+1;
end
    level_z = level_z + level_step;
end
    OD1 = OD1 - (2*t/[Thick_layers]);
    level = 1;
end
spotweld

%****SPOTWELD MATERIAL PROPERTIES****

sprintf('%s','Spotweld Material Properties.')
mat_spotweld_1(1,1) = 100;
mat_spotweld_1(1,2) = input('What is the MASS DENSITY of the material [kg/m^3]? ');
mat_spotweld_1(1,3) = input('What is the YOUNG'S MODULUS of the material [GPa]? ');
mat_spotweld_1(1,4) = input('What is the Poissons ratio of the material [kg/m^3]? ');
mat_spotweld_1(1,5) = 400E06;

mat_spotweld_2(1,1) = 0.5;           %What is the strain-to-failure of the spotwelds?;
mat_spotweld_2(1,2) = 38;           %What is the axial failure force for spotweld failure?;
mat_spotweld_2(1,3) = 70.806;       %What is the shear failure force for spotweld failure?;
mat_spotweld_2(1,4) = 25.0;         %Number of vectors for force filtering;

mat_spotweld_3(1,1) = 0;             %0 = force based failure.

%****DATA FOR SPOTWELD MODELLING****

%*contact_tied_shell_edge_to_surface
spot_con_1(1,1) = 100;
spot_con_1(1,2) = 200;
spot_con_1(1,3) = 3;
spot_con_1(1,4) = 2;

%*set_part
set_part_1(1,1) = 200;

set_part_2(1,1) = 1;
set_part_2(1,2) = Thick_layers;

%*section_beam
section_beam_1(1,1) = 100;
section_beam_1(1,2) = 9;
section_beam_1(1,3) = 1;

section_beam_2(1,1) = 0.0009;
section_beam_2(1,2) = 0.0009;

%*part
spotweld_part_1(1,1) = 100;
spotweld_part_1(1,2) = 100;
spotweld_part_1(1,3) = 100;

%*****SPOTWELD MODELLING*****
%*****

level = 1;
layer = 1;
layers = Thick_layers-1;
i=1;

for x = 1:layers;
    for spot_no = 1:((nodes_circ)*(Length_levels-5));
        spot(i,1) = spot_no+(x*1000000);
        spot(i,2) = 100;
        spot(i,3) = spot(i,1);
        spot(i,4) = 0;
        spot(i,5) = 0;
        i=i+1;
        level=level+1;
    end
end

spot

%****ORGANISE TUBE NODAL NUMBERS AND POSITIONS****

degree_step = 360/(nodes_circ)*(2*pi/360);
level_step = L/(Length_levels - 1);
i=1;

for layer = 1:Thick_layers;
    level_z = 0.00305;
    for level = 1:Length_levels;
        degrees = 0;
        for node_no = ((level-1)*nodes_circ)+1+(layer*100000):(nodes_circ*level)+(layer*100000);
            node(i,1) = node_no;
            node(i,2) = (OD/2 - (0.5*t/[Thick_layers]))*cos(degrees);
            node(i,3) = (OD/2 - (0.5*t/[Thick_layers]))*sin(degrees);
            node(i,4) = level_z;
            degrees = degrees + degree_step;
            i=i+1;
        end
        level_z = level_z + level_step;
    end
    OD = OD - (2*t/[Thick_layers]);
    level = 1;
end
node

```

```

OD = OD + 2 * t;                                % RESET OD FOR PRINTING

%ORGANISE TUBE ELEMENTS AND THEIR NODAL CONNECTIONS
i=1;
layer = 0;
part_no = 1;
for layer = 1:Thick_layers;
    element_no = 1+(layer*100000);
    for level = 1:(Length_levels-1);
        for node_no = (level-1)*nodes_circ+1+(layer*100000):(nodes_circ*level)-1+(layer*100000);
            element_shell(i,1) = element_no;
            element_shell(i,2) = part_no;
            element_shell(i,3) = node_no;
            element_shell(i,4) = node_no+1;
            element_shell(i,5) = node_no+nodes_circ+1;
            element_shell(i,6) = node_no+nodes_circ;
            element_no = element_no+1;
            i=i+1;
        end
        for node_no = level*nodes_circ+(layer*100000);
            element_shell(i,1) = element_no;
            element_shell(i,2) = part_no;
            element_shell(i,3) = node_no;
            element_shell(i,4) = ((level-1)*nodes_circ)+1+(layer*100000);
            element_shell(i,5) = ((level-1)*nodes_circ)+nodes_circ+1+(layer*100000);
            element_shell(i,6) = (level+1)*nodes_circ+(layer*100000);
            element_no = element_no+1;
            i=i+1;
        end
    end
    level = 1;
    part_no = part_no + 1;
end
element_shell

%*****
%****Material Modelling****
%*****

material = 3;    %input('Which material model-enhanced_comp_damage [1], composite_failure_shell_model [2], laminated_composite_fabric?
','s');
tube_material = input('What is the tube material? ','s');

if material == 1
    sprintf('%s','Composite Material Properties.')
    mat_composite_1(1,1) = 1;
    mat_composite_1(1,2) = 4800;
    mat_composite_1(1,3) = 10.1E09;
    mat_composite_1(1,4) = 10.1E09;
    mat_composite_1(1,5) = 6.5E09;
    mat_composite_1(1,6) = 0.296;
    mat_composite_1(1,7) = 0.227;
    mat_composite_1(1,8) = 0.227;

    mat_composite_2(1,1) = 4.25E09;
    mat_composite_2(1,2) = 1.7E09;
    mat_composite_2(1,3) = 1.7E09;
    mat_composite_2(1,4) = 0;
    mat_composite_2(1,5) = 0;

    mat_composite_3(1,1) = 0;
    mat_composite_3(1,2) = 0;
    mat_composite_3(1,3) = 0;
    mat_composite_3(1,4) = 0;

    mat_composite_4(1,1) = 0;
    mat_composite_4(1,2) = 0;
    mat_composite_4(1,3) = 0;
    mat_composite_4(1,4) = 0;
    mat_composite_4(1,5) = 0;
    mat_composite_4(1,6) = 0;
    mat_composite_4(1,7) = 0.015;
    mat_composite_4(1,8) = 0.04;

    mat_composite_5(1,1) = 0.16E-09;
    mat_composite_5(1,2) = 0.25;
    mat_composite_5(1,3) = 0.95;
    mat_composite_5(1,4) = 0.95;
    mat_composite_5(1,5) = 0.95;
    mat_composite_5(1,6) = 0.015;
    mat_composite_5(1,7) = -0.022;
    mat_composite_5(1,8) = 0.0;

    mat_composite_6(1,1) = 221E06;
    mat_composite_6(1,2) = 153E06;
    mat_composite_6(1,3) = 221E06;
    mat_composite_6(1,4) = 153E06;
    mat_composite_6(1,5) = 87E06;
    mat_composite_6(1,6) = 54.0;
    mat_composite_6(1,7) = 0.0;

elseif material == 2
    sprintf('%s','Composite Material Properties for *MAT_COMPOSITE_FAILURE_SHELL_MODEL.')
    mat_composite_1(1,1) = 1;
    mat_composite_1(1,2) = 1200;
    mat_composite_1(1,3) = 10.1E09;
    mat_composite_1(1,4) = 10.1E09;
    mat_composite_1(1,5) = 6.5E09;
    mat_composite_1(1,6) = 0.296;
    mat_composite_1(1,7) = 0.227;
    mat_composite_1(1,8) = 0.227;

    mat_composite_2(1,1) = 4.25E09;
    mat_composite_2(1,2) = 1.7E09;

```

APPENDIX THREE – MATLAB INPUT DECK GENERATOR

```

mat_composite_2(1,3) = 1.7E09; %input('What is the G32 value (c-b direction) of the material [N/m^2]? ');
mat_composite_2(1,4) = 0; %input('What is the Kfail value (BULK MODULUS) of the material [? ]? ');
mat_composite_2(1,5) = 0; %AOPT
mat_composite_2(1,6) = 0; %MAFLAG

mat_composite_3(1,1) = 0; % X1
mat_composite_3(1,2) = 0; % Y1
mat_composite_3(1,3) = 0; % Z1
mat_composite_3(1,4) = 0; % A1
mat_composite_3(1,5) = 0; % A2
mat_composite_3(1,6) = 0; % A3

mat_composite_4(1,1) = 0; % V1
mat_composite_4(1,2) = 0; % V2
mat_composite_4(1,3) = 0; % V3
mat_composite_4(1,4) = 0; % D1
mat_composite_4(1,5) = 0; % D2
mat_composite_4(1,6) = 0; % D3
mat_composite_4(1,7) = 0; % BETA

mat_composite_5(1,1) = 0.16E-09; %TSIZE
mat_composite_5(1,2) = 0.25; %ALP
mat_composite_5(1,3) = 0.95; %SOFT
mat_composite_5(1,4) = 0.95; %FBRT
mat_composite_5(1,5) = 0; %SR
mat_composite_5(1,6) = 0; %SF

mat_composite_6(1,1) = 221E06; %input('What is the XC value (LONGITUDINAL COMPRESSIVE STRENGTH) of the material [Pa]? ');
mat_composite_6(1,2) = 153E06; %input('What is the XT value (LONGITUDINAL TENSILE STRENGTH) of the material [Pa]? ');
mat_composite_6(1,3) = 221E06; %input('What is the YC value (TRANSVERSE COMPRESSIVE STRENGTH) of the material [Pa]? ');
mat_composite_6(1,4) = 153E06; %input('What is the YT value (TRANSVERSE TENSILE STRENGTH) of the material [Pa]? ');
mat_composite_6(1,5) = 87E06; %input('What is the SC value (SHEAR STRENGTH) of the material [Pa]? ');

elseif material == 3
    sprintf('%s','Composite Material Properties for *MAT_LAMINATED_COMPOSITE_FABRIC. ');
    mat_composite_1(1,1) = 1; %input('What is the MASS DENSITY of the material [kg/m^3]? ');
    mat_composite_1(1,2) = 4800; %input('What is the Ea value (YOUNGS MODULUS in the a-direction) of the material [N/m^2]? ');
    mat_composite_1(1,3) = 10.1E09; %input('What is the Eb value (YOUNGS MODULUS in the b-direction) of the material [N/m^2]? ');
    mat_composite_1(1,4) = 10.1E09; %input('What is the Ec value (YOUNGS MODULUS in the c-direction) of the material [N/m^2]? ');
    mat_composite_1(1,5) = 6.5E09; %input('What is the Pr(b-a) value (POISSONS RATIO in the b-a direction) of the material [? ]? ');
    mat_composite_1(1,6) = 0.296; %input(' [? ]? ');
    % mat_composite_1(1,7) = ; %input(' [? ]? ');
    % mat_composite_1(1,8) = ; %input(' [? ]? ');

    mat_composite_2(1,1) = 4.25E09; %input('What is the G12 value (a-b direction) of the material [N/m^2]? ');
    mat_composite_2(1,2) = 1.7E09; %input('What is the G13 value (a-c direction) of the material [N/m^2]? ');
    mat_composite_2(1,3) = 1.7E09; %input('What is the G32 value (c-b direction) of the material [N/m^2]? ');
    mat_composite_2(1,4) = 0.5; %SLIMT1
    mat_composite_2(1,5) = 1.0; %SLIMC1
    mat_composite_2(1,6) = 0.5; %SLIMT2
    mat_composite_2(1,7) = 1.0; %SLIMC2
    mat_composite_2(1,8) = 0.5; %SLIMS

    % mat_composite_3(1,1) = ; % TSIZE
    mat_composite_3(1,1) = 0.95; % ERODS
    % mat_composite_3(1,3) = ; % SOFT
    mat_composite_3(1,2) = 1.0; % FS

    %INSERT 2 BLANK LINES.../n

    mat_composite_4(1,1) = 0.0214; % E11C
    mat_composite_4(1,2) = 0.0151; % E11T
    mat_composite_4(1,3) = 0.0214; % E22C
    mat_composite_4(1,4) = 0.0151; % E22T
    mat_composite_4(1,5) = 0.02; % GMS

    mat_composite_5(1,1) = 221E06; %input('What is the XC value (LONGITUDINAL COMPRESSIVE STRENGTH) of the material [Pa]? ');
    mat_composite_5(1,2) = 153E06; %input('What is the XT value (LONGITUDINAL TENSILE STRENGTH) of the material [Pa]? ');
    mat_composite_5(1,3) = 221E06; %input('What is the YC value (TRANSVERSE COMPRESSIVE STRENGTH) of the material [Pa]? ');
    mat_composite_5(1,4) = 153E06; %input('What is the YT value (TRANSVERSE TENSILE STRENGTH) of the material [Pa]? ');
    mat_composite_5(1,5) = 87E06; %input('What is the SC value (SHEAR STRENGTH) of the material [Pa]? ');
end

%*****
%****DEBRIS WEDGE MODELLING****
%*****

Thick_layers_d = 1;

%1,000 series
i=1;
level_z = 0.00005;
for debris_no = 1001:nodes_circ+1000;
    debris1(i,1) = debris_no;
    debris1(i,2) = ((OD-0.003)/2 - (0.5*(t/[Thick_layers_d]))) * cos(degrees);
    debris1(i,3) = ((OD-0.003)/2 - (0.5*(t/[Thick_layers_d]))) * sin(degrees);
    debris1(i,4) = level_z;
    degrees = degrees + degree_step;
    i=i+1;
end
debris1

%2,000 series
i=1;
level_z = 0.00005;
for debris_no = 2001:nodes_circ+2000;
    debris2(i,1) = debris_no;
    debris2(i,2) = ((OD+0.003)/2 - (0.5*(t/[Thick_layers_d]))) * cos(degrees);
    debris2(i,3) = ((OD+0.003)/2 - (0.5*(t/[Thick_layers_d]))) * sin(degrees);
    debris2(i,4) = level_z;
    degrees = degrees + degree_step;
    i=i+1;
end
debris2

```

```

%3,000 series
i=1;
level_z = 0.0004;
for debris_no = 3001:nodes_circ+3000;
    debris3(i,1) = debris_no;
    debris3(i,2) = ((OD-0.00167)/2 - (0.5*(t/[Thick_layers_d])))*cos(degrees);
    debris3(i,3) = ((OD-0.00167)/2 - (0.5*(t/[Thick_layers_d])))*sin(degrees);
    debris3(i,4) = level_z;
    degrees = degrees + degree_step;
    i=i+1;
end
debris3

%4,000 series
i=1;
level_z = 0.0004;
for debris_no = 4001:nodes_circ+4000;
    debris4(i,1) = debris_no;
    debris4(i,2) = ((OD+0.00167)/2 - (0.5*(t/[Thick_layers_d])))*cos(degrees);
    debris4(i,3) = ((OD+0.00167)/2 - (0.5*(t/[Thick_layers_d])))*sin(degrees);
    debris4(i,4) = level_z;
    degrees = degrees + degree_step;
    i=i+1;
end
debris4

%5,000 series
i=1;
level_z = 0.0009;
for debris_no = 5001:nodes_circ+5000;
    debris5(i,1) = debris_no;
    debris5(i,2) = ((OD-0.0008)/2 - (0.5*(t/[Thick_layers_d])))*cos(degrees);
    debris5(i,3) = ((OD-0.0008)/2 - (0.5*(t/[Thick_layers_d])))*sin(degrees);
    debris5(i,4) = level_z;
    degrees = degrees + degree_step;
    i=i+1;
end
debris5

%6,000 series
i=1;
level_z = 0.0009;
for debris_no = 6001:nodes_circ+6000;
    debris6(i,1) = debris_no;
    debris6(i,2) = ((OD+0.0008)/2 - (0.5*(t/[Thick_layers_d])))*cos(degrees);
    debris6(i,3) = ((OD+0.0008)/2 - (0.5*(t/[Thick_layers_d])))*sin(degrees);
    debris6(i,4) = level_z;
    degrees = degrees + degree_step;
    i=i+1;
end
debris6

%7,000 series
i=1;
level_z = 0.0016;
for debris_no = 7001:nodes_circ+7000;
    debris7(i,1) = debris_no;
    debris7(i,2) = ((OD-0.0003)/2 - (0.5*(t/[Thick_layers_d])))*cos(degrees);
    debris7(i,3) = ((OD-0.0003)/2 - (0.5*(t/[Thick_layers_d])))*sin(degrees);
    debris7(i,4) = level_z;
    degrees = degrees + degree_step;
    i=i+1;
end
debris7

%8,000 series
i=1;
level_z = 0.0016;
for debris_no = 8001:nodes_circ+8000;
    debris8(i,1) = debris_no;
    debris8(i,2) = ((OD+0.0003)/2 - (0.5*(t/[Thick_layers_d])))*cos(degrees);
    debris8(i,3) = ((OD+0.0003)/2 - (0.5*(t/[Thick_layers_d])))*sin(degrees);
    debris8(i,4) = level_z;
    degrees = degrees + degree_step;
    i=i+1;
end
debris8

%9,000 series
i=1;
level_z = 0.003;
for debris_no = 9001:nodes_circ+9000;
    debris9(i,1) = debris_no;
    debris9(i,2) = ((OD)/2 - (0.5*(t/[Thick_layers_d])))*cos(degrees);
    debris9(i,3) = ((OD)/2 - (0.5*(t/[Thick_layers_d])))*sin(degrees);
    debris9(i,4) = level_z;
    degrees = degrees + degree_step;
    i=i+1;
end
debris9

%****ORGANISE DEBRIS WEDGE ELEMENTS****

%6-noded pentahedrons
i=1;
five = 5000;
six = 6000;
seven = 7000;
eight = 8000;
nine = 9000;
for debris_elem = 9000:9000+nodes_circ-2;
    element_d_shell1(i,1) = debris_elem;
    element_d_shell1(i,2) = 80;
    element_d_shell1(i,3) = seven+1;

```

```

element_d_shell1(i,4) = eight+1;
element_d_shell1(i,5) = eight+2;
element_d_shell1(i,6) = seven+2;
element_d_shell1(i,7) = nine+1;
element_d_shell1(i,8) = nine+1;
element_d_shell1(i,9) = nine+2;
element_d_shell1(i,10) = nine+2;
seven=seven+1;
eight=eight+1;
nine=nine+1;
i=i+1;
end
for debris_elem = 9000:nodes_circ-1;
element_d_shell1(i,1) = debris_elem;
element_d_shell1(i,2) = 80;
element_d_shell1(i,3) = seven+1;
element_d_shell1(i,4) = eight+1;
element_d_shell1(i,5) = eight-(nodes_circ-2);
element_d_shell1(i,6) = seven-(nodes_circ-2);
element_d_shell1(i,7) = nine+1;
element_d_shell1(i,8) = nine+1;
element_d_shell1(i,9) = nine-(nodes_circ-2);
element_d_shell1(i,10) = nine-(nodes_circ-2);
i=i+1;
end

%8-noded hexahedrons
i=1;
five = 5000;
six = 6000;
seven = 7000;
eight = 8000;
nine = 9000;
for debris_elem = 8000:8000+nodes_circ-2;
element_d_shell2(i,1) = debris_elem;
element_d_shell2(i,2) = 80;
element_d_shell2(i,3) = five+1;
element_d_shell2(i,4) = six+1;
element_d_shell2(i,5) = six+2;
element_d_shell2(i,6) = five+2;
element_d_shell2(i,7) = seven+1;
element_d_shell2(i,8) = eight+1;
element_d_shell2(i,9) = eight+2;
element_d_shell2(i,10) = seven+2;
five=five+1;
six=six+1;
seven=seven+1;
eight=eight+1;
nine=nine+1;
i=i+1;
end
for debris_elem = 8000+nodes_circ-1;
element_d_shell2(i,1) = debris_elem;
element_d_shell2(i,2) = 80;
element_d_shell2(i,3) = five+1;
element_d_shell2(i,4) = six+1;
element_d_shell2(i,5) = six-(nodes_circ-2);
element_d_shell2(i,6) = five-(nodes_circ-2);
element_d_shell2(i,7) = seven+1;
element_d_shell2(i,8) = eight+1;
element_d_shell2(i,9) = eight-(nodes_circ-2);
element_d_shell2(i,10) = seven-(nodes_circ-2);
i=i+1;
end

i=1;
three = 3000;
four = 4000;
five = 5000;
six = 6000;

for debris_elem = 7000:7000+nodes_circ-2;
element_d_shell3(i,1) = debris_elem;
element_d_shell3(i,2) = 80;
element_d_shell3(i,3) = three+1;
element_d_shell3(i,4) = four+1;
element_d_shell3(i,5) = four+2;
element_d_shell3(i,6) = three+2;
element_d_shell3(i,7) = five+1;
element_d_shell3(i,8) = six+1;
element_d_shell3(i,9) = six+2;
element_d_shell3(i,10) = five+2;
three=three+1;
four=four+1;
five=five+1;
six=six+1;
i=i+1;
end
for debris_elem = 7000+nodes_circ-1;
element_d_shell3(i,1) = debris_elem;
element_d_shell3(i,2) = 80;
element_d_shell3(i,3) = three+1;
element_d_shell3(i,4) = four+1;
element_d_shell3(i,5) = four-(nodes_circ-2);
element_d_shell3(i,6) = three-(nodes_circ-2);
element_d_shell3(i,7) = five+1;
element_d_shell3(i,8) = six+1;
element_d_shell3(i,9) = six-(nodes_circ-2);
element_d_shell3(i,10) = five-(nodes_circ-2);
i=i+1;
end

i=1;
one = 1000;

```

```

two = 2000;
three = 3000;
four = 4000;

for debris_elem = 6000:6000+nodes_circ-2;
    element_d_shell4(i,1) = debris_elem;
    element_d_shell4(i,2) = 80;
    element_d_shell4(i,3) = one+1;
    element_d_shell4(i,4) = two+1;
    element_d_shell4(i,5) = two+2;
    element_d_shell4(i,6) = one+2;
    element_d_shell4(i,7) = three+1;
    element_d_shell4(i,8) = four+1
    element_d_shell4(i,9) = four+2;
    element_d_shell4(i,10) = three+2;
    one=one+1;
    two=two+1;
    three=three+1;
    four=four+1;
    i=i+1;
end
for debris_elem = 6000+nodes_circ-1;
    element_d_shell4(i,1) = debris_elem;
    element_d_shell4(i,2) = 80;
    element_d_shell4(i,3) = one+1;
    element_d_shell4(i,4) = two+1;
    element_d_shell4(i,5) = two-(nodes_circ-2);
    element_d_shell4(i,6) = one-(nodes_circ-2);
    element_d_shell4(i,7) = three+1;
    element_d_shell4(i,8) = four+1;
    element_d_shell4(i,9) = four-(nodes_circ-2);
    element_d_shell4(i,10) = three-(nodes_circ-2);
    i=i+1;
end

%DEBRIS WEDGE MATERIAL DATA
mat_rigid_d_1(1,1) = 80;
mat_rigid_d_1(1,2) = mat_composite_1(1,2);
mat_rigid_d_1(1,3) = mat_composite_1(1,3);
mat_rigid_d_1(1,4) = mat_composite_1(1,6);
mat_rigid_d_1(1,5) = 0.0;
mat_rigid_d_1(1,6) = 0.0;
mat_rigid_d_1(1,7) = 0.0;
mat_rigid_d_2(1,1) = 1.0;
mat_rigid_d_2(1,2) = 7;
mat_rigid_d_2(1,3) = 7;
mat_rigid_d_3(1,1) = 0.0;
mat_rigid_d_3(1,2) = 0.0;
mat_rigid_d_3(1,3) = 0.0;
mat_rigid_d_3(1,4) = 0.0;
mat_rigid_d_3(1,5) = 0.0;
mat_rigid_d_3(1,6) = 0.0;

mat_rigid_d_1
mat_rigid_d_2
mat_rigid_d_3

%DEBRIS WEDGE SECTION_SHELL DATA
debris_shell_1(1,1) = 80;
debris_shell_1(1,2) = 2;

debris_shell_1

%DEBRIS WEDGE PART DATA
debris_part(1,1) = 80;
debris_part(1,2) = 80;
debris_part(1,3) = 80;
debris_part(1,4) = 0;
debris_part(1,5) = 0;
debris_part(1,6) = 0;
debris_part(1,7) = 0;

debris_part

%DEBRIS WEDGE CONTACT DATA
z=1
for debris_wedge_contact = 1:Thick_layers;
    debris_wedge_contact_1(z,1) = debris_wedge_contact;

    debris_wedge_contact_2a(z,1) = debris_wedge_contact;
    debris_wedge_contact_2a(z,2) = 80;
    debris_wedge_contact_2a(z,3) = 3;
    debris_wedge_contact_2a(z,4) = 3;
    debris_wedge_contact_2b(z,1) = 1;
    debris_wedge_contact_2b(z,2) = 1;

    debris_wedge_contact_3(z,1) = 0.3; %input('What is the static (PEAK) coefficient of FRICTION between TUBE and CONTACT SURFACE? ');
    debris_wedge_contact_3(z,2) = 0.2; %input('What is the dynamic (SLIDING) coefficient of FRICTION? ');
    debris_wedge_contact_3(z,3) = 1.0; %input('What is the exponential DECAY coefficient? ');
    debris_wedge_contact_3(z,4) = (430000000)/(sqrt(3));
    debris_wedge_contact_3(z,5) = 20.0;
    debris_wedge_contact_3(z,6) = 1;
    debris_wedge_contact_3(z,7) = 0.0;
    debris_wedge_contact_3(z,8) = 1.0E+20;

    debris_wedge_contact_4a(z,1) = 1.0;
    debris_wedge_contact_4a(z,2) = 1.0;
    debris_wedge_contact_4b(z,1) = 1.0;
    debris_wedge_contact_4b(z,2) = 1.0;
    debris_wedge_contact_4b(z,3) = 1.0;
    debris_wedge_contact_4b(z,4) = 1.0;
    z = z + 1;
end

```

```

%*****Section Shell Modelling*****

elemform = 16;      %input('what element formulation would you like to use?');
intpoint = 3;      %input('How many INTEGRATION POINTS should be used?');

y=1;

for section_shellx = 1:Thick_layers
    sectionshell(y,1) = section_shellx;
    sectionshell(y,2) = elemform;
    sectionshell(y,3) = 1.0;
    sectionshell(y,4) = intpoint;
    sectionshell(y,5) = 0;
    sectionshell(y,6) = -1;
    sectionshell(y,7) = 1;

    sectionshell2(y,1) = (t/Thick_layers)-(0.00005*t);
    sectionshell2(y,2) = (t/Thick_layers)-(0.00005*t);
    sectionshell2(y,3) = (t/Thick_layers)-(0.00005*t);
    sectionshell2(y,4) = (t/Thick_layers)-(0.00005*t);
    sectionshell2(y,5) = 0.0;

    sectionshell3(y,1) = 90;
    sectionshell3(y,2) = 90;
    sectionshell3(y,3) = 90;
    sectionshell3(y,4) = 90;
    sectionshell3(y,5) = 90;
    y=y+1;

end
sectionshell
sectionshell2
sectionshell3

%*****INTEGRATION_SHELL*****

integrationshell(1,1) = 1;
integrationshell(1,2) = intpoint;
integrationshell(1,3) = 1;

integrationshell

%*****PART MODELLING*****

z=1;
for section_partx = 1:Thick_layers
    sectionpart(z,1) = section_partx;
    sectionpart(z,2) = section_partx;
    sectionpart(z,3) = 1;
    sectionpart(z,4) = 0;
    sectionpart(z,5) = 0;
    sectionpart(z,6) = 0;
    sectionpart(z,7) = 0;
    z=z+1;
end

sectionpart

sprintf('%s','*****')
sprintf('%s','*****CONTACT SURFACE MODELLING*****')
sprintf('%s','*****')

%****Contact Surface Mesh*****

sprintf('%s','WIDTH and BREADTH of contact surface are taken to be 0.15 m')
surf_width = 0.15;
surf_breadth = 0.15;
surf_width_no_levels = 6;          %NODES ALONG EDGE OF CONTACT SURFACE
surf_breadth_no_levels = surf_width_no_levels;

surf_width_step = surf_width/(surf_width_no_levels -1);
surf_breadth_step = surf_breadth/(surf_breadth_no_levels -1);

surf_node_no = 1;
surf_level_x = 0.075;
surf_level_z = -0.01;

for surf_width_level = 1:surf_width_no_levels
    surf_level_y = -0.075
    for surf_node_no = ((surf_width_level-1)*surf_breadth_no_levels)+1:(surf_breadth_no_levels*surf_width_level);
        surf_node(surf_node_no,1) = 100000+surf_node_no;
        surf_node(surf_node_no,2) = surf_level_x;
        surf_node(surf_node_no,3) = surf_level_y;
        surf_node(surf_node_no,4) = surf_level_z;
        surf_level_y = surf_level_y + surf_breadth_step;
    end
    surf_level_x = surf_level_x - surf_width_step;
end
surf_node

surf_node_no = 1;
surf_level_x = 0.075;
surf_level_z = 0.0;

for surf_width_level = 1:surf_width_no_levels
    surf_level_y = -0.075
    for surf_node_no = ((surf_width_level-1)*surf_breadth_no_levels)+1:(surf_breadth_no_levels*surf_width_level);
        surf_node2(surf_node_no,1) = 101000+surf_node_no;
        surf_node2(surf_node_no,2) = surf_level_x;
        surf_node2(surf_node_no,3) = surf_level_y;
        surf_node2(surf_node_no,4) = surf_level_z;
        surf_level_y = surf_level_y + surf_breadth_step;
    end
end
surf_node2

```

```

end
surf_level_x = surf_level_x - surf_width_step;
end
surf_node2

%ORGANISE CONTACT SURFACE ELEMENTS AND THEIR NODAL CONNECTIONS
surf_part_no = 1;
surf_element_no = 1;
for surf_width_level = 1:(surf_width_no_levels-1);
    for surf_node_no = ((surf_width_level-1)*surf_breadth_no_levels)+1:(surf_breadth_no_levels*surf_width_level)-1;
        surf_element_shell(surf_element_no,1) = 1000000+surf_element_no;
        surf_element_shell(surf_element_no,2) = 1000000+surf_part_no;
        surf_element_shell(surf_element_no,3) = 1000000+surf_node_no;
        surf_element_shell(surf_element_no,4) = 1000000+surf_node_no+1;
        surf_element_shell(surf_element_no,5) = 1000000+surf_node_no+1+surf_breadth_no_levels;
        surf_element_shell(surf_element_no,6) = 1000000+surf_node_no+surf_breadth_no_levels;
        surf_element_shell(surf_element_no,7) = 1010000+surf_node_no;
        surf_element_shell(surf_element_no,8) = 1010000+surf_node_no+1;
        surf_element_shell(surf_element_no,9) = 1010000+surf_node_no+1+surf_breadth_no_levels;
        surf_element_shell(surf_element_no,10) = 1010000+surf_node_no+surf_breadth_no_levels;
        surf_element_no = surf_element_no + 1;
    end
end
surf_element_shell

%****Material Modelling****

sprintf('%s','Material Type 20, *MAT_RIGID with full translational and rotational constraint')

mat_rigid_1(1,1) = 100001;
mat_rigid_1(1,2) = 7800; %CONTACT SURFACE MASS DENSITY
mat_rigid_1(1,3) = 205000000000; %CONTACT SURFACE YOUNG'S MODULUS
mat_rigid_1(1,4) = 0.3; %CONTACT SURFACE POISSONS RATIO
mat_rigid_1(1,5) = 0.0;
mat_rigid_1(1,6) = 0.0;
mat_rigid_1(1,7) = 0.0;
mat_rigid_2(1,1) = 1.0;
mat_rigid_2(1,2) = 7;
mat_rigid_2(1,3) = 7;
mat_rigid_3(1,1) = 0.0;
mat_rigid_3(1,2) = 0.0;
mat_rigid_3(1,3) = 0.0;
mat_rigid_3(1,4) = 0.0;
mat_rigid_3(1,5) = 0.0;
mat_rigid_3(1,6) = 0.0;

mat_rigid_1
mat_rigid_2
mat_rigid_3

%*****SECTION SHELL MODELLING*****

sprintf('%s','Shell Modelling, *SECTION_SOLID')
surf_section_shell_1(1,1) = 100001;
surf_section_shell_1(1,2) = 2;

surf_section_shell_1

%*****PART MODELLING*****

surf_part(1,1) = 1000000+surf_part_no;
surf_part(1,2) = surf_section_shell_1(1,1);
surf_part(1,3) = mat_rigid_1(1,1);
surf_part(1,4) = 0;
surf_part(1,5) = 0;
surf_part(1,6) = 0;
surf_part(1,7) = 0;

surf_part

sprintf('%s','*****')
sprintf('%s','*****RAM MODELLING*****')
sprintf('%s','*****')

%****Contact Surface Mesh****

sprintf('%s','WIDTH and BREADTH of ram are taken to be 0.1 m')
ram_width = 0.1;
ram_breadth = 0.1;
ram_width_no_levels = 6; %NUMBER OF NODES ALONG EDGE OF CONTACT SURFACE
ram_breadth_no_levels = ram_width_no_levels;

ram_width_step = ram_width/(ram_width_no_levels -1);
ram_breadth_step = ram_breadth/(ram_breadth_no_levels -1);

ram_width_step = ram_width/(ram_width_no_levels -1);
ram_breadth_step = ram_breadth/(ram_breadth_no_levels -1);

ram_node_no = 1;
ram_level_x = 0.05;
ram_level_z = L+0.00389; %0.005

for ram_width_level = 1:ram_width_no_levels
    ram_level_y = -0.05
    for ram_node_no = ((ram_width_level-1)*ram_breadth_no_levels)+1:(ram_breadth_no_levels*ram_width_level);
        ram_node(ram_node_no,1) = 2000000+ram_node_no;
        ram_node(ram_node_no,2) = ram_level_x;
        ram_node(ram_node_no,3) = ram_level_y;
        ram_node(ram_node_no,4) = ram_level_z;
        ram_level_y = ram_level_y + ram_breadth_step;
    end
    ram_level_x = ram_level_x - ram_width_step;
end
ram_node

```

```

%ORGANISE RAM ELEMENTS AND THEIR NODAL CONNECTIONS
ram_part_no = 1;
ram_element_no = 1;
for ram_width_level = 1:(ram_width_no_levels-1);
    for ram_node_no = ((ram_width_level-1)*ram_breadth_no_levels)+1:(ram_breadth_no_levels*ram_width_level)-1;
        ram_element_shell(ram_element_no,1) = 2000000+ram_element_no;
        ram_element_shell(ram_element_no,2) = 2000000+ram_part_no;
        ram_element_shell(ram_element_no,3) = 2000000+ram_node_no;
        ram_element_shell(ram_element_no,4) = 2000000+ram_node_no+1;
        ram_element_shell(ram_element_no,5) = 2000000+ram_node_no+1+ram_breadth_no_levels;
        ram_element_shell(ram_element_no,6) = 2000000+ram_node_no+ram_breadth_no_levels;
        ram_element_no = ram_element_no + 1;
    end
end
ram_element_shell

%****Material Modelling****

sprintf('%s','Material Type 20, *MAT_RIGID with x,z translational and all rotational constraint')

mat_rigid2_1(1,1) = 200001;
mat_rigid2_1(1,2) = 7800; %RAM MASS DENSITY
mat_rigid2_1(1,3) = 205000000000; %RAM YOUNGS MODULUS
mat_rigid2_1(1,4) = 0.3; %RAM POISSONS RATIO
mat_rigid2_1(1,5) = 0.0;
mat_rigid2_1(1,6) = 0.0;
mat_rigid2_1(1,7) = 0.0;
mat_rigid2_2(1,1) = 1.0;
mat_rigid2_2(1,2) = 4;
mat_rigid2_2(1,3) = 7;
mat_rigid2_3(1,1) = 0.0;
mat_rigid2_3(1,2) = 0.0;
mat_rigid2_3(1,3) = 0.0;
mat_rigid2_3(1,4) = 0.0;
mat_rigid2_3(1,5) = 0.0;
mat_rigid2_3(1,6) = 0.0;

mat_rigid2_1
mat_rigid2_2
mat_rigid2_3

%*****Section Shell Modelling*****

sprintf('%s','Shell Modelling, *SECTION_SHELL. assuming 1mm thick ram')
ram_section_shell_1(1,1) = 200001;
ram_section_shell_1(1,2) = 2;
ram_section_shell_1(1,3) = 1.0;
ram_section_shell_1(1,4) = 2;
ram_section_shell_1(1,5) = 0.0;
ram_section_shell_1(1,6) = 0.0;
ram_section_shell_1(1,7) = 0;

ram_section_shell_2(1,1) = 0.001;
ram_section_shell_2(1,2) = 0.001;
ram_section_shell_2(1,3) = 0.001;
ram_section_shell_2(1,4) = 0.001;
ram_section_shell_2(1,5) = 0.0;

ram_section_shell_1
ram_section_shell_2

%*****Part Modelling*****

ram_part(1,1) = 2000000+ram_part_no;
ram_part(1,2) = ram_section_shell_1(1,1);
ram_part(1,3) = mat_rigid2_1(1,1);
ram_part(1,4) = 0;
ram_part(1,5) = 0;
ram_part(1,6) = 0;
ram_part(1,7) = 0;

ram_part

sprintf('%s','*****')
sprintf('%s','*****Loading Conditions*****')
sprintf('%s','*****')

%FOUR CONTACTS PLUS RAM DISPLACEMENT DATA

friction = 2 %input('Would you like to alter the FRICTION COEFFICIENTS [(1 for YES) or (2 for NO)]? ');

if friction == 1
    staticf = input('What is the STATIC COEFFICIENT OF FRICTION between tube and platen? ');
    dynamicf = input('What is the DYNAMIC COEFFICIENT OF FRICTION between tube and platen? ');
    decayf = input('What is the EXPONENTIAL DECAY COEFFICIENT between tube and platen? ');
    tubestaticf = input('What is the STATIC COEFFICIENT OF FRICTION for tube-tube contact? ');
    tubedynamicf = input('What is the DYNAMIC COEFFICIENT OF FRICTION for tube-tube contact? ');
    tubedecayf = input('What is the EXPONENTIAL DECAY COEFFICIENT for tube-tube contact? ');
elseif friction == 2
    sprintf('Friction values are assumed to be static=0.3, dynamic=0.2, decay=1 ');
    staticf = 0.3;
    dynamicf = 0.28;
    decayf = 1;
    tubedynamicf = 0.3;
    tubestaticf = 0.28
    tubedecayf = 1;
end

%TUBE-SURFACE CONTACT
sprintf('%s','*****Tube Surface Contact*****')
tube_surf_contact_1(1,1) = 1;

z=1

```

```

for loop5 = 1:Thick_layers;
    tube_surf_contact_1(z,1) = loop5;

    tube_surf_contact_2a(z,1) = loop5;
    tube_surf_contact_2a(z,2) = surf_part(1,1);
    tube_surf_contact_2a(z,3) = 3;
    tube_surf_contact_2a(z,4) = 3;
    tube_surf_contact_2b(z,1) = 1;
    tube_surf_contact_2b(z,2) = 1;

    tube_surf_contact_3(z,1) = staticf;           %input('What is the static (PEAK) coefficient of FRICTION between TUBE and CONTACT SURFACE? ');
    tube_surf_contact_3(z,2) = dynamicf;         %input('What is the dynamic (SLIDING) coefficient of FRICTION? ');
    tube_surf_contact_3(z,3) = decayf;           %input('What is the exponential DECAY coefficient? ');
    tube_surf_contact_3(z,4) = (430000000)/(sqrt(3));
    tube_surf_contact_3(z,5) = 20.0;
    tube_surf_contact_3(z,6) = 1;
    tube_surf_contact_3(z,7) = 0.0;
    tube_surf_contact_3(z,8) = 1.0E+20;

    tube_surf_contact_4a(z,1) = 1.0;
    tube_surf_contact_4a(z,2) = 1.0;
    tube_surf_contact_4b(z,1) = 1.0;
    tube_surf_contact_4b(z,2) = 1.0;
    tube_surf_contact_4b(z,3) = 1.0;
    tube_surf_contact_4b(z,4) = 1.0;
    z = z + 1;
end

%TUBE-SELF CONTACT
sprintf('%s','*****Tube Self Contact*****')

z=1
for loop12 = 1:Thick_layers;
    tube_self_contact_1(z,1) = loop12;

    tube_self_contact_2a(z,1) = loop12;
    tube_self_contact_2a(z,2) = loop12;
    tube_self_contact_2a(z,3) = 3;
    tube_self_contact_2a(z,4) = 3;
    tube_self_contact_2b(z,1) = 1;
    tube_self_contact_2b(z,2) = 1;

    tube_self_contact_3(z,1) = staticf;           %input('What is the static (PEAK) coefficient of FRICTION between TUBE and CONTACT SURFACE? ');
    tube_self_contact_3(z,2) = dynamicf;         %input('What is the dynamic (SLIDING) coefficient of FRICTION? ');
    tube_self_contact_3(z,3) = decayf;           %input('What is the exponential DECAY coefficient? ');
    tube_self_contact_3(z,4) = (430000000)/(sqrt(3));
    tube_self_contact_3(z,5) = 20.0;
    tube_self_contact_3(z,6) = 1;
    tube_self_contact_3(z,7) = 0.0;
    tube_self_contact_3(z,8) = 1.0E+20;

    tube_self_contact_4a(z,1) = 1.0;
    tube_self_contact_4a(z,2) = 1.0;
    tube_self_contact_4b(z,1) = 1.0;
    tube_self_contact_4b(z,2) = 1.0;
    tube_self_contact_4b(z,3) = 1.0;
    tube_self_contact_4b(z,4) = 1.0;
    z = z + 1;
end

%TUBE-LAYER CONTACT
sprintf('%s','*****Tube Layer Contact*****')

z=1
for loop13 = 1:Thick_layers-1;
    tube_layer_contact_1(z,1) = loop13+1;

    tube_layer_contact_2a(z,1) = loop13;
    tube_layer_contact_2a(z,2) = loop13+1;
    tube_layer_contact_2a(z,3) = 3;
    tube_layer_contact_2a(z,4) = 3;
    tube_layer_contact_2b(z,1) = 1;
    tube_layer_contact_2b(z,2) = 1;

    tube_layer_contact_3(z,1) = staticf;         %input('What is the static (PEAK) coefficient of FRICTION between TUBE and CONTACT SURFACE? ');
    tube_layer_contact_3(z,2) = dynamicf;         %input('What is the dynamic (SLIDING) coefficient of FRICTION? ');
    tube_layer_contact_3(z,3) = decayf;           %input('What is the exponential DECAY coefficient? ');
    tube_layer_contact_3(z,4) = (430000000)/(sqrt(3));
    tube_layer_contact_3(z,5) = 20.0;
    tube_layer_contact_3(z,6) = 1;
    tube_layer_contact_3(z,7) = 0.0;
    tube_layer_contact_3(z,8) = 1.0E+20;

    tube_layer_contact_4a(z,1) = 1.0;
    tube_layer_contact_4a(z,2) = 1.0;
    tube_layer_contact_4b(z,1) = 1.0;
    tube_layer_contact_4b(z,2) = 1.0;
    tube_layer_contact_4b(z,3) = 1.0;
    tube_layer_contact_4b(z,4) = 1.0;

    tube_layer_contact_5(z,1) = 1;

    z = z + 1;
end

%TUBE-RAM CONTACT INPUTS
sprintf('%s','*****Tube Ram Contact*****')

z = 1;
for loop6 = 1:Thick_layers;
    tube_ram_contact_1(z,1) = loop6;

```

```

tube_ram_contact_2a(z,1) = loop6;
tube_ram_contact_2a(z,2) = ram_part(1,1);
tube_ram_contact_2a(z,3) = 3;
tube_ram_contact_2a(z,4) = 3;
tube_ram_contact_2b(z,1) = 1;
tube_ram_contact_2b(z,2) = 1;

tube_ram_contact_3(z,1) = staticf;
tube_ram_contact_3(z,2) = dynamicf;           %DEFINES TUBE-RAM FRICTION THE SAME AS CONTACT SURFACE FRICTION
tube_ram_contact_3(z,3) = decayf;
tube_ram_contact_3(z,4) = (430000000)/(sqrt(3));
tube_ram_contact_3(z,5) = 20.0;
tube_ram_contact_3(z,6) = 1;
tube_ram_contact_3(z,7) = 0.0;
tube_ram_contact_3(z,8) = 1.0E+20;

tube_ram_contact_4a(z,1) = 1.0;
tube_ram_contact_4a(z,2) = 1.0;
tube_ram_contact_4b(z,1) = 1.0;
tube_ram_contact_4b(z,2) = 1.0;
tube_ram_contact_4b(z,3) = 1.0;
tube_ram_contact_4b(z,4) = 1.0;
z = z + 1;
end

%PRESCRIBED MOTION OF RAM
ram_motion_1a(1,1) = ram_part(1,1);
ram_motion_1a(1,2) = 3;
ram_motion_1a(1,3) = 0;
ram_motion_1a(1,4) = 5;
ram_motion_1a(1,5) = -1;
ram_motion_1b(1,1) = 1E28;
ram_motion_1b(1,2) = 0.0;

%*****
%*****WRITE TO LS_DYNA KEY FILE*****
%*****

```

## A4 Effective Beam Stiffness Calculation

Representation of the elastic interlaminar material with discrete elements is possible provided the representative stiffness is maintained. This is done by calculating an equivalent stiffness and modifying the Young's modulus to suit. Below is a description and example of how the experimental data is converted into the equivalent stiffness and hence, Young's modulus, for the Toray material.

### A4.1 Toray Example

---

The through-thickness compression test is made up of 50 layers, totalling 18.7mm in thickness, which was cut to 13mm wide and 13mm deep. Assuming the fibre layers in the through-thickness direction are very thin, it is primarily the behaviour of the resin that controls the loading response in this direction. This can be conceptualised as a spring connecting each fibrous layer with a spring whose Young's modulus is 7.45GPa, determined experimentally in a through-thickness compression test. Since the distance between each fibrous layer is known together with the cross-sectional area, we can calculate the stiffness or 'k' (from the spring function  $F=kx$ ) using  $k = \frac{EA}{L}$ . Once the stiffness of the resin is known, we insert the cross-sectional area of the beams together with the beam's length. The length of the beam is different from the delamination simulations (1.35mm) to the tube simulations (0.5mm). These steps are shown below;

Each interlaminar resin layer is  $\frac{t}{no.layers} = \frac{0.0187}{50} = 0.000374\text{m}$  thick.

The cross-sectional area of resin is,  $A = 0.013\text{m}^2 = 0.000169\text{m}^2$ .

The experimental Young's modulus is  $E_3 = 7.45\text{GPa}$ .

With these we can calculate  $K_{\text{exp}}$ ;

$$K_{\text{exp}} = \frac{E_3 \times A_{\text{exp}}}{L} = \frac{7.45\text{GPa} \times 0.000169}{0.000374} = 3.366 \times 10^9$$

Now for the stiffness to remain equivalent the following must be true;

$$\frac{K_{\text{exp}}}{A_{\text{exp}}} = \frac{K_{\text{beam}}}{A_{\text{beam}}}$$

So, given that  $A_{\text{beam}} = \pi(0.00045)^2 = 6.36 \times 10^{-7} \text{m}^2$ ,

$$K_{\text{beam}} = 1.267 \times 10^7.$$

Now, using the element lengths given above, we can calculate our equivalent Young's modulus through;

$$K_{\text{beam}} = \frac{E_{\text{beam}} \times A_{\text{beam}}}{L_{\text{beam}}}$$

$$E_{\text{DCB,ENF}} = 26.899\text{GPa}$$

$$E_{\text{TUBE}} = 9.963\text{GPa}$$

∴ Employing these moduli in the respective simulations, we can expect an equivalent stiffness to that demonstrated experimentally.

## A5 Force-Based Delamination - Tube Modelling Results

### A5.1 Flat-platen load-displacement response

#### A5.1.1 CFRM

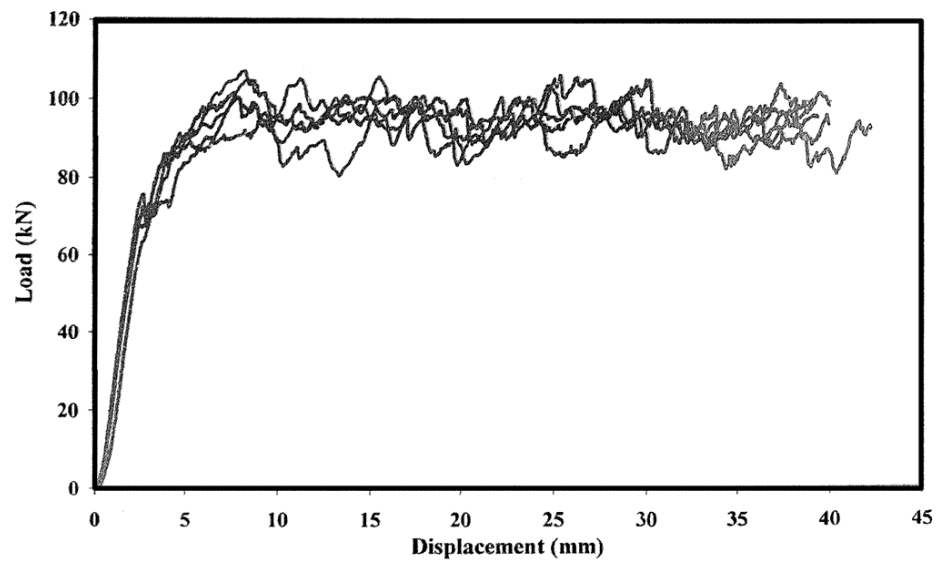


Figure A5.1. Experimental load-displacement response of CFRM flat-platen crush tests [55].

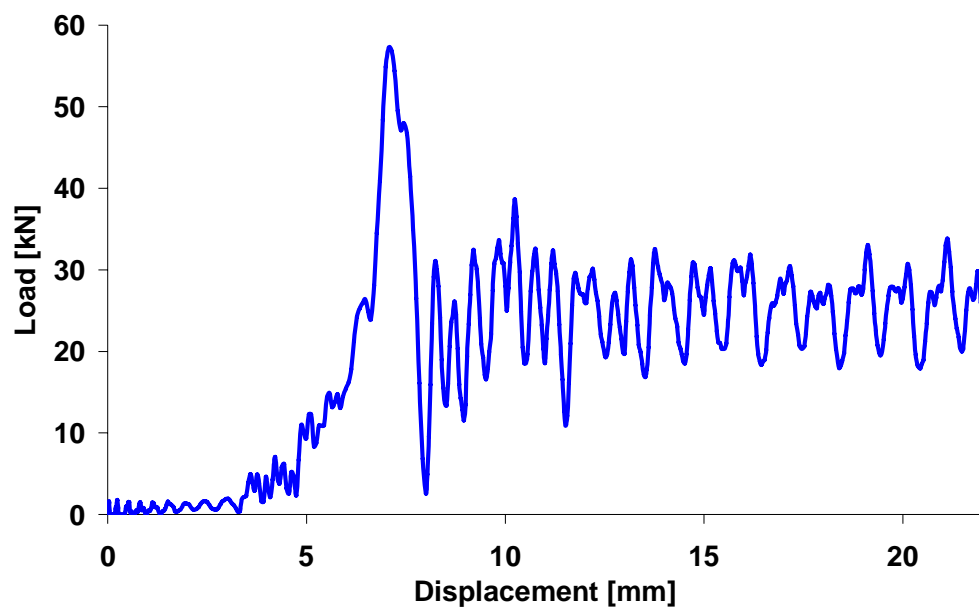


Figure A5.2. Simulated load-displacement response of CFRM flat-platen crush test.

**A5.1.2 Toray**

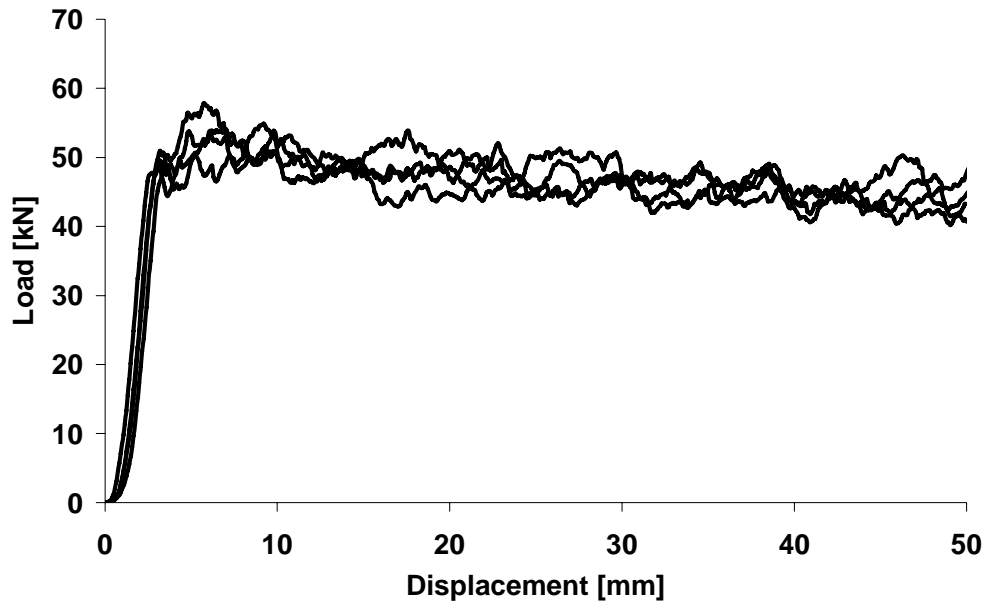


Figure A5.3. Experimental load-displacement response of Toray flat-platen crush test.

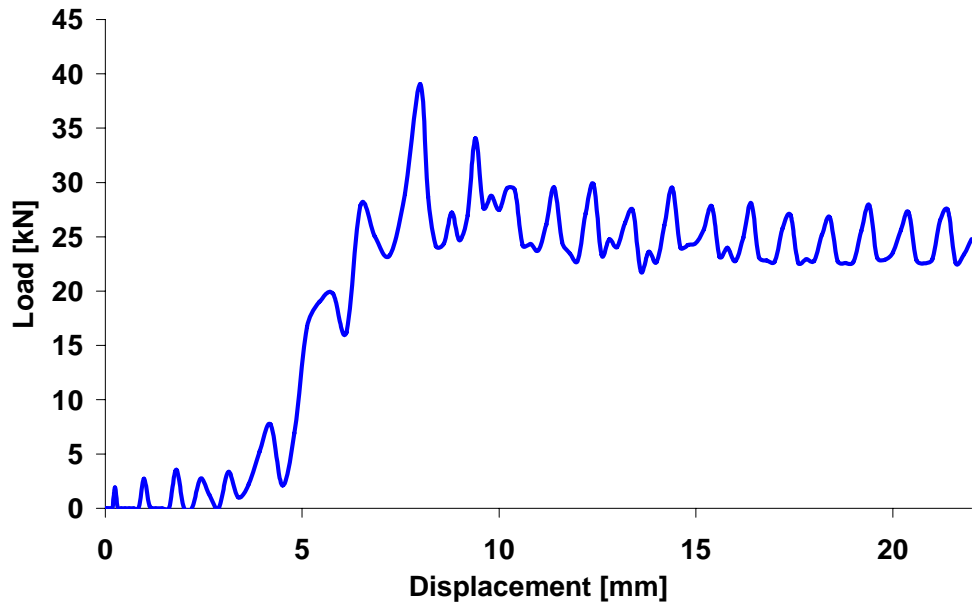


Figure A5.4. Simulated load-displacement response of Toray flat-platen test.

## A5.2 Plug initiator load-displacement response

### A5.2.1 CFRM

*5mm Radius*

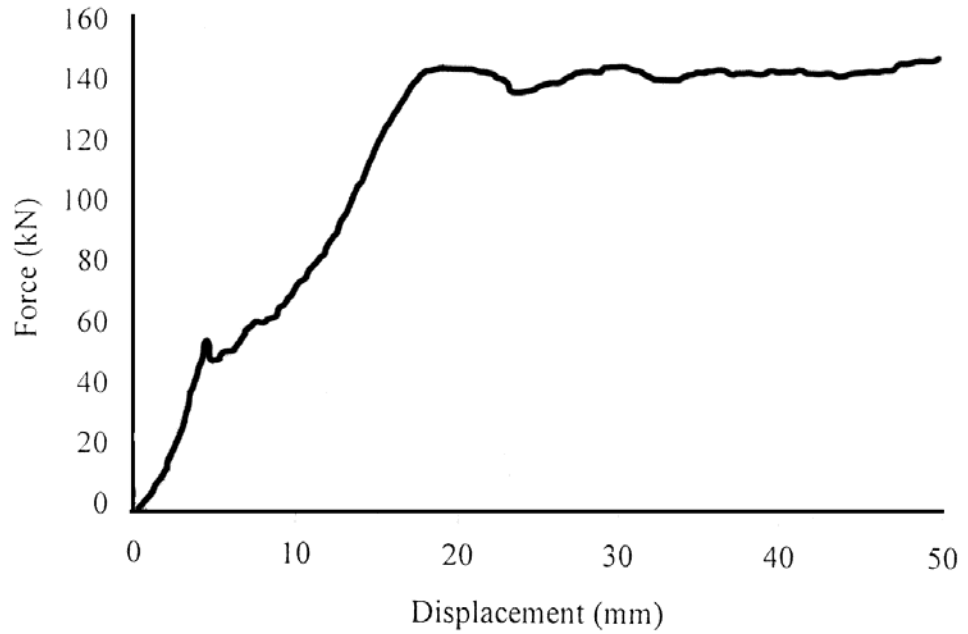


Figure A5.5. Experimental load-displacement response of CFRM tube crushed on 5mm radius plug-initiator (enhanced for clarity) [54].

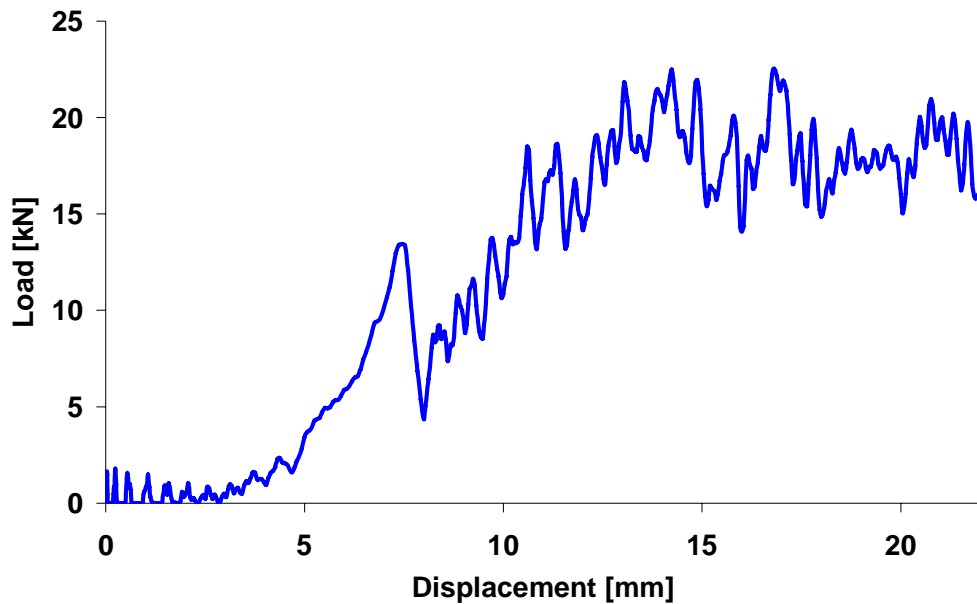


Figure A5.6. Simulated load-displacement response of CFRM 5mm plug-initiator test.

7.5mm Radius

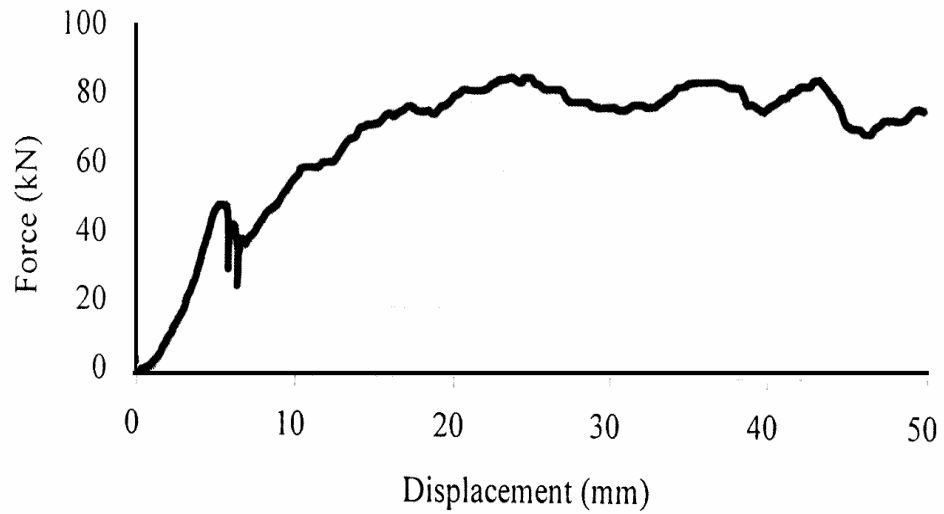


Figure A5.7. Experimental load-displacement response of CFRM tube crushed on 7.5mm radius plug initiator (enhanced for clarity) [54].

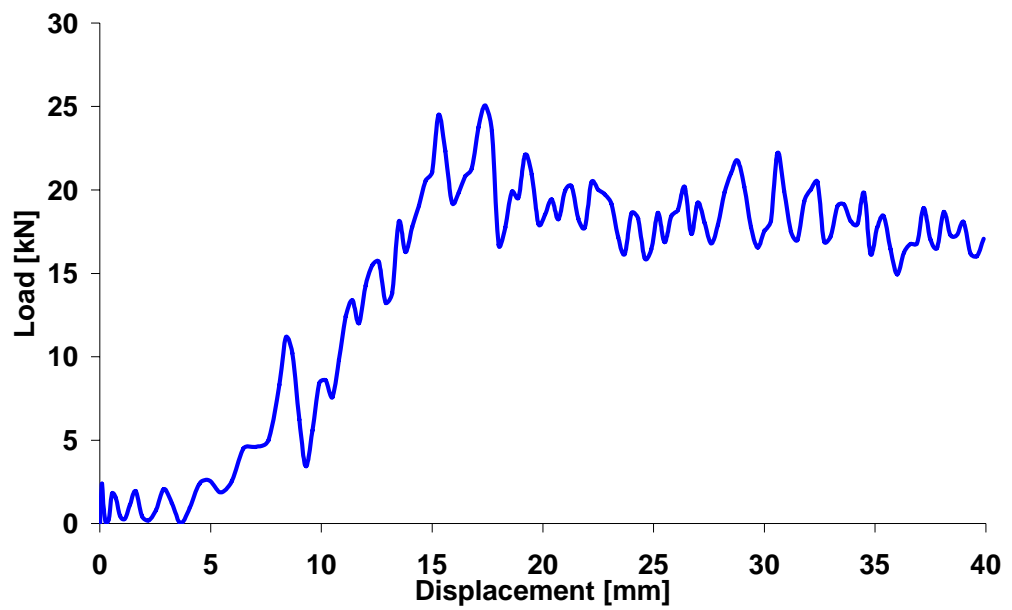


Figure A5.8. Simulated load-displacement response of CFRM tube crushed on 7.5mm radius plug initiator.

*10mm Radius*

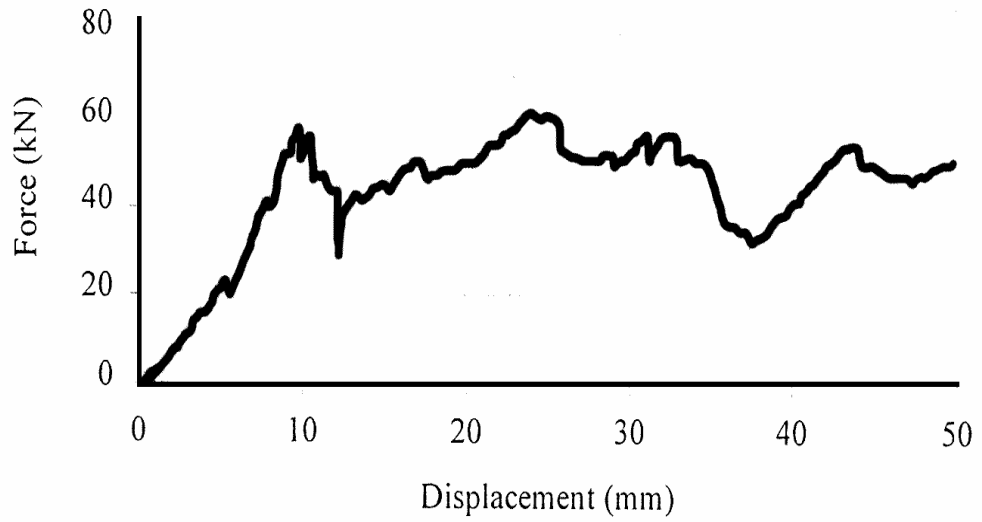


Figure A5.9. Experimental load-displacement response of CFRM tube crushed on 10mm radius plug-initiator (enhanced for clarity) [54].

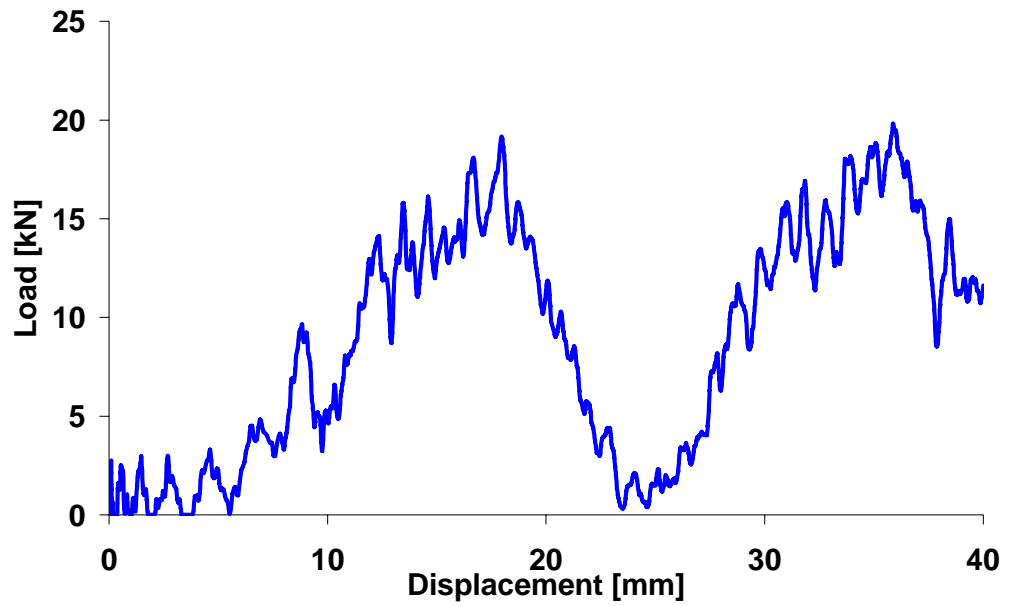


Figure A5.10. Simulated load-displacement response of CFRM tube crushed on 10mm radius plug initiator.

### A5.2.2 Toray

*5mm Radius*

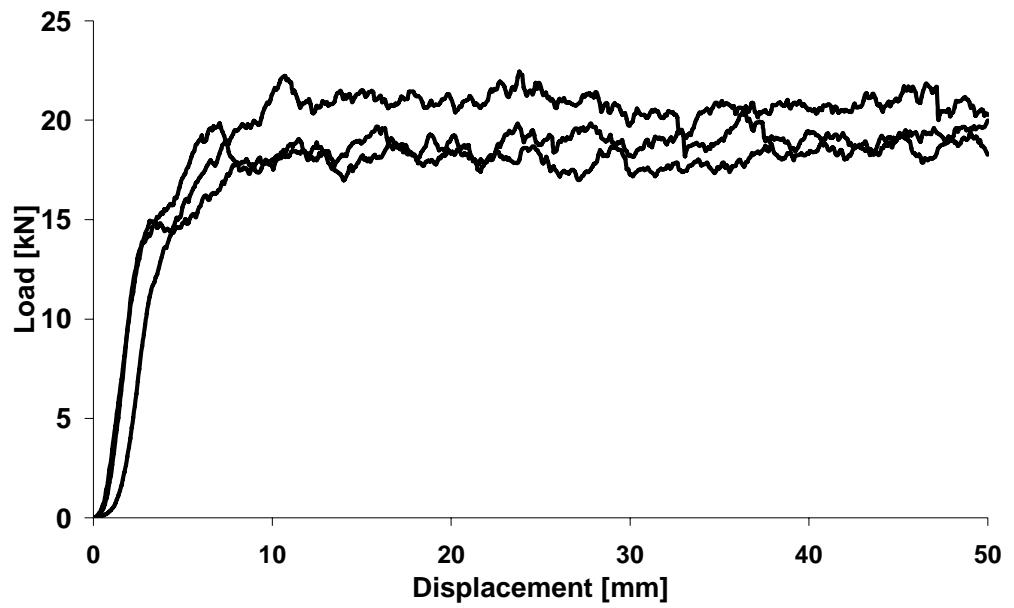


Figure A5.11. Experimental load-displacement response of 5mm radius plug initiated Toray tubes.

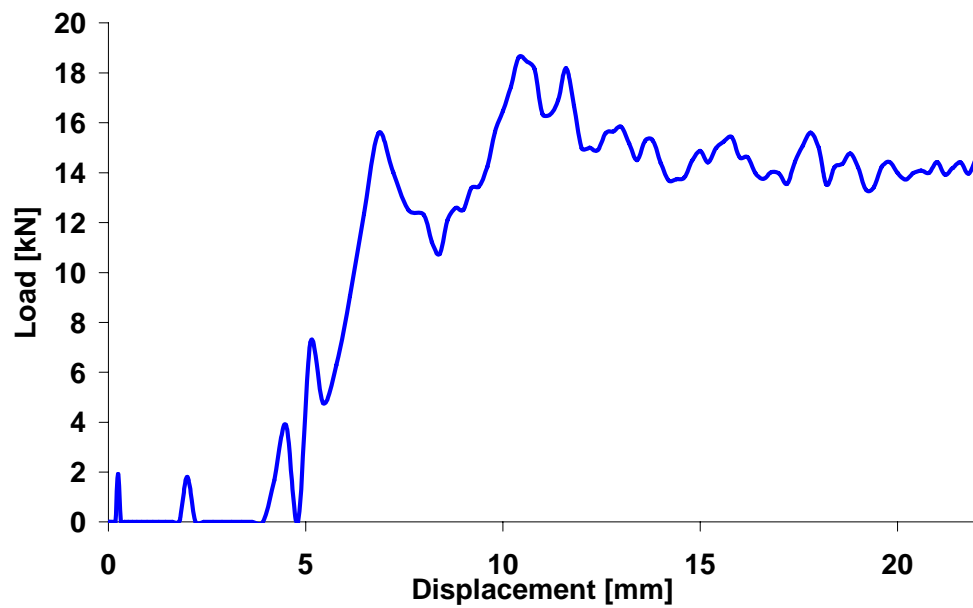


Figure A5.12. Simulated load-displacement response of 5mm radius plug initiated Toray tube.

7.5mm Radius

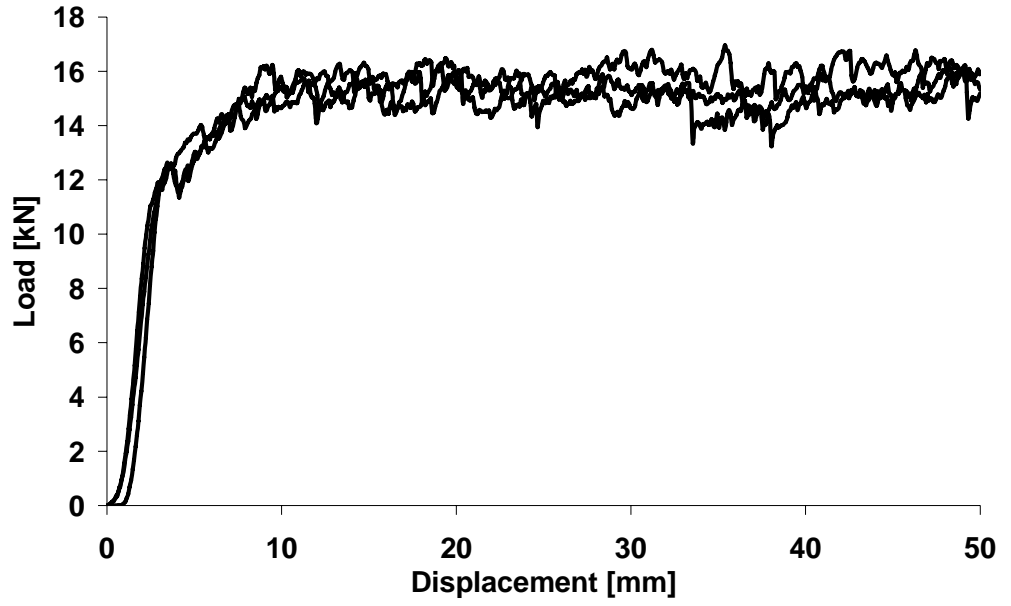


Figure A5.13. Experimental load-displacement response of 7.5mm radius plug initiated Toray tubes.

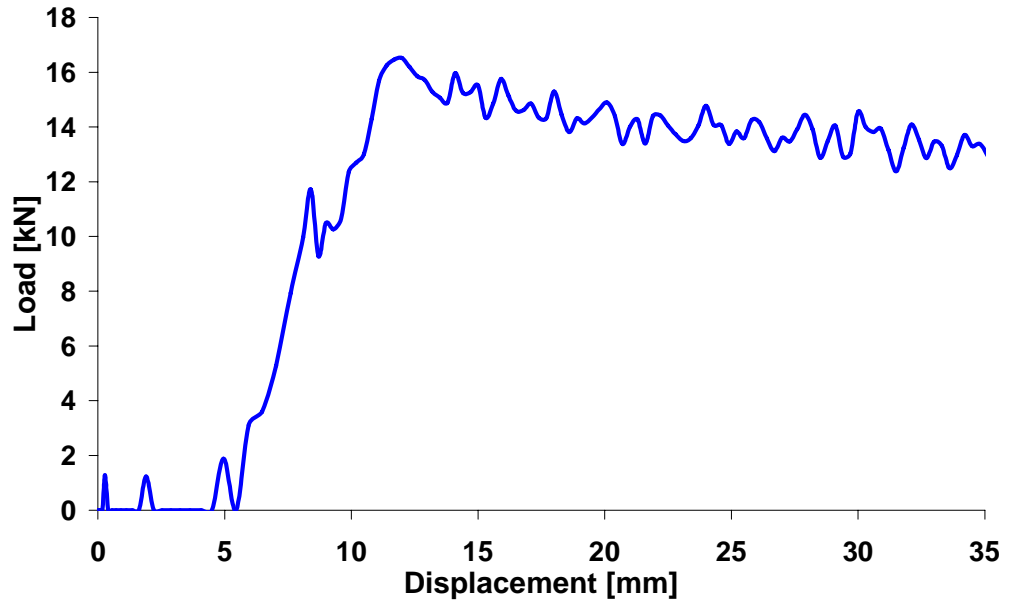


Figure A5.14. Simulated load-displacement response of 7.5mm radius plug initiated Toray tube.

*10mm Radius*

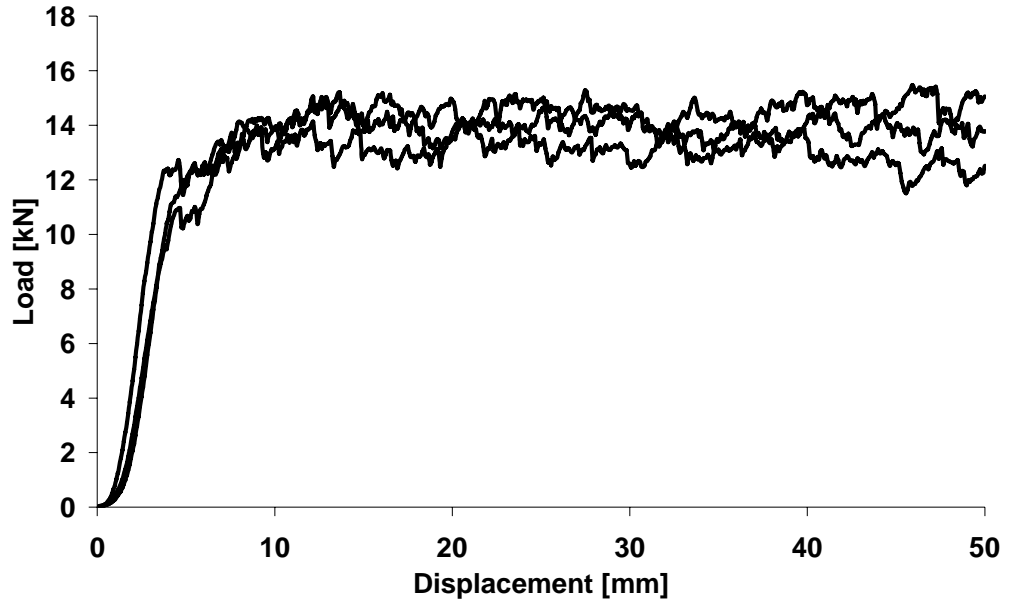


Figure A5.15. Experimental load-displacement response of 10mm radius plug initiated Toray tube.

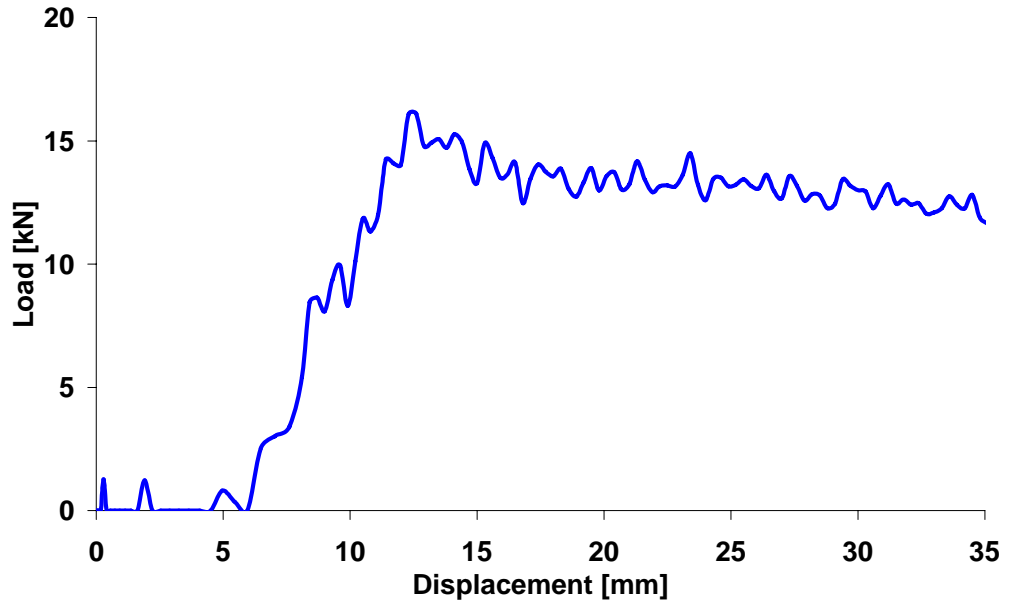


Figure A5.16. Simulated load-displacement response of 10mm radius plug initiated Toray tube.

## A6 Strain-Controlled Delamination - Tube Modelling Results

This section presents the graphical results of the tube simulations in which a strain-controlled delamination model was used, together with the respective experimental response.

### A6.1 Flat-platen load-displacement response

#### A6.1.1 CFRM

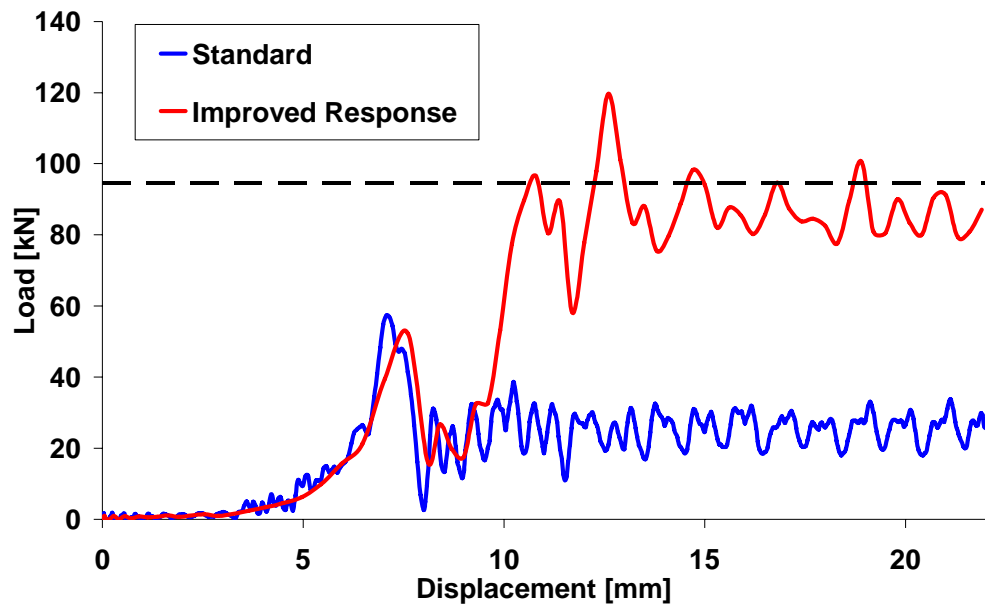


Figure A6.1. Load-displacement plot of CFRM flat-platen simulation using standard spotweld and improved spotweld delamination models. Dashed line represents the experimental steady-state load.

### A6.1.2 Toray

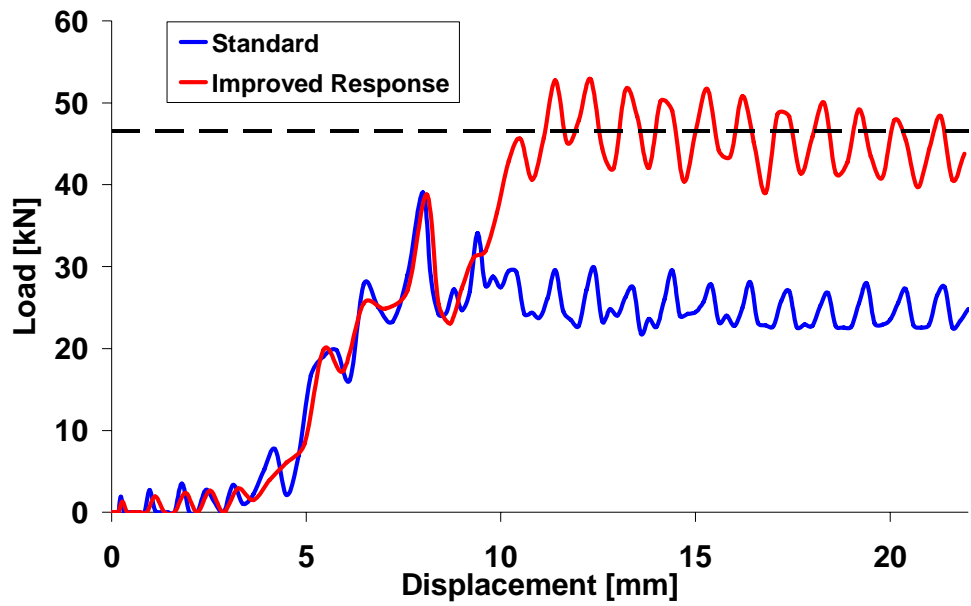


Figure A6.2. Load-displacement plot of Toray flat-platen simulation using standard spotweld and improved spotweld delamination models. Dashed line represents the experimental steady-state load.

## A6.2 Plug Initiator load-displacement response

### A6.2.1 CFRM

*5mm Radius*

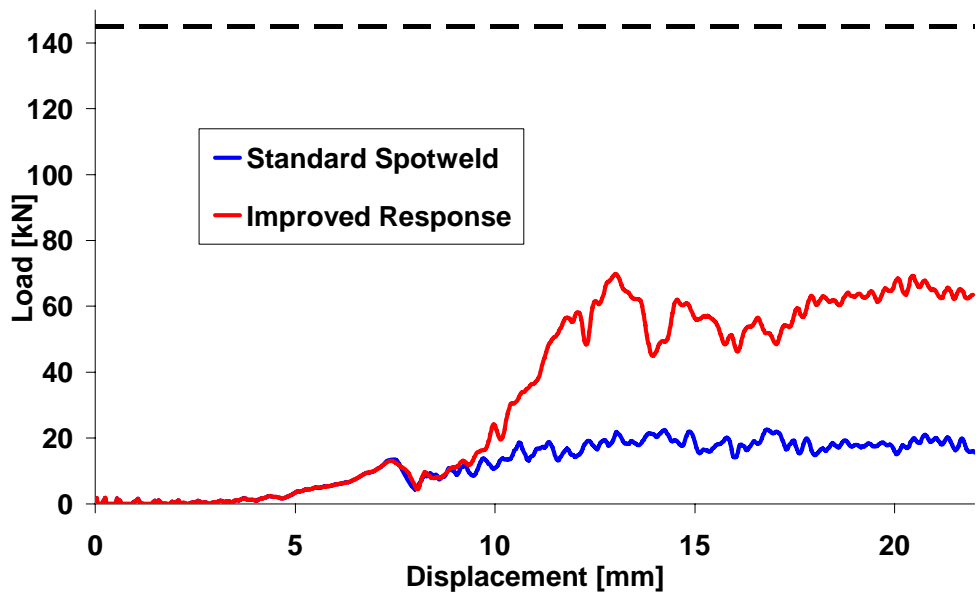


Figure A6.3. Load-displacement plot of CFRM 5mm radius plug initiated simulation using standard spotweld and improved spotweld delamination models. Dashed line represents the experimental steady-state load.

7.5mm Radius

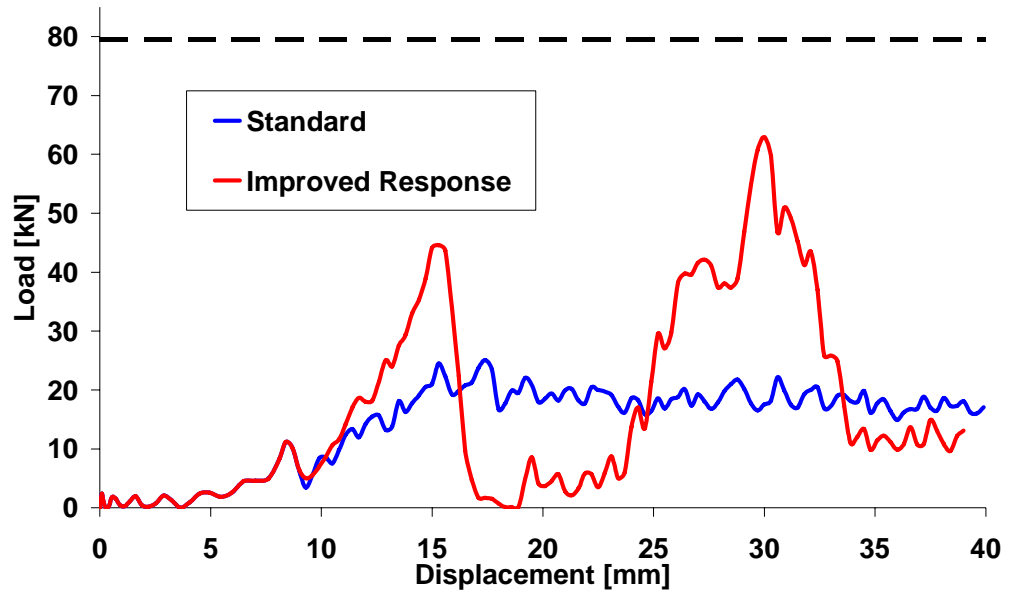


Figure A6.4. Load-displacement plot of CFRM 7.5mm radius plug initiated simulation using standard spotweld and improved spotweld delamination models. Dashed line represents the experimental steady-state load. NOTE: Improved response caused a change in the failure mode.

10mm Radius

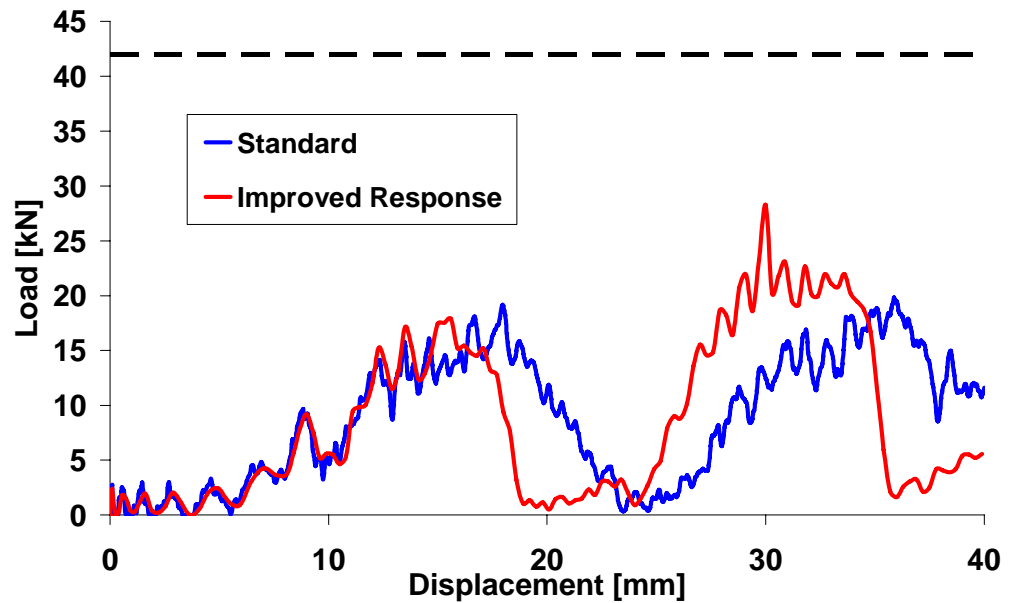


Figure A6.5. Load-displacement plot of CFRM 10mm radius plug initiated simulation using standard spotweld and improved spotweld delamination models. Dashed line represents the experimental steady-state load.

### A6.2.2 Toray

5mm Radius

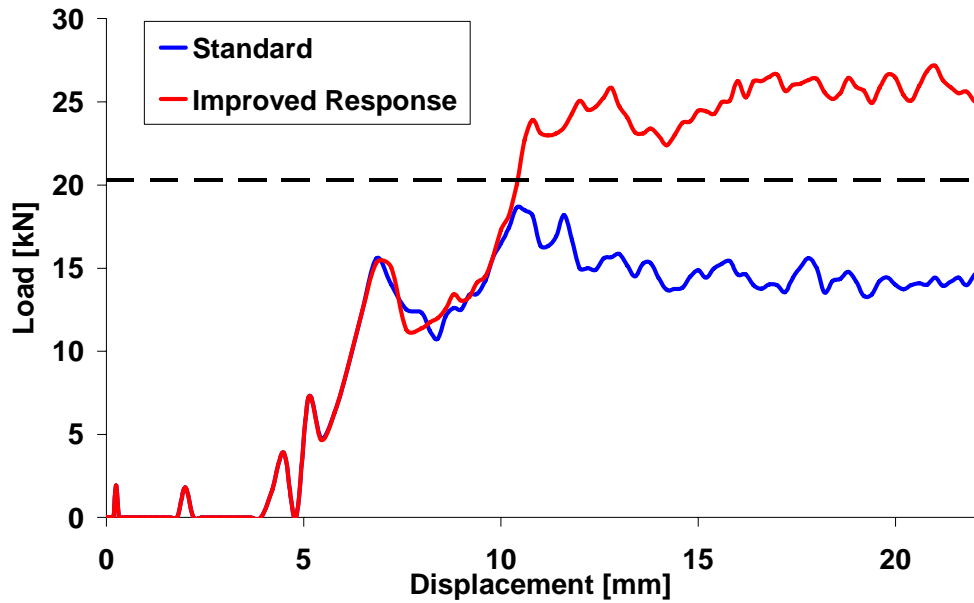


Figure A6.6. Load-displacement plot of Toray 5mm radius plug initiated simulation using standard spotweld and improved spotweld delamination models. Dashed line represents the experimental steady-state load.

7.5mm Radius

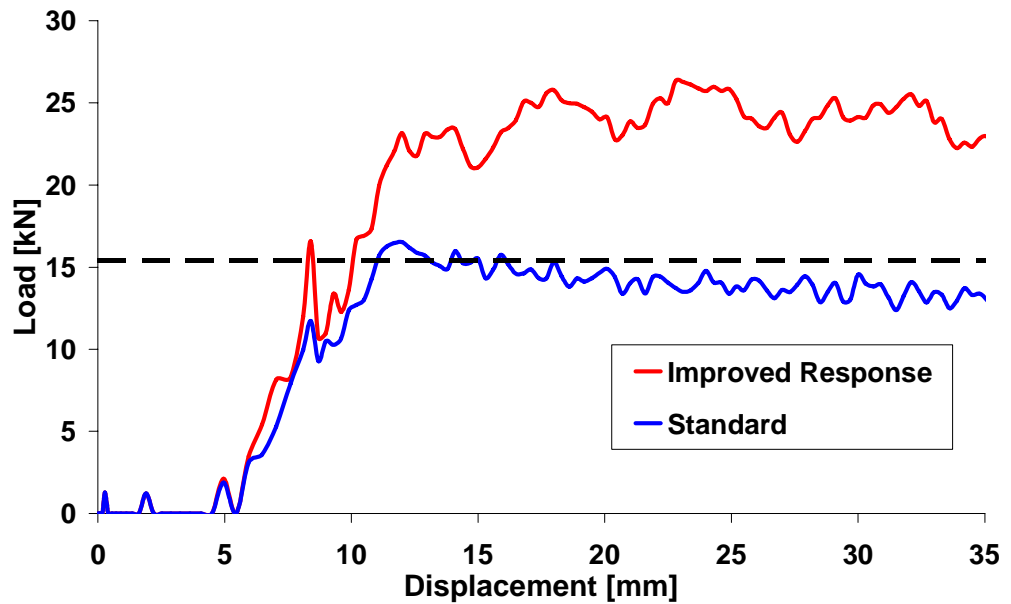


Figure A6.7. Load-displacement plot of Toray 7.5mm radius plug initiated simulation using standard spotweld and improved spotweld delamination models. Dashed line represents the experimental steady-state load.

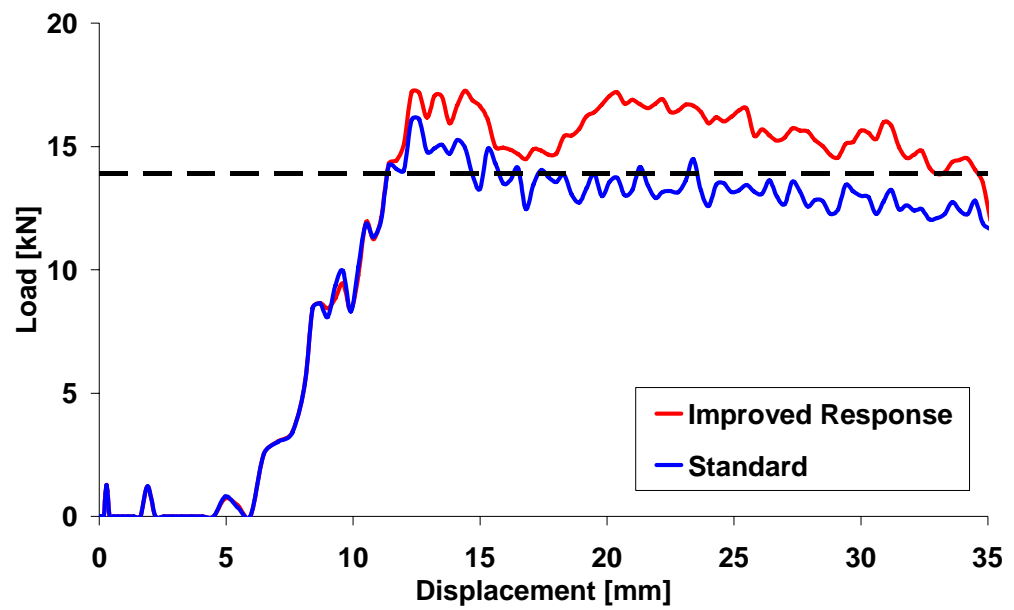
*10mm Radius*

Figure A6.8. Load-displacement plot of Toray 10mm radius plug initiated simulation using standard spotweld and improved spotweld delamination models. Dashed line represents the experimental steady-state load.

## References

1. Worley, H., *Road Traffic Accidents Increase Dramatically Worldwide*, <http://www.prb.org/Template.cfm?Section=PRB&template=/ContentManagement/ContentDisplay.cfm&ContentID=13658>. Accessed on 12/5/06
2. NCSA, *Traffic Safety Facts 2004*, <http://www-nrd.nhtsa.dot.gov/pdf/nrd-30/NCSA/TSF2004/809911.pdf>. Accessed on 12/5/06
3. Lu, G. and T. Yu, *Energy Absorption of Structures and Materials*. (2003): Woodhead Publishers Limited
4. Lloyd, J., *Road Deaths in 2004 Amongst Lowest Since 1950*, [http://www.ministers.dotars.gov.au/jl/releases/2005/January/17\\_2005.htm](http://www.ministers.dotars.gov.au/jl/releases/2005/January/17_2005.htm). Accessed on 13/5/06
5. *Report 102, Road Crash Costs in Australia*, <http://www.btre.gov.au/docs/reports/r102/r102.aspx>. Accessed on 12/5/06
6. Du Bois, P., *et al.*, *Vehicle Crashworthiness and Occupant Protection*. (2004). Southfield, MI, USA: American Iron and Steel Institute
7. Giovanni, B., A. Massimiliano, and C. Agostino. *Crushing Behaviour of Aluminium Circular Tubes*, In ATA-MAT. (1994). Tonino; Italy. p.137-144
8. Botkin, M., A. Browne, and N. Johnson. *Development of a Composite Front Structure for Automotive Crashworthiness*, In *Crashworthiness, Occupant Protection and Biomechanics in Transportation Systems*. (1998). Anaheim, California, USA: American Society of Mechanical Engineers. AMD-vol 230 and BED-vol 41. p.95-114
9. Das, S., *The Cost of Automotive Polymer Composites: A Review and Assessment of DoE's Lightweight Materials Composites Research*, Oak Ridge National Laboratory (ORNL), ORNL/TM-2000/283 (2001). p.36
10. Simunovic, S., M. Botkin, N. Johnson, and E. Zywiec. *Crashworthiness Simulation of Composite Automotive Structures*, In *13th Annual Engineering Society of Detroit Advanced Composites Technology Conference and Exposition*. (1998). Detroit, USA. p.30
11. Mamalis, A.G., D.E. Manolakos, M.B. Ioannidis, P.K. Kostazos, and E.C. Chirwa, *Static and Dynamic Axial Collapse of Fibreglass*

- Composite Thin-Walled Tubes: Finite Element Modelling of the Crush Zone*. IJCrash, (2003). **8**(3) p.247-254
12. Johnson, A.F. and D. Kohlgruber, *Modelling the Crash Response of Composite Structures*. Journal of Physics IV, (1997). **Colloque C3, Supplement to Journal of Physics III** p.981-986
  13. Lee, H.K. and S. Simunovic, *A Micromechanical Constitutive Damage Model of Progressive Crushing in Random Carbon Fiber Polymer Matrix Composites*, Oak Ridge National Laboratory (ORNL), ORNL/TM-1999/158 (1999). p.55
  14. Tay, T.E., K.H. Lee, S. Ramakrishna, and F. Shen, *Modelling the Crushing Behaviour of Composite Tubes*. Key Engineering Materials, (1998). **141-143** p.777-790
  15. McGregor, C., R. Vaziri, A. Poursartip, and X. Xiao. *Simulation of Energy Absorption in Braided Composite Tubes*, In American Society for Composites - 20th Technical Conference. (2006). Detroit, USA. p.16
  16. Feillard, P., *Crash Modelling of Automotive Structural Parts Made of Composite Materials*. SAE International Congress, (1999). **1999-01-0298** p.13-21
  17. Starbuck, J.M., S. Simunovic, and G.C. Jacob. *Test Methodologies for Determining Energy Absorbing Mechanisms of Automotive Composite Materials Systems*, In Future Car Congress. (2000). Arlington, VA, USA. SAE paper 2000-01-1575. p.6
  18. EuroNCAP, *European New Car Assessment Programme - Frontal Impact Testing Protocol - Version 4.0*, [www.euroncap.com](http://www.euroncap.com). Accessed on 12/02/06
  19. Beard, S.J. and F.K. Chang, *Energy Absorption of Braided Composite Tubes*. IJCrash, (2002). **7**(2) p.191-206
  20. Takahashi, M., *Development of High Strength Steels for Automobiles*, Nippon Steel Technical Report, 88 (2003). p.6
  21. Thornton, P.H. and R.A. Jeryan, *Crash Energy Management in Composite Automotive Structures*. International Journal of Impact Engineering, (1988). **7**(2) p.167-180
  22. Brylawski, M.M. and A.B. Lovins, *Advanced Composites: The Car is at the Crossroads*, Hypercar, Inc., (1998). p.15

23. Brosius, D., *Carbon Fiber Gains Traction with Automakers*, in *Composites Technology*. (2003)
24. Mills, A., *Carbon Fibre reinforced Composite Car*, [http://www.azom.com/details.asp?ArticleID=1662#\\_Composite\\_Car\\_bodies](http://www.azom.com/details.asp?ArticleID=1662#_Composite_Car_bodies). Accessed on 12/11/03
25. Soutis, C. and V. Ramany Bala Poubady, *Evaluation of Crush Energy Absorption of Woven CFRP Laminates*. *Advanced Composite Letters*, (1998). **7**(1) p.23-27
26. Jacob, G.C., J.F. Fellers, S. Simunovic, and M.J. Starbuck, *Energy Absorption in Polymer Composite Materials for Automotive Crashworthiness*. *Journal of Composite Materials*, (2002). **36**(7) p.813-884
27. Lee, H.K. and S. Simunovic, *A Damage Mechanics Model of Crack-Weakened, Chopped Fiber Composites Under Impact Loading*. *Composites*, (2002). **33** p.25-34
28. Carruthers, J.J., A.P. Kettle, and A.M. Robinson, *Energy Absorption Capability and Crashworthiness of Composite Material Structures: A Review*. *Applied Mechanics Reviews*, (1998). **51**(10) p.635-649
29. Garcia, J.G., J. Marsolek, and H.G. Reimerdes, *Determination of the Energy Absorption of Cylindrical Shells Under Axial Loading by Analysis of the Dynamic Buckling and Folding Process*. *IJCrash*, (1999). **4**(4) p.351-364
30. Abramowicz, W. and N. Jones, *Dynamic Axial Crushing of Circular Tubes*. *International Journal of Impact Engineering*, (1984). **2**(3) p.263-281
31. Fernie, R., *Loading Rate Effects on the Energy Absorption of Lightweight Tubular Crash Structures*, PhD thesis submitted at School of Mechanical, Material, Manufacturing Engineering and Management, University of Nottingham. (2002).
32. Alexander, J.M., *An Approximate Analysis of the Collapse of Thin Cylindrical Shells Under Axial Loading*. *Journal of Mechanics and Applied Mathematics*, (1960). **13** p.10
33. Wierzbicki, T. and S.U. Bhat, *A Moving Hinge Solution for Axisymmetric Crushing of Tubes*. *International Journal of Mechanical Sciences*, (1986). **28**(3) p.135-151
34. Andrews, K.R.F., G.L. England, and E. Ghani, *Classification of the Axial Collapse of Cylindrical Tubes Under Quasi-Static Loading*. *International Journal of Mechanical Sciences*, (1983). **25** p.687-696

35. Guillow, S.R., G. Lu, and R.H. Grzebieta, *Quasi-static Compression of Thin-Walled Circular Aluminium Tubes*. International Journal of Mechanical Sciences, (2001). **43** p.2103-2123
36. Ramakrishna, S. and H. Hamada, *Energy Absorption Characteristics of Crash Worthy Structural Composite Materials*. Key Engineering Materials, (1998). **141-3** p.585-620
37. Singace, A.A. and H. El-Sobky, *Behaviour of Axially Crushed Corrugated Tubes*. International Journal of Mechanical Sciences, (1997). **39**(3) p.249-268
38. Stronge, W.J., T.X. Yu, and W. Johnson, *Long Stroke Energy Dissipation in Splitting Tubes*. International Journal of Mechanical Sciences, (1983). **25**(9-10) p.637-647
39. Mamalis, A.G., *et al.*, *Crashworthy Capability of Composite Material Structures: A Review*. Composite Structures, (1997). **37**(2) p.109-134
40. Thornton, P.H., *Energy Absorption in Composite Structures*. Journal of Composite Materials, (1979). **13**(July) p.247-262
41. Gupta, N.K., R. Velmurugan, and S.K. Gupta, *An Analysis of Axial Crushing of Composite Tubes*. Journal of Composite Materials, (1997). **31**(13) p.1262-1286
42. Hull, D., *A Unified Approach to Progressive Crushing of Fibre-Reinforced Composite Tubes*. Composites Science and Technology, (1991). **40** p.377-421
43. Hamada, H. and S. Ramakrishna, *A FEM Method for Prediction of Energy Absorption Capability of Crashworthy Polymer Composite Materials*. Journal of Reinforced Plastics and Composites, (1997). **16**(3) p.226-242
44. Farley, G.L., *Energy Absorption of Composite Materials*. Journal of Composite Materials, (1983). **17**(5) p.267-279
45. Mamalis, A.G., D.E. Manolacos, G.A. Demosthenous, and M.B. Ioannidis, *Analysis of Failure Mechanisms Observed in Axial Collapse of Thin-Walled Circular Fibreglass Composite Tubes*. Thin Walled Structures, (1996). **24** p.335-352
46. Farley, G., R. Wolterman, and J. Kennedy, *The Effects of Crushing Surface Roughness on the Crushing Characteristics of Composite Tubes*. Journal of the American Helicopter Society, (1992). **37** p.53-60

47. Fairfull, A.H. and D. Hull, *Energy Absorption of Polymer Matrix Composite Structures: Frictional Effects*, in *Structural Failure*. (1988). p.255-279
48. Mamalis, A.G., D.E. Manolakos, G.A. Demosthenous, and M.B. Ioannidis, *Analytical Modelling of the Static and Dynamic Axial Collapse of Thin-Walled Fibreglass Composite Conical Shells*. *International Journal of Impact Engineering*, (1997). **19**(5-6) p.477-492
49. Farley, G.L., *Analogy for the Effect of Material and Geometrical Variables on Energy-Absorption Capability of Composite Tubes*. *Journal of Composite Materials*, (1992). **26**(1) p.78-89
50. Farley, G.L. and R. Jones, M., *Prediction of the Energy-Absorption Capability of Composite Tubes*. *Journal of Composite Materials*, (1992). **26**(3) p.388-404
51. Farley, G.L. and R. Jones, *Crushing Characteristics of Continuous Fiber-Reinforced Composite Tubes*. *Journal of Composite Materials*, (1992). **26**(1) p.37-50
52. Inai, R., *et al.*, *Experimental Investigation on the Crushing Properties of Carbon Fibre Braided Composite Tubes*. *IJCrash*, (2003). **8**(5) p.513-521
53. Hamada, H. and S. Ramakrishna, *Comparison of Static and Impact Energy Absorption of Carbon Fiber/PEEK Composite Tubes*, in *Composite Materials: Testing and Design*, R.B. Deo and C.R. Saff, Editors. (1996). ASTM STP 1274
54. Cooper, E., *An Elastic-Plastic Finite Element Model for Composite Crash Structures*, PhD thesis submitted at School of Mechanical, Material, Manufacturing Engineering and Management, University of Nottingham. (2002).
55. Duckett, M.J., *Rate Dependent Effects on the Energy Absorption and Material Properties of Polymer Composites*, PhD thesis submitted at School of Mechanical, Materials, Manufacturing Engineering and Management, University of Nottingham. (2001).
56. Curtis, C.D., *Energy Absorption and Crush Behaviour of Composite Tubes*, PhD thesis submitted at School of Mechanical, Materials, Manufacturing Engineering and Management, University of Nottingham. (2000).
57. Mamalis, A.G., D.E. Manolakos, G.A. Demosthenous, and M.B. Ioannidis, *The Static and Dynamic Axial Crumpling of Thin-Walled Fibreglass Composite Square Tubes*. *Composite Structures*, (1997). **34**(1) p.77-90

58. Mamalis, A.G., D.E. Manolakos, G.A. Demosthenous, and M.B. Ioannidis, *The Static and Dynamic Axial Collapse of Fibreglass Composite Automotive Frame Rails*. *Composite Structures*, (1996). **34** p.77-90
59. Mamalis, A.G., Y. Yuan, and G. Viegelahn, *Collapse of Thin-Wall Composite Sections Subjected to High Speed Axial Loading*. *International Journal of Vehicle Design*, (1992). **13**(5/6) p.564-579
60. Fleming, D.C. and A.J. Vizzini, *The Effect of Side Loads on the Energy Absorption of Composite Structures*. *Journal of Composite Materials*, (1992). **26**(4) p.486-500
61. Karbhari, V.M. and X. Chaoling, *Energy Absorbing Characteristics of Circular Frustra*. *IJCrash*, (2003). **8**(2) p.471-479
62. Farley, G.L., *The Effects of Crushing Speed on the Energy-Absorption Capability of Composite Tubes*. *Journal of Composite Materials*, (1991). **25** p.1314-1330
63. Karbhari, V.M. and J.E. Haller, *Rate and Architecture Effects on Progressive Crush of Braided Tubes*. *Composite Structures*, (1998). **43** p.93-108
64. Kohlgruber, D. and A. Kamoulakos. *Validation of Numerical Simulation of Composite Helicopter Sub-floor Structures Under Crash Loading*, In American Helicopter Society 54th Annual Forum. (1998). Washington DC, USA: American Helicopter Society. p.340-349
65. Ribeaux, M. and N. Warrior. *Effect of Impact Damage on the Specific Energy Absorption of Glass/Polyester Composites*, In American Society for Composites 17th Technical Conference. (2002). Purdue University, USA.
66. Davis, B., P. Gramann, and A. Rios. *Using Computer Aided Engineering to Design Better Thermoset Composite Parts*, In SPE Automotive Composites Conference. (2002). Troy, Michigan.
67. Sigalas, I., M. Kumosa, and D. Hull, *Trigger Mechanisms in Energy-Absorbing Glass Cloth/Epoxy Tubes*. *Composite Science and Technology*, (1991). **40**(3) p.265-287
68. Schultz, M.R., *Energy Absorption Capacity of Graphite-Epoxy Composite Tubes*, PhD thesis submitted at Virginia Polytechnic Institute and State University, Virginia Polytechnic Institute and State University. (1998).
69. Astrom, B.T., *Manufacturing of Polymer Composites*. (1997). London: Chapman and Hall

70. Peters, S.T., *Handbook of Composites*. (1997): Kluwer Academic Publishers
71. Gauthier, M.M., *et al.*, *Engineered Materials Handbook - Desk Edition*. (1995). Materials Park, USA: ASM International. p.1317
72. Saito, H., E. Chirwa, C., R. Inai, and H. Hamada, *Energy Absorption of Braiding Pultrusion Process Composite Rods*. *Composite Structures*, (2002). **55**(4) p.407-417
73. Zhang, J. and B.L. Fox. *Manufacturing Process Effects on the Mode I Interlaminar Fracture Toughness and Nanocreep Properties of CFRP*, In Proceedings of the 26th International SAMPE Europe Conference. (2005). Paris, April 5-7. p.537-543
74. Davies, L.W., *et al.* *Effect of Cure Cycle Heat Transfer Rates on the Physical Properties of an Epoxy Matrix Composite*, In 5th Asian-Australasian Conference on Composite Materials (ACCM-5). (2006). Hong-Kong.
75. Shelton, J. *Vehicle Safety Engineering - An Australian Perspective on the Global Environment*, In ICrash. (2002). Melbourne, Australia.
76. Nguyen, M.Q., D.J. Elder, J. Bayandor, R.S. Thomson, and M.L. Scott, *A Review of Explicit Finite Element Software for Composite Impact Analysis*. *Journal of Composite Materials*, (2005). **39**(4) p.375-386
77. Jacob, P. and L. Goulding, *An Explicit Finite Element Primer*. (2002): NAFEMS Ltd. p.127
78. Hibbitt, Karlson, and Sorensen, *ABAQUS User Manual - Version 5.8*. (1998)
79. Johnson, A.F. and A.K. Pickett. *Impact and Crash Modelling of Composite Structures: A Challenge for Damage Mechanics*, In European Conference on Computational Mechanics - ECCM'99. (1999). Munich, Germany.
80. Zywicz, E., *et al.*, *Modeling of Composite Materials for Energy Absorption*. (2004)
81. Lee, H.K. and S. Simunovic, *Constitutive Modeling and Impact Simulation of Random Carbon Fiber Polymer Matrix Composites for Automotive Applications*. Society of Automotive Engineers, (1998). **00FCC-120**
82. Tabiei, A. and I. Ivanov, *Materially & Geometrically Nonlinear Woven Composite Micro-Mechanical Model with Failure for Finite Element*

- Simulations*. International Journal of Nonlinear Mechanics, (2004). **39** p.175-188
83. Zhu, C. and C.T. Sun, *Micromechanical Modeling of Fiber Composites Under Off-Axis Loading*. Journal of Thermoplastic Composite Materials, (2003). **16**(July) p.333-345
  84. Williams, K.V., A.M. Floyd, R. Vaziri, and A. Poursartip. *Numerical Simulation of In-Plane Damage Progression in Laminated Composite Plates*, In 12th International Conference on Composite Materials. (1999). Paris, France. ICCM/12.
  85. Zheng, X., R.K. Goldberg, W.K. Binienda, and G.D. Roberts. *LS-DYNA Implementation of Polymer Matrix Composite Model Under High Strain Rate Impact*, In 35th International Technical Conference sponsored by the midwest chapter of the society for the Advancement of Materials and Process Engineering. (2003). Dayton, Ohio: NASA. NASA/TM-2003-212583. p.15
  86. Tabiei, A., W. Yi, and R.K. Goldberg. *Strain Rate Dependent Micromechanical Composite Material Model for Finite Element Impact Simulation*, In 7th International LS-DYNA User's Conference. (2002). Dearborn, USA: Livermore Software Technology Corporation (LSTC). p.22
  87. Hallquist, J.O., *LS-DYNA Theoretical Manual*. (1998). Livermore: Livermore Software Technology Corporation. p.498
  88. Fleming, D.C. *Modeling Delamination Growth in Composites using MSC.Dytran*, In 2nd MSC Worldwide Automotive Conference. (2000). Dearborn, USA: MSC.
  89. Lourenco, N.F.S., *Predictive Finite Element Method for Axial Crush of Composite Tubes*, PhD thesis submitted at School of Mechanical, Materials, Manufacturing, Engineering and Management, University of Nottingham. (2002).
  90. Silcock, M., W. Hall, B.L. Fox, and N. Warrior, *Finite Element Modelling of Metallic Tubular Crash Structures with an Explicit Code*. International Journal of Vehicle Safety, (2006). **Accepted 15/05/06**
  91. Morthorst, M. and P. Horst, *Failure Model for Composite Materials under Quasi-Static Crushing Conditions*. Journal of Strain Analysis, (2004). **39**(5) p.411-421
  92. Botkin, M., N. Johnson, E. Zywiec, and S. Simunovic. *Crashworthiness Simulation of Composite Automotive Structures*, In 13th Annual Engineering Society of Detroit Advanced Composites Technology Conference and Exposition. (1998). Detroit, USA.

93. Hamada, H., S. Ramakrishna, Z. Maekawa, M. Nakamura, and T. Nishiwaki. *Energy Absorption Characteristics of Composite Tubes with Different Cross-Sectional Shapes*, In 10th Annual ASM/ESD Advanced Composites Conference. (1994). Dearborn, Michigan, USA.
94. Hamada, H. and S. Ramakrishna, *Effect of Fiber Orientation on the Energy Absorption Capability of Carbon Fiber/PEEK Composite Tubes*. Journal of Composite Materials, (1996). **30** p.947-963
95. Pinho, S.T., P.P. Camanho, and M.F. de Moura, *Numerical Simulation of the Crushing Process of Composite Materials*. International Journal of Crashworthiness, (2004). **9**(3) p.263-276
96. Laananen, D.H. and A.O. Bolukbasi, *Prediction of Energy Absorption in Composite Stiffeners*. Composite Structures, (1995). **32** p.173-186
97. Bolukbasi, A.O. and D.H. Laananen, *Analytical and Experimental Studies of Crushing Behavior in Composite Laminates*. Journal of Composite Materials, (1995). **29**(8) p.1117-1123
98. Deslauriers, P.F., D.S. Cronin, and A. Duquette. *Numerical Modeling of Woven Carbon Composite Failure*, In 8th International LS-DYNA User's Conference. (2004). Dearborn, Michigan.
99. Hormann, M. and M. Wacker. *Simulation of the Crash Performance of Crash Boxes Based on Advanced Thermoplastic Composite*, In 5th European LS-DYNA User's Conference. (2005). Birmingham, UK. 5d-31.
100. Xiao, X., N. Johnson, and M. Botkin. *Challenges in Composite Tube Crash Simulations*, In American Society for Composites 18th Technical Conference. (2003). Gainesville, Florida, USA. ASC 154.
101. Smith, J.R., L.C. Bank, and M.E. Plesha. *Preliminary Study of the Behavior of Composite Material Box Beams Subjected to Impact*, In 6th International LS-DYNA User's Conference. (2000). Dearborn, USA. 11. p.1-15
102. Fleming, D.C., *Delamination Modeling of Composites for Improved Crash Analysis*, NASA, NASA/CR-1999-209725 (1999)
103. Reedy, E.D., *Modeling the Initiation and Growth of Delaminations in Composite Structures*. Journal of Composite Materials, (1997). **31**(8) p.812-831
104. Meo, M. and E. Thieulot, *Delamination Modelling in a Double Cantilever Beam*. Composite Structures, (2005). **71** p.429-434

105. Rybicki, E.F. and M.F. Kanninen, *A Finite Element Calculation of Stress Intensity Factors by a Modified Crack Closure Integral*. Engineering Fracture Mechanics, (1977). **9** p.931-938
106. Sankar, B.V. and S. Hu, *Dynamic Delamination Propagation in Composite Beams*. Journal of Composite Materials, (1991). **25** p.1414-1426
107. Jiang, W.G., S.R. Hallett, and M.R. Wisnom. *Modelling of Damage in Composite Materials using Interface Elements*, In 5th European LS-DYNA Users Conference. (2005). Birmingham, UK.
108. Fleming, D.C. and E.L. Fasanella. *Modeling the Crushing of a Scaled Composite Fuselage Subfloor Structure*, In 15th American Society of Composites (ASC) Technical Conference. (2000). College Station, USA.
109. Coenen, V., *et al.* *A Feasibility Study of Quickstep Processing of an Aerospace Composite Material*, In SAMPE Europe. (2005). Paris, France, April 5-7. p.470-475
110. Li, W. and K. Miwa, *Quick Cure Carbon Fiber Reinforced Epoxy Resin*, Toray Composites (America) Inc., (2003).
111. Vacher, P., S. Dumoulin, F. Morestin, and S. Mguil-Touchal, *Bidimensional Strain Measurement using Digital Images*. Proceedings of the IMECHE Part C Journal of Mechanical Engineering Science, (1999). **213**(8) p.811-817
112. *Prepreg Technology*,  
<http://www.hexcel.com/NR/rdonlyres/230A6C2A-FDFA-4EC7-B048-E4EB28E3BC8C/0/PrepregTechnology2.pdf>. Accessed on 21/09/06
113. *SP Systems - CBS ST86 Product Data Sheet*,  
[http://www3.gurit.com/pdfs/SPRINT/CBS\\_86.pdf](http://www3.gurit.com/pdfs/SPRINT/CBS_86.pdf). Accessed on 21/09/06
114. Hull, D. and T.W. Clyne, *An Introduction to Composite Materials*. 2nd ed. (1996). Cambridge, UK: University of Cambridge Press Syndicate. p.326
115. Fang, X. and D.A. Scola, *Investigation of Microwave Energy to Cure Carbon Fiber Reinforced Phenylethynyl-Terminated Polyimide Composites, PETI-5/IM7*. Journal of Polymer Science: Part A: Polymer Chemistry, (1999). **37**(24) p.4616-4628
116. Schweizerhof, K., W. Schmid, and H. Klamser. *Improved Spotweld Simulation with LS-DYNA - Numerical Simulation and Comparison to*

- Experiments*, In 3rd European LS-DYNA Conference. (2001). Paris, France.
117. Matzenmiller, A., J. Lubliner, and R.L. Taylor, *A Constitutive Model for Anisotropic Damage in Fiber-Composites*. Mechanics of Materials, (1995). **20** p.125-152
118. Schweizerhof, K., K. Weimar, T. Munz, and T. Rottner. *Crashworthiness Analysis with Enhanced Composite Material Models in LS-DYNA - Merits and Limits*, In LS-DYNA World Conference. (1998). Detroit, USA. p.17
119. Agaram, V., S.S. Bilkhu, S. Fidan, M. Botkin, and N. Johnson. *Simulation of Controlled Failure of Automotive Composite Structures with LS-DYNA*, In Annual Advanced Composites Conference. (1997).
120. Bilkhu, S.S., M. Founas, W. Fong, and V. Agaram. *Dynamic Response of CSM Composite Plates - Simulation Using Material #58 in LS-DYNA3D*, In Annual Advanced Composites Conference. (1997). Detroit, Michigan.
121. Hashin, Z., *Failure Criteria for Unidirectional Composites*. Journal of Applied Mechanics, (1980). **47**(June) p.329-334
122. DeTeresa, S., *et al.*, *Experimental Results in Support of Simulating Progressive Crush in Carbon-Fiber Textile Composites*, Lawrence Livermore National Laboratory, UCRL-ID-143287 (2001). p.114
123. Mamalis, A.G., D.E. Manolakos, G.A. Demosthenous, and M.B. Ioannidis, *Crashworthiness of Composite Thin-Walled Structural Components*. (1998). Lancaster, USA: Technomic Publishers
124. *Altair Hypermesh User's Guide, Version 6.0*. (2003): Altair Engineering
125. Nailadi, C.L., D.F. Adams, and D.O. Adams, *An Experimental and Numerical Investigation of the Free Edge Problem in Composite Laminates*. Journal of Reinforced Plastics and Composites, (2002). **21**(1) p.3-39
126. Cooper, E. and N. Warrior. *An Elastic-Plastic Material Model for Finite Element Analysis of Composite Tubes Crushed using Plug Initiators*, In ICrash. (2002). Melbourne, Australia.
127. Simunovic, S., P.K.V.V. Nukala, J. Fekete, D. Meuleman, and M. Milititsky, *Modeling of Strain-Rate Effects in Automotive Impact*. Society of Automotive Engineers, (2003). **2003-01-1383**

128. Silcock, M. and N. Graham, *Composite Tube Production*, Quickstep Technologies Pty Ltd, (2006). PCT/AU2006/000382
129. Otubushin, A., *Detailed Validation of a Non-Linear Finite Element Code using Dynamic Axial Crushing of a Square Tube*. International Journal of Impact Engineering, (1998). **21**(5) p.349-368
130. Mamalis, A.G., D.E. Manolakos, M.B. Ioannidis, and G. Hassiotis, *Finite Element Simulation of the Axial Collapse of Thin-wall Square Frustra*. IJCrash, (2001). **6**(2) p.155-164
131. Webb, D.C., J. Webster, and K. Kormi, *Finite Element Simulation of Energy Absorption Devices under Axial Static Compressive and Impact Loading*. International Journal of Crashworthiness, (2001). **6**(3) p.399-423
132. *MATLAB User's Guide, Version 5.2*. (1998): The Mathworks, Inc.
133. Belytschko, T. and C.S. Tsay, *Explicit Algorithms for Nonlinear Dynamics of Shells*. American Society of Mechanical Engineers, (1981). **AMD-Vol. 48** p.209-231
134. Belytschko, T., J. Lin, and C.S. Tsay, *Explicit Algorithms for Nonlinear Dynamics of Shells*. Computer Methods in Applied Mechanics and Engineering, (1984). **42** p.225-251
135. Konter, A., *How to Undertake a Contact and Friction Analysis*. (2000): NAFEMS Ltd.